NASA CONTRACTOR REPORT

NASA CR-1517

NASA CR-1517

HYDRODYNAMIC JOURNAL BEARING TEST AND ANALYSIS

by R. J. Rossbach

Prepared by
GENERAL ELECTRIC COMPANY
Cincinnati, Ohio
for Lewis Research Center

NATIONAL AERONAUTICS AND SPACE ADMINISTRATION • WASHINGTON, D. C. • JUNE 1970

1. Report No. NASA CR-1517	2. Government Accession No.	3. Recipient's Catalog No.
4. Title and Subtitle HYDRODYNAMIC JOURNAL BEARING TEST AND ANALYSIS		5. Report Date June 1970
		6. Performing Organization Code
7. Author(s) R. J. Rossbach		8. Performing Organization Report No. GESP-133
9. Performing Organization Name and Address General Electric Company Missile and Space Division Cincinnati, Ohio 45215		10. Work Unit No.
		11. Contract or Grant No. NAS 3-6479
		13. Type of Report and Period Covered Contractor Report
12. Sponsoring Agency Name and Address National Aeronautics and Space Administration Washington, D.C. 20546		
		14. Sponsoring Agency Code

15. Supplementary Notes

1. Journal Bearing (handwritten)

16. Abstract

Steady-state and dynamic test data, carried out with distilled water at 75 and 120°F as the lubricant, are presented for a pivoted-pad and a three-lobe bearing having an L/D of 1.0 and a preload (ratio of assembled to machined clearance) of approximately 0.5. Tests were made with the bearing centers aligned and misaligned to determine the effect on bearing stability. The test series with artificially misaligned bearings established (but to a known degree) what could occur with unfavorable thermal gradients. The maximum misalignment for the selected bearing and shaft combination was 467 seconds. Because of the requirement to determine the effects of misalignment on bearing performance, the diametral clearance selected for the three-lobe bearing was 5 mils while that for the self-aligning four-pad pivoted-pad bearing was 3.125 mils. The shaft diameter was 1.25 inches. The pivoted-pad bearing was also subjected to the selective fixture of pads. The speed and steady load test ranges were 8,000 to 32,000 rpm and 0 to 70 lb/bearing, respectively. The objective was to determine the performance change resulting from the misalignment or, in the case of the pivoted-pad bearing, the effect of fixing a pad. The pivoted-pad bearing was stable at all speeds up to 31,000 rpm and the three lobe bearing was stable up to rotational speeds of 26,000 rpm with elevated lubricant supply pressure.

17. Key Words *(Suggested by Author(s))* Bearing Misalignment Hydrodynamic Stability Journal	18. Distribution Statement Unclassified - unlimited		
19. Security Classif. (of this report) Unclassified	20. Security Classif. (of this page) Unclassified	21. No. of Pages 127	22. Price* $3.00

*For sale by the Clearinghouse for Federal Scientific and Technical Information
Springfield, Virginia 22151

FOREWORD

The research described herein was conducted by the General Electric Company under NASA Contract NAS 3-6479. Mr. J. P. Joyce, of the NASA Lewis Research Center Space Power Systems Division, was the Project Manager for NASA, and Mr. E. Schnetzer was the Project Manager for the General Electric Company. The report was originally issued as General Electric report GESP-133.

TABLE OF CONTENTS

LIST OF ILLUSTRATIONS

LIST OF TABLES

I. SUMMARY

The attempt to simplify Rankine cycle space power systems by using the working fluid as a lubricant for the turbomachinery and alternator has led to the necessity of investigating bearings operating with low viscosity fluids at virtually no unidirectional load. The combination of a low-viscosity lubricant, very light radial load and high rotational speeds lead to bearing instability in the form of fractional frequency whirl with most fixed geometry self-acting journal bearings.

Tests of the three-lobe and the pivoted-pad bearings were carried out without fractional frequency whirl to a speed of 21,000 rpm on the Low Viscosity Bearing Stability Investigation, NASA Contract NAS3-2111, and the results are presented in the report NASA-CR-54039. NASA requested further tests with: (1) improved instrumentation, (2) the capability of testing with a known misalignment and (3) provisions for the selective fixture of pads on the pivoted-pad bearing.

In the present program the effects of steady unidirectional load, speed, dynamic unbalance, and bearing misalignment upon the steady-state and dynamic performance of the two types of bearing with a journal diameter of 1.25 inches, an L/D of 1.0 and a preload of about 0.5 were investigated. In addition, the effect of lubricant pressure on the stability of the three-lobe bearing was investigated and the effect of the selective fixture of pads was determined on the four-pad, pivoted-pad bearings. The diametral clearance of the three-lobe bearing was 5 mils to accommodate a total of 467 seconds misalignment. Because the pivoted-pad bearing was self-aligning the clearance used was 3.125 mils.

The rotative speed range of stability for the pivoted-pad bearing exceeded the stability range for the three-lobe bearings. The pivoted-pad bearing was insensitive to misalignment and to the selective fixture of one pad at light steady loads. The dimensionless load capacity of the two bearings was the same but the dimensionless torque of the pivoted-pad bearing was over 2 times that of the three-lobe bearing.

II. INTRODUCTION

The attempt to simplify Rankine cycle space power systems by using the working fluid as a lubricant for the turbomachinery and alternator has led to the necessity of investigating bearings operating with low viscosity fluids and at virtually no unidirectional load. The combination of a low-viscosity lubricant and very light loads leads to bearing instability in the form of fractional frequency whirl when attempts are made to run turbomachinery at the high rotative speeds required by Rankine cycle space powerplants on fixed geometry self-acting journal bearings. As a result, the General Electric Company, under NASA Contract NAS3-2111, undertook a low-viscosity bearing stability investigation (Reference 1) in order to study the stability characteristics of a number of hydrodynamic journal bearings which were shown by analysis to have potential for stable operation with close to zero radial load. The bearings selected were tested in water because this avoided the additional difficulties associated with liquid metal testing, and were tested in an experimental apparatus having a light (7 lb) vertical shaft. Shown below is a comparison of absolute and kinematic viscosity values for water and potassium at two temperatures. For water the test temperatures are given; for potassium the range of interest is given.

Lubricant	Temperature, $^\circ$F	Absolute Viscosity, lb sec/in^2	Kinematic Viscosity, in^2/sec
Water	75	1.35×10^{-7}	1.45×10^{-3}
Water	120	0.82×10^{-7}	0.89×10^{-3}
Potassium	600	0.36×10^{-7}	0.50×10^{-3}
Potassium	1000	0.24×10^{-7}	0.36×10^{-3}

For the case of the same journal diameter and rotative speed the ratio of water-lubricated to potassium-lubricated bearing clearance for the same Reynolds and Taylor numbers is equal to the ratios of water to potassium kinematic viscosity to the 1.0 and 0.667 power, respectively. For the same Sommerfeld number the clearance ratio is equal to the square root of the absolute viscosity ratio. On this basis water at 120°F simulates potassium at 600°F as a lubricant by making the clearance in water between 1.47 and 1.78 times the clearance in potassium, the exact number depending upon whether simulation of Reynolds, Taylor or Sommerfeld number is desired. The bearings tested along with their length to diameter ratios and diametral clearances are presented in Table I.

The test results for the two axial-groove bearing indicated that fractional frequency whirl (FFW) could be supressed through static or dynamic loading. It was further demonstrated that the instability region of such a bearing with a length to diameter ratio of 1.5 and a diametral clearance of 2 mils had an upper (but relatively low) speed limit. At higher speeds the FFW instability was eliminated and a maximum speed of 34,200 was attained. None of the bearings tested permitted the rotor speed to be increased to more than 21,000 rpm without the application of a unidirectional load. Higher rotational speeds were achieved with the two axial-groove bearing by increasing the static load to a maximum of 34.4 lbs per bearing. The maximum test speed for a lightly loaded bearing (8.6 lbs) was 24,000 rpm which was also achieved with the two axial-groove bearing having L/D of 1.5.

The compound-cylindrical bearing entered FFW at zero load at the lowest test speed, 3,600 rpm. The orthogonally-displaced elliptical

4

TABLE I

BEARINGS TESTED ON LOW-VISCOSITY BEARING
STABILITY INVESTIGATION

Type	Length/Diameter	Diametral Clearance, mils
2-Axial Groove	1, 1.5	2, 3, 5
Pivoted-Pad (4)	1	3.2, 4.3, 6
3-Lobe		1
Compound Cylindrical	1	3
Displaced Elliptical	1	3, 5.4

bearing entered FFW at zero load at a speed of 16,200 rpm. The compound-cylindrical bearing exhibited a reduced load carrying capacity compared to the other bearing types. Synchronous whirl amplitudes limited the test speed of the displaced-elliptical bearing.

Tests of the three-lobe and the pivoted-pad bearing were carried out without FFW. However, at 21,000 rpm the shaft orbit radius resulting from unbalanced loads attained a limiting value and the further increases in speed were not possible. As a result of the tests of stability on the three-lobe and the pivoted-pad bearings, it was decided to carry out further investigations with an improved test unit in attempt to increase the maximum attainable speed from 21,000 rpm up to 30,000 rpm.

Attempts were made in the previously-mentioned, low-viscosity bearing stability program to measure the equilibrium displacement of the shaft by means of Bentley variable-reluctance proximity probes near the bearing locations. However, only one proximity probe was used in each of two mutually perpendicular directions and a zero shift of the bearing center position was obtained as the rotating shaft increased speed beyond 6,000 rpm. In the present program four proximity probes in pairs were provided in each of four planes inboard and outboard of each test bearing. Other changes were deemed necessary in the refurbishing of the test unit. Means were to be provided for finding the torque of the loader bearings over expected test conditions. In order to attack the bearing operational problems associated with misalignment, the test unit was modified to permit the linear misalignment of the bearings by 4 mils and the additional angular misalignment of the bottom bearing by 400 seconds. This required a modification of the loader bearings so that they would not influence

6

shaft position when operating with shaft misalignment. The present hydrodynamic journal bearing program also permitted the investigation of the effects of selective fixture of pads on the pivoted-pad bearing performance. It was deemed necessary to provide a lubricant supply pressure of 150 psig and means for applying 70 lbs steady load to each bearing. Means were to be provided for obtaining improved shaft balancing. In addition, it was decided that dynamic force measurements associated with the bearing reactions should be made in attempt to determine the dynamic bearing coefficients experimentally. Finally, shaft centering devices were to be provided for establishing bearing center position.

The following objectives were established for the Hydrodynamic Journal Bearing Program:

-   To obtain stability and dynamic data of pivoted-pad and three-lobe bearings above 21,000 rpm.

-   To determine the effects of steady load, unbalance, bearing misalignment, lubricant supply pressure, and the selective fixture of pads upon bearing dynamics.

-   To determine the effects of intentional rotor unbalance, misalignment and the selective fixture of pads on bearing load capacity and torque.

-   To determine experimentally the bearing dynamic coefficients.

III. TEST EQUIPMENT

In this section the details of the Hydrodynamic Journal Bearing test unit will be described along with the instrumentation used and the facility required to carry out the tests. An instrumentation and equipment list is presented in Table II.

A. TEST UNIT

Shown in Figure 1 is a drawing depicting the Hydrodynamic Journal Bearing test unit. The test unit includes a test shaft, test bearings 12.5 inches apart, loader bearings, instrumentation stations, a torque meter, electric drive motor, and a casing to hold all these parts in their proper position with respect to all other parts. The test bearings are shown at either end of the test shaft. The upper bearing is mounted rigidly in the casing while the lower bearing has provisions for misalignment of that bearing either linearly or angularly. The two loader bearings are 130-degree partial arc bearings 1.875 inches long having a machined radial clearance of 1 mil and are located near the central portion of the shaft. They are fabricated from SAE 660 bronze. These bearings are permitted to pivot on the ends of the rods connecting them to the pneumatic loader pistons. On each end of the test shaft are unbalance discs. These discs contain two threaded holes 180-degrees apart, one inch from the center. In these threaded holes screws are placed of known weight which permits purposely unbalancing the shaft. At the left side of the upper unbalance disc a magnetic pickup can be seen. This unbalance disc has a single tooth which actuates the adjacent magnetic pickup. The two holes

8

TABLE II

INSTRUMENTATION AND EQUIPMENT LIST

	Name	Model No.	Manufacturer
1.	Differential Voltmeter	801	John Fluke Co.
2.	Single Channel Recorder	19301-01-01	Honeywell Corp.
3.	Proximity Probe	H-1-084-3	Bently Nevada
4.	Proximity Detector	D152 D252R	Bently Nevada
5.	Power Supply	802B	Harrison Lab. Inc.
6.	Dial-A-Volt	DAV46n	General Resistance Inc.
7.	Accutron Transistor Amplifier	51	Sheffield Corp.
8.	Electrojet Cartridges	59230108 59230119	Sheffield Corp.
9.	Linearchek Gage Calibrator		Sheffield Corp.
10.	Sundstrand Bench Centers	BC 6"x36"	Sundstrand Machine Tool
11.	Leitz Optical Stage	1"x1"	Opto-Metric Tools Inc.
12.	Oscilloscope	RM561A	Tektronix Corp.
13.	Oscilloscope	RM535	Tektronix Corp.
14.	Oscilloscope	8151R	Beckman
15.	Phase Meter	320-AB	Technology Inst. Corp.
16.	Differential Comparator	3A7	Tektronix Corp.
17.	Scope Camera		Dumont
18.	Balance Machine	Mu-6	Micro Balancing Inc.
19.	Differential Voltmeter	871A	John Fluke Co.
20.	Charge Amplifier	504	Kistler Inst. Corp.
21.	Piezoelectric Force Trans.	902A	Kistler Inst. Corp.
22.	Accelerometers	2213C	ENDEVCO
23.	Cathode Follower	2608	ENDEVCO
24.	Power Supply	2621	ENDEVCO
25.	Power Supply	160A	Tektronix Inc.
26.	Wave form Generator	162	Tektronix Inc.
27.	Scope Indicator	360	Tektronix Inc.
28.	Temperature Recorder (Speedomax G)	60362	Leeds and Northrup Co.
29.	Speed Counter	5500	Berkeley Corp.
30.	Power Supply (dc)	6263A	Harrison Labs

TABLE II
(Continued)

Name	Model No.	Manufacturer
31. Carrier Demodulator	CD11	Pace Engineering
32. Oscillator Pre-Amplifier	55GE2239	Fisher and Portor Co.
33. Pressure Transducers	P76-100 psig	Pace Engineering
34. Turbine Flowmeter	10C1510A	Fisher and Portor Co.
35. Power Supply	C1580	Lambda
36. Power Supply	C280M	Lambda
37. Universal Microalignment-telescope	112/637	Rank Taylor Hobson Inc.
38. Right Angle Eye Piece	112/568	Rank Taylor Hobson Inc.
39. 43x Eye Piece	112/383	Rank Taylor Hobson Inc.
40. Telescope Lamphouse Assy	112/638	Rank Taylor Hobson Inc.
41. Heat Exchanger	4810	Heliflow Corp.
42. Filter (20 micron)	55B10D-3/4	Commercial Filters Inc.
43. 3 Way Air Operated Valve (½")	½"-3 way	Taylor Inst. Corp.
44. Lin-E-Aire Control Valve	240VM1240-21995	Taylor Inst. Corp.
45. 80 gal. Hot Water Heater	200YRGF821525	GE Company
46. Water Pump-Lube Supply	SRM 204-22	Robbins and Meyers Inc.
47. Water Pump-Sump Scavange	EM 818	Robbins and Meyers Inc.
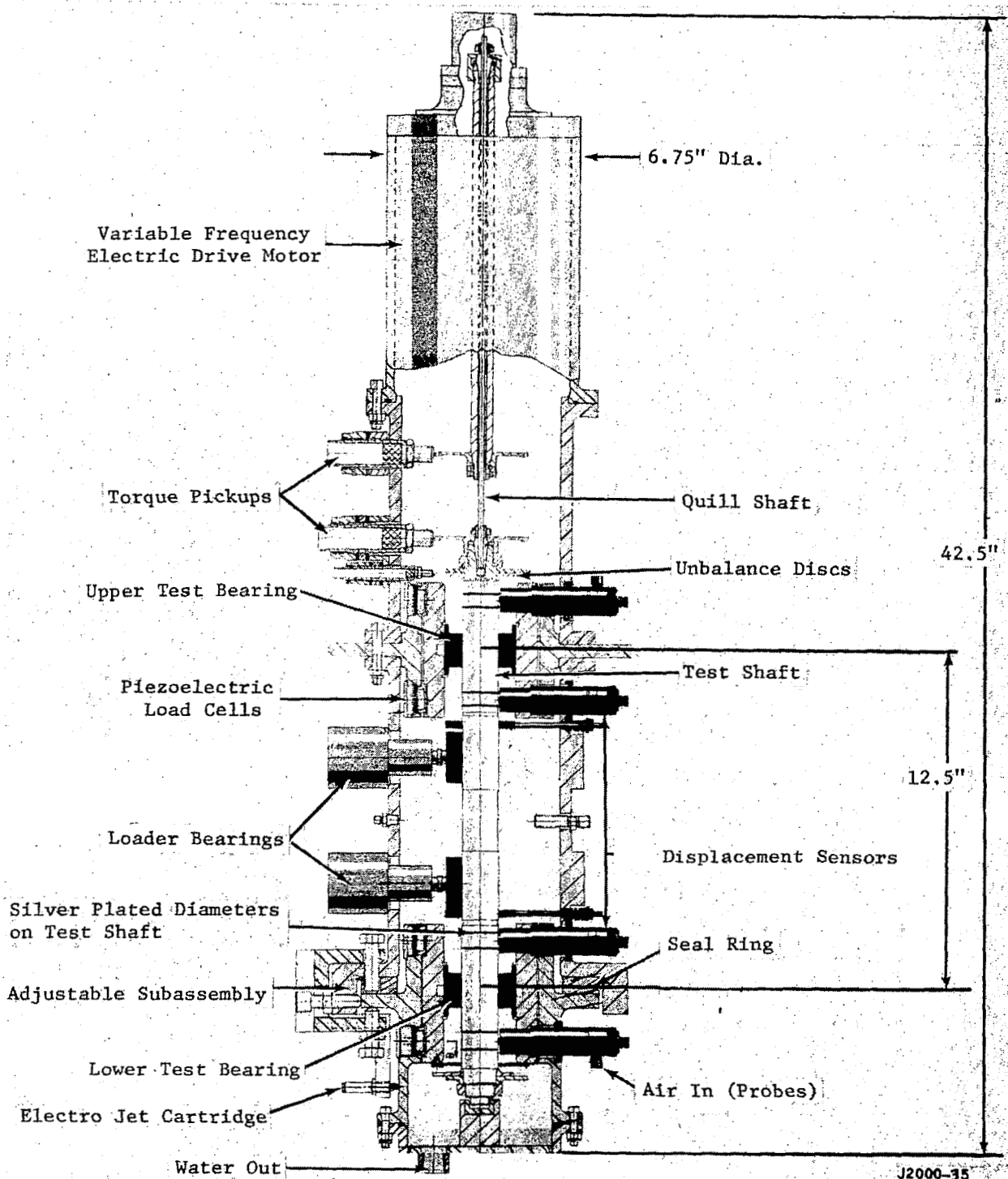
Figure 1. Hydrodynamic Journal Bearing Test Unit.

11

in the unbalance discs are situated at 0 and 180 degrees from the single tooth. Thus the magnetic pickup provides a signal in-phase or out-of-phase with the unbalance.

The test shaft is driven by the 15 horsepower synchronous electric motor which is at the top of the test unit. The motor shaft is hollow permitting the insertion of a beryllium-copper quill shaft from the upper end of the electric motor shaft down to the test shaft. The quill shaft is small enough in diameter (0.125 in.) so as to twist under torque loads. Shown at the upper end of the test shaft and the lower end of the motor shaft are wheels with 18 equally spaced teeth. On the left side of the test unit are magnetic pickups which are actuated by the teeth on the two gears just described. The torque is measured by measuring the phase angle between the teeth of the two 18-toothed wheels. The quill shaft then is calibrated in inch pounds of torque versus degrees of twist.

There are displacement and force measuring instrumentation stations inboard and outboard of each test bearing. On the right hand side of the drawing are shown the displacement sensor holders and on the left side of the drawing are shown force measuring devices at each of these four instrumentation planes. The test bearings are mounted in an inner bearing housing which is supported from outer bearing housing by the piezoelectric load cells. The outer bearing housings are firmly fastened to the casing of the test unit.

Shown in Figure 2 is an exploded view of the 316 stainless-steel test housings which make up the casing of the hydrodynamic journal

INSTRUMENTATION SECTION

TEST BEARING

INNER BEARING HOUSING
(UPPER)

OUTER BEARING HOUSING
(UPPER)

BEARING HOUSING SUPPORT SECTION

OUTER BEARING HOUSING
(LOWER)

INNER BEARING HOUSING
(LOWER)

TEST BEARING

BOTTOM END CAP
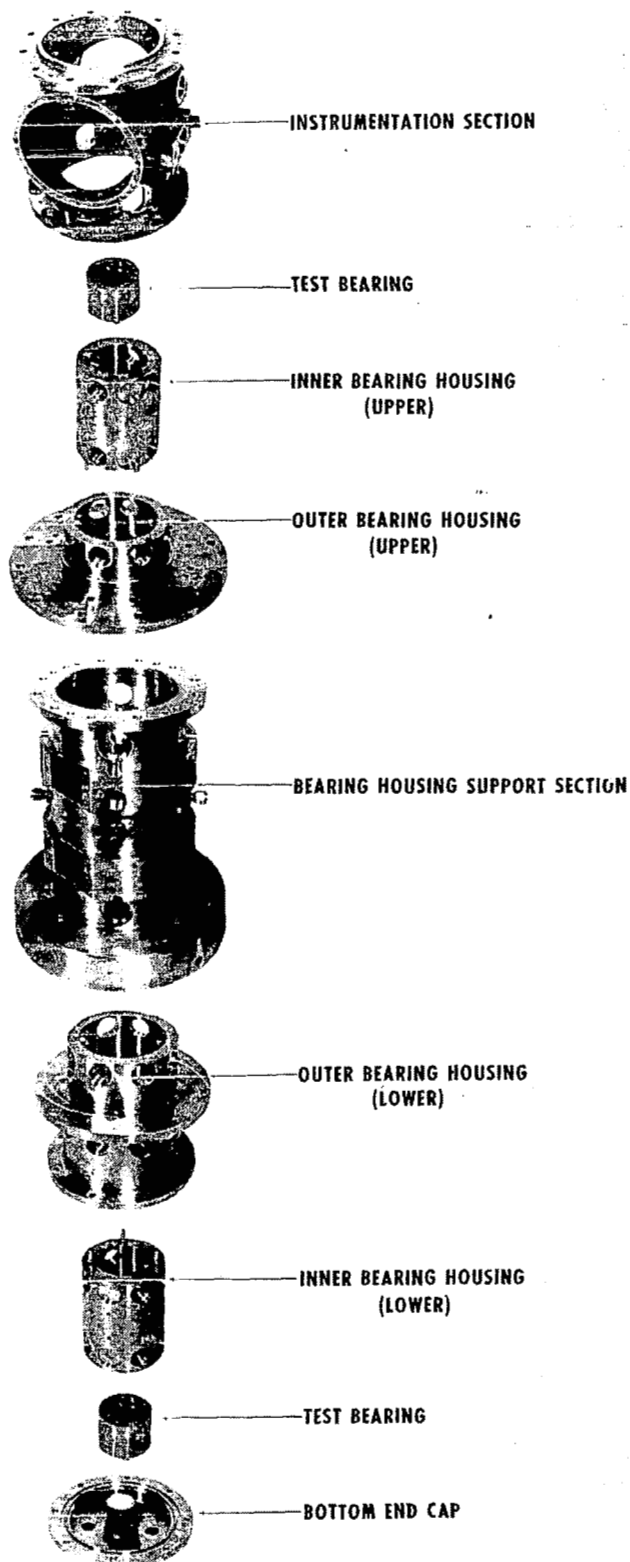
Figure 2. Exploded View of Test Unit Housings.

13

bearing test unit. Each one of the parts is identified in the photograph and these parts may also be found in the previous figure.

Shown in Figure 3 is the installation of the test unit with its instrumentation into the test stand adjacent to the test facility. The electrical drive motor which is about 12 inches long can be seen at the top of the test unit. The test bearings and shaft are in the portion of the test unit which lies below the electrical drive motor.

Since it was planned to carry out most of the bearing testing at a temperature of 120°, the test unit was provided with environmental chamber which would permit holding this temperature constant. Shown in Figure 4 is the test unit with some of the environmental chamber in place.

Shown in Figure 5 is an exploded photograph of the pivoted-pad bearings. The assembly drawing of the pivoted-pad bearing is shown in Figure 6. Pivoted-pad bearings have four pads made of SAE 660 bronze which are pivoted on Haynes Stellite No. 3 pivots. These pivots contact Haynes Stellite No. 3 discs placed in sockets in each pad. The four pivot studs are mounted on the 304 stainless-steel retainer ring sub-assembly. The preload on the bearing is adjusted by the insertion of washers of various thicknesses between the shoulder on the pivot stud and the retainer ring. The bearing is completed by the installation of the upper and lower screw seals. The pertinent dimensions of the pivoted-pad bearing are presented in Table III and the inspection data are presented in Table IV.

14

12"

J1164-38
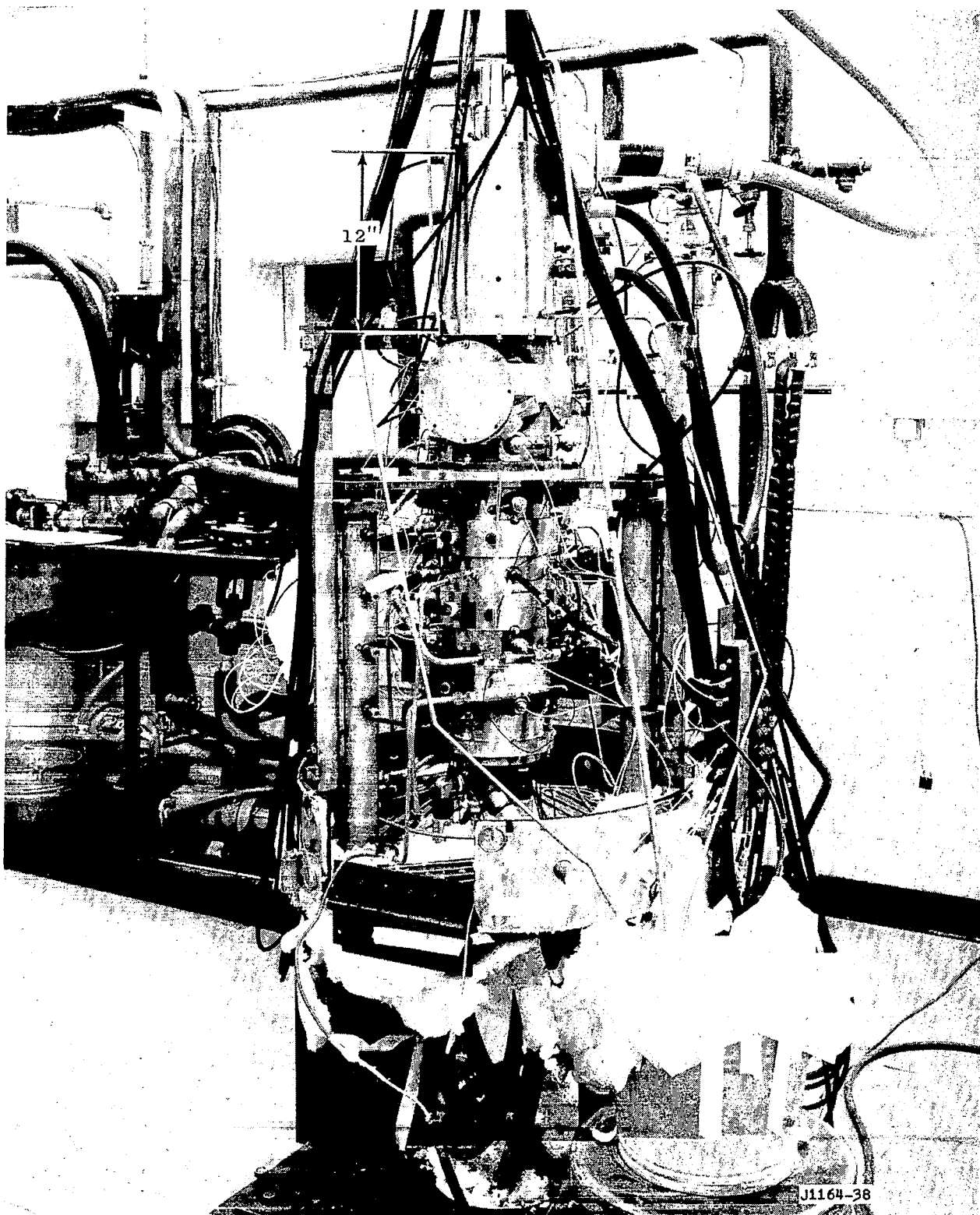
Figure 3. Installation of Test Unit into Test Stand.

15
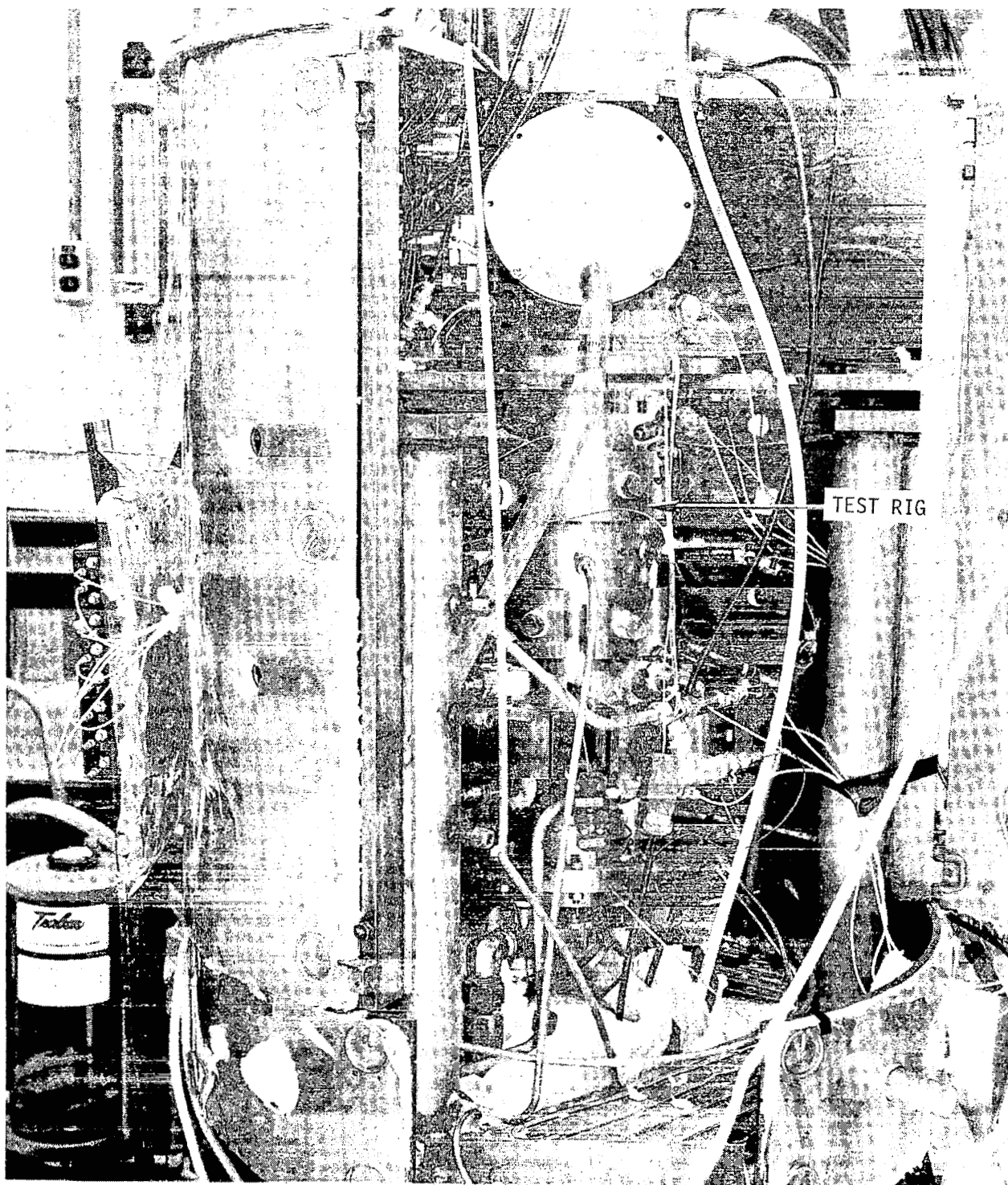
Figure 4. Test Unit Partially Enclosed in Environmental Chamber.
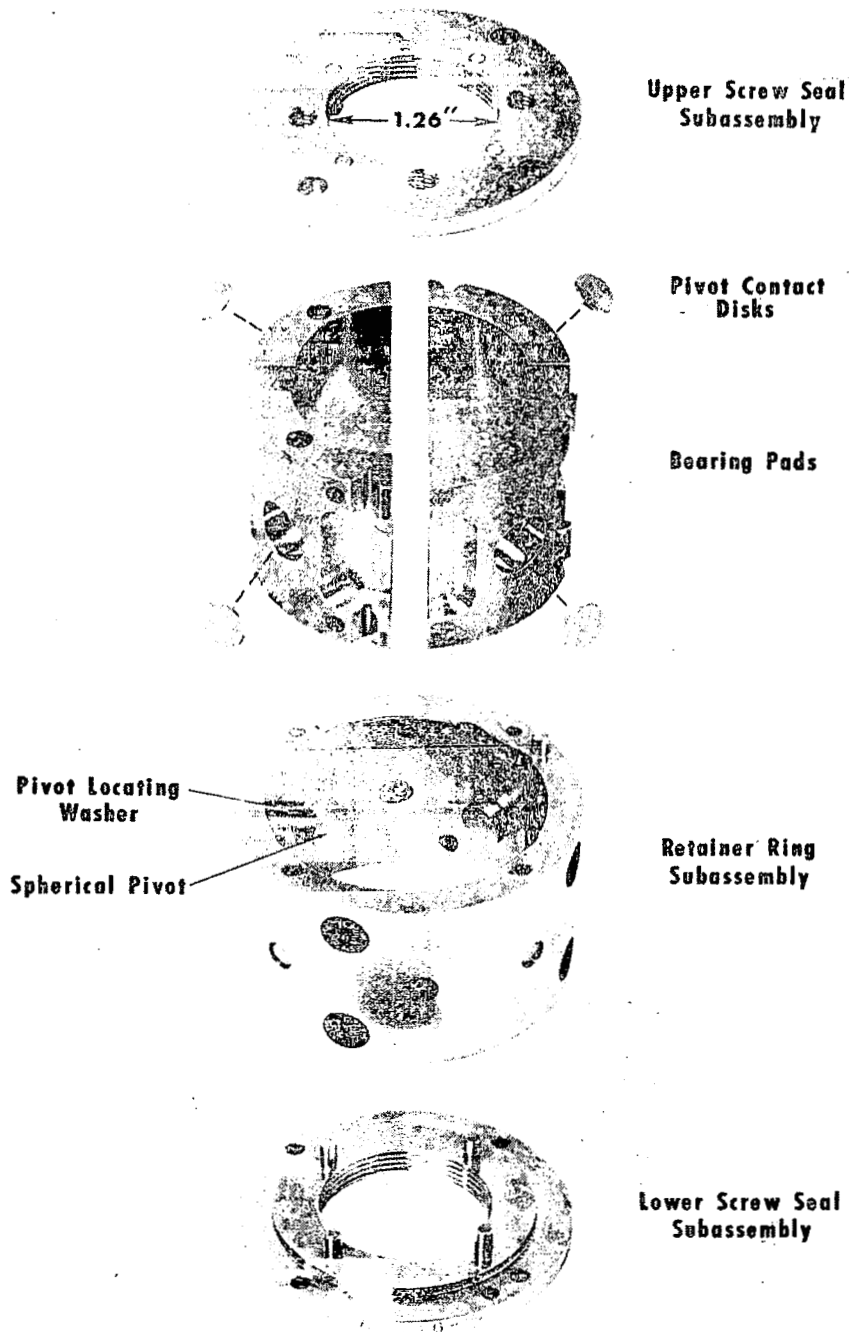
Figure 5. Self-Aligning Pivoted Pad Bearing Assembly.

Figure 6. Self-Aligning Pivoted Pad Bearing.

18

J5578-6
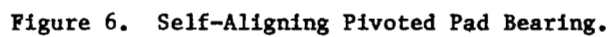
TABLE III

DIMENSIONS OF PIVOTED-PAD BEARING

Journal Radius, in.	0.625
Pad Radius, in.	0.628125
Length, in.	1.25
Pad Angular Extent, deg.	80
Angle Leading Edge to Pivot	44
Pad (Machined) Radial Clearance, in.	0.003125
Bearing (Assembled) Radial Clearance, in.	0.0015
Preload Coefficient	0.52

TABLE IV

SELF-ALIGNING PIVOTED-PAD BEARING MACHINING INSPECTION SUMMARY

P/N 941D118 Rev C

Condition	Specifications, in.	Recorded Dimensions, in.			
		Ring #1		Ring #2	
Diameter of OD of Retainer Ring [1]	2.5004-2.5001	2.50010		2.50010	
		Pad 1	Pad 2	Pad 3	Pad 4
Diameter of ID of Pads [1]	1.2563-1.2562	1.25630	1.25628	1.25627	1.25627
Concentricity of ID to OD [2]	Within 0.0001 FIR	0.0001	0.0001	0.000075	0.000075
Taper of ID [2]	Within 0.0001 FIR	< 0.0001	< 0.0001	< 0.0001	< 0.0001
Roundness of ID [2]	Within 0.00005 FIR	0.00005	0.00005	0.00005	< 0.00005
Torque Requirement of Pad Lock Bolts	4.5 in-lbs.	4.5 in-lbs.	4.5 in-lbs.	4.5 in-lbs.	4.5 in-lbs.
Surface Finish of ID [3]	Within 8/ ∨	8/ ∨	8/ ∨	8/ ∨	8/ ∨
Squareness of ID With End Surface (B) [2]	Within 0.0001 FIR	< 0.0001	< 0.0001	< 0.0001	< 0.0001

[1] Measured with Electronic amplifier and comparison blocks.

[2] Indi-Ron

[3] Profilometer

Shown in Figures 7 and 8 are photographs of the three-lobe bearing and the manufacturing drawing for this bearing. The bearings themselves are made of SAE 660 bronze and have lubricant supply slots between each of the pairs of lobes. The pertinent dimensions for the three-lobe bearing are presented in Table V and the inspection data for this bearing are presented in Table VI.

Shown in Figure 9 is a photograph of the test shaft used for the test results described herein. The shaft is made of 420 stainless-steel and is hardened to 50 to 53 Rockwell C. The shaft has 420 stainless-steel unbalance discs at each end of the shaft. Also visible in the photograph are rings where silver, 5 ± 0.1 mils thick, has been plated in grooves on the shaft. These rings correspond to the locations of the displacement sensors in the hydrodynamic journal bearing test unit. The sensitivity of the sensor is a strongly decreasing function of the resistivity of the shaft. By using a low-resistivity homogenious material adjacent to the sensor the sensitivity is increased and the effect of the non-homogeneity of the shaft material is eliminated. The dimensional inspection data for the two shafts is presented in Table VII.

B. INSTRUMENTATION

Shown in Figure 10 is a Bently Instrumentation Corp. induction-type displacement sensor and holder assembly. Because the sensors are required to operate in water environment, a Teflon covering, which can be seen in the photograph, was used to eliminate wetting, and hence, maintain the sensitivity of the sensor in the presence of water. Although the brass holder for the proximity sensors provided an air current around

21

Figure 7.   Three-Lobe Bearings.
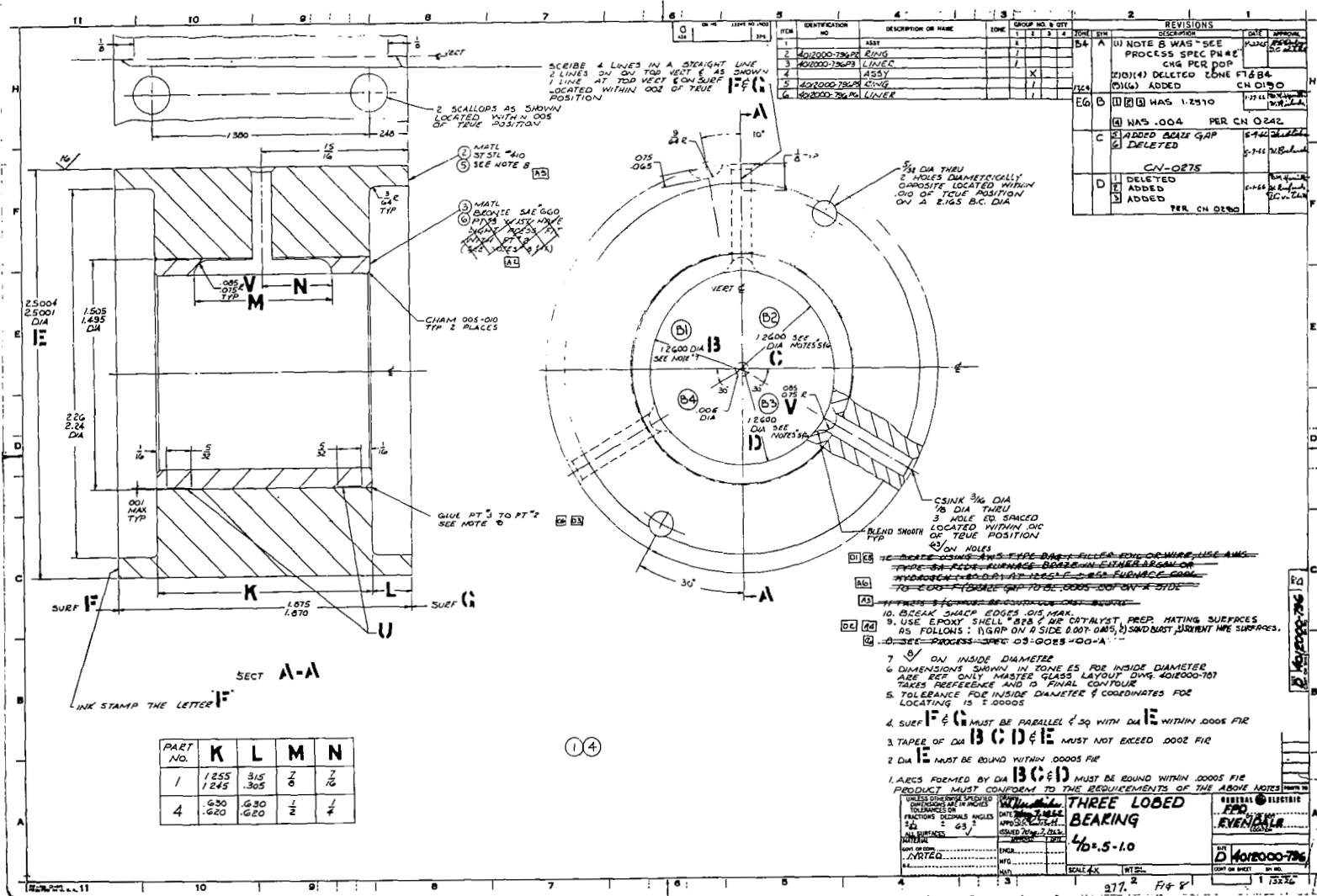
Figure 8.   Drawing of Three-Lobe Bearing.

J5578-8

Shown in Figures 7 and 8 are photographs of the three-lobe bearing and the manufacturing drawing for this bearing. The bearings themselves are made of SAE 660 bronze and have lubricant supply slots between each of the pairs of lobes. The pertinent dimensions for the three-lobe bearing are presented in Table V and the inspection data for this bearing are presented in Table VI.

Shown in Figure 9 is a photograph of the test shaft used for the test results described herein. The shaft is made of 420 stainless-steel and is hardened to 50 to 53 Rockwell C. The shaft has 420 stainless-steel unbalance discs at each end of the shaft. Also visible in the photograph are rings where silver, 5 ± 0.1 mils thick, has been plated in grooves on the shaft. These rings correspond to the locations of the displacement sensors in the hydrodynamic journal bearing test unit. The sensitivity of the sensor is a strongly decreasing function of the resis tivity of the shaft. By using a low-resistivity homogenious material adjacent to the sensor the sensitivity is increased and the effect of the non-homogeneity of the shaft material is eliminated. The dimensional inspection data for the two shafts is presented in Table VII.

B. INSTRUMENTATION

Shown in Figure 10 is a Bently Instrumentation Corp. induction-type displacement sensor and holder assembly. Because the sensors are required to operate in water environment, a Teflon covering, which can be seen in the photograph, was used to eliminate wetting, and hence, maintain the sensitivity of the sensor in the presence of water. Although the brass holder for the proximity sensors provided an air current around

24

TABLE VI

THREE (3) LOBED BEARING INSPECTION SUMMARY

P/N 4012000-796 P1 REV D

Condition	Specification (in)	Actual (in)	
		Pt #1	Pt #2
Diameter of Lobes[1]	1.2600	1.2600 - 1.2602	1.2600 - 1.25995
Roundness of Lobes[1]	W/in 0.000050	0.000050	0.000050
Diameter of O.D.[1]	2.5001 - 2.5004	2.50026	2.50037
Roundness of O.D.[1]	W/in 0.000050	0.000020	0.000020
Taper of Lobes[1] (Axially)	W/in 0.0002	0.00011	0.000050
Tolerance of Loc.[1] Coordinates	W/in 0.000050	0.000050	0.000050
Surface Finish, I.D.[2]	$\overset{8}{\vee}$	$\overset{8}{\vee}$	$\overset{8}{\vee}$

[1] Indi-Ron

[2] Profilometer
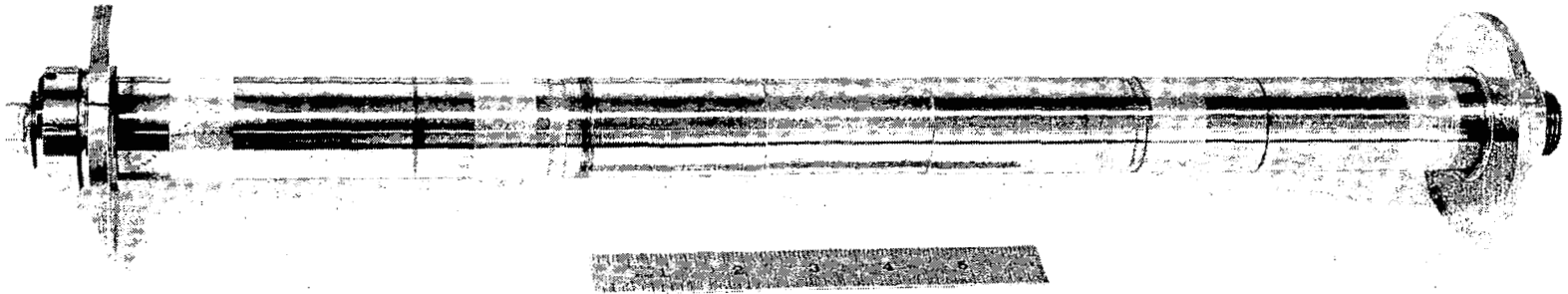
Figure 9. Assembled Test Shaft.

TABLE VII

DIMENSIONAL INSPECTION OF TEST SHAFTS[1]

Shaft for	Tolerance	Measurements		
		Pad Bearing	3-Lobe Bearing	
Roundness	50 micro-inches	30	50	FIR
Concentricity	300 micro-inches	30	20	FIR
Taper	50 micro-inches	40	50	FIR
Plating Thickness	± 50 micro-inches	± 10	± 25	
Finish	8 AA	4.5 AA	5 AA	

[1] Indi-Ron

27

Sensor With
Teflon Cap
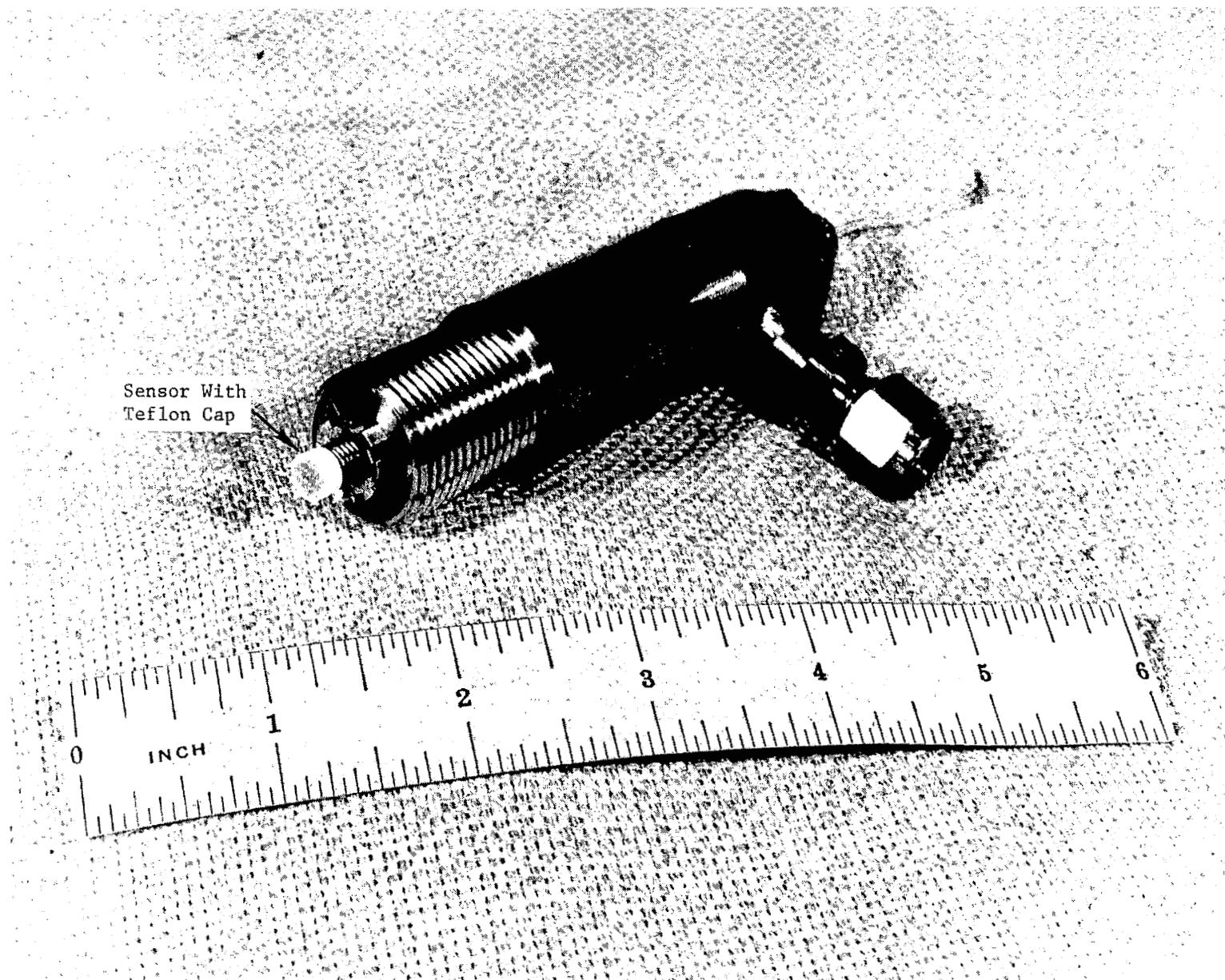
Figure 10. Displacement Sensor and Holder Assembly.

the sensor to further assure a dry environment, it was never used during test.

Shown in Figure 11 are the piezoelectric load cells for the measurement of dynamic forces under operating conditions and those parts which are required for their installation. The centering stud is threaded into the inner bearing housing and the Kistler Model 902A load cell is placed over this centering stud. A 45-mil washer is placed over the load cell followed by a thrust-bearing washer. A thrust bearing containing ball bearings is placed over this washer followed by a top thrust-bearing washer. Threaded into the outer bearing housing is a plug which holds these parts together and permits adjusting the preload on the load cell. Diametrically opposed to each load cell is a carbide ball between the inner and outer bearing housing. The ball is in contact with a small and large plate and the whole load-cell assembly can be adjusted in the radial direction by adjusting the threaded plug in the outer bearing housing.

Shown in Figure 12 is a detail of the four instrumentation planes used in the hydrodynamic journal bearing test unit. In the diagram the steady load acts downward on the shaft. To measure that reaction, a piezoelectric load cell is placed beneath the shaft. The thrust bearing on this load cell is visible on the drawing. Above the shaft is placed the carbide ball which is held in place by the threaded plug in the outer bearing housing. In the picture the direction of rotation of the shaft is counterclockwise. To the right of the shaft is shown a second piezoelectric load cell and to the left of the shaft is shown the carbide ball and tool steel plate assembly, which opposes the load cell.

29

OUTER BEARING HOUSING
PLUG

THRUST BEARING
TOP WASHER

EW-5/16
THRUST BEARING

THRUST BEARING BOTTOM
WASHER

45 MIL WASHER

KISTLER 902A
LOAD CELL

CENTERING STUD

OUTER BEARING HOUSING
PLUG

SMALL PLATE

CARBIDE BALL

(CENTERING SPONGE)
NOT SHOWN

LARGE PLATE
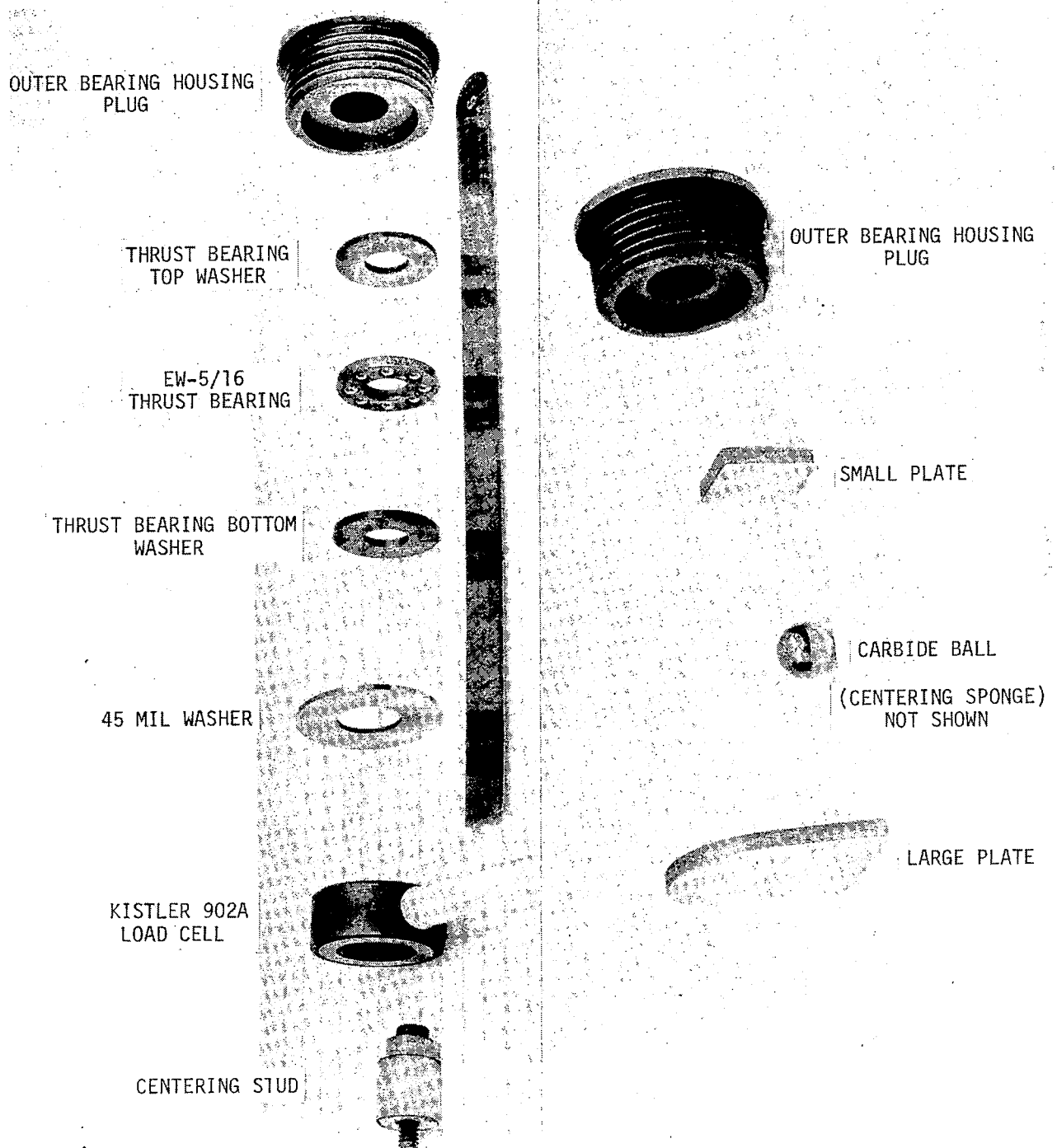
Figure 11. Load-Cell Assembly Components.
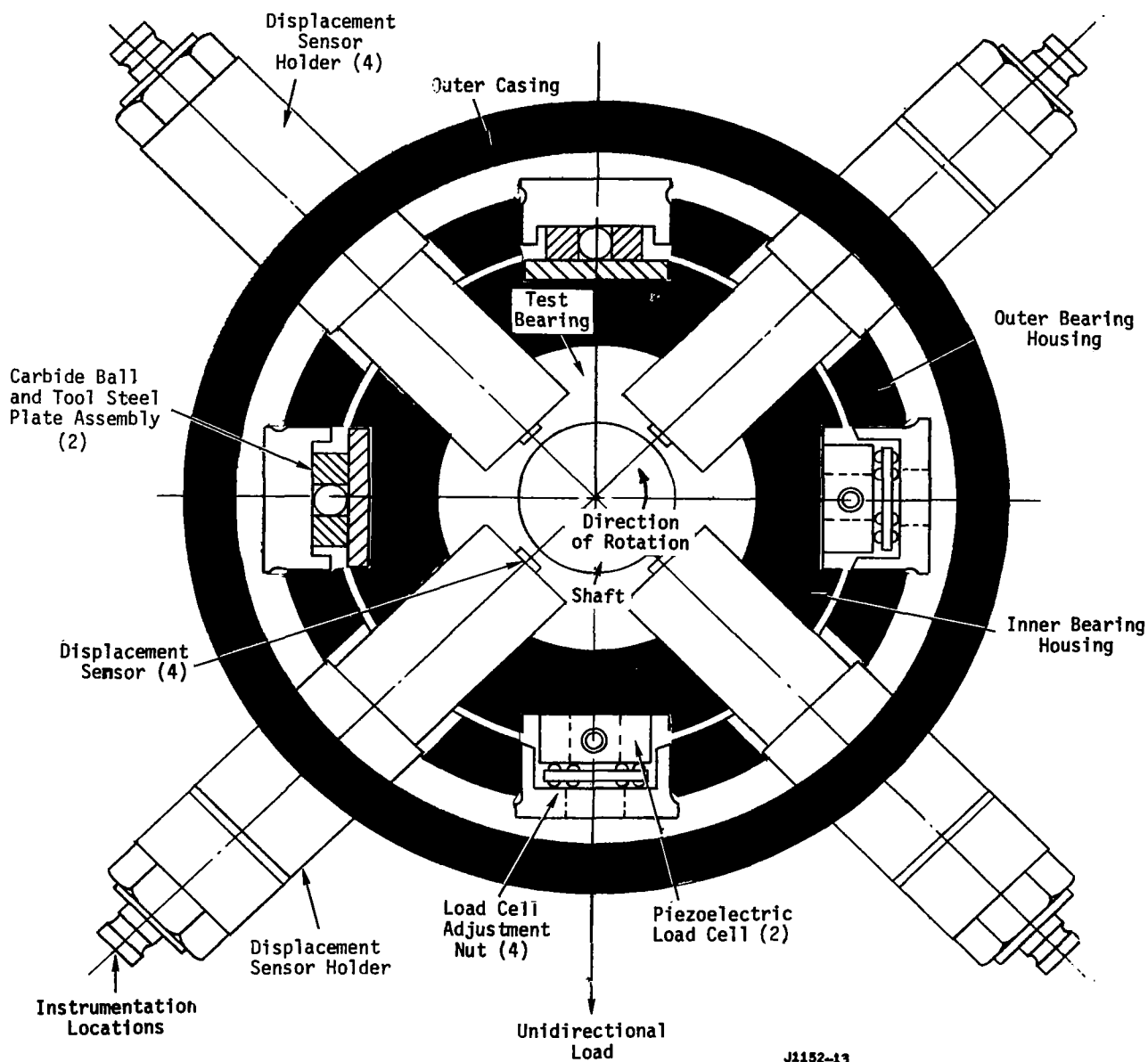
Figure 12. Arrangement of Instrumentation in Each of Four Planes.

31

Shown at 45° to the load cells are two pairs of displacement
sensors. These sensors are rigidly held in brass probe holders threaded
into the inner bearing housing. The radial placement of the displacement
sensors in these holders is carefully adjusted on assembly of the bearing
test unit. During testing the two sensors in each pair are summed
electrically so that axisymmetric temperature changes in the inner
bearing housing which cause these sensors to move in and out in a radial
direction will be eliminated. Shown in Figure 13 is the outer and inner
bearing housing with the three-lobe bearings inserted. The leads to the
piezoelectric load cells are seen in the foreground.

In order to facilitate the taking of steady state and dynamic data,
all the pertinent measurements in the bearing tests were read with the
digital data acquisition system. In order to obtain the readings from
the displacement sensors and the load cells. considerable electronic
innovation was required to condition the signals so that the digital
data acquisition system could record the proper readings. Shown in
Figure 14 is a schematic diagram showing how the readings from the dis-
placement sensors and load cells were obtained by the digital data
acquisition system. For simplicity only four out of the eight pairs of
displacement sensors and only four of the Kistler load cells are shown.
In the course of a digital scan when it is necessary to read the
equilibrium position of the test shaft, the signal travels from the
displacement sensor through the detector to a switch which is part of
the digital data acquisition system. This switch is programmed to pass
the signal through to the average-level detector and then into the
readout portion of the digital data acquisition system. The average-
level detector is an electronic device which takes the sinosoidial
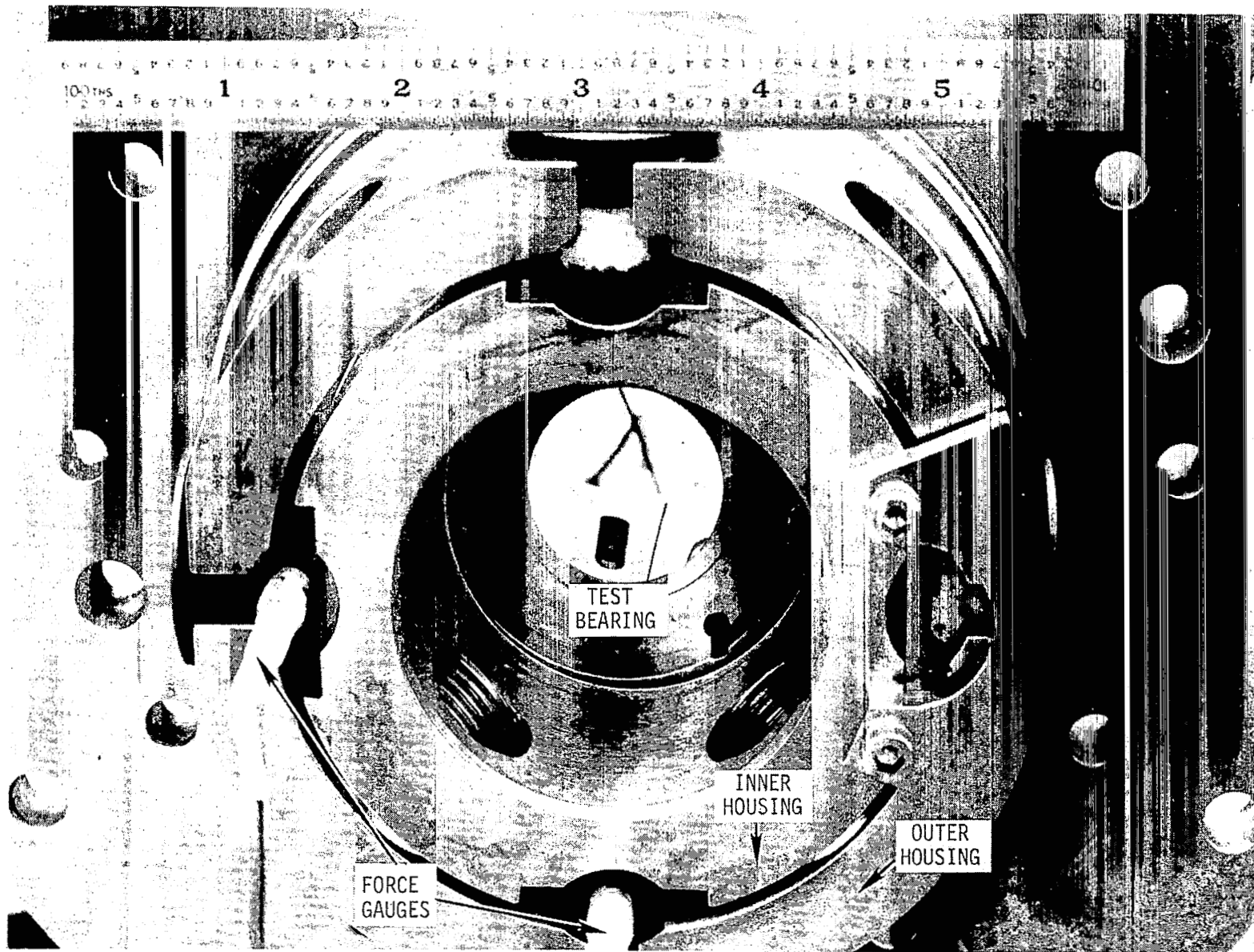
Figure 13. Bearing Sub-Assembly.

33

SHAFT DISPLACEMENT

BENTLY → DETECTOR →
BENTLY → DETECTOR →
BENTLY → DETECTOR →
BENTLY → DETECTOR → SWITCH →

AVERAGE LEVEL DETECTOR →

BEARING FORCE

KISTLER →
KISTLER →
KISTLER → SWITCH →
KISTLER →

CHARGE AMPLIFIER →

SYNCHRONOUS FILTER →

PHASE METER →

DIGITAL DATA SYSTEM

PEAK TO PEAK DETECTOR →

1 TOOTH GEAR

MAGNETIC PICKUP → PULSE TO SINE CONVERTER → SYNCHRONOUS CONVERTER
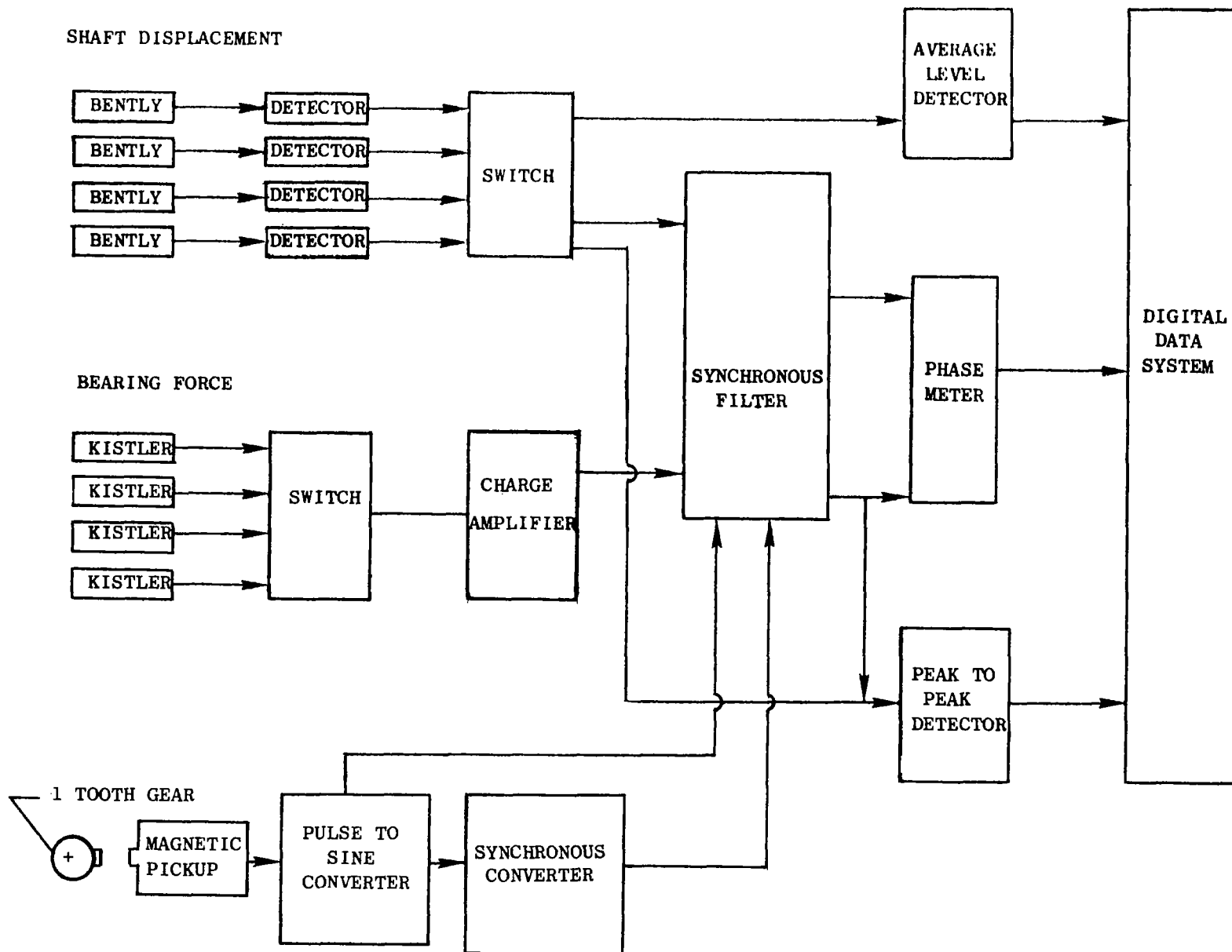
Figure 14. Digitalizing Bearing Dynamic Measurements. J5578-14

34

signal from the displacement sensor and measures the absolute distance
to a reading midway between the peak and trough on the sine wave.

In order to obtain the orbit size for a particular test point the
digital data acquisition system caused the switching mechanism to send
a signal to the peak-to-peak detector and then on to the digital data
acquisition system. The peak-to-peak detector is an electronic device
which measures the distance between the peak and the trough of the sino-
soidal wave setup by the displacement sensor.

When it becomes time in the digital scan to read the dynamic forces,
the digital data acquisition system programs a series of switches so
that the signal can move from the Kistler load cells to a charge ampli-
fier. The signal from the charge amplifier then goes through one channel
of a synchronous filter and through the peak-to-peak detector. The
synchronous filter is dual-channelled and is automatically set to the
frequency corresponding to the rotative speed of the test. In order to
obtain the phase angles between the unbalance force and either a dis-
placement or a force, a phase meter is connected to the digital data
acquisition system. A single-tooth gear on the unbalance disc of the
test shaft actuates a magnetic pickup once each revolution and this
pulse is converted into a sine wave in a pulse-to-sine converter. The
signal next goes into a synchronous converter. The signal from this
converter causes the synchronous filter to operate at the rotative speed
of the test shaft. The signal from the pulse-to-sine converter goes
through one channel of the synchronous filter and into one channel of
the phase meter. In addition, either a displacement or a force signal
enters the second channel of the synchronous filter and the second
channel of the phase meter. Thus, the phase meter reads the angle of

35

any displacement or force signal with respect to the unbalance of the test bearing shaft. In addition to the dynamic measurements, pressures, temperatures, flows, torque, and steady load are read by the digital data acquisition system during any one scan of the data.

As indicated, the test unit was made so that the lower test bearing could be misaligned angularly as much as 40 sec. and so that the test bearing shaft could be put out of alignment by 4 mils. Both the angular and linear misalignments of the lower test bearing was accomplished by the use of an alignment telescope. This device mounted on top of the test unit is shown in Figure 15. The alignment telescope was chosen over the Talyrand Proficorder because of its operational convenience and the fact that its estimated linear and angular errors are 90 microinches and 10 sec compared to 97 microinches and 29 sec for the Talyrand. Shown in Figure 16 is the drawing showing the alignment telescope attached to the test unit and Figure 17 shows the precision target which is inserted in the bearing in order to carry out alignment determination. The alignment in all cases was carried out to an accuracy of 12 seconds angular and 500 microinches linear, the tolerances required by contract.

Shown in Figure 18 is a photograph of the digital data acquisition system. This system can handle 600 pairs of leads and can read instruments at the rate of 3 per second. The digital data acquisition system provides the readouts in the form of punches and/or printed tape. In the case of the present program the printed tape was utilized to check on the repeatability of each test run which was repeated once. In addition, the punched tape was used to punch computer cards automatically which were processed through a data reduction computer program.

36

Right Angle Adapter

Micro Alignment
Telescope

43X Eye Piece

Lamp House
Assembly

Telescope
Holding
Collar

Horizontal
Roughing
Screws

Mounting Bracket
Adjusting Plane

Angular Movement
Screws

Locking Set
Screws

Mounting
Bracket
Base

Modified
Instrumentation
Housing
P/N941D845

4 Volt
Transformer

J1164-52
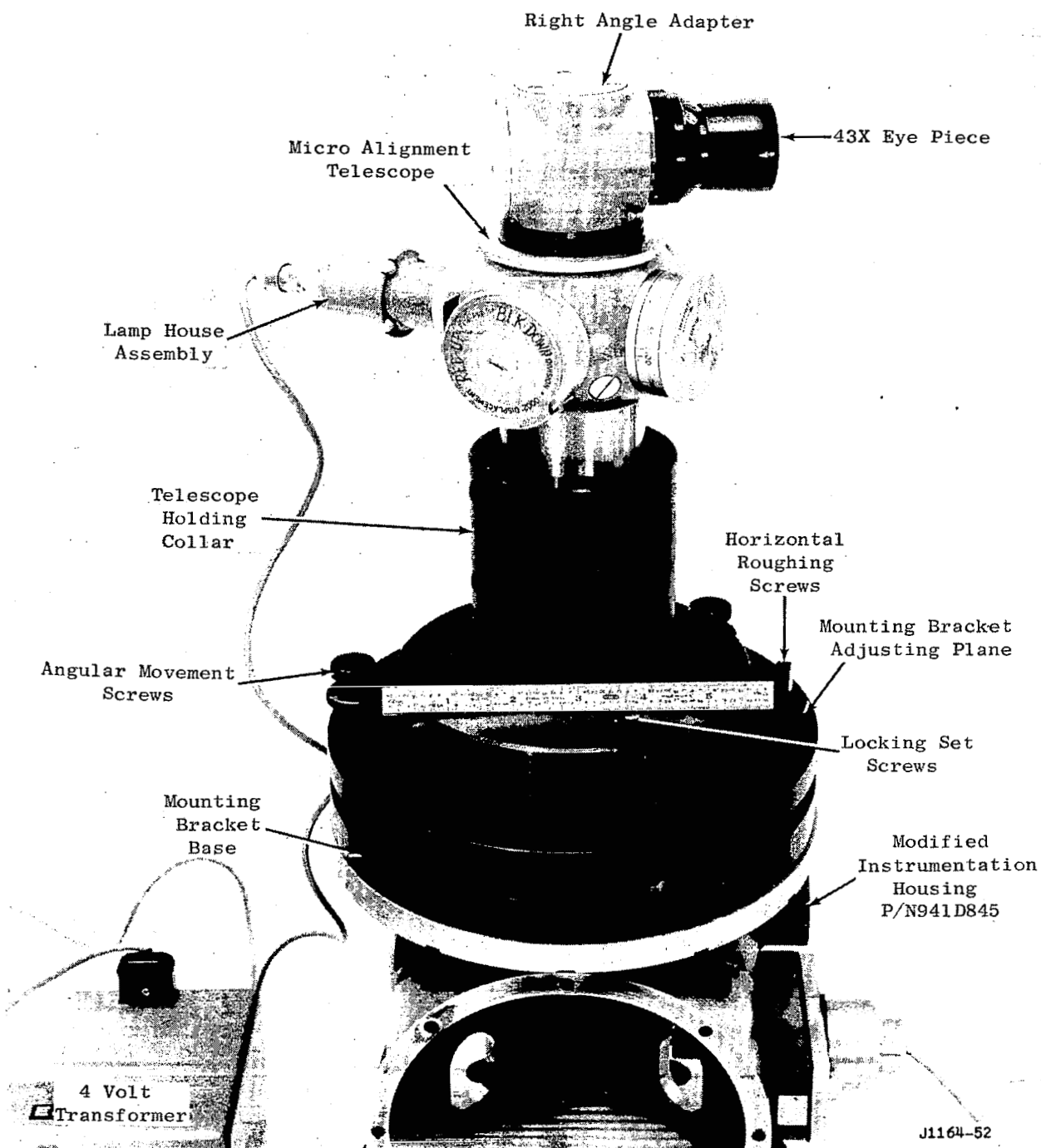
Figure 15. Alignment Telescope.

Alignment Telescope

Reflecting Target Assembly
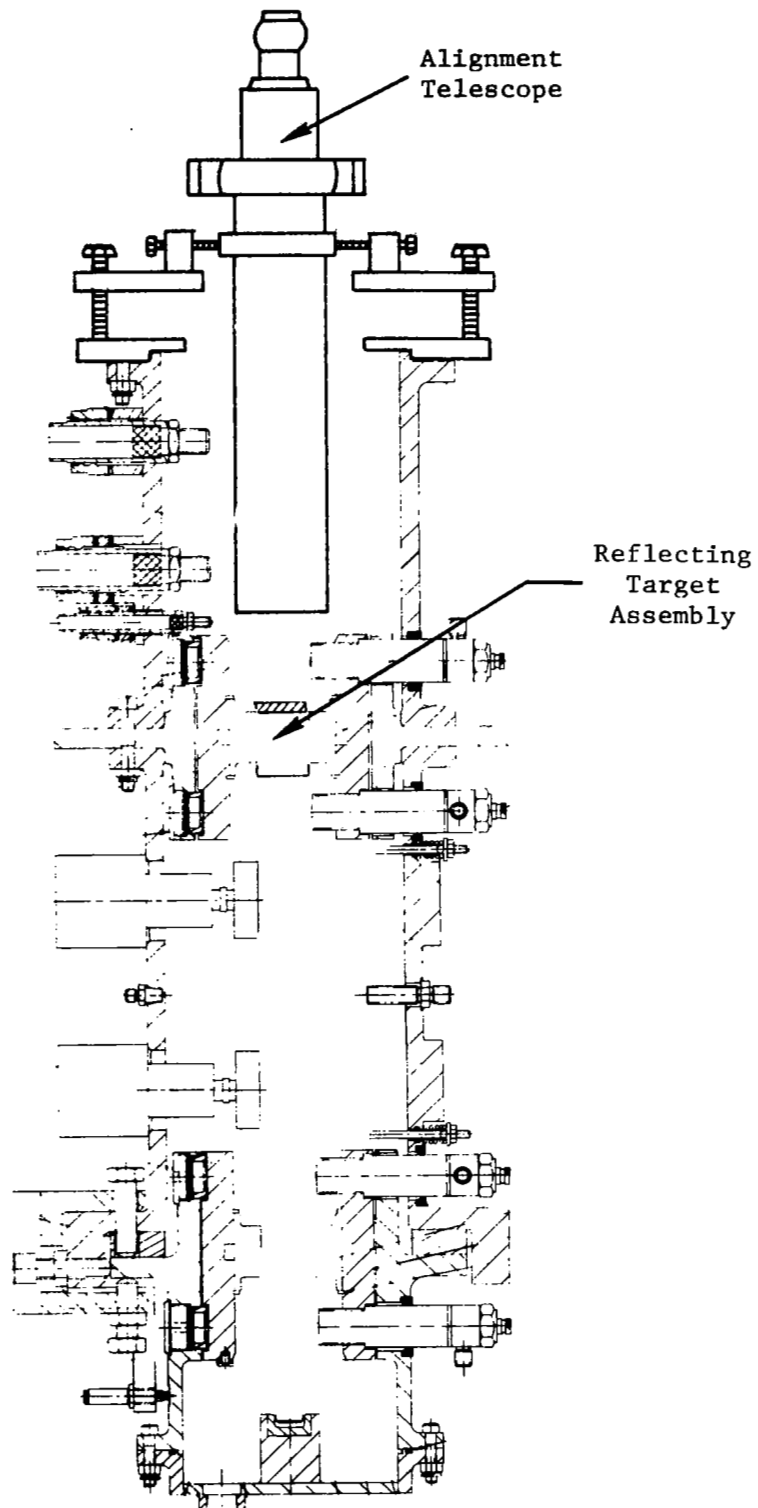
J1077-9

Figure 16. Bearing Alignment Using Telescope.

1"

J1164-30
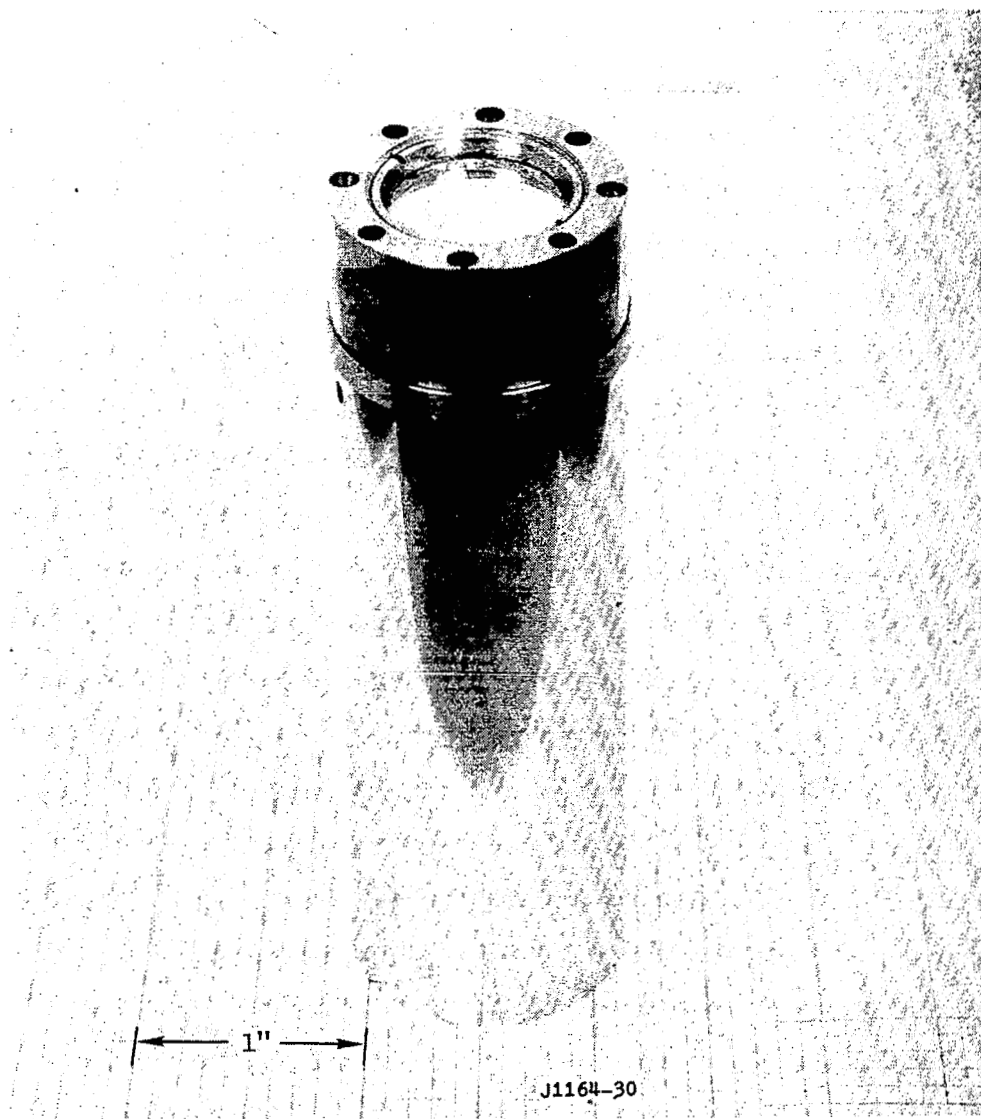
Figure 17. Reflecting Target Assembly For Alignment Telescope.

Digital Cables
From Test Unit

J5578-18
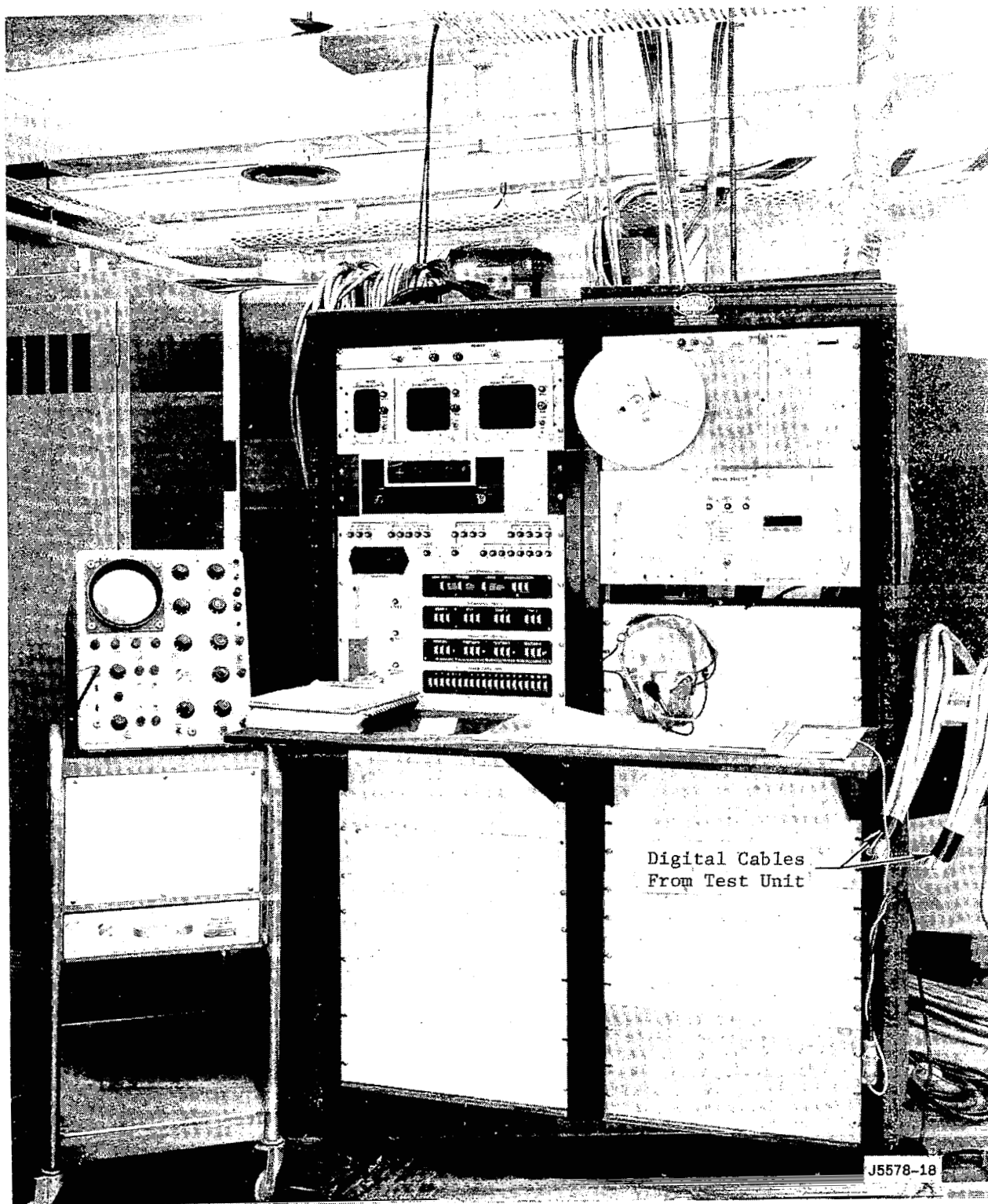
Figure 18.   Digital Data Recording Station.

40

C. TEST FACILITY

Shown in Figure 19 is the facility for providing distilled water at 120° as the test lubricant. It consists of an 80-gallon water heater, several pumps, filters and a heat exchanger used to control accurately the water temperature. Shown in Figure 20 is the instrumentation panel at the test site used for monitoring the test data. Shown in the photograph are the locations of the phase measuring equipment, the accelerometers, torque measurement readout, printed circuit board cabinets, speed indicator, oscilloscopes, temperature recorder, power supply and amplifiers.

In order to accurately control the speed of the test unit, a synchronous motor was used to drive the test shaft. This synchronous motor was driven by a variable-frequency power supply unit pictured in Figure 21. The heart of the power supply is a Ward-Leonard motor-generator set. The power supply was capable of driving the test unit shaft at rotative speeds between 8,000 and 31,000 rpm and controlling speed to $\pm$ 20 rpm.
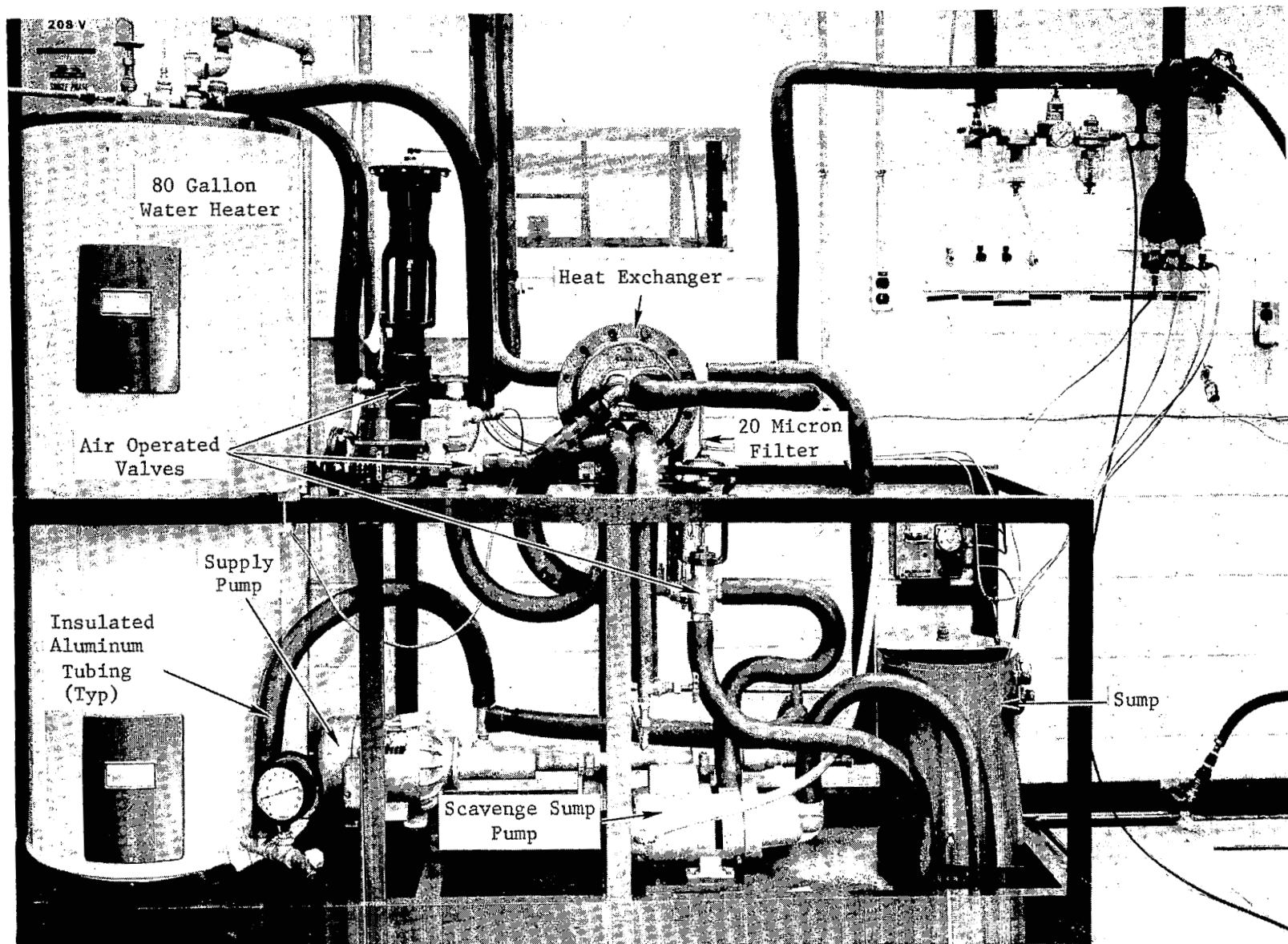
Figure 19. Lubricant (Distilled-Water) Supply System.
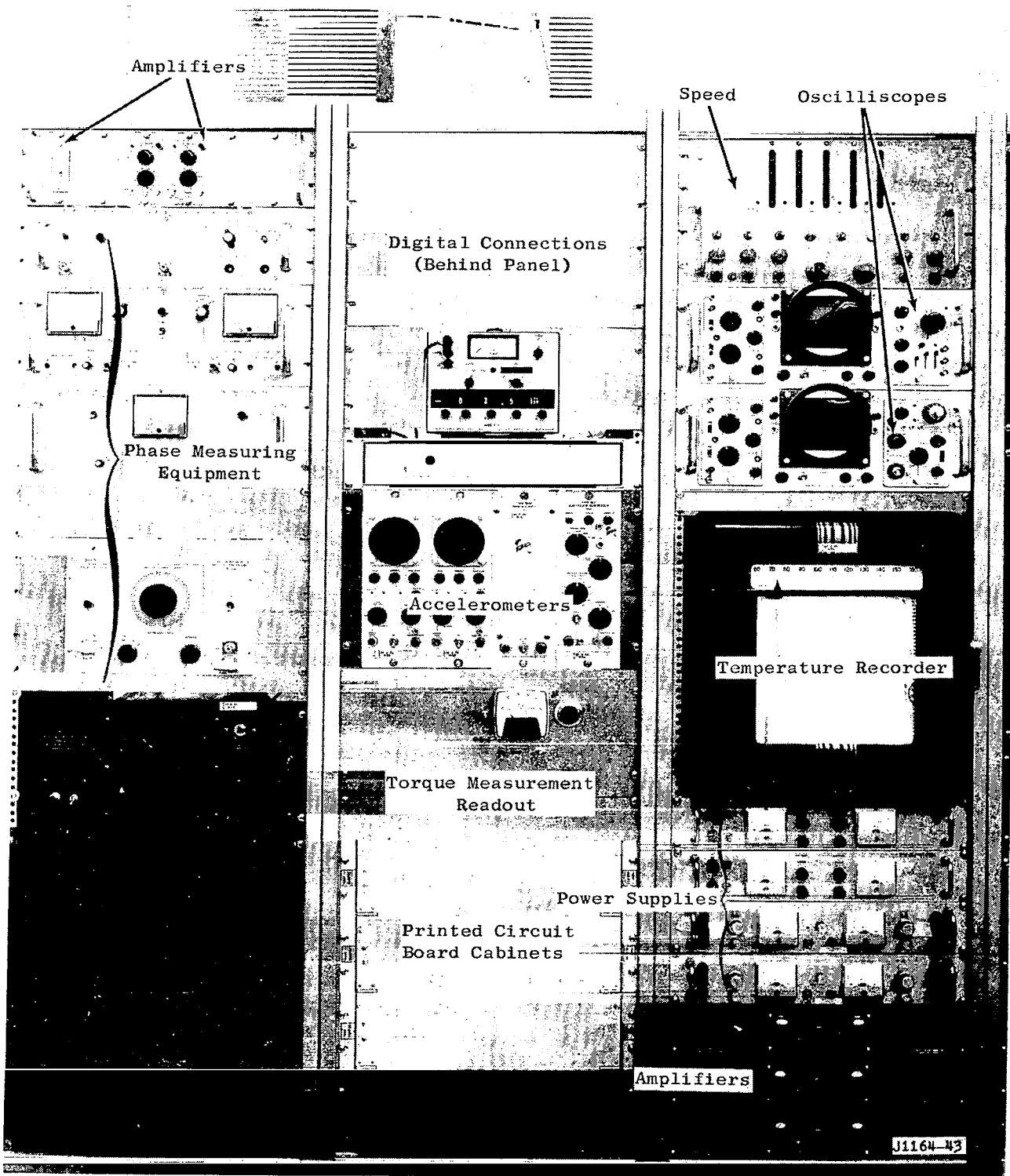
Figure 20. Instrumentation Console Panels.

To Test Unit Drive Motor

Drives

d.c. Motor

AC Motor

Drives

Drives

Drives

AC Generator

DC Generator

J5578-21

44
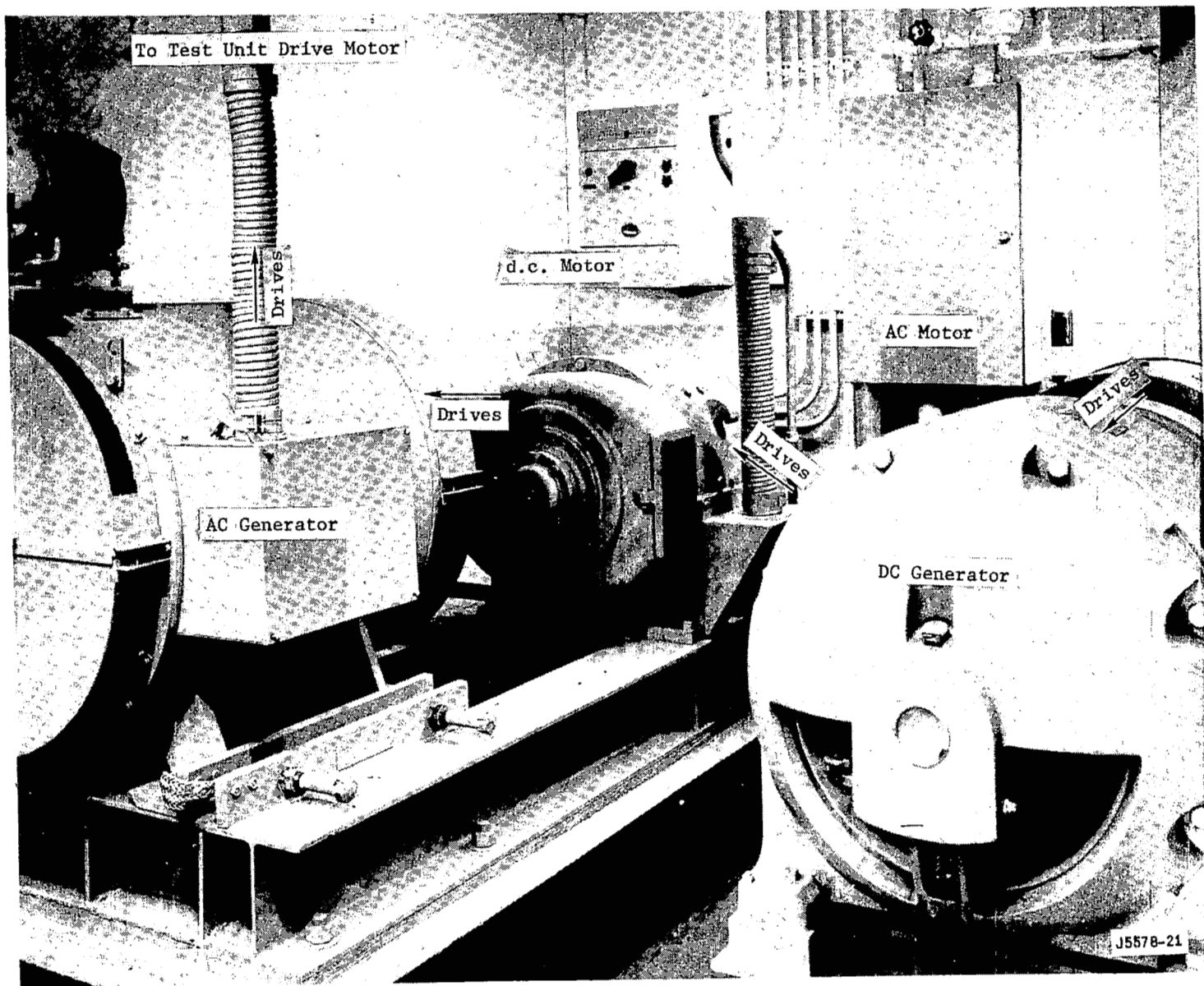
Figure 21. Motor Generator Set.

IV. CALIBRATION

Routine calibrations were carried out on all test unit instrumentation, with the exception of thermocouples. For these the manufacturer's guarantee of accuracy was accepted. For the displacement sensors and the load cells extensive calibrations were carried out in order to completely define all side effects on these two types of instrumentation. Several independent calibrations were necessary for the measuring of torque.

A. DISPLACEMENT SENSORS

The effects of temperature and the presence of water on the readings for the displacement sensors were thoroughly investigated and are discussed in References 2 and 3. Room temperature (77°F) calibrations were carried on all displacement sensors in order to determine the sensitivity of these devices. The sensitivities of two displacement sensors which were to be placed diametrically opposite each other were adjusted to be equal and opposite in sign. This procedure is discussed in Reference 5. The bench calibration of the displacement sensors was carried out in pairs in the insulated chamber pictured in Figure 22. Bench calibrations were carried out at two test temperatures, namely, 75 and 120°F. Each pair of displacement sensors was calibrated over a range of 6 to 14 mils gap between the sensor and the shaft. The probes were Bently Nevada Model H1084 and the detector drivers were either Bently Nevada D152 or D252R. The calibration standard for these tests was a Sheffield Corp., Linearchek gage calibrator which has a guaranteed accuracy traceable to the National Bureau of Standards of ± 25 micro-inches.
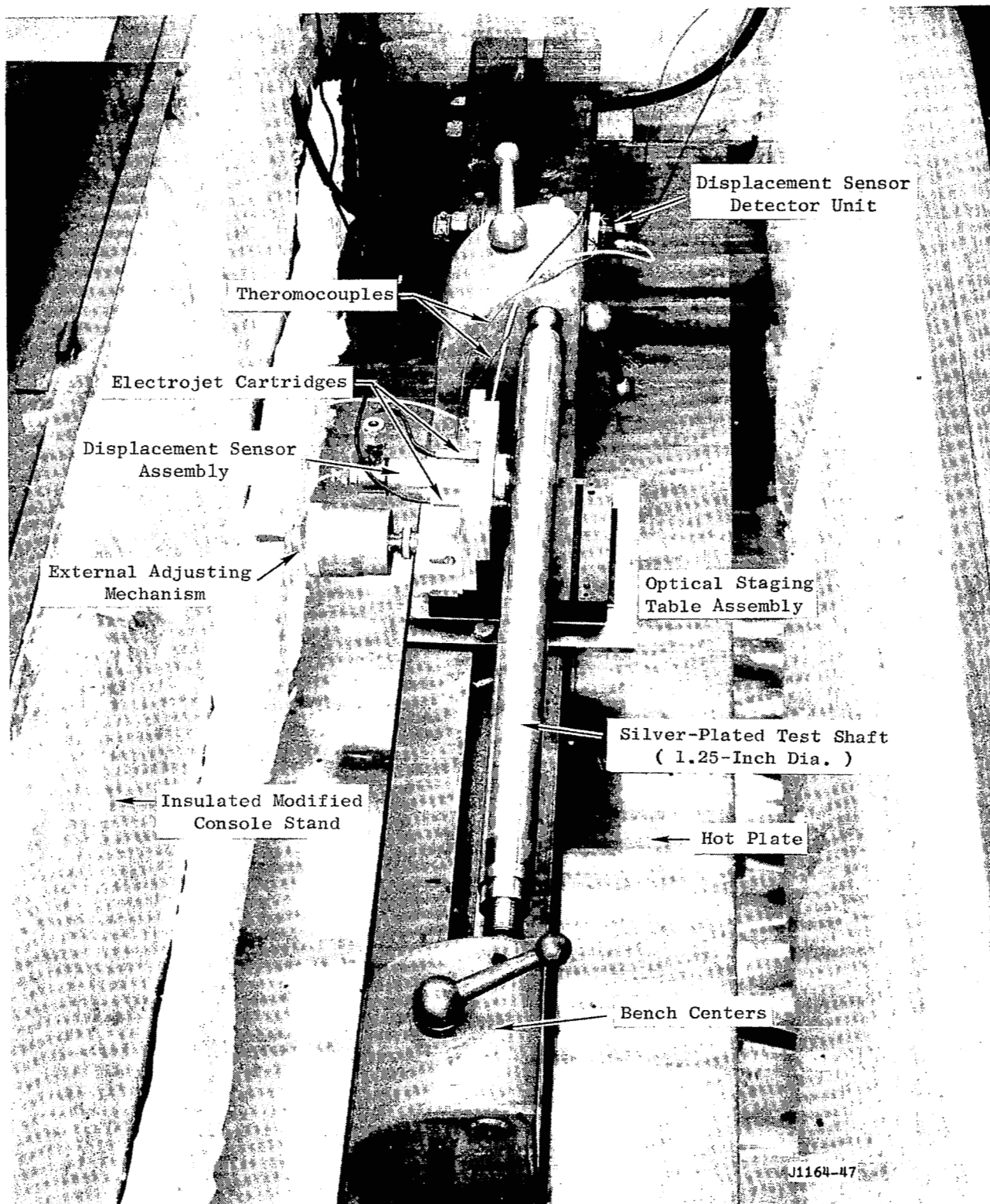
Figure 22. Displacement-Sensor Elevated-Temperature Calibration Equipment.

This device was used to calibrate the electrojet cartridges which were used in conjunction with Accutron transistor amplifier and read on a John Fluke Company differential volt meter to measure the shaft displacement during calibration.

The average measured sensitivity of the eight pairs of displacement sensors is presented in Table VIII for the two test temperatures.

Initially an attempt was made to establish the voltage reading of the displacement sensors when the shaft was in the center of the bearing by moving the shaft first in the x and then in the y-direction from contact with one side of the bearing to contact with the other side of the bearing. However, it was found that these center positions differed from the rotating center position by as much as 240 micro-inches. The rotating center positions were obtained by retracting the loader bearings and running the vertical test shaft over the permissible speed range with several levels of unbalance. Because of the large discrepancy between the statically determined bearing center positions and the dynamically determined positions it was decided that the dynamically determined bearing center positions would be utilized to reduce the data. Shown in Table IX are the bearing center positions in mils for each of the levels of unbalance used throughout the bearing testing. Shown in Table X is the average deviation of the rotating center positions with speed for all unbalance levels for the two types of bearings. It can be seen that for a given level of unbalance the average deviation of the center positions did not exceed 30 micro-inches. At one period during testing it appeared that the rotating center position was changing, possibly from day

TABLE VIII

DISPLACEMENT SENSOR AVERAGE SENSITIVITY

Nominal Calibration Temperature, °F	Probe Pair	Direction and Plane	Average Sensitivity Measured Sum, volts/mils	Calibration Date
120	1	y 1	1.006	9/14/66
	2	x 1	0.993	9/13/66
	3	y 2	1.013	9/14/66
	4	x 2	1.009	9/15/66
	5	y 3	0.993	9/15/66
	6	x 4	0.994	9/15/66
	7	y 4	1.012	9/15/66
	8	x 3	0.998	11/9/66
75	1	y 1	1.078	9/17/66
	2	x 1	1.057	9/17/66
	3	y 2	1.093	9/17/66
	4	x 2	1.110	9/17/66
	5	y 3	1.083	9/17/66
	6	x 4	1.102	9/17/66
	7	y 4	1.076	9/16/66
	8	x 3	1.062	11/1/66

TABLE IX

BEARING CENTER POSITIONS, MILS

Driven End ──

Instrumentation Planes

Upper Bearing ──→

4

3

Loader Bearings ──

Test Shaft

Down

2

Lower Bearing ──→

1

Unbalance Disc ──→
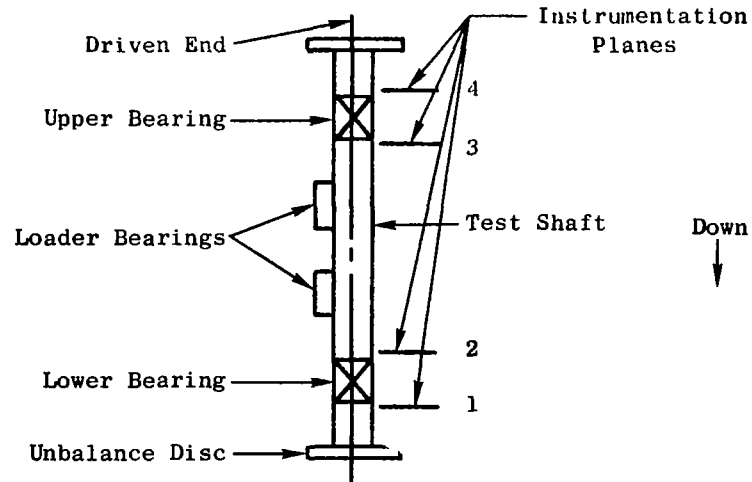
Digital Channel	206	224	233	215	207	225	234	216
Probe Pair	2	4	8	6	1	3	5	7
Direction and Plane	X 1	X 2	X 3	X 4	Y 1	Y 2	Y 3	Y 4

Bearing	Temp., °F	Misalign sec	Misalign mils	Pads	Unbal., gr.-in.								
Pivoted-Pad	120	0	0	Free	+ 1	.0292	-.0038	.1146	.1149	-.0038	.2976	.1901	.1097
					- 1	.0178	-.0159	.1428	.0899	-.0232	.3120	.1803	.1122
					0	.0062	.0201	-.0246	.1381	.0137	.3011	.1410	.0458
					+ 0.5	-.0153	-.0232	.0439	.1906	-.0110	.2924	.1628	.0735
					± 0.5	.0063	.0260	-.0056	.1588	.0168	.3206	.1852	.1133

TABLE IX (Continued)

Bearing	Temp., °F	Misalign sec	Misalign mils	Pads	Unbal., gm.-in.	X 1	X 2	X 3	X 4	Y 1	Y 2	Y 3	Y 4
	75				+ 0.5	.0796	.0109	.0063	.0809	.0897	.3544	.1409	.0978
					± 0.5	-.1085	-.0421	.0166	.0419	-.1079	.3288	.1185	.0820
Pivoted-Pad	120	400	4	Free	0	.105	-.007	-.113	-.073	.067	.174	-.071	-.045
					+ 0.5	.101	-.036	-.074	-.054	.055	.135	-.037	-.047
					± 0.5	.154	-.001	-.025	-.048	.047	.164	-.006	.003
Pivoted-Pad	120	0	0	Symmetric	- 1	.0908	-.1477	.1669	.0697	.4428	.4832	.1444	-.1003
					+ 1	.1266	-.1227	.2030	.1087	.4878	.5124	.1448	-.0715
					0	.0082	-.1351	.0878	.1422	.5166	.5405	.2879	-.0661
					+ 0.5	.0362	-.1523	.0615	.2098	.5303	.4940	.3051	-.0774
					± 0.5	.0932	-.1115	.1251	.1748	.5202	.4914	-.4442	-.0839
Pivoted-Pad	120	0	0	Askew	- 1	.1065	-.0995		.3497	-.1650	.2804	.1098	.0673
					+ 1	.0576	-.1920		.2356	-.2676	.2012	.0850	.0073
					0	.0860	-.1165		.2788	-.1066	.3470	.2763	.0632
					+ 0.5	.0904	-.1223		.2722	-.1529	.3219	-.2346	.0534
					± 0.5	.1290	-.0768		.3381	-.0938	.3176	-.0071	.0969
3-Lobe	120	0	0	----	- 2	.4225	.1163	.5023	.3529	.2149	.4449	.4034	.1119
					+ 2	.4694	.1625	.4900	.4175	---	.398	.408	.078
					+ 2	.4460	.1394	.4962	.3852	---	.4214	.4057	.0950
					± 1	.4093	.1454	.4363	.4145	---	.4005	.3246	.0333
					± 1	.4689	.1880	.4807	.4336	---	.4550	.3388	.074
					0	.4418	.1625	.4425	.3055	.1600	.4087	.3188	.0168
3-Lobe	120	400	4	----	- 2	.371	.250	.521	.386	.311	.284	.112	-.517
					+ 2	.453	.173	.086	-.195	.190	.328	.535	.068
					+ 2	.412	.239	.303	.096	.250	.306	.324	-.224
					± 1	.384	.305	.503	-.979	.452	.278	.085	-.418
					± 1	.385	.344	.541	-.972	.446	.285	---	-.443
					0	.370	.255	.520	.303	.285	.270	.122	-.533
3-Lobe	120	400	0	----	- 2	.565	.344	.596	-.323	.325	.455	.262	-.042
					+ 2	.621	.257	.236	-.784	.275	.490	.616	.417
					+ 2	.593	.300	.416	.554	.300	.472	.439	.188
					± 1	.534	.309	.549	-.311	.361	.381	.185	-.108
					± 1	.618	.269	.729	-.745	.278	.484	.628	.428
					0	.603	.258	.177	-.782	.267	.498	.602	.429

50

TABLE X

AVERAGE DEVIATION OF ROTATING CENTER POSITIONS WITH
SPEED FOR ALL UNBALANCE LEVELS

	Average Deviation, microinches	
	3-Lobe	Pivoted-Pad
Lower Bearing		
Outboard Instrumentation Station		
X - Direction	21	21
Y - Direction	30	15
Inboard Instrumentation Station		
X - Direction	28	22
Y - Direction	22	19
Upper Bearing		
Inboard Instrumentation Station		
X - Direction	20	26
Y - Direction	23	16
Outboard Instrumentation Station		
X - Direction	25	18
Y - Direction	30	18

to day. As a result during the latter tests with the pivoted-pad bearing, the rotating center positions were established before and after each day's test running with the same test conditions. Shown in Table XI is the average standard deviation of these center positions on a day-to-day basis. It is seen that these center positions have an average standard deviation that varies from approximately 10 to 95 micro-inches. This variation in center position had to be accepted as the best that can be expected under the conditions of the test.

Shown in Table XII is the displacement sensor bench calibration error analysis. The several errors which enter into the determination of shaft displacement are listed on this chart and are considered to be random errors. For that reason, the total error is shown to be the square roots of the sum of the squares of the individual errors. Shown in Table XIII is the displacement sensor equilibrium position error analysis. This error analysis begins with the bench calibration error from the previous chart, $\pm$ 52 micro-inches. The effects of water, temperature, non-linearity, average-level detector error, digital recorder error, detector driver error, and drift are taken into account. Also an estimate of the shaft centering position and accuracy is included as part of the error analysis. The square root of the sum of the squares of all these errors amounts to $\pm$ 89 micro-inches. This number compares with the variation in center position on a day-to-day basis shown in the previous table. Shown in Table XIV is the displacement sensor amplitude error analysis. Again the first entry in the table is the bench calibration error $\pm$ 52 micro-inches. This error analysis includes many of the items shown

52

TABLE XI

DAY-TO-DAY AVERAGE STANDARD DEVIATION IN PIVOTED-PAD
BEARING CENTER POSITION

| | Pads Free | One Locked Pad | |
	Misaligned	Symmetric	Askew
Lower Bearing			
Outboard Instrumentation Plane			
X - Direction	18.4	33.6	24.9
Y - Direction	21.4	95.2	62.4
Inboard Instrumentation Plane			
X - Direction	19.9	28.9	18.3
Y - Direction	23.9	90.5	70.1
Upper Bearing			
Inboard Instrumentation Plane			
X - Direction	38.3	51.7	----
Y - Direction	38.2	53.8*	28.1
Outboard Instrumentation Plane			
X - Direction	35.2	17.5	10.9
Y - Direction	17.2	19.8	15.6

* This instrument failed during this test series, some readings deleted.

53

TABLE XII

DISPLACEMENT SENSOR BENCH CALIBRATION ERROR ANALYSIS

Error Source	Estimated Error* micro inches	Square of Error
Bench Calibration		
Calibration Standard (Guaranteed)	$\pm$ 25	625
Electrojet Readability	$\pm$ 15	225
Electrojet Non Linearity	$\pm$ 10	100
Bently System Non Linearity	$\pm$ 35	1225
Summing Circuit Drift	$\pm$ 20	400
Power Supply Drift	$\pm$ 5	25
Calibration Readout Instrument	$\pm$ 10	100
Sum		2700
Error (Square Root of Sum of Squares)	$\pm$ 52 micro inches	

* Conversion from volts to micro inches is based on a nominal probe pair

sensitivity of 1.0 volts per 1 mil.

TABLE XIII

DISPLACEMENT SENSOR EQUILIBRIUM POSITION ERROR ANALYSIS

Error Source	Estimated Error* micro inches	Square of Error
Bench Calibration Error	± 52	2704
Effect of Water	± 40	1600
Temperature Non-Uniformity	± 20	400
Average Level Detector Non-Linearity	± 5	25
Average Level Calibration Error	± 5	25
Digital Recorder Error	± 5	25
Long Term Drift, Detector Driver	± 20	400
Summing Circuit Drift	± 20	400
Power Supply Drift	± 5	25
Bias Voltage Drift	± 5	25
Shaft Centering Procedure Inaccuracy	± 48	2304
Sum		7933

Error (Square Root of Sum of Squares)   ± 89 micro inches

*Conversion from volts to micro inches is based on a nominal probe pair sensitivity of 1.0 volts per 1 mil.

55

TABLE XIV

DISPLACEMENT SENSOR AMPLITUDE ERROR ANALYSIS

Error Source	Estimated Error* micro inches	Square of Error
Bencn Calibration Error	+ 52	2704
Effect of Water	+ 20	400
Temperature Non Uniformity	+ 20	400
Peak Detector Non-Repeatability & Ripple	+ 25	625
Peak Detector Calibration Error	+ 30	900
Digital Recorder Error	+ 5	25
Long Term Drift, Detector Driver	+ 20	400
Summing Circuit Drift	+ 20	400
Power Supply Drift	+ 5	25
Sum		5879
Error (Square Root of Sum of Squares)	+ 77 micro inches	

* Conversion from volts to micro inches is based on a nominal probe pair sensitivity of 1.0 volts per 1 mil.

in the previous table but since the amplitude does not depend upon the shaft centering procedure that item is omitted. As a result, the displacement sensor amplitude error analysis indicates a square root of the sum of the square of the individual errors of $\pm$ 77 micro-inches. This indicates that the displacement amplitude measurements should be slightly more accurate than the equilibrium position, which require the knowledge of bearing dynamic center position.

B. LOAD CELLS

Model 902A Kistler Instrument Corp. piezoelectric force transducers were utilized to measure the dynamic forces of the bearings during test. The calibration of the load cells is thoroughly discussed in Reference 3. The original intent was to use the piezoelectric load cells in pairs similar to the procedure used for the displacement sensors. However, the load cells selected had a maximum load capability of 8,000 lbs. For this reason it was necessary to preload the load cells to approximately 750 lbs. in order to assure that they were operating in a linear range. The required large preload on the load cells caused a large friction force and, therefore, reduced the sensitivity of the load cells in a direction perpendicular to the direction of loading. As a result, as indicated earlier the load cells were mounted opposite a carbide ball and on the ball thrust bearings. Shown in Figure 23 is the calibration setup used to calibrate these load cells. When possible, the load cells were calibrated before and after a series of tests. The values of sensitivity used to reduce the experimental data is presented in Table XV and where possible is the average of the sensitivities
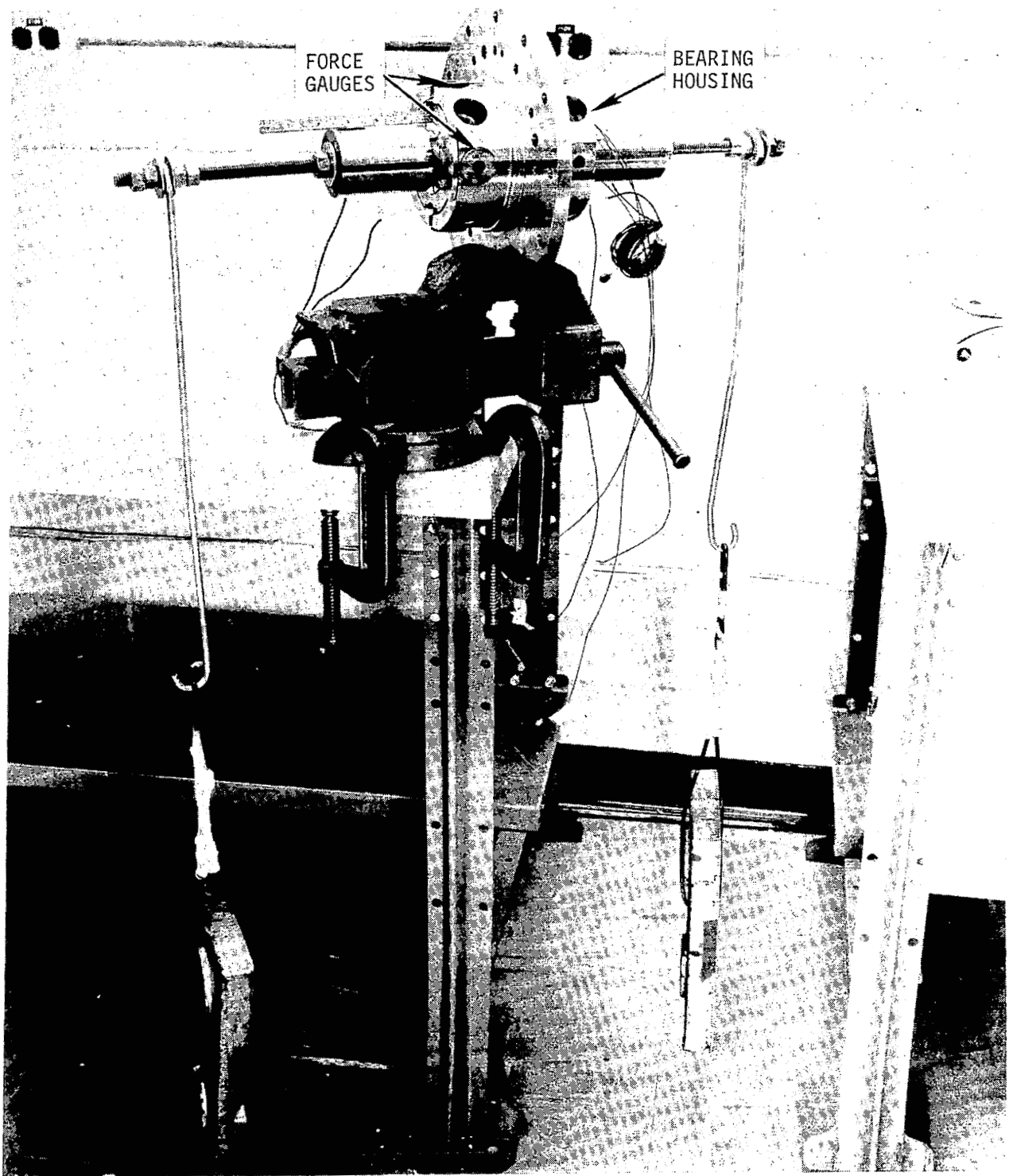
Figure 23. Force-Gāuge Calibration Equipment.

TABLE XV

LOAD–CELL SENSITIVITIES

(Pico Coulombs/lb)

Serial number			20464	20461	20455	20458	20469	20462	20465	20468
Direction and Plane			X 1	Y 1	X 4	Y 4	X 2	Y 2	X 3	Y 3
Bearing Test	**Test Date**									
Calibration Data										
Three-Lobe	1/30, 31/67		18.165	17.979	13.389	15.704	10.861	11.175	14.409	14.656
Three-Lobe	4/24/67		15.811	16.124	17.033		14.968	15.075	10.836	
Pivoted-Pad	4/27-5/1/67				13.797	15.373			14.596	14.107
Pivoted-Pad	8/23/67		13.777	15.593	15.255	14.894	12.580	13.776	14.349	13.183
Average Sensitivities										
Three-Lobe			16.988	17.052	13.389	15.704	12.914	13.125	14.409	14.656
Pivoted-Pad			14.794	15.858	14.526	15.134	13.774	14.426	14.472	13.645

before and after the test series. Shown in Table XVI is the variation in the sensitivity of the load cells before and after the test series. It is seen that the sensitivity of the load cells varies from approximately 1 to 16 percent.

C. TORQUE METER

The calibration of the torque measuring system was carried out in two steps. First, using the test setup shown in Figure 24 the angle of twist of the quill shaft was calibrated against dead weight torque measurements. Shown in Figure 25 is a typical calibration curve for a quill shaft used in the bearing testing. The next step in torque meter calibration was dynamic calibration of the phase meter. The calibration was carried out in the test equipment shown in Figure 26 and typical results are shown in Figure 27. The torque meter calibrations are thoroughly discussed in Reference 4.

A separate calibration was necessary to determine the torque on the test shaft imposed by the loader bearings. The calibration of the loader bearings is discussed in Reference 5. The data was obtained at approximately 70°F and it was non-dimensionalized by using the following dimensionless numbers:

A shaft moment coefficient

$$M_c = \frac{T_L}{6R_L C_L L_L \mu \omega} \left(\frac{C_L}{R_L}\right)^2 \qquad (1)$$

A Reynolds number

$$Re = \frac{\rho U_L C_L}{\mu} \qquad (2)$$

TABLE XVI

PERCENT DEVIATION OF KISTLER LOAD-CELL SENSITIVITIES

BEFORE AND AFTER TESTING

	Deviation, percent	
	3-Lobe	Pivoted-Pad
Lower Bearing		
Outboard Instrumentation Station		
X - Direction	6.9	6.9
Y - Direction	5.4	1.7
Inboard Instrumentation Station		
X - Direction	15.9	8.7
Y - Direction	14.9	4.5
Upper Bearing		
Inboard Instrumentation Station		
X - Direction	14.2	0.86
Y - Direction	----	3.4
Outboard Instrumentation Station		
X - Direction	12.0	5.0
Y - Direction	----	1.6
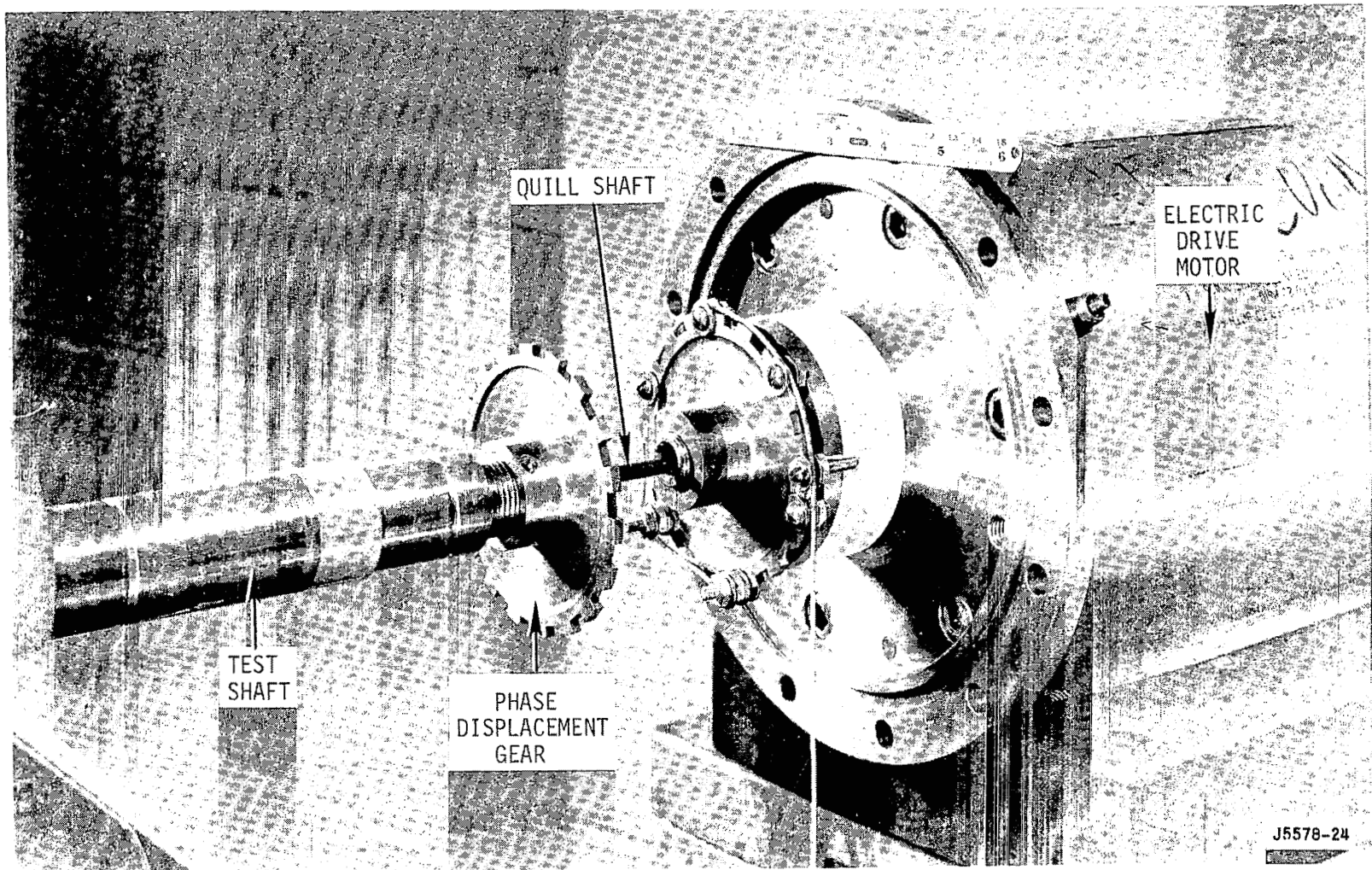
Figure 24. Quill-Shaft Torque Calibration Equipment.
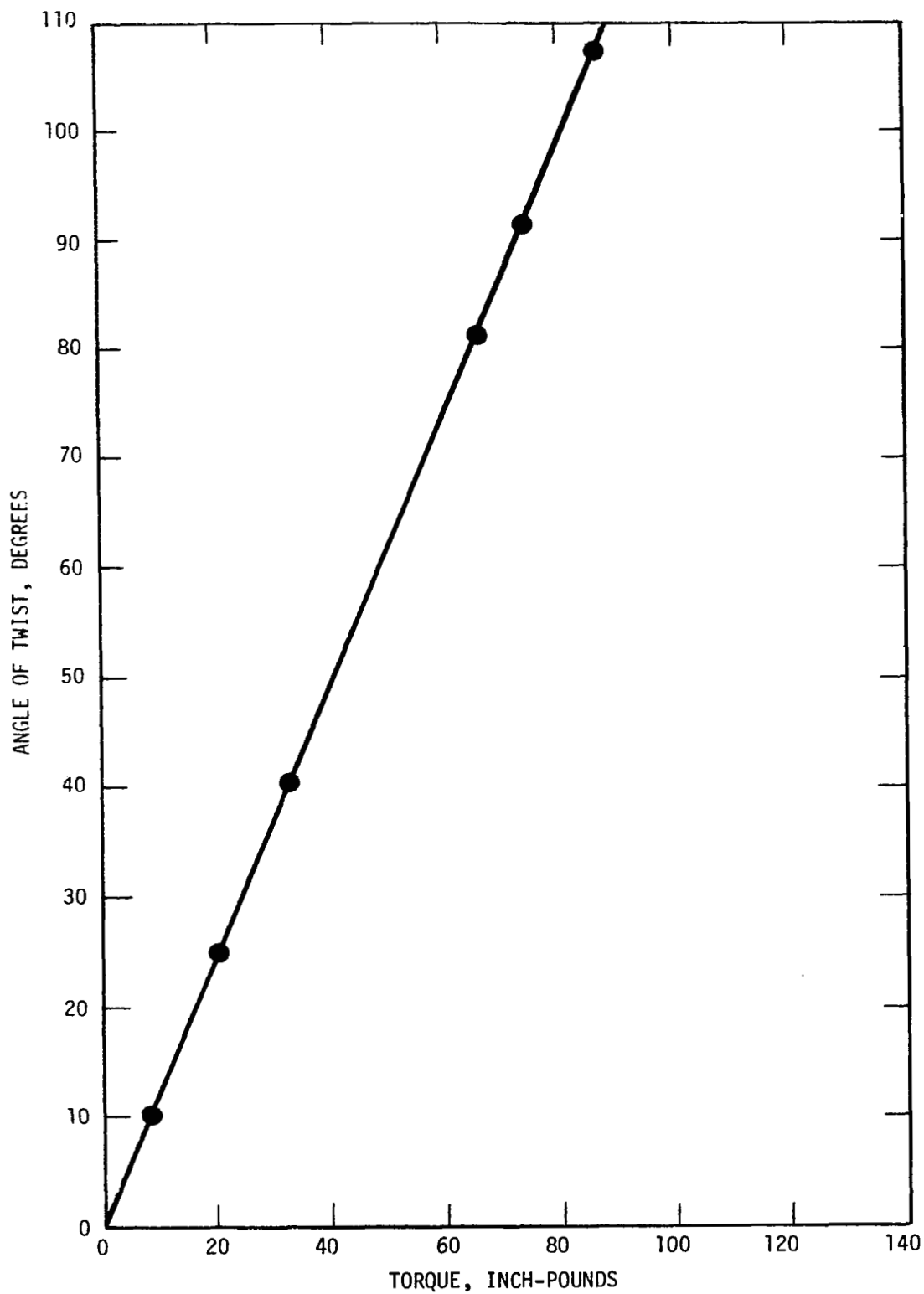
Figure 25.   Quill Shaft Torque Calibration.   Diameter, 0.125 Inches.
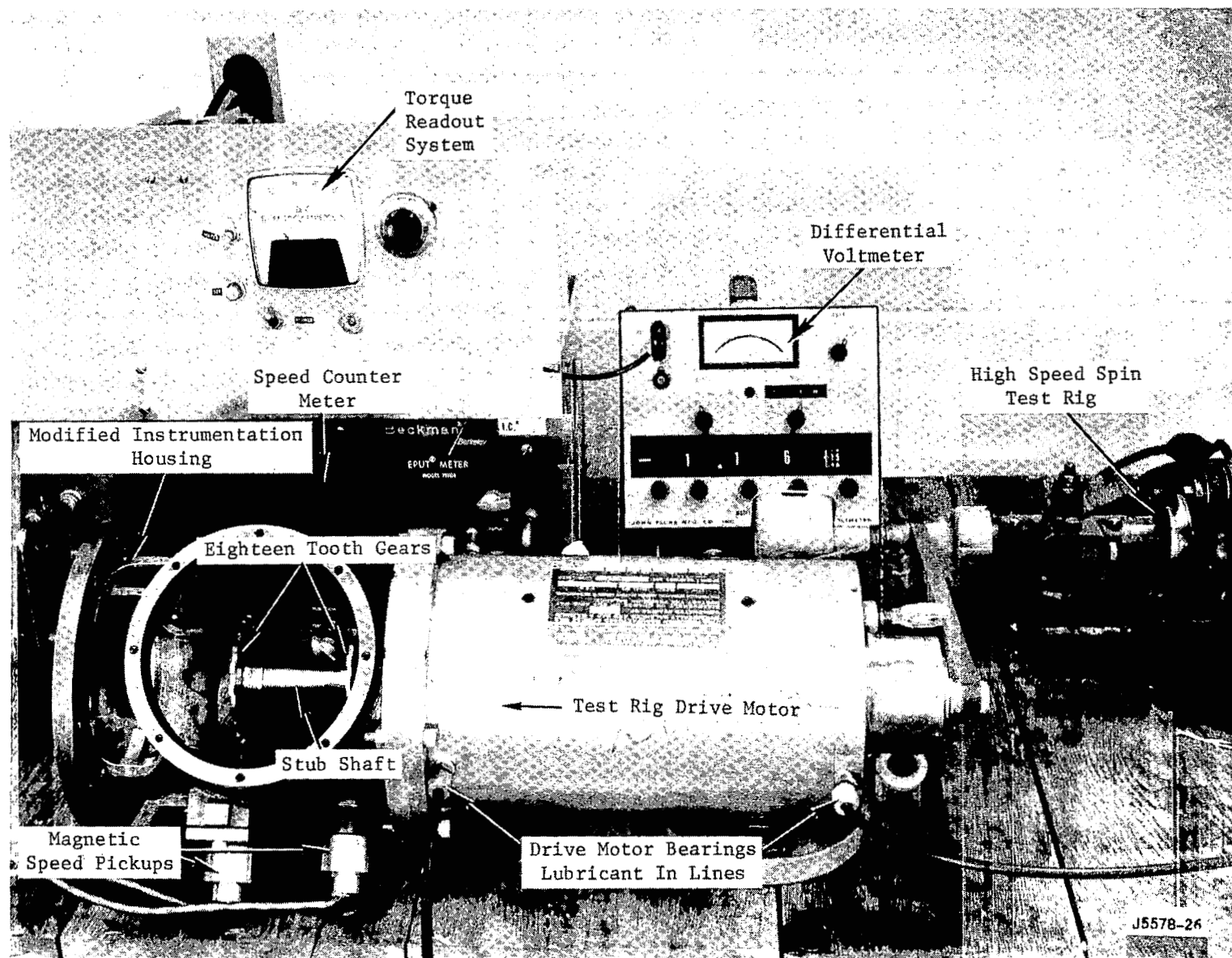
Figure 26. Torque-Meter Readout Circuit Calibration Equipment.

Figure 27. Torque-meter Readout Circuit Calibration.

65
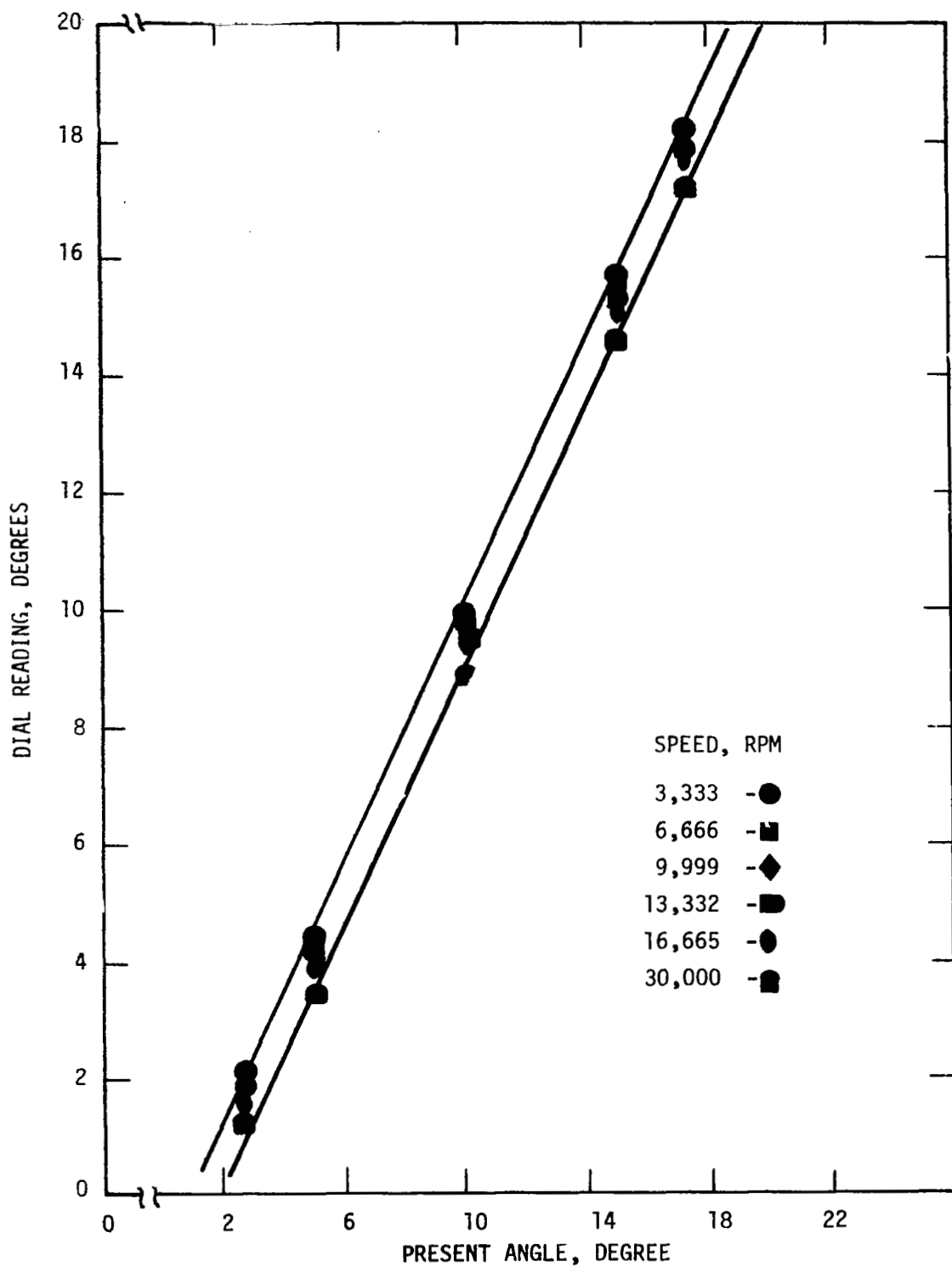
and a Sommerfeld number

$$S_L = \frac{\mu NL_L D_L}{60W} \cdot (\frac{R_L}{C_L})^2 \qquad (3)$$

(The symbols used in these equations can be found in the Nomenclature
List at the end of the Appendix.)   The results are shown in Figure 28.
Some extrapolation of the data, shown by dashed lines, was required to
cover bearing testing at 120°F. When calibrating the loader bearings,
the flow supplied to the bearing was also recorded. The resulting data
are plotted in Figure 29. During bearing testing the flow as a function
of side load shown on this graph were used as test conditions so as to
assure that the conditions would be the same as during calibration.

D. REMAINING INSTRUMENTATION

The calibration of some of the remaining instrumentation is dis-
cussed in Reference 3. These calibrations include the peak-to-peak
level detector for displacements and forces and the loader pistons.
Presented in Tables XVII, XVIII and XIX are the calibration data for
these devices.

66
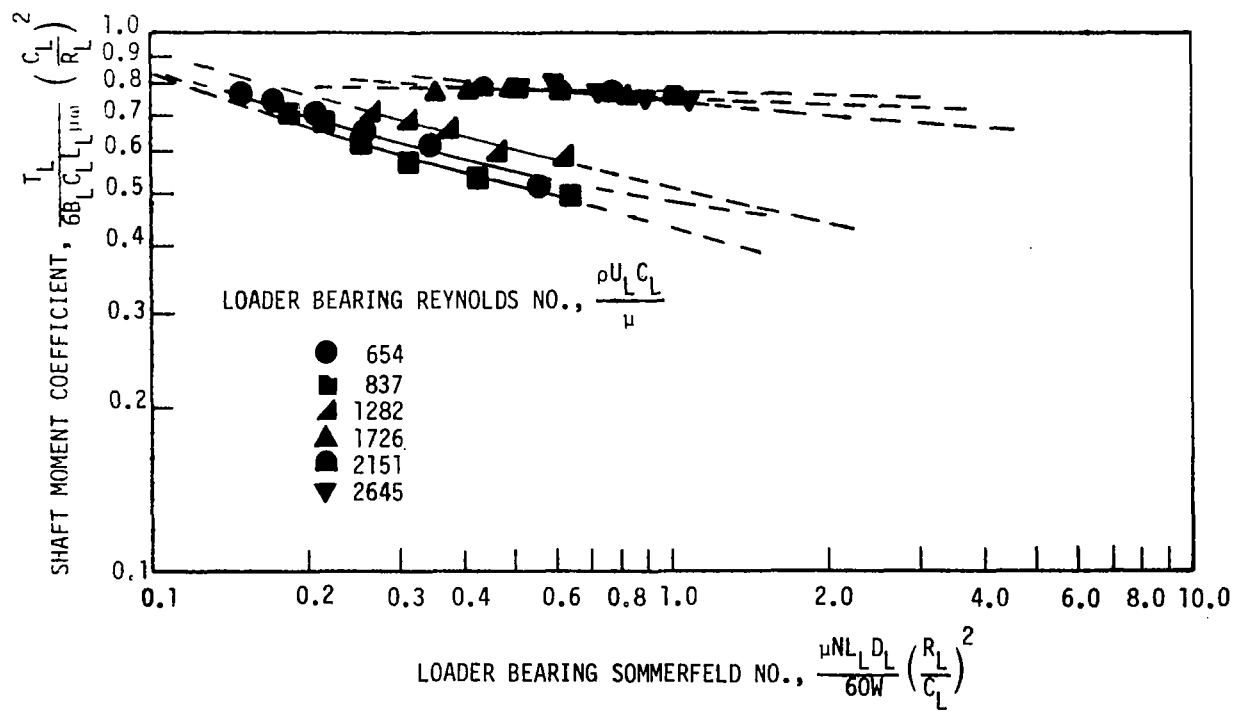
Figure 28. Loader Bearing Torque Calibration Data.
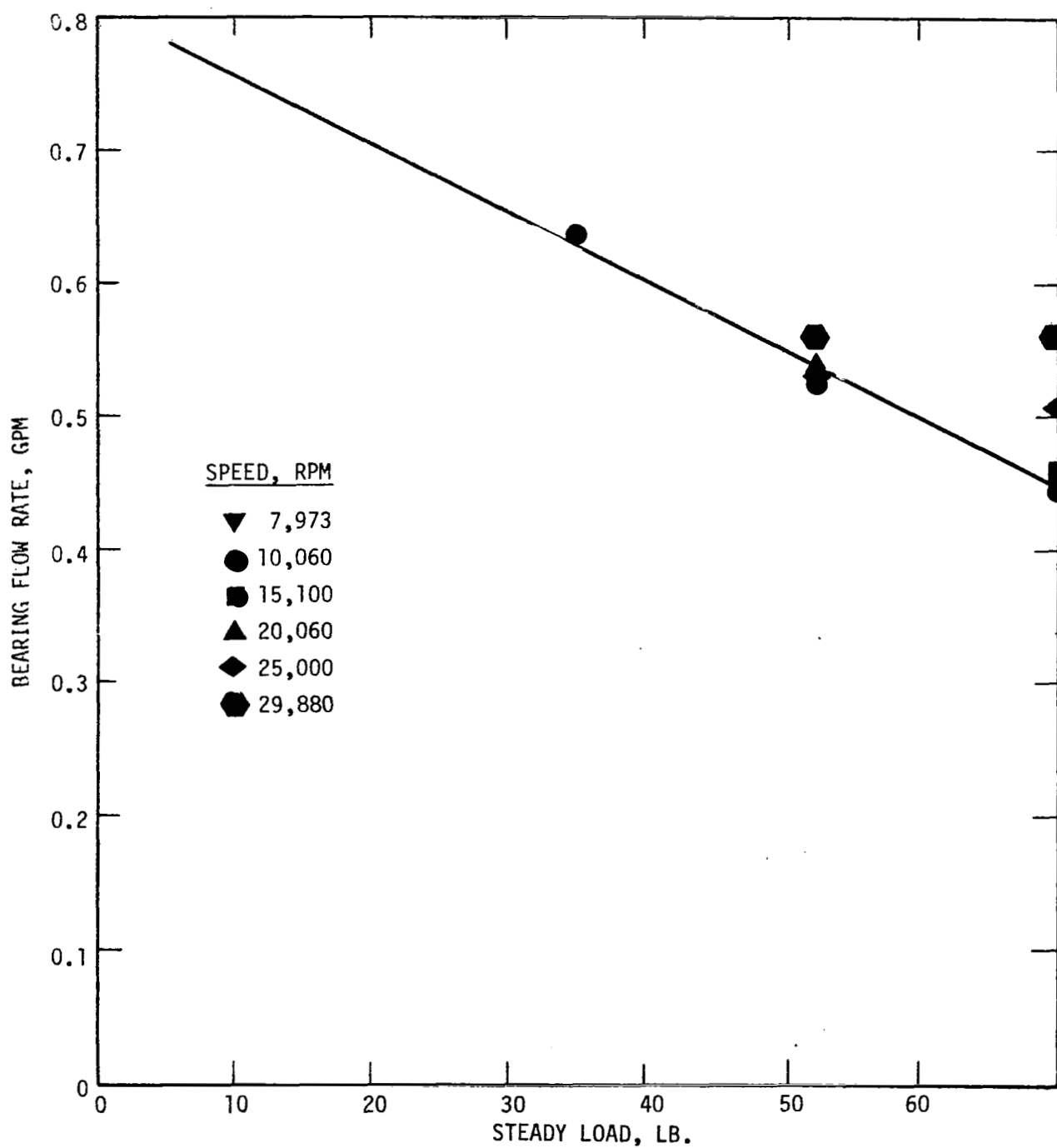
Figure 29.   Variation of Lubricant Flow With Steady Load During Loader Bearing
             Calibration.

TABLE XVII

CALIBRATION OF PEAK-TO-PEAK DETECTOR FOR DISPLACEMENT AMPLITUDE

Input,[1,3] volts	Frequency, cps	Output,[2] counts
4.0	150	8100
4.0	300	7975
4.0	500	8050
4.0	1000	8000
3.0	150	5888
3.0	300	5780
3.0	500	5847
3.0	1000	5802
2.0	150	3712
2.0	300	3645
2.0	500	3678
2.0	1000	3658
1.0	150	1619
1.0	300	1616
1.0	500	1591
1.0	1000	1614
0.5	150	662
0.5	300	657
0.5	500	646
0.5	1000	660

[1] Audio oscillator, voltage measured on a Dana Precision A.C. Voltmeter.

[2] Digital Data Acquisition System.

[3] Refer to Table VIII for sensor average sensitivity.

TABLE XVIII

CALIBRATION OF PEAK-TO-PEAK DETECTOR FOR FORCE AMPLITUDE

Input,[1,3] volts	Frequency, cps	Output,[2] Counts
4.0	150	8378
4.0	300	8283
4.0	500	8160
4.0	1000	8000
3.0	150	6240
3.0	300	6197
3.0	500	6124
3.0	1000	6009
2.0	150	4070
2.0	300	4030
2.0	500	3984
2.0	1000	3900
1.0	150	2022
1.0	300	1998
1.0	500	1966
1.0	1000	1913
0.5	150	989
0.5	300	979
0.5	500	962
0.5	1000	923

[1] Audio oscillator, voltage measured on a Dana Precision A.C. Voltmeter.

[2] Digital Data Acquisition System.

[3] Refer to Table XV for sensor sensitivities.

70

TABLE XIX

LOADER BEARING PISTON CALIBRATION

Load Applied, lbs/bearing	Pressure Applied, in. Hg			
	Lower Loader Piston		Upper Loader Piston	
2.11	2.99		2.99	
12.15	14.70	14.75	14.65	14.65
24.68	29.40		29.20	
37.20	44.30	44.40	43.70	43.80
57.23	68.90	68.70	67.20	67.30
77.25	92.80		91.00	
82.28	99.20	99.20	97.10	97.10
77.25	93.00		91.1	
57.23	69.00		67.4	
37.20	44.60	44.58	43.80	43.90
24.68	29.50		29.20	
12.15	14.70	14.70	14.60	14.62
2.11	3.00	3.00	3.00	3.00
0	0	0	0	0

V. BEARING TESTING

The ranges of the test variables were as follows:

Speed, rpm	7,800 to 31,000
Steady Load, lb/bearing	0 to 70
Unbalance, gr-in.	0 to 2 (in phase and 180° out of phase)
Lubricant Supply Pressure, psig	3.5 to 67
Lubricant Supply Temperature, °F	75 to 120
Known Angular Misalignment, sec	0 to 400
Known Linear Misalignment, mil	0 to 4

The schedules of test points for the pivoted-pad and three-lobe bearings are presented in Tables XX and XXI. Shown in Figure 30 is the variation of pad Reynolds number (as defined by equation 7) with speed. Shown in Table XXII are the values of Reynolds number for initiation of turbulence using the Taylor criterion (8) for the zero eccentricity of a 360-degree plain journal bearing having the same clearance as the machined clearance of the pivoted pad or three-lobe bearings. In the same table the values of lubricant (water) viscosity (9) and density (9) used are tabulated.

Initially for each bearing type speed runs were made at several levels of lubricant pressure. From these tests the constant lubricant pressures to be utilized for the remainder of the tests were determined. For the pivoted-pad bearing the lubricant pressure was held at constant 3 to 3.5 psig because this pressure could be held constant over the entire speed range. For the three-lobe bearing it was found that the

speed range could be transversed at lubricant pressures between 35 and 55 psig. Most of the testing was carried out at 35 psig but some tests were repeated at 45 and 55 psig. Pressures as high as 67 psig were utilized in an attempt to stabilize the bearing.

The test data was obtained in the following manner. The unbalance screws called for were inserted and the test unit was allowed to run until temperature equilibrium was reached. For each steady load a loader-bearing lubricant flow rate was set that was equal to the value used in calibrating the loader bearings. Next the speed and steady load were set. The specified lubricant temperature was checked and the specified lubricant pressures for each test bearing were set. Two digital-data-acquisition-system scans were made. Specified channels (phase angles), which experience had shown were sensitive indicators of steady conditions, were checked between the two scans for the specified repeatability (6 degrees). If the data was within the tolerance the conditions for the next point were set. If not, the point was either repeated until it met the tolerance or marked that the tolerance could not be met. While the scans of the data were being made a photograph of the two oscilloscopes showing the displacement orbits in planes 1, 2, and 4, were made and sufficient data to identify the test point were logged.

One of the oscilloscopes had a reinforced signal once each revolution. When more than one dot appeared in an orbit the shaft was in fractional-frequency whirl and a panoramic analyzer gave the frequencies. For the three-lobe bearing tests, the speed at which the oscilloscope indicated fractional-frequency whirl first occurred was

73

recorded and photographed, but no higher test speeds were investigated. For the pivoted-pad bearings the speed run at a set of test conditions was aborted when the synchronous shaft orbit was judged to endanger the bearings. Because of the danger to the test unit under such test conditions, it was not possible to take a photograph of the oscilloscopes.

During testing each data point having a number ending in five or zero was repeated with at least one intervening test point between. These additional test points were gotten to establish repeatibility (or test precision).

TABLE XX

PIVOTED-PAD BEARING TEST PLAN

All Pads Free-Aligned
Lubricant Pressure 3.0-3.5 psig, Lube Temperature 120°F

Unbalance,[1] gr.-in. ⟶

Sideload, lbs/brg.	Unbalance = 0				Unbalance = +0.5				Unbalance = ±0.5				Unbalance = +1.0				Unbalance = −1.0			
	Point No.	Speed, $rpm \times 10^{-3}$	Notes	Stable and Repeat	Point No.	Speed, $rpm \times 10^{-3}$	Notes	Stable and Repeat	Point No.	Speed, $rpm \times 10^{-3}$	Notes	Stable and Repeat	Point No.	Speed, $rpm \times 10^{-3}$	Notes	Stable and Repeat	Point No.	Speed, $rpm \times 10^{-3}$	Notes	Stable and Repeat
0	1031	8.0	O	S	1067	8.1		S	5067	8.1		S	1019	8.0		S	1025	8.0		S R
	1032	11.6	O	S	1068	11.5		S	5068	11.5		S	1020	11.7		S R	1026	11.6		S
	1033	15.3	O	S	1069	15.3		S	5069	15.1		S	1021	15.2		S	1027	15.2		S
	1034	18.8		S	1070	18.9		S R	5070	18.9		S R	1022	18.8		S	1028	18.8		S
	1035	22.4		S R	1071	22.3		S	5071	22.4		S	1023	22.5	△	S	1029	22.4	△	S
	1036	26.0		S	1072	24.9	△	S	5072	26.1		S								
	1121	27.0	△	S					1124	26.9		S								
5	1037	8.0	O	S	1073	8.0		S	5073	8.1		S								
	1038	11.6	O	S R	1074	11.7		S	5074	11.6		S								
	1039	15.2		S	1075	15.2		S R	5075	15.2		S R								
	1040	18.8		S	1076	18.8		S	5076	18.8		S								
	1041	22.4		S	1077	22.4	□	S	5077	22.4	□	S								
	1042	25.4	△	S																
15	1043	8.0	O	S	1079	8.0		S	5079	8.0		S								
	1044	11.6		S	1080	11.6		S R	5080	11.6		S R								
	1045	15.2		S R	1081	15.2		S	5081	15.2		S								
	1046	18.8		S	1082	18.8		S	5082	18.8		S								
	1047	22.4		S	1083	22.4		S	5083	22.4		S								
	1048	26.0		S	1084	23.0		S	5084	24.1	△	S								
25	1049	8.0	O	S	1085	8.0		S	5085	8.0		S								
	1050	11.6		S	1086	11.6		S R	5086	11.5		S R								
	1051	15.3	O	S	1087	15.1	O	S	5087	15.2		S								
	1052	18.8		S R	1088	18.9	O	S	5088	18.8		S								
	1053	22.4		S	1089	22.5		S	5089	22.4		S								
	1054	26.0		S	1090	23.8	△	S R	5090	26.0		S R								
50	1055	8.0	O	S R	1091	8.0		S	5091	8.0		S								
	1056	11.7	O	S	1092	11.6		S	5092	11.7		S								
	1057	15.3	O	S	1093	15.3	O	S	5093	15.7		S								
	1058	18.7	O	S	1094	16.8		S	5094	18.8		S								
	1059	22.5		S	1095	22.5		S R	5095	22.4		S R								
	1060	26.0	⊛	S R	1096	23.6		S	5096	25.9		S								
	1122	28.0		S																
70	1061	8.1	O	S	1097	8.0		S	5097	8.0		S								
	1062	11.5	O	S	1098	11.7		S	5098	11.6		S								
	1063	15.3	O	S	1099	15.3		S	5099	15.2		S								
	1064	18.8		S	1100	18.8		S R	5100	18.8		S R								
	1065	22.4		S R	1101	22.5		S	5101	22.4		S								
	1066	26.0	O	S	1102	23.0		S	5102	25.4		S								
	1129	30.0		S																

○ Some or all phase angles out of tolerance. □ Maximum speed due to erratic loader bearing pad motion. ▽ Maximum speed due to unsteady orbits.
△ Maximum speed due to maximum orbit size. ◣ Forces and displacements too low.

[1] (+) unbalance weight at single tooth, (−) unbalance weight 180° from single tooth.

TABLE XX (Continued)

Pads Free Misaligned 4 mil, 400 sec.
Lubricant Pressure 3.0-3.5 psig, Lubricant Temperature, 120°F

Unbalance, gr.-in. ⟶

Sideload, lbs/brg.	Point No.	Speed, rpmx10⁻³	Notes	Stable and Repeat	Point No.	Speed, rpmx10⁻³	Notes	Stable and Repeat	Point No.	Speed, rpmx10⁻³	Notes	Stable and Repeat	Point No.	Speed, rpmx10⁻³	Notes	Stable and Repeat	Point No.	Speed, rpmx10⁻³	Notes	Stable and Repeat
		0				+ 0.5				+ 0.5				+ 1.0				- 1.0		
0	2031	8.0	O △	S	2067	8.0		S	6067	8.0		S								
	2032	11.6	O	S	2068	11.6		S	6068	11.6		S								
	2033	15.2	O	S	2069	15.2		S	6069	15.2		S								
	2034	18.8	⊙	S	2070	18.8		S R	6070	18.8	®	S R								
	2035	22.4	®	S R	2071	22.4		S	6071	22.4		S								
	2036	26.0		S	2072	24.5	△	S	6072	26.0		S								
5																				
15																				
25																				
50																				
70	2061	8.0	⊙	S	2097	8.0		S	6097	8.0		S								
	2062	11.6	O	S	2098	11.6		S	6098	11.6		S								
	2063	15.2		S	2099	15.2		S	6099	15.2		S								
	2064	18.8	O	S	2100	18.8	®	S R	6100	18.9		S R								
	2065	22.4		S R	2101	22.4		S	6101	22.4		S								
	1150	30.5		S	2102	23.5	△	S	6102	24.0	△	S								

76

TABLE XX (Continued)

All Pads Free-Aligned
Lubricant Pressure 3.0-3.5 psig, Lubricant Temperature 75°F

Unbalance, gr.-in. →	0				+0.5				±0.5				+1.0				-1.0			
Sideload, lbs/brg.	Point No.	Speed, rpmx10^{-3}	Notes	Stable and Repeat	Point No.	Speed, rpmx10^{-3}	Notes	Stable and Repeat	Point No.	Speed, rpmx10^{-3}	Notes	Stable and Repeat	Point No.	Speed, rpmx10^{-3}	Notes	Stable and Repeat	Point No.	Speed, rpmx10^{-3}	Notes	Stable and Repeat
0					1103	8.0	○	S	5103	8.0	○	S								
					1104	11.6		S	5104	11.6		S								
					1105	15.2		S R	5105	15.2		S R								
					1106	18.8	○	S	5106	18.8		S								
					1107	22.4		S	5107	22.4		S								
					1108	23.9	△	S	5108	25.7	△	S								
5																				
15																				
25					1109	8.0		S	5109	8.0		S								
					1110	11.7	○	S R	5110	11.6		S R								
					1111	15.2		S	5111	15.2		S								
					1112	18.8		S	5112	18.8		S								
					1113	22.4		S	5113	22.4	○	S								
					1114	23.3	△	S	5114	24.6	○△	S								
50																				
70					1115	8.0	○	S R	5115	8.0		S R								
					1116	11.6		S	5116	11.6		S								
					1117	15.2		S	5117	15.3		S								
					1118	18.8	○	S	5118	18.8		S								
					1119	22.4	○△	S	5119	22.4		S								
									5120	24.3	△	S R								

TABLE XX (Continued)

Pads Locked Aligned
Lubricant Pressure 3.0-3.5 psig, Lubricant Temperature, 120°F

Unbalance,[1] gr.-in. ⟶

Sideload, lbs/brg.	0				+0.5				+0.5				+1.0				-1.0			
	Point No.	Speed, rpmx10⁻³	Notes	Stable and Repeat	Point No.	Speed, rpmx10⁻³	Notes	Stable and Repeat	Point No.	Speed, rpmx10⁻³	Notes	Stable and Repeat	Point No.	Speed, rpmx10⁻³	Notes	Stable and Repeat	Point No.	Speed, rpmx10⁻³	Notes	Stable and Repeat
0	3031	8.0	○	S	3067	8.0	⊕	S	7067	8.0	○	S	3019	8.0		S	3025	8.0		S R
	3032	11.6	○	S	3068	11.6		S	7068	11.6		S	3020	11.6		S R	3026	11.6		S
	3033	15.2		S	3069	15.2		S	7069	15.3		S	3021	15.2		S	3027	15.2		S
	3034	18.8		S	3070	18.8		S R	7070	18.8		S R	3022	18.8		S	3028	18.8		S
	3035	22.4		S R	3071	22.4		S	7071	22.3		S	3023	22.4		S	3029	22.4		S
	3036	26.0		S	3072	23.5	△	S	7072	25.9		S	3024	23.5	△	S	3030	23.3	△	S R
5	3037	8.0	○	S	3073	8.0	○	S	7073	8.0	○	S								
	3038	11.6	○	S	3074	11.6		S	7074	11.5		S								
	3039	15.3		S	3075	15.2		S R	7075	15.2		S R								
	3040	18.8		S R	3076	18.8		S	7076	18.8		S								
	3041	22.4		S	3077	22.4		S	7077	22.3		S								
					3078	24.4	△	S	7078	25.9		S								
15	3043	8.0	○	S	3079	8.0	○	S	7079	8.0	○	S								
	3044	11.6	○	S	3080	11.5		S R	7080	11.7		S R								
	3045	15.2		S R	3081	15.2		S	7081	15.3		S								
	3046	18.8		S	3082	18.8		S	7082	18.9		S								
	3047	22.4		S	3083	22.4		S	7083	22.5		S								
	3048	24.4	△	S	3084	24.5		S	7084	26.0		S								
25	3049	8.0	○	S	3085	8.0	○	S R	7085	8.0		S R								
	3050	11.6	○	S	3086	11.6		S	7086	11.6		S								
	3051	15.2		S	3087	15.2		S	7087	15.2		S								
	3052	18.8		S	3088	18.8	○	S	7088	18.8		S								
	3053	22.4		S	3089	22.5		S	7089	22.4		S R								
	3054	24.2	△	S	3090	24.0	△	S R	1150	25.0		S								
50	3055	8.0	○	S R	3091	8.0		S	7091	8.0		S								
	3056	11.6	⊕	S	3092	11.6		S	7092	11.6		S								
	3057	15.2		S	3093	15.2		S	7093	15.2		S								
	3058	18.8		S	3094	18.8		S	7094	18.8		S								
	3059	22.4		S	3095	22.4		S R	7095	22.4		S R								
	3060	24.0	△	S R	3096	23.5	△	S	7096	26.0		S								
70	3061	8.0	○	S	3097	8.0	○	S	7097	8.0		S								
	3062	11.6	⊕	S	3098	11.6		S	7098	11.7		S								
	3063	15.3		S	3099	15.2		S	7099	15.2		S								
	3064	18.8		S	3100	18.8		S R	7100	18.8		S R								
	3065	22.4		S R	3101	22.4		S	7101	22.4		S								
	1149	23.4		S	3102	23.5	△	S	7102	26.0		S								

78

TABLE XX (Continued)

Pads Locked Askew
Lubricant Pressure 3.0-3.5 psig, Lubricant Temperature, 120°F

Unbalance,[1] gr.-in. ⟶

Sideload, lbs/brg.	Unbalance 0				Unbalance +0.5				Unbalance ±0.5				Unbalance +1.0				Unbalance -1.0			
	Point No.	Speed, rpmx10^{-3}	Notes	Stable and Repeat	Point No.	Speed, rpmx10^{-3}	Notes	Stable and Repeat	Point No.	Speed, rpmx10^{-3}	Notes	Stable and Repeat	Point No.	Speed, rpmx10^{-3}	Notes	Stable and Repeat	Point No.	Speed, rpmx10^{-3}	Notes	Stable and Repeat
0	4031	8.0	O	S	4067	8.0	◔	S	8067	8.0	O	S	4025	8.0	O	S R	4019	8.0		S
	4032	11.5	O	S	4068	11.6		S	8068	11.6		S	4026	11.6		S	4020	11.6		S R
	4033	15.2	O	S	4069	15.2		S	8069	15.2		S	4027	15.2		S	4021	15.3		S
	4034	18.9	O	S R	4070	18.8	O	S R	8070	18.8	(R)	S R	4028	18.8		S	4022	18.8		S
	4035	22.4		S R	4071	22.4		S	8071	22.4	O	S	4029	22.4	△	S	4023	22.4		S
	4036	26.0		S	4072	24.5	△	S	8072	26.0		S					4024	23.0	△	S
	1151	27.5	△	S																
5	4037	8.0	O	S	4073	8.0	O	S	8073	8.0		S								
	4038	11.6	O	S	4074	11.6		S	8074	11.6		S								
	4039	15.2		S	4075	15.2		S R	8075	15.2	O	S R								
	4040	18.8	O	S R	4076	18.8	O	S	8076	18.8		S								
	4041	22.4	O	S	4077	22.4		S	8077	22.4	O	S								
	4042	26.0		S	4078	24.4	△	S	8078	26.0		S								
	1152	27.5	△	S																
15	4043	8.0		S	4079	8.0	O	S	8079	8.0		S								
	4044	11.6	O	S	4080	11.6		S R	8080	11.6		S R								
	4045	15.3	O	S R	4081	15.2		S	8081	15.2		S								
	4046	18.8		S	4082	18.8	O	S	8082	18.8		S								
	4047	22.4	O	S	4083	22.4		S	8083	22.4	O	S								
	4048	26.0		S	4084	23.5	▽	S	8084	26.0	O	S								
	1153	27.0		S																
25	4049	8.0	O	S	4085	8.0	O	S R	8085	8.0		S R								
	4050	11.6	O	S R	4086	11.7		S	8086	11.7		S								
	4051	15.2	O	S	4087	15.2		S	8087	15.2		S								
	4052	18.8	O	S	4088	18.8		S	8088	18.9		S								
	4053	22.4		S	4089	22.4		S	8089	22.4		S								
	4054	26.0		S	4090	23.5	△	S R	8090	26.0		S R								
	1154	27.3	△	S																
50	4055	8.1	◑	S R	4091	8.0	O	S	8091	8.1		S								
	4056	11.7	O	S	4092	11.6	O	S	8092	11.6		S								
	4057	15.3	O	S	4093	15.2		S	8093	15.2		S								
	4058	18.8		S	4094	18.8	O	S	8094	18.8		S								
	4059	22.4	O	S	4095	22.4	O	S R	8095	22.4		S R								
	4060	26.0		S R	4096	23.0	△	S	8096	26.0		S								
	1156	31.0		S																
70	4061	8.0	O	S	4097	8.0	O	S	8097	8.0		S								
	4062	11.6	O	S	4098	11.6		S	8098	11.7		S								
	4063	15.3	O	S	4099	15.2		S	8099	15.3		S								
	4064	18.9	O	S	4100	18.8	O	S R	8100	18.8		S R								
	4065	22.4	O	S R	4101	22.4		S	8101	22.4		S								
	4066	26.0		S	4102	22.5	△	S	8102	26.0		S								
	1158	30.9		S																

TABLE XXI

THREE-LOBE BEARING TEST PLAN

Aligned
Lubricant Pressure 35 psig, Lube Temperature 120°F

Unbalance, gr.-in. → | 0 | +1 | ±1 | +2 | -2 | ±2

Sideload, lbs/brg.	Point No.	Speed rpmx10⁻³	Notes	Stable and Repeat	Point No.	Speed rpmx10⁻³	Notes	Stable and Repeat	Point No.	Speed rpmx10⁻³	Notes	Stable and Repeat	Point No.	Speed rpmx10⁻³	Notes	Stable and Repeat	Point No.	Speed rpmx10⁻³	Notes	Stable and Repeat	Point No.	Speed rpmx10⁻³	Notes	Stable and Repeat
0	2079	8.0		S	2044	8.1		S	2037	8.0	○	Uns	2019	8.0		S	2007	8.0		S				
	2080	11.1		S R	2045	11.0		S R	2038	10.9		S					2008	11.0	◊	S				
	2081	14.1		S	2046	14.0		S	2039	14.2		S												
	2082	17.1		S	2047	17.1		S	2040	17.0		S R					2087	18.9	◊	Uns				
	2083	20.2		Uns	2048	20.0		Uns	2041	20.0		Uns												
25	2073	8.2		S	2049	8.0		S																
	2074	11.0		S	2050	11.0		S R	2056	11.0		S												
	2075	14.0		S R	2051	14.0		S	2057	14.0		S												
	2076	17.0		S	2052	17.1		S	2058	17.0		S R												
	2077	20.0		S R	2053	20.0		S	2059	20.0		Uns												
	2078	21.5		Uns	2054	20.5		Uns																
					2005	10.0		S	2001	10.0		S												
					2006	12.5		S	2002	12.6		S R												
					2007	15.5		S I	2003	15.5		S												
					2008	18.5	○	S	2004	18.5		S												
									2085	19.7		Uns												
50	2067	8.0		S									2025	8.0		S R					2031	8.0		S
	2068	11.0		S									2026	11.0		S R					2032	11.0		S
	2069	14.0		S									2027	13.9		S					2033	14.0		S
	2070	17.0		S R									2028	17.1		S R					2034	17.1		S
	2071	20.0		S R									2029	19.8		Uns					2035	20.0		S R
	2072	21.4		Uns																	2036	23.0		S
													2013	10.0		S					2009	10.0		S
													2014	12.6		S R					2010	12.5		S R
													2015	15.5		S					2011	15.5		S
													2016	18.5		S					2012	18.5		S
70	2061	8.0		S																				
	2062	11.2		S																				
	2063	14.0		S																				
	2064	17.0		S																				
	2065	20.0		S R																				
	2066	20.9		Uns																				

○ Some or all phase angles out of tolerance. ◊ Pressure varies 40-49 psig. △ Maximum speed due to orbit size.
◊ Pressure varies 35-39 psig. △ Pressure varies 50-59 psig.

TABLE XXI (Continued)

Misaligned 400 Sec.
Lubricant Pressure 35 psig, Lube Temperature 120°F

81

Unbalance, gr.-in. →	0				+1				±1				+2				-2				±2			
Sideload, lbs/brg.	Point No.	Speed, rpmx10⁻³	Notes	Stable and Repeat	Point No.	Speed, rpmx10⁻³	Notes	Stable and Repeat	Point No.	Speed, rpmx10⁻³	Notes	Stable and Repeat	Point No.	Speed, rpmx10⁻³	Notes	Stable and Repeat	Point No.	Speed, rpmx10⁻³	Notes	Stable and Repeat	Point No.	Speed, rpmx10⁻³	Notes	Stable and Repeat
0	2279	8.1	O	S	2243	8.1		S	2237	8.1		S	2207	8.0		S	2201	8.0		S				
	2280	11.0	O	S R	2244	11.0		S	2238	11.0		S	2208	11.0		S	2202	11.0		S				
	2281	14.0	O	S	2245	14.0		S R	2239	14.0		S	2209	14.0		S	2203	14.0		S				
	2282	17.0	O	S	2246	17.0		S	2240	17.0		S R	2210	17.0		S R	2204	17.0		S R				
	2283	19.9		Uns	2247	19.5	O	Uns	2241	19.7	O	Uns	2211	18.5		Uns	2205	19.2	O	Uns				
					2248	19.3		S	2242	19.4		S					2206	18.0		S				
25	2273	8.0	O	S	2249	8.0		S	2255	8.0		S R												
	2274	11.0	O	S	2250	11.0		S R	2256	11.0		S												
	2275	14.0	O	S R	2251	14.0		S	2257	14.0		S												
	2276	17.0	O	S	2252	17.0		S	2258	17.0		S R												
	2277	19.6	O	Uns	2253	19.7	O	Uns	2259	20.0	O	Uns												
					2296	9.5		S	2292	9.5		S												
					2297	12.5		S	2293	12.5		S												
					2298	15.5		S	2294	15.5		S												
					2299	18.5		S	2295	18.5		S												
50	2267	8.0	O	S									2225	8.0		S R					2231	8.0		S
	2268	11.0	O	S									2226	11.0		S					2232	11.0	O	S
	2269	14.0	O	S									2227	14.0		S					2233	14.0		S R
	2270	17.0		S R									2228	17.0		S					2234	17.0		S
	2271	19.9	O	Uns									2229	19.5	O	Uns								
													2288	9.6		S					2287	9.5		S
													2289	12.5		S					2286	12.5		S
													2290	15.5		S					2285	15.5		S
													2291	18.5		S								
70	2261	8.0	O	S																				
	2262	11.0	O	S																				
	2263	14.0		S																				
	2264	17.0	®	S R																				
	2265	19.8	O	Uns																				

TABLE XXI (Continued)

Aligned
Lubricant Pressure 45 psig, Lube Temperature 120°F

Unbalance[1] gr.-in. Sideload, lbs/brg.	0				+1				±1				+2				−2				±2			
	Point No.	Speed, rpmx10^{-3}	Notes	Stable and Repeat	Point No.	Speed, rpmx10^{-3}	Notes	Stable and Repeat	Point No.	Speed, rpmx10^{-3}	Notes	Stable and Repeat	Point No.	Speed, rpmx10^{-3}	Notes	Stable and Repeat	Point No.	Speed, rpmx10^{-3}	Notes	Stable and Repeat	Point No.	Speed, rpmx10^{-3}	Notes	Stable and Repeat
0	2085	8.1		S R	2043	8.0		S	2037	8.0		S												
	2086	11.0		S	2044	11.2		S	2038	11.0		S	2020	11.0	◇	S R								
	2087	14.0		Uns	2045	14.0		S R	2039	14.0		S	2021	14.0	◇	S	2009	14.0	◇	S				
	2088	17.0		S	2046	17.3		S	2040	17.0		S R					2010	17.0	◇	S				
	2089	20.2		S	2047	20.2		S	2041	20.0		S												
	2091	23.4		Uns	2048	23.0		Uns	2042	22.0		Uns												
25									2090	17.0		S												
50													2087	17.0		S					2085	17.1		S
70																								

TABLE XXI (Continued)

Aligned
Lubricant Pressure 55 psig, Lube Temperature 120°F

Unbalance, gr.-in.	0			+1			±1			+2			-2			±2		
Sideload, lbs/brg.	Point No.	Speed, rpmx10⁻³	Notes / Stable and Repeat	Point No.	Speed, rpmx10⁻³	Notes / Stable and Repeat	Point No.	Speed, rpmx10⁻³	Notes / Stable and Repeat	Point No.	Speed, rpmx10⁻³	Notes / Stable and Repeat	Point No.	Speed, rpmx10⁻³	Notes / Stable and Repeat	Point No.	Speed, rpmx10⁻³	Notes / Stable and Repeat
0	2092	14.2	S	2044	11.0	S	2038	11.0	S									
	2093	16.8	S	2045	14.0	S R	2039	14.0	S									
	2094	20.0	S	2046	17.0	S	2040	17.0	S R	2022	17.0	△ S	2010	17.1	△ S			
	2090	24.7	△ Uns	2047	20.0	S	2041	20.1	S	2023	20.0	△ S	2011	19.7	△ S			
				2048	23.1	S	2042	23.4	S				2088	21.4	S			
							2085	24.0	Uns				2089	23.3	△ S			
25				2089	14.0	S	2091	17.0	S				2092	19.0	△ S			
50																2086	17.1	S
70																		

TABLE XXI (Continued)

Misaligned 4 mils, 400 sec.
Lubricant Pressure, 35 psig, Lube Temperature 120°F

Unbalance, gr.-in. → values across groups: 0, +1, ±1, +2, -2, ±2

Sideload 0 lbs/brg.

Unbalance	0				+1				±1				+2				-2			
	Point No.	Speed rpmx10^-3	Notes	Stable and Repeat	Point No.	Speed rpmx10^-3	Notes	Stable and Repeat	Point No.	Speed rpmx10^-3	Notes	Stable and Repeat	Point No.	Speed rpmx10^-3	Notes	Stable and Repeat	Point No.	Speed rpmx10^-3	Notes	Stable and Repeat
	2179	8.0	O	S	2143	8.0		S	2137	8.0		S	2107	8.0		S	2101	8.0		S
	2180	11.0	O	S R	2144	11.0		S	2138	11.0		S	2108	11.0		S	2102	11.0		S
	2181	14.0	O	S	2145	14.0		S R	2139	14.0		S	2109	14.0		S	2103	14.0		S R
	2182	17.0	O	S	2146	17.0		S	2140	17.1	O	S R	2110	17.0		S R	2104	17.0		S
	2183	19.9	O	Uns	2147	19.7	O	Uns	2141	19.4		Uns	2111	20.8		Uns	2105	17.2		Uns
													2198	22.3	△	S	2106	19.7		Uns

Sideload 25 lbs/brg.

Unbalance	0				+1				±1				+2
	Point No.	Speed rpmx10^-3	Notes	Stable and Repeat	Point No.	Speed rpmx10^-3	Notes	Stable and Repeat	Point No.	Speed rpmx10^-3	Notes	Stable and Repeat	
	2173	8.0	O	S	2149	8.0		S	2155	8.0		S R	
	2174	11.0	O	S	2150	11.1		S R	2156	11.0		S	
	2175	14.0	O	S R	2151	14.0		S R	2157	14.0		S R	
	2176	17.0	O	S	2152	17.0		S	2158	17.0		S R	
	2177	20.0	O	Uns	2153	19.7	O	Uns	2159	19.7	O	Uns	
					2185	9.5		S	2189	9.5		S	
					2186	12.5		S	2190	12.5		S	
					2187	15.5		S	2191	15.5		S	
					2188	18.5		S	2192	18.5		S	

Sideload 50 lbs/brg.

Unbalance	0				+2				±2			
	Point No.	Speed rpmx10^-3	Notes	Stable and Repeat	Point No.	Speed rpmx10^-3	Notes	Stable and Repeat	Point No.	Speed rpmx10^-3	Notes	Stable and Repeat
	2167	8.0	O	S	2125	8.0		S R	2131	8.0		S
	2168	11.0	O	S	2126	11.0		S	2132	11.0		S
	2169	14.0	O	S	2127	14.0		S	2133	14.0		S R
	2170	17.0	O	S R	2128	17.0		S	2134	17.0	△	S
	2171	19.9	O	Uns	2129	19.0	O	Uns				
					2194	9.5		S	2185	9.5		S
					2195	12.6		S	2186	12.5		S
					2196	15.5		S	2187	15.5		S
					2197	18.5		S				

Sideload 70 lbs/brg.

Unbalance	0			
	Point No.	Speed rpmx10^-3	Notes	Stable and Repeat
	2161	8.0	O	S
	2162	11.0	O	S
	2163	14.1	O	S
	2164	17.0	O	S R
	2165	19.8	O	Uns

TABLE XXI (Continued)

Misaligned 4 mils, 400 sec.
Lubricant Pressure, 45 psig, Lube Temperature 120°F

Unbalance,[1] gr.-in.		0				+1				±1				+2				−2				±2		
Sideload, lbs/brg.	Point No.	Speed, $rpm \times 10^{-3}$	Notes	Stable and Repeat	Point No.	Speed, $rpm \times 10^{-3}$	Notes	Stable and Repeat	Point No.	Speed, $rpm \times 10^{-3}$	Notes	Stable and Repeat	Point No.	Speed, $rpm \times 10^{-3}$	Notes	Stable and Repeat	Point No.	Speed, $rpm \times 10^{-3}$	Notes	Stable and Repeat	Point No.	Speed, $rpm \times 10^{-3}$	Notes	Stable and Repeat
0	2180	11.0	◯	S	2144	11.0		S	2138	11.0		S												
	2181	14.0	◯	S	2145	14.0		S	2139	14.0		S												
	2182	17.0	◯	S	2146	17.0		S	2140	17.0		S												
	2183	20.0	◯	S	2147	20.0		S	2141	20.0		S												
	2184	22.7	◯	S	2148	22.2	◯	Uns	2142	22.6	◯	Uns												
25					2151	14.0		S	2157	14.0		S												
					2152	17.0		S	2158	17.0		S												
50																								
70																								

TABLE XXI (Continued)

Misaligned 4 mils, 400 sec.
Lubricant Pressure, 55 psig, Lube Temperature 120°F

Unbalance,[1] gr.-in.	0				+1				±1				+2				-2				±2			
Sideload, lbs/brg.	Point No.	Speed, rpmx10^{-3}	Notes	Stable and Repeat	Point No.	Speed, rpmx10^{-3}	Notes	Stable and Repeat	Point No.	Speed, rpmx10^{-3}	Notes	Stable and Repeat	Point No.	Speed, rpmx10^{-3}	Notes	Stable and Repeat	Point No.	Speed, rpmx10^{-3}	Notes	Stable and Repeat	Point No.	Speed, rpmx10^{-3}	Notes	Stable and Repeat
0	2181	14.0		S	2144	11.0		S	2139	14.0		S												
	2182	17.0	○	S	2145	14.0		S	2140	17.1		S												
	2183	20.0	○	S	2146	17.0		S	2141	20.0		S												
	2184	23.0	○	S	2147	20.0		S	2142	23.0		S												
	2199	24.8	○	Uns	2148	23.0		S	2193	24.7	○	Uns												
					2149	24.3	○	Uns																
25					2152	17.1		S	2157	14.0		S												
									2158	17.0		S												
50																								
70																								

96

Figure 30. Variation of Reynolds Number with Rotative Speed for Pivoted-Pad and Three-Lobe Bearings

87

TABLE XXI-I

REYNOLDS NUMBER FOR INITIATION OF TURBULENCE*

	Pivoted-Pad Bearing		Three-Lobe Bearing	
Lubricant Temperature, °F	75	120	75	120
Viscosity, lb sec/in^2	1.335×10^{-7}	$.823 \times 10^{-7}$	1.335×10^{-7}	$.823 \times 10^{-7}$
Density, lb sec^2/in^4	9.323×10^{-5}	9.247×10^{-5}	9.323×10^{-5}	9.247×10^{-5}
Pad Reynolds Number	581		460	
Speed, rpm	4069	2520	2011	1250

* According to Taylor's criterion for 360-degree journal bearings
having the same clearance as the machined clearance of the pivoted-
pad and three-lobe bearings.

VI. DATA REDUCTION PROCEDURES

The reduction of speed, torque, pressure, flow, steady load, and temperature data was a straight-forward application of the pertinent instrument calibration data to the reading and the conversion of the result to engineering units. These methods, therefore, will not be covered. The methods for obtaining at the bearing central plane the shaft eccentricity ratios, the displacement and force amplitudes, and the phase angles from measurements inboard and outboard of the bearings are presented in the Appendix.

All displacement measurements were made at 45 degrees from the load line. Therefore, besides vectorially combining the measurements at each end of the bearing to determine the displacements at the bearing central plane, the measurements must be rotated 45 degrees. In finding the bearing central plane displacements the shaft was assumed to be straight between instrumentation planes for each bearing. Shown in Table XXIII are the calculated static displacements of the shaft loaded with 100 lbs./bearing.

A perusal of these data indicates that the bending occurs mainly in the central section of the shaft and not between the instrumentation planes of either bearing

The measured x and y displacement and force amplitudes are assumed to form an ellipse. At the bearing central plane the semi-major and semi-minor axes of these ellipses are found as well as the inclination of the ellipses to the x axis, taken as the steady load line.

TABLE XXIII

CALCULATED SHAFT STATIC BENDING DEFLECTIONS

Location	Distance, in.	Deflection, mils
Plane 1	- 1.83	0.9193
Lower bearing center	0.00	0.00
Plane 2	1.83	-0.8890
Lower loader bearing	3.96	-1.6819
Shaft center line	6.25	-1.9900
Upper loader bearing	8.54	-1.6819
Plane 3	10.67	-0.8890
Upper bearing center	12.50	0.00
Plane 4	14.33	0.9193

The following non-dimensional parameters are used in the presentation of the data (The symbols are defined at the end of the Appendix.):

Bearing eccentricity ratio

$$\epsilon_B = \frac{e}{C_B} \tag{4}$$

Sommerfeld number

$$S = \frac{\mu N L D_S}{60\ W} \left(\frac{R}{C_P}\right)^2 \tag{5}$$

Reciprocal Sommerfeld number or load capacity

$$\frac{1}{S} = \frac{60\ W}{\mu\ NLD} \left(\frac{C_P}{R}\right)^2 \tag{6}$$

Pad Reynolds number

$$Re_p = \frac{\rho\ U\ C_P}{\mu} \tag{7}$$

Attitude angle

$$\bar{\varphi} = \tan^{-1} \frac{\bar{y}_1 + \bar{y}_2}{\bar{x}_1 + \bar{x}_2} \tag{8}$$

Dimensionless torque parameter

$$\tau = \frac{T}{W\ C_P} \tag{9}$$

Load parameter

$$\bar{w} = \frac{\pi\ \rho}{2\ \mu^2} \left(\frac{D_S}{L}\right) \left(\frac{C_P}{R}\right)^3\ W \tag{10}$$

91

Ratio of displacement semi-major axis to displacement of the center of gravity

$$J = \frac{A \; W_S}{2u} \qquad (11)$$

Ratio of displacement semi-major axis to bearing clearance

$$J_C = \frac{A}{C_B} \qquad (12)$$

Ratio of force semi-major axis to unbalance force

$$K = \frac{g}{u}(\frac{60}{2 \; \pi \; N})^2 \; A_F \qquad (13)$$

Shaft moment coefficient

$$M_C = \frac{T}{\smile NLD_S C_p}(\frac{C_p}{R})^2 \qquad (14)$$

92

VII. MEASURED PERFORMANCF

For a given set of test conditions, consisting of steady load. unbalance, and lubricant temperature and pressure, data were to be recorded at six speeds. For the pivoted-pad bearing the speed was limited by excessive synchronous whirl orbits and for the three-lobe bearing the speed was limited by fractional-frequency whirl. Therefore, the steady state data which is the only data used for most of the plots may consist of five or six test points depending upon the speed at which the test had to be aborted. The highest speed reached for each set of test conditions was recorded so that the effect of test conditions upon this speed could be found.

As indicated previously, approximately twenty percent of the data points were taken a second time after an intervening test point as a check on the repeatability of the data. Shown in Table XXIV is the standard deviation of repeated, aligned data points for both bearing types. The standard deviation values for eccentricity of the pivoted-pad bearing compares favorably with the average deviations of the rotating center positions in Table X. However, the standard deviations of the repeated data for the three-lobe bearing in Table XXIV are higher but consistent with the displacement sensor equilibrium error analysis in Table XIII. The attitude angles showed some variation in Table XXIV. This is due to including data from zero steady load in the standard deviations. In these instances, due to the error in center positions the x- or y-displacements or both could be negative placing the attitude angles in second, third or fourth quandrants. The standard deviations of the displacement semi-major axis were some better for the

TABLE XXIV

STANDARD DEVIATION OF REPEATED ALIGNED DATA POINTS

Derived Quantity	Pivoted-Pad	Three-Lobe
Speed, rpm	70	91
Steady Load, lb	0.3	0.4
Eccentricity, micro inches	17	101
Attitude Angle, degrees	42.7	28
Displacement Semi-Major Axis, micro inches	12.8	9.5
Force Semi-Major Axis, lb	1.38	1.34

pivoted-pad bearing and considerably better for the three-lobe bearing than the eccentricities. Some improvement was to be expected from the comparison of the estimated error analyses for equilibrium and amplitude in Tables XIII and XIV. The level of force semi-major axis standard deviations is explained by the fact observed during testing, namely, that the forces were more erratic than the displacement amplitudes. At one point in the test the force amplitudes were put through at synchronous filter to remove unwanted higher frequency disturbances.

Almost all of the data to be presented has been non-dimensionalized. Before discussing this non-dimensionalized data, however, some data will be shown in both the dimensional and non-dimensional form.

A.   PIVOTED-PAD BEARING

The design type data can relate to equilibrium position or it can relate to dynamic motion. The relationship between equilibrium displacement data and dynamic response data is shown in the schematic diagram of Figure 31. The square represents the clearance locus for the 4-pad pivoted-pad bearing. During test this bearing was loaded between adjacent pivots, thus the load line is shown in a downward direction and forms the diagonal of the square. The assembled clearance or the bearing clearance is depicted in the sketch. Also shown is an elliptical orbit which was typical of those obtained with this pivoted-pad bearing. Shown is the eccentricity of the bearing measured from its center and also the semi-major axis of the orbital ellipse. The attitude angle, which is the angle between the equilibrium position of the
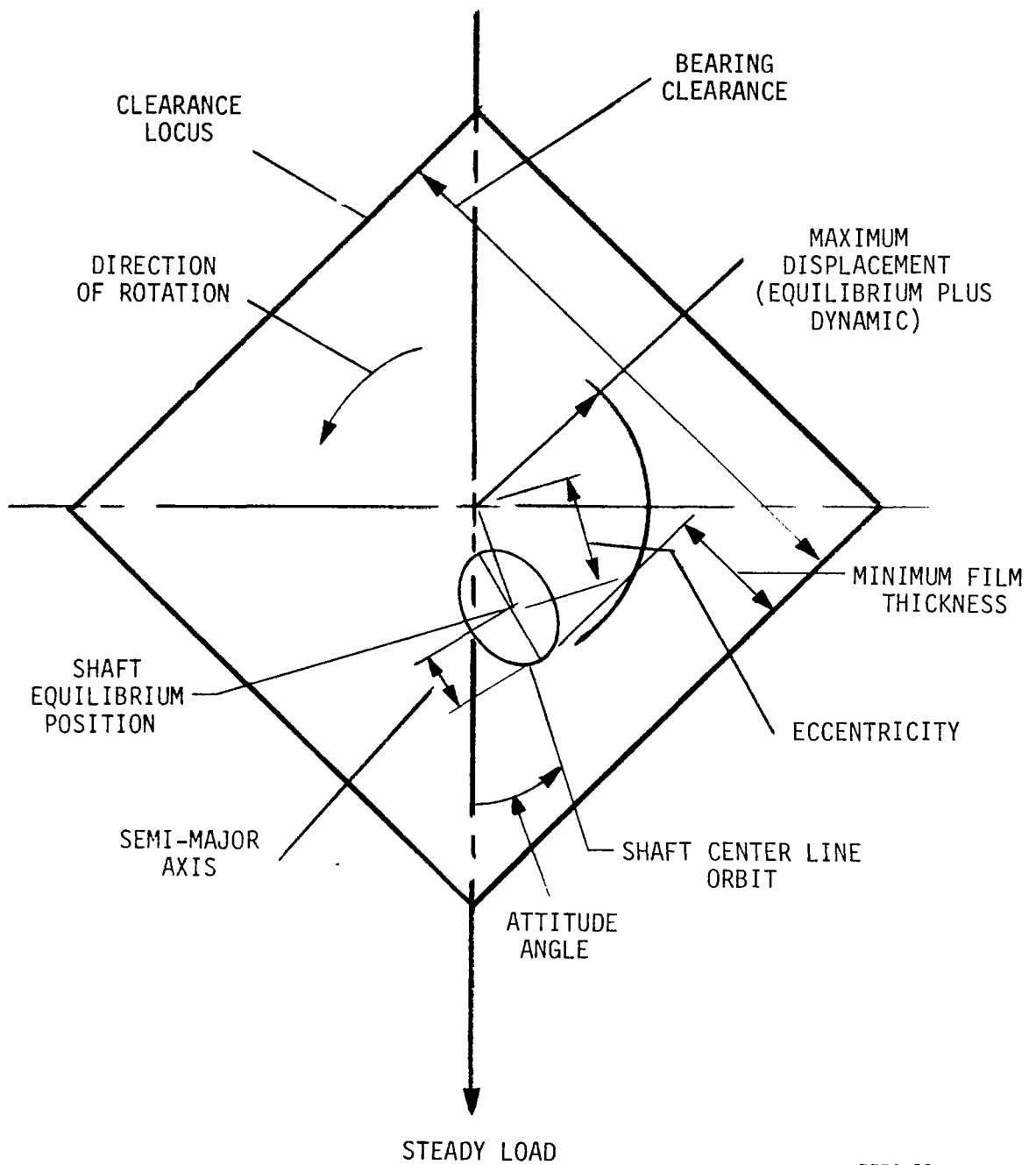
Figure 31.   Typical Shaft Orbit for a Loaded Pivoted-Pad Bearing.

shaft center and the steady load line, is also shown on the sketch. The maximum displacement attained by the bearing is the vectorial combination of the eccentricity and the semi-major axis of the orbital ellipse. Finally, the average minimum film thickness is the shortest distance between the shaft equilibrium position and the clearance locus. In order to relate the data obtained here for certain rotor unbalance levels to other rotor-bearing systems, the unbalance level is rendered dimensionless by dividing the value of unbalance by the shaft weight per bearing and the pad (machined) radial clearance. The following table gives the dimensionless unbalance for the specific values of unbalance used in testing:

Experimental Unbalance, gr.-in.	Dimensionless Unbalance
0.5	0.184
1.0	0.368
2.0	0.736

In order to compare unidirectional and dynamic loads the following table which applies per bearing can be used.

Speed, rpm Unbalance, gr.-in.	Centrifugal Force, lbs		
	10,000	20,000	30,000
0.5	3.2	12.5	28
1.0	6.3	25	56
2.0	12.6	50	112

1. Examples of Design-Type Data

Shown in Figures 32, 33, and 34 are typical displacement data, in this case for a steady load of 50 lbs/bearing and an unbalance of 0.5 gr.-in./bearing. In the upper half of Figure 32 the bearing eccentricity is plotted against the rotational speed. In the lower half of the figure the same data has been non-dimensionalized resulting in the bearing eccentricity ratio (Equation 4) plotted against the Sommerfeld number (Equation 5). The unbalance may be stated as the ratio of the displacement of the center of gravity from the center of geometry of the rotor to the bearing clearance. The steady load also can be non-dimensionalized by dividing the pad Reynolds number (Equation 7) by the Sommerfeld number. Shown in Figure 33 is the variation of the semi-major axis of the orbital ellipse with the rotative speed. In the lower half of the figure the semi-major axis is normalized by dividing by the bearing clearance. The Sommerfeld number if used as a non-dimensional speed. As would be expected the semi-major axis of the orbital ellipse increases in magnitude as the rotative speed is increased toward the first bending critical speed of the shaft which occurs around 28,000 or 29,000 rpm. Shown in Figure 34 is the combination of the previous two figures, both in dimensional and normalized form. The lower curve formed by the circles represents the equilibrium position of the center of the shaft and the triangles represents the total displacement of the shaft from the bearing center.

a. DIMENSIONAL PLOT

b. DIMENSIONLESS PLOT
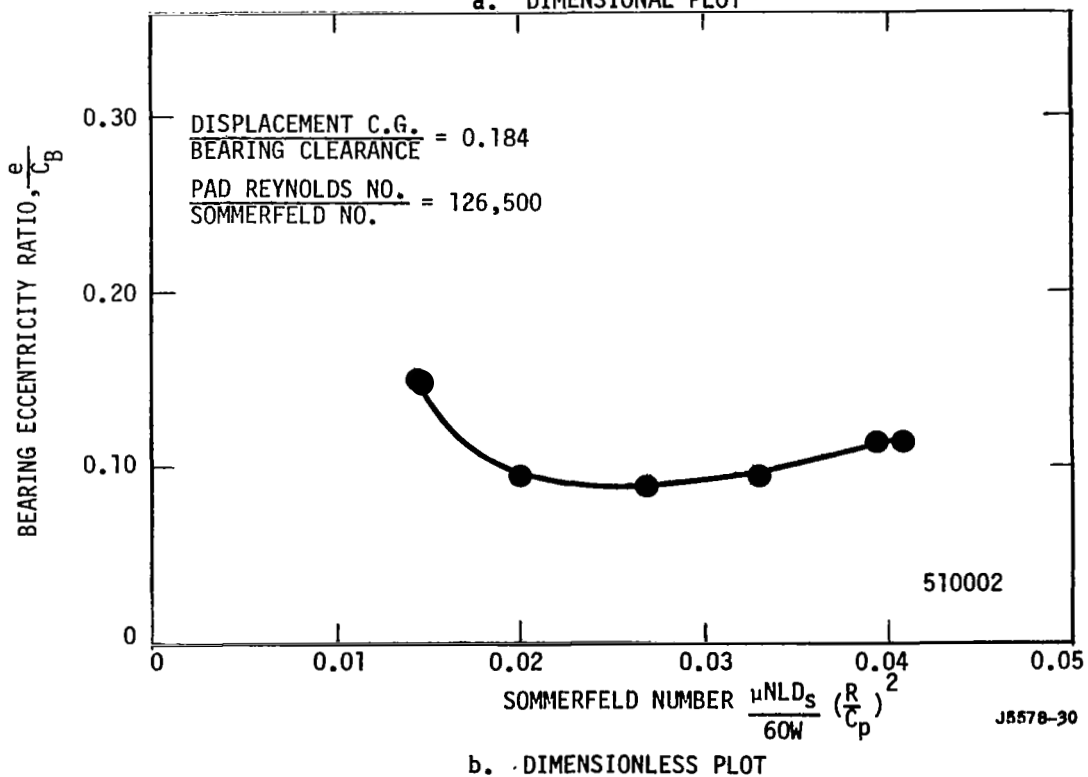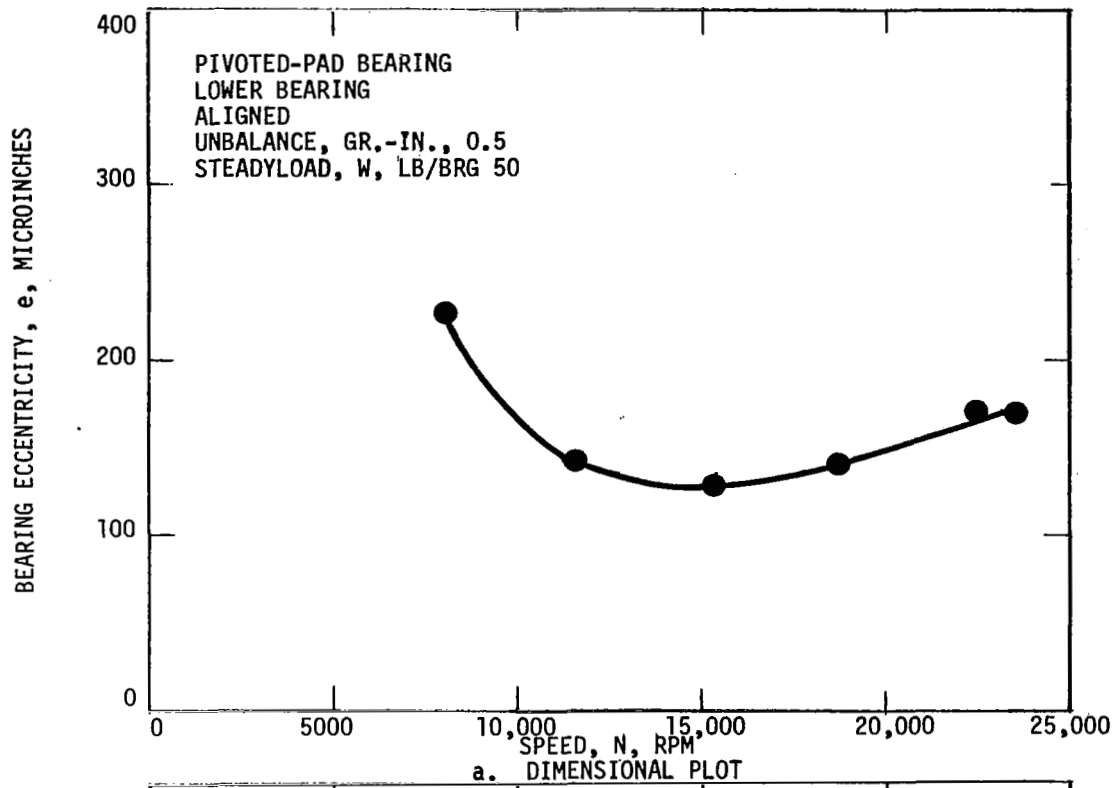
Figure 32. Variation of Eccentricity with Speed at Constant Steady Load.

a. DIMENSIONAL PLOT

DISPLACEMENT C.G. / BEARING CLEARANCE = 0.184

PAD REYNOLDS NO. / SOMMERFELD NO. = 126,500

510003

5578-31

b. DIMENSIONLESS PLOT
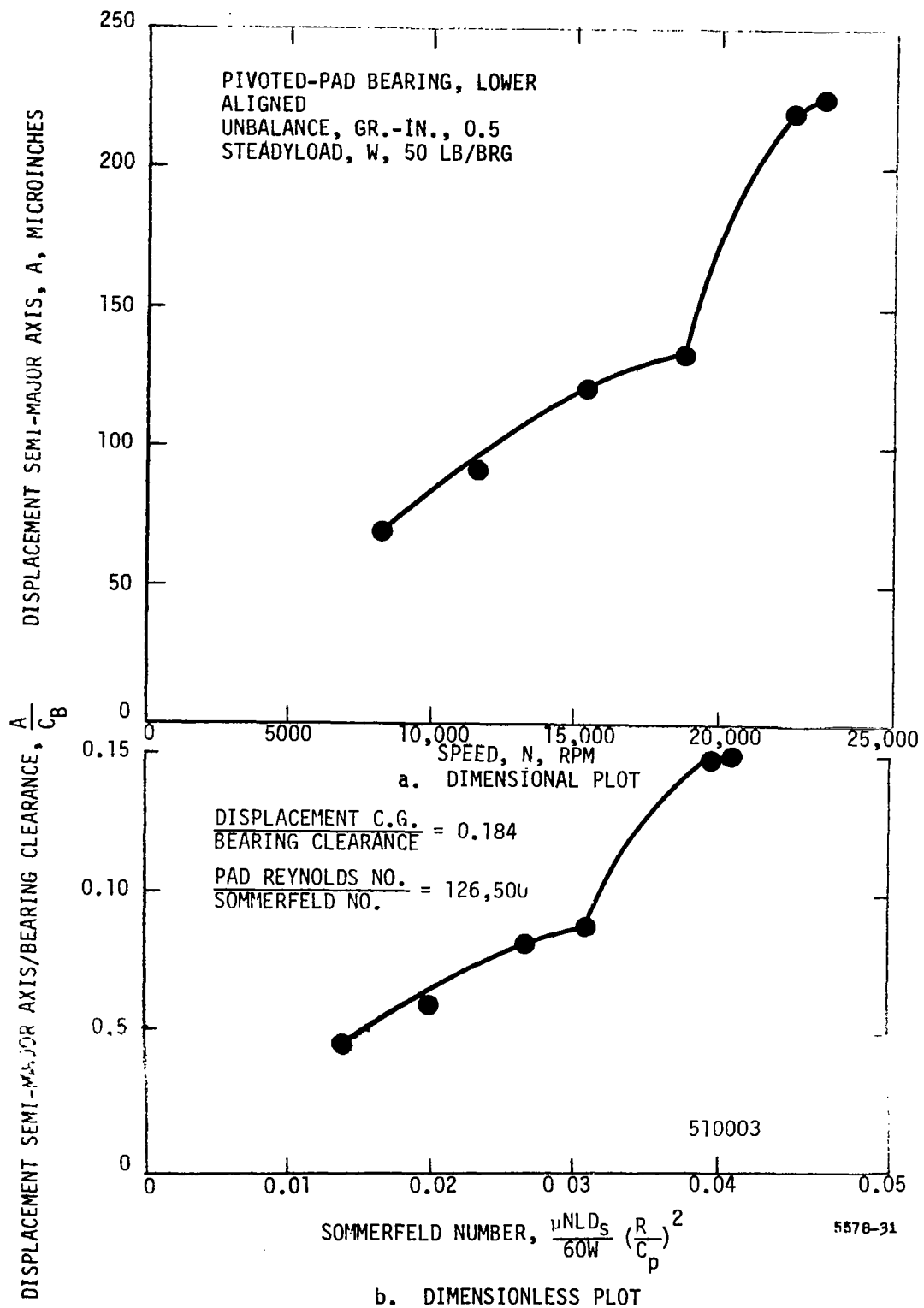
Figure 33. Variation of Displacement Semi-Major Axis with Speed at Constant Steady Load.

100

PIVOTED-PAD BEARING
LOWER BEARING
ALIGNED
UNBALANCE, GR.-IN., 0.5
STEADYLOAD, W, LB/BRG 50
▲ EQUILIBRIUM+DYNAMIC
● EQUILIBRIUM

a. DIMENSIONAL PLOT

$\dfrac{\text{DISPLACEMENT, C.G.}}{\text{BEARING CLEARANCE}} = 0.184$

$\dfrac{\text{PAD REYNOLDS NO.}}{\text{SOMMERFELD NO.}} = 126,500$

510008

SOMMERFELD NUMBER, $\dfrac{\mu NLD_S}{60W} \left(\dfrac{R}{C_p}\right)^2$

J5578-32

b. DIMENSIONLESS PLOT

Figure 34. Variation of Displacement with Speed at Constant Steady Load.

101

Shown in Figure 35 is the variation of torque with rotative speed for the same conditions as those shown on the previous three charts. In the lower half of the figure the torque has been normalized by dividing by the steady load and the machined clearance of the bearing. The speed has been normalized by using the Sommerfeld number.

Shown in Figures 36, 37 and 38 are the effects of steady load on bearing eccentricity, torque, and displacement semi-major axis. These plots are all made for an unbalance of 0.5 gr.-in./bearing and a rotative speed of 8,000 rpm, which corresponds to a Reynolds number of approximately 1822. The data in Figure 36 follows the expected trend that as the steady load is increased at constant speed, the bearing eccentricity increases. The small discrepancy of the point near the origin of these figures results from the small error in center position associated with the variation of the center position with rotative speed. Shown in Figure 37 is the variation of torque with steady load. Generally the trend is downward as the steady load increases, however, unexplained is the point at zero load which is lower than all the points on a plot. This type of curve has of course been checked by plotting the same information for several values of rotative speed and the trends including the point at zero load are similar. Shown in Figure 38 is the variation in the displacement semi-major axis as a function of steady load. The trend of decreasing displacement semi-major axis as the steady load increases can be attributed to the fact that the bearing stiffness increases as the eccentricity of the shaft increases. The load capacity used in the plots to represent steady load is simply the reciprocal of the Sommerfeld number.

PIVOTED-PAD BEARING
ALIGNED
UNBALANCE, GR.-IN., 0.5
STEADY LOAD, W, LB/BRG., 50

a. DIMENSIONAL PLOT

b. DIMENSIONLESS PLOT

510005

J5578-33

Figure 35. Variation of Torque with Speed at Constant Steady Load.

103

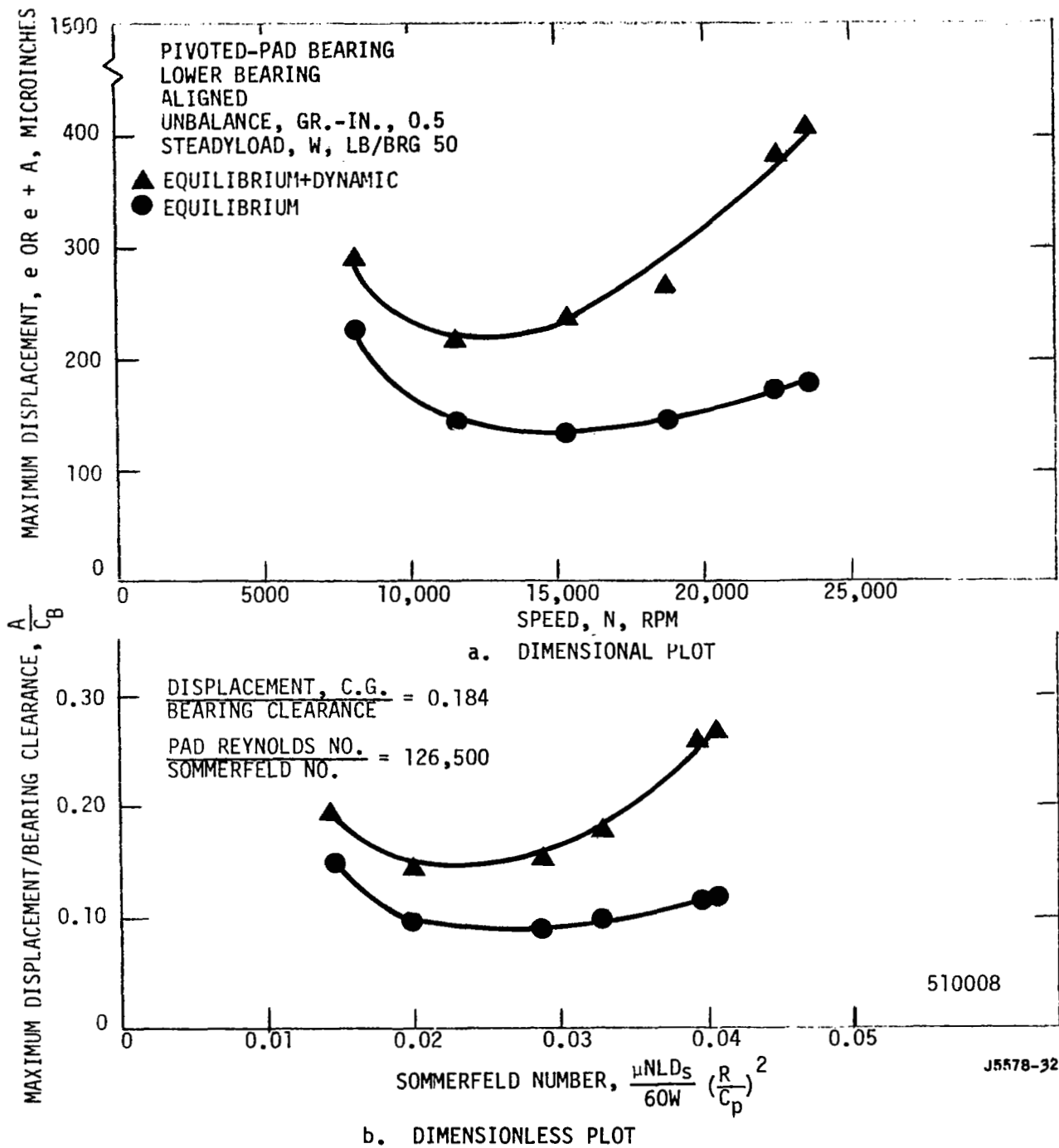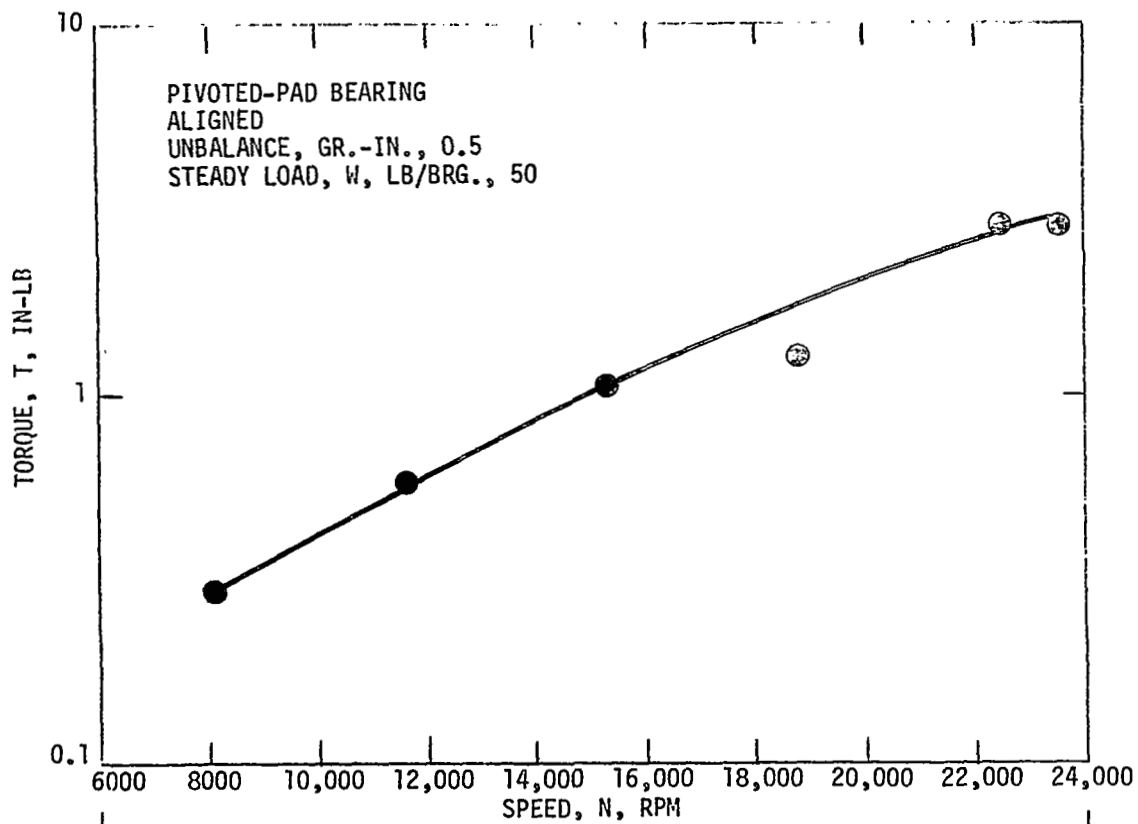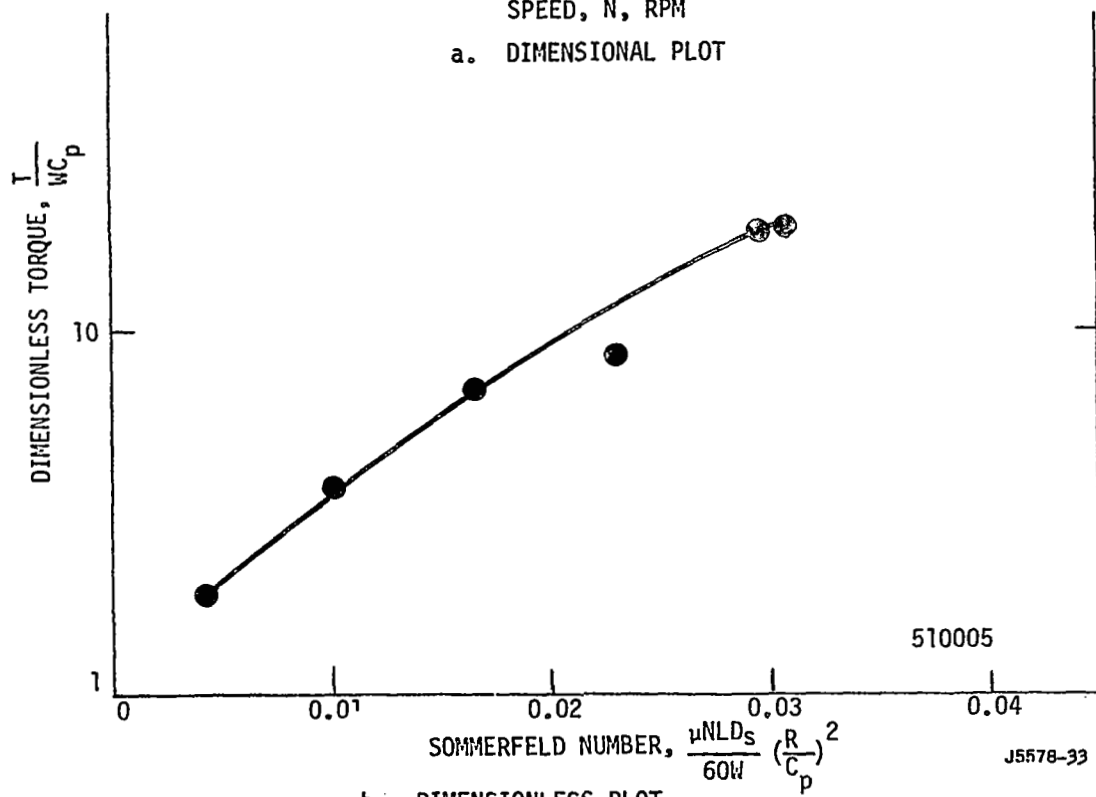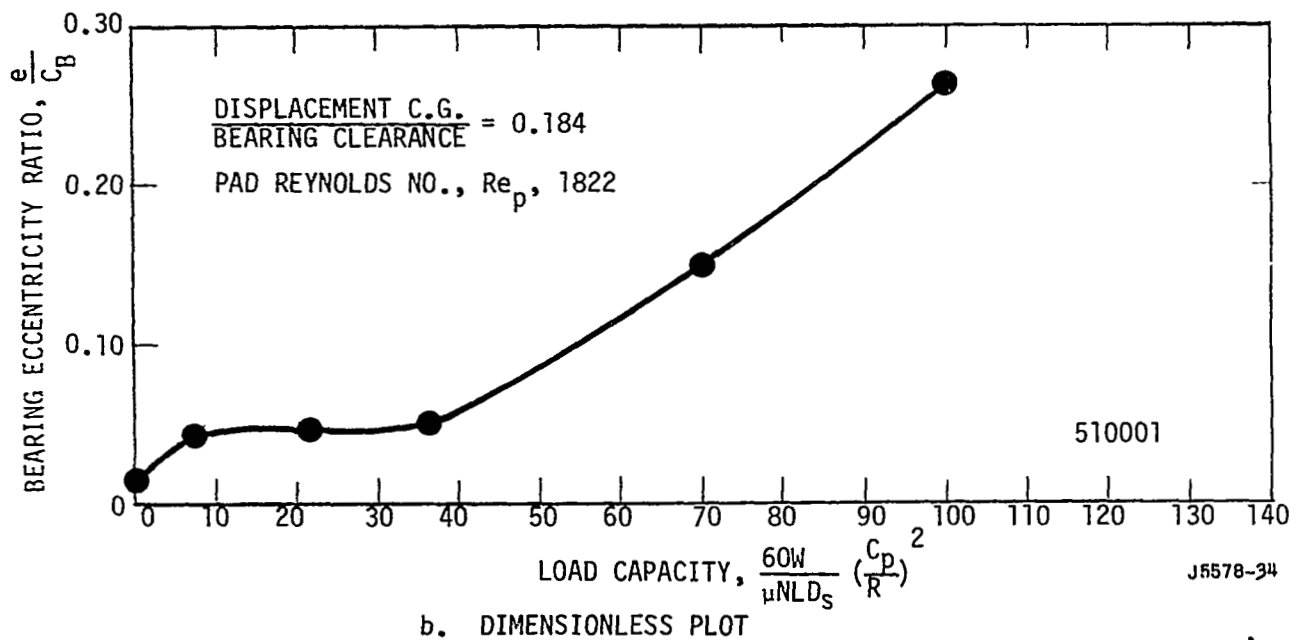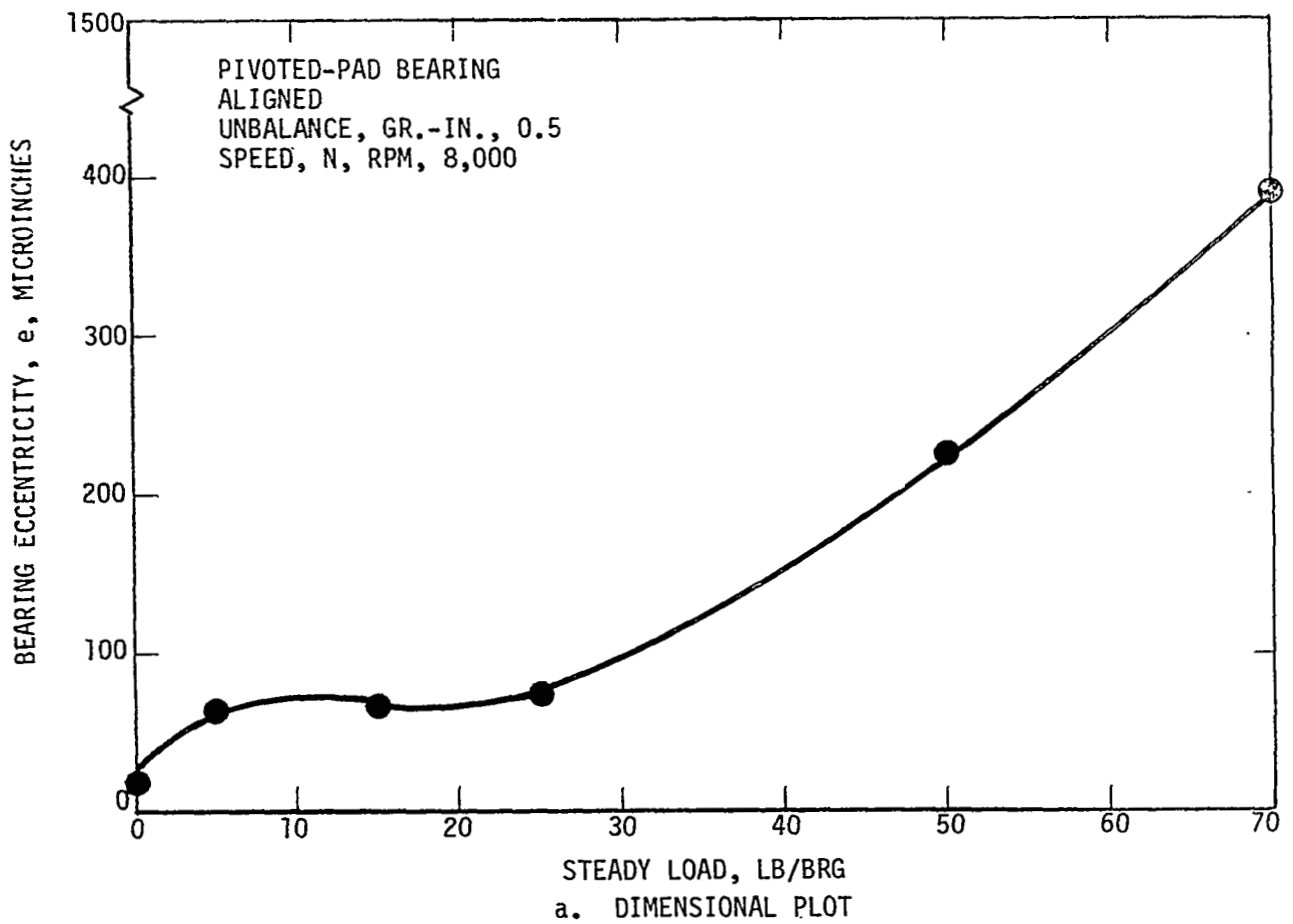Figure 36. Variation of Eccentricity with Steady Load at Constant Speed.

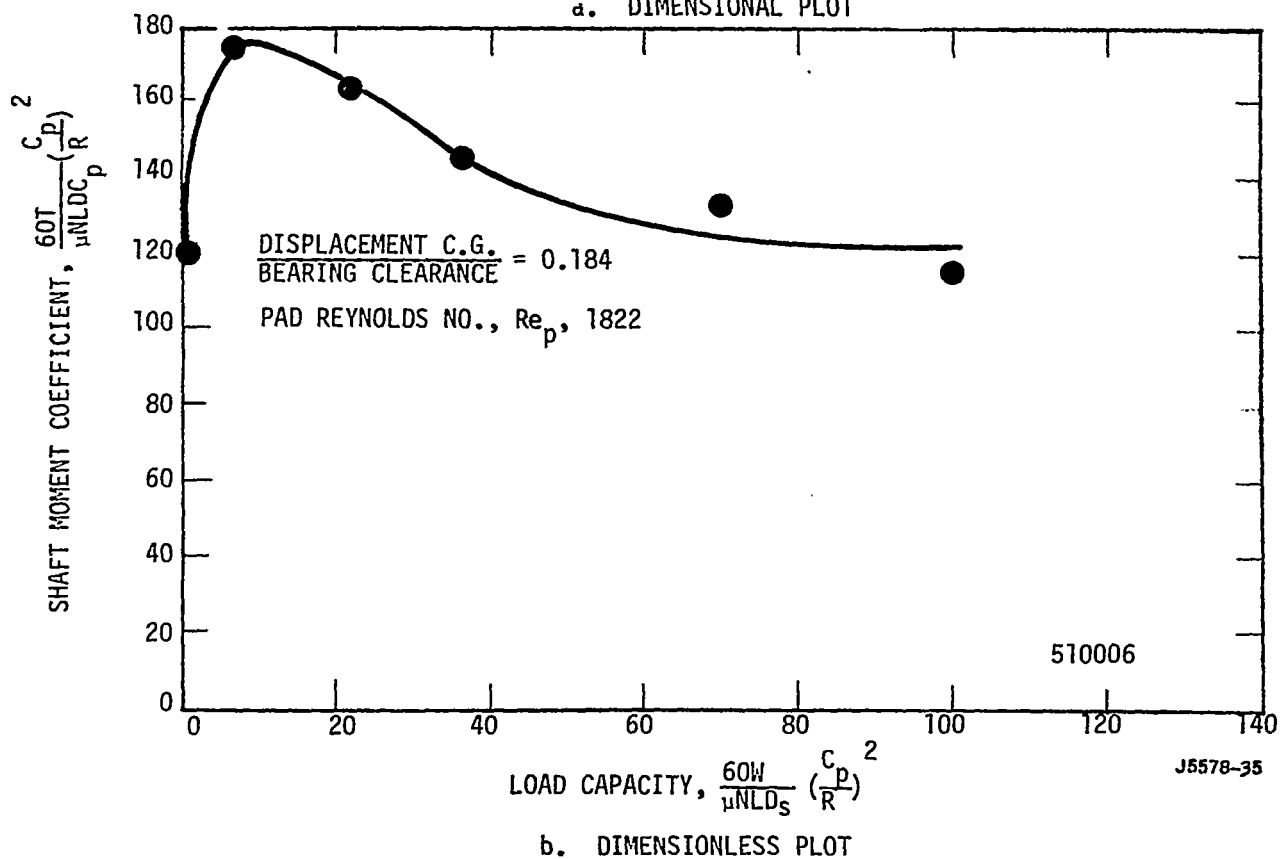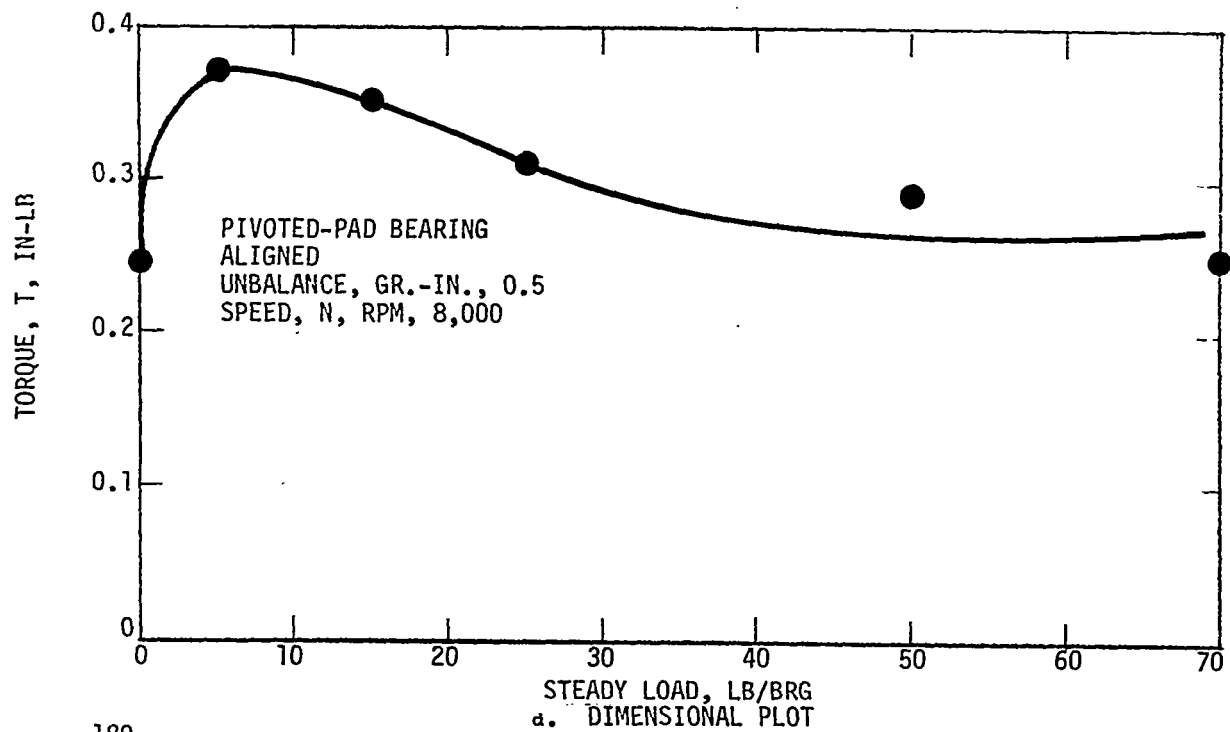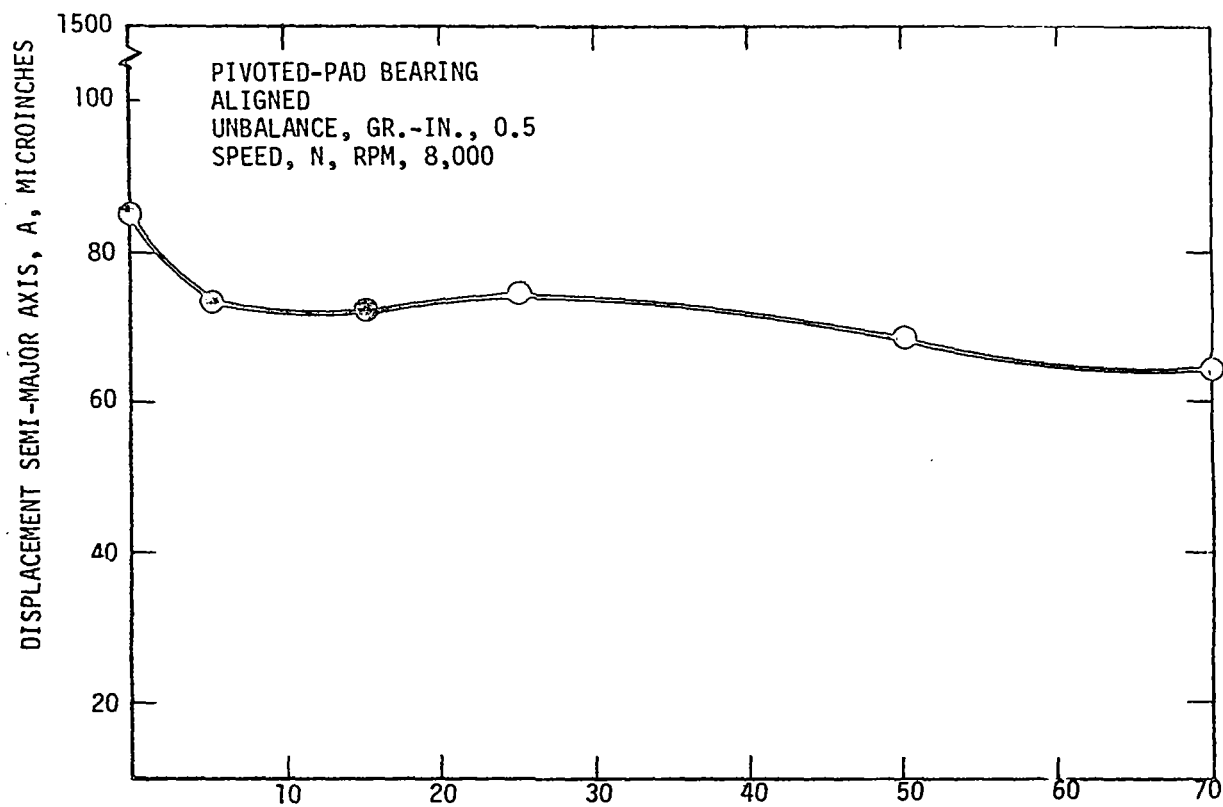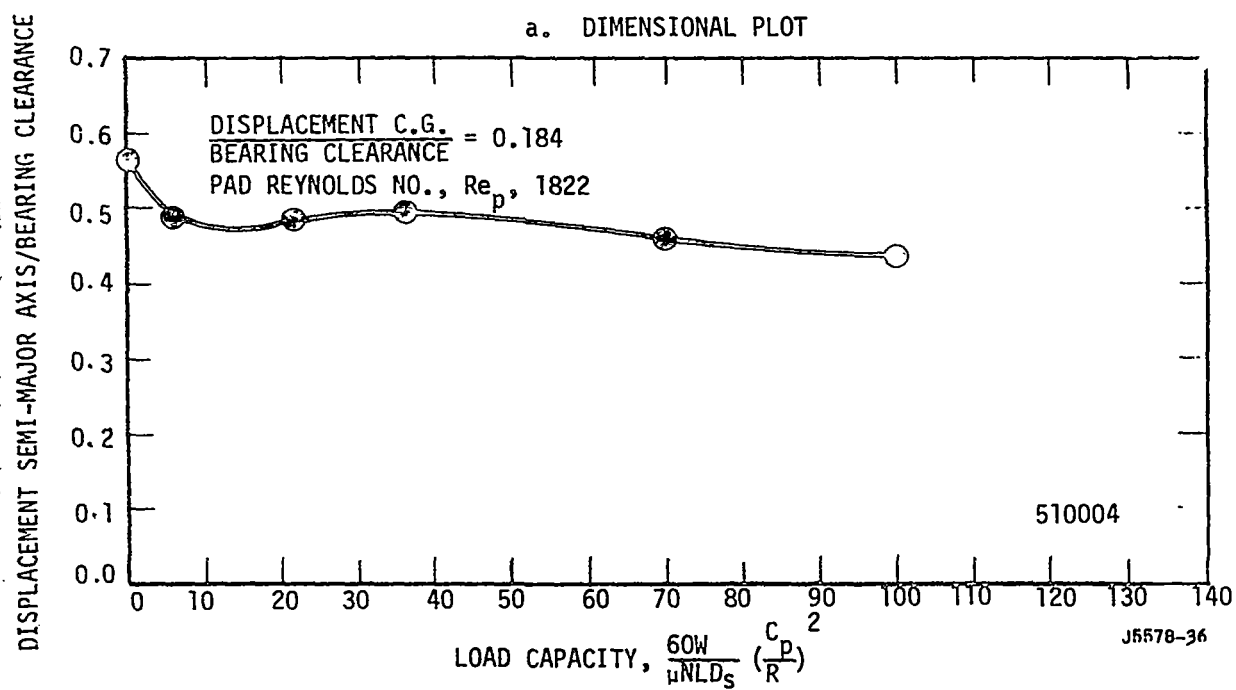Figure 37. Variation of Torque with Steady Load at Constant Speed.

Figure 38. Variation of Displacement Semi-Major Axis with Steady Load at Constant Speed.

106

2. Aligned Data

Shown in Figure 39 is the effect of steady load on the variation of bearing eccentricity ratio with Sommerfeld number. The unbalance is constant at $\pm$ 0.5 gram-inches per bearing (anti-symmetrical). It will be noted that with the heaviest load (70 lb/bearing) available for the test, an eccentricity ratio no higher than 0.22 was attained. This is consistent with the requirements of space power systems which would require lightly loaded journal bearings. The curve depicted by the diamonds which is for a steady load of 70 lbs/bearing will appear in several curve sheets to follow as the basis of comparison. Shown in Figure 40 is the effect of rotor unbalance on the variation of bearing eccentricity ratio with Sommerfeld number. The line for a load of 70 lbs/bearing from the previous figure is shown by the diamonds. It is seen that the anti-symmetric and the residual (0.0033 and 0.0054 gr-in. on the lower and upper ends of the shaft, respectively) unbalances have nearly the same load capacity as a function of bearing eccentricity ratio. A possible explanation for this is that with anti-symmetric unbalance the shaft is statically balanced. Although for a given Sommerfeld number the eccentricity ratios for the symmetric unbalance are somewhat larger than those for the other two unbalances, at a reasonable operating value of eccentricity ratio (above 0.22) the difference in load capacity is negligible. Shown in Figure 41 is the theoretical variation of the bearing eccentricity ratio with Sommerfeld number. The curve is for a pivoted-pad bearing having a preload of 0.5 and for Reynolds number of 1860. Shown also on the figure are the test data for a Reynolds number of 1860.
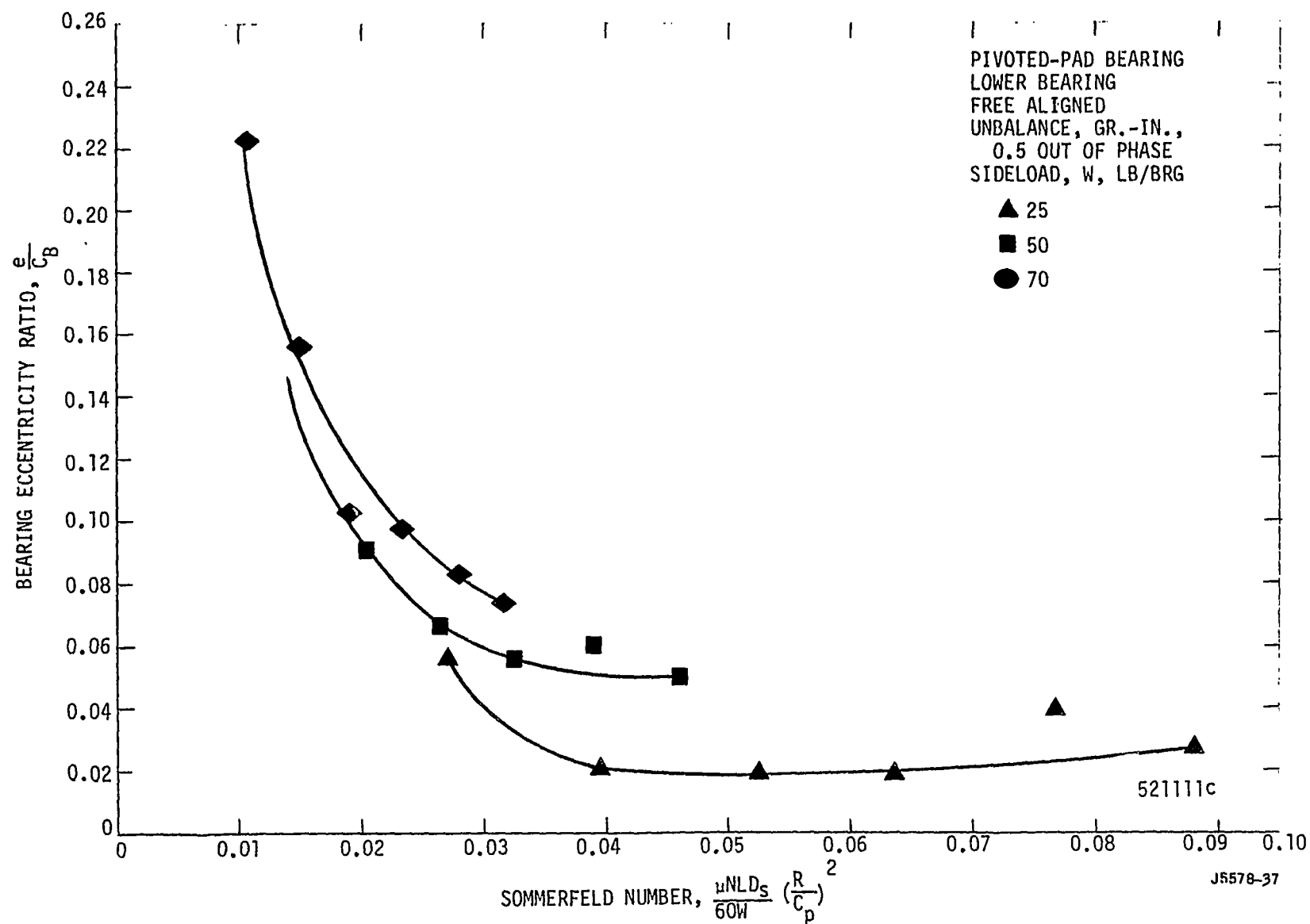
Figure 39. Variation of Eccentricity Ratio with Sommerfeld Number and Steady Load.
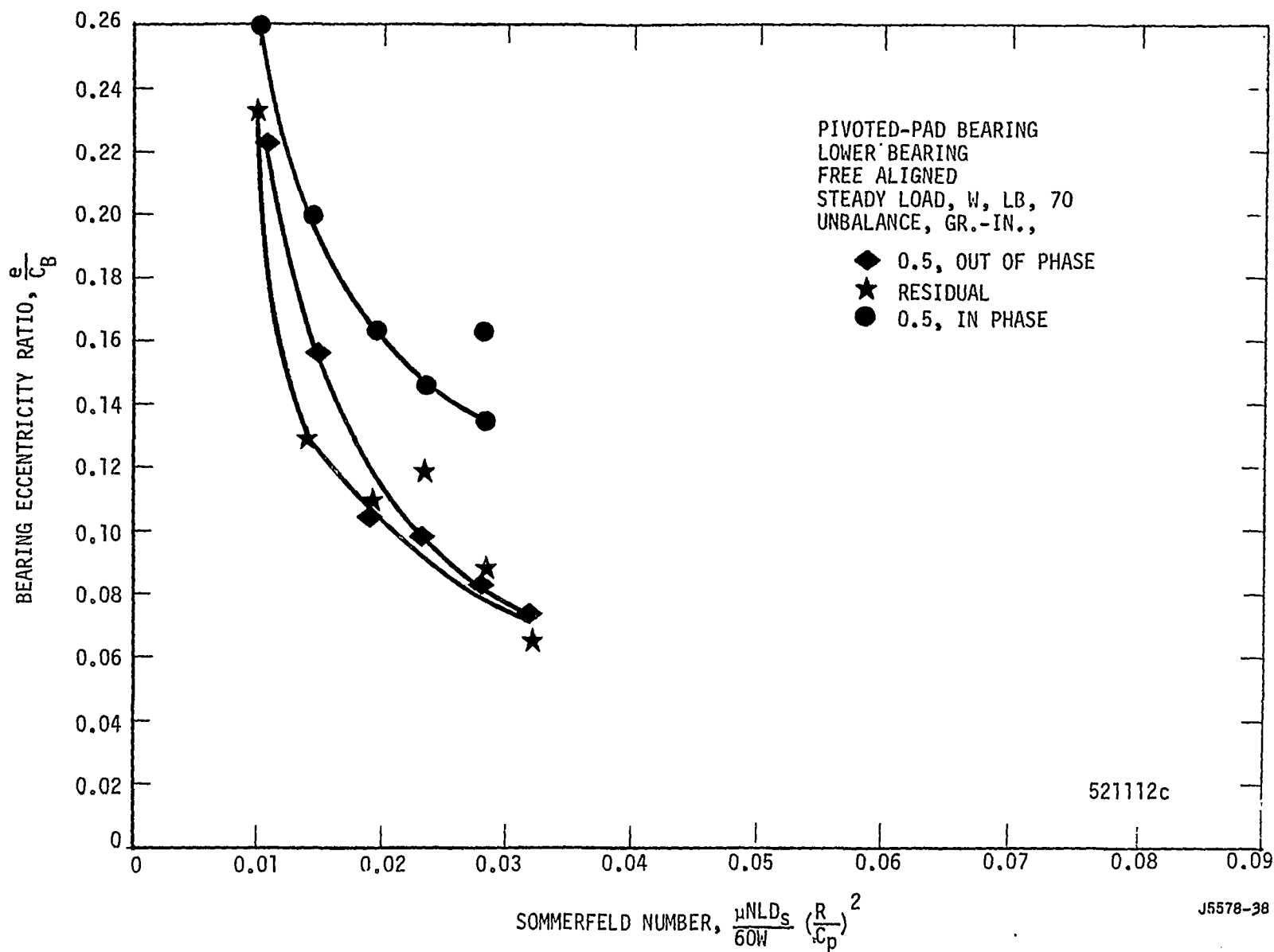
Figure 40. Variation of Eccentricity Ratio with Sommerfeld Number and Unbalance.

J5578-38
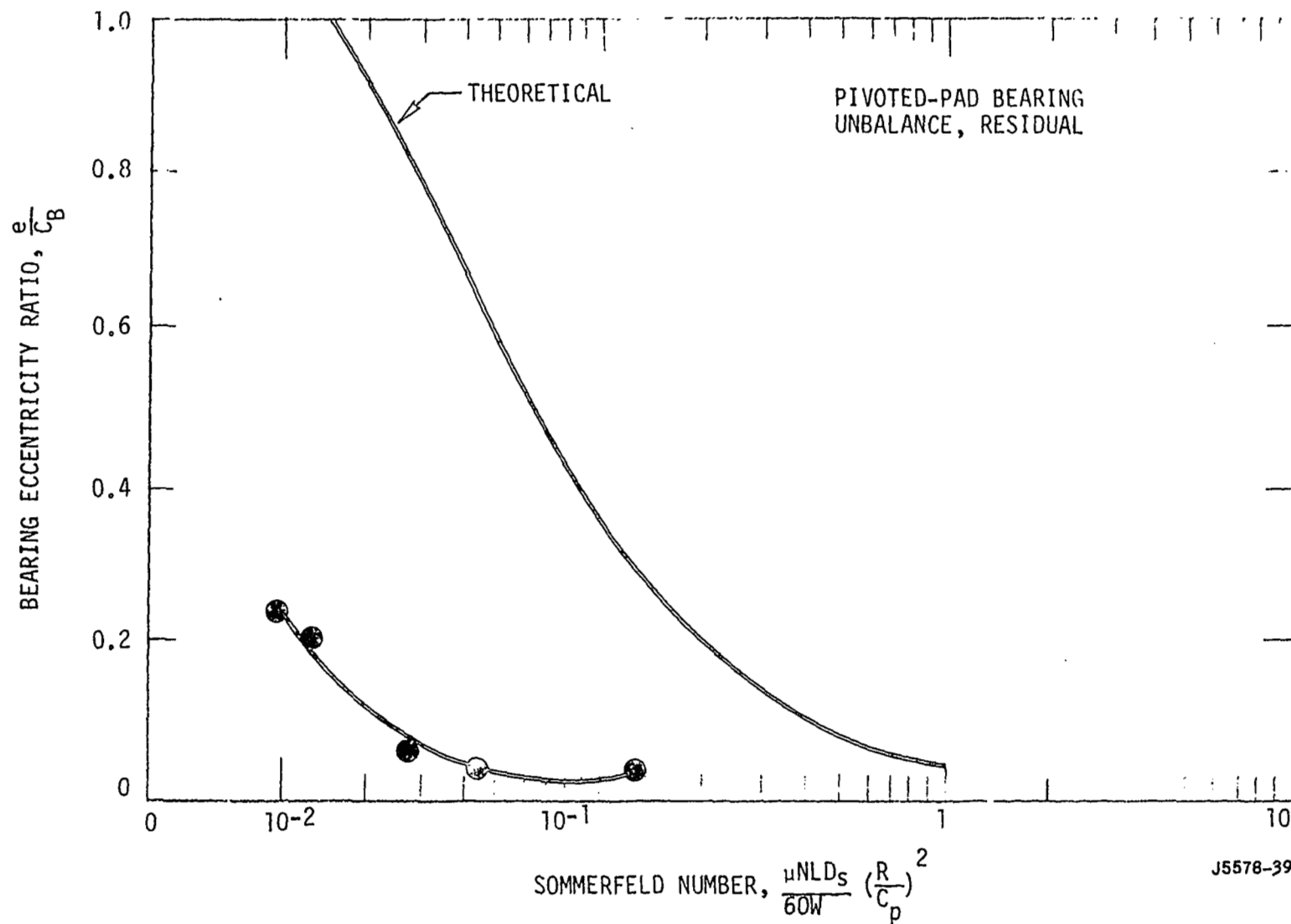
Figure 41. Comparison of Experimental and Theoretical Eccentricity Ratio – Sommerfeld Number Data. Reynolds Number, 1860; Preload Coefficient, 0.52.

110

The comparison indicates that a substantially larger load capacity was being obtained in the test than would be predicted from theoretical considerations. The theoretical data was obtained from Reference 7. Shown in Figure 42 is a plot similar to the previous one. This plot is for an antisymmetric unbalance of 0.5 gr-in/bearing. In this case, however, the steady load is constant at 70 lbs/bearing and the rotative speed is allowed to vary and is reflected by the Sommerfeld number. Both the theoretical curve and the experimental data are shown. Again the conclusion is that the measured load capacity was substantially higher than would be expected from theoretical considerations.

Shown in Figure 43 is the variation of attitude angle with bearing eccentricity ratio for three levels of steady load. Theoretically, the attitude angle for a four-pad pivoted-pad bearing loaded symmetrically between pivots should be zero for all operating conditions. However, in the test unit, which was used to obtain the data, partial-arc bearings were utilized to apply the steady load in the central portion of the shaft. Since these partial-arc bearings do not operate with zero attitude angles, they superimpose their motion upon the shaft in the region of pivoted-pad bearings, resulting in attitude angles greater than zero. The data in Figure 44 is similar to that in Figure 43 except in Figure 44 various levels of rotor unbalance are compared. Again substantial attitude angles are shown at eccentricity ratios approaching zero.

Shown in Figure 45 is the variation of non-dimensional torque with reciprocal Sommerfeld number. The data are shown for two rotative speeds which correspond
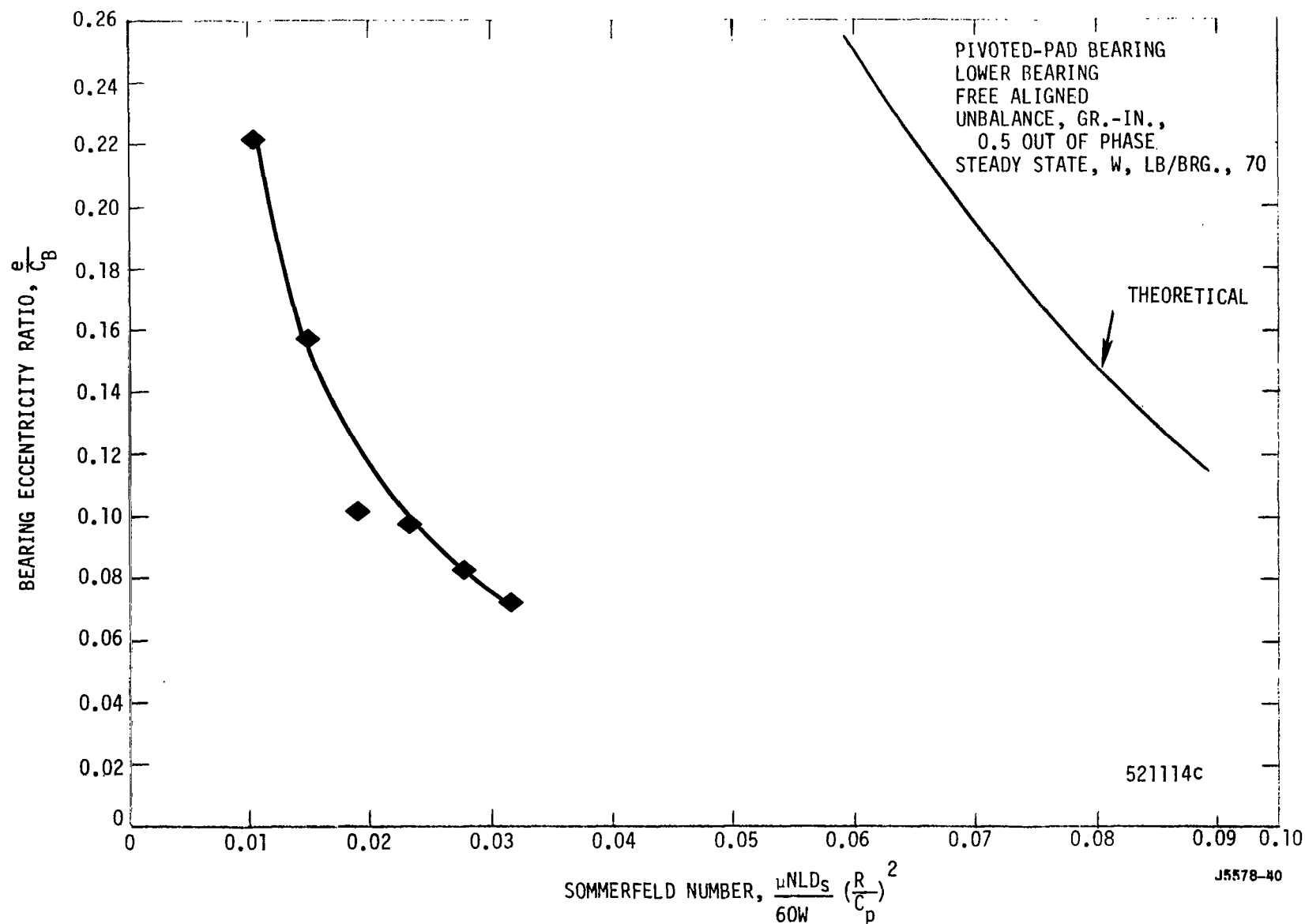
111

Figure 42. Comparison of Experimental and Theoretical Eccentricity Ratio –
Sommerfeld Number Data at Constant Steady Load.
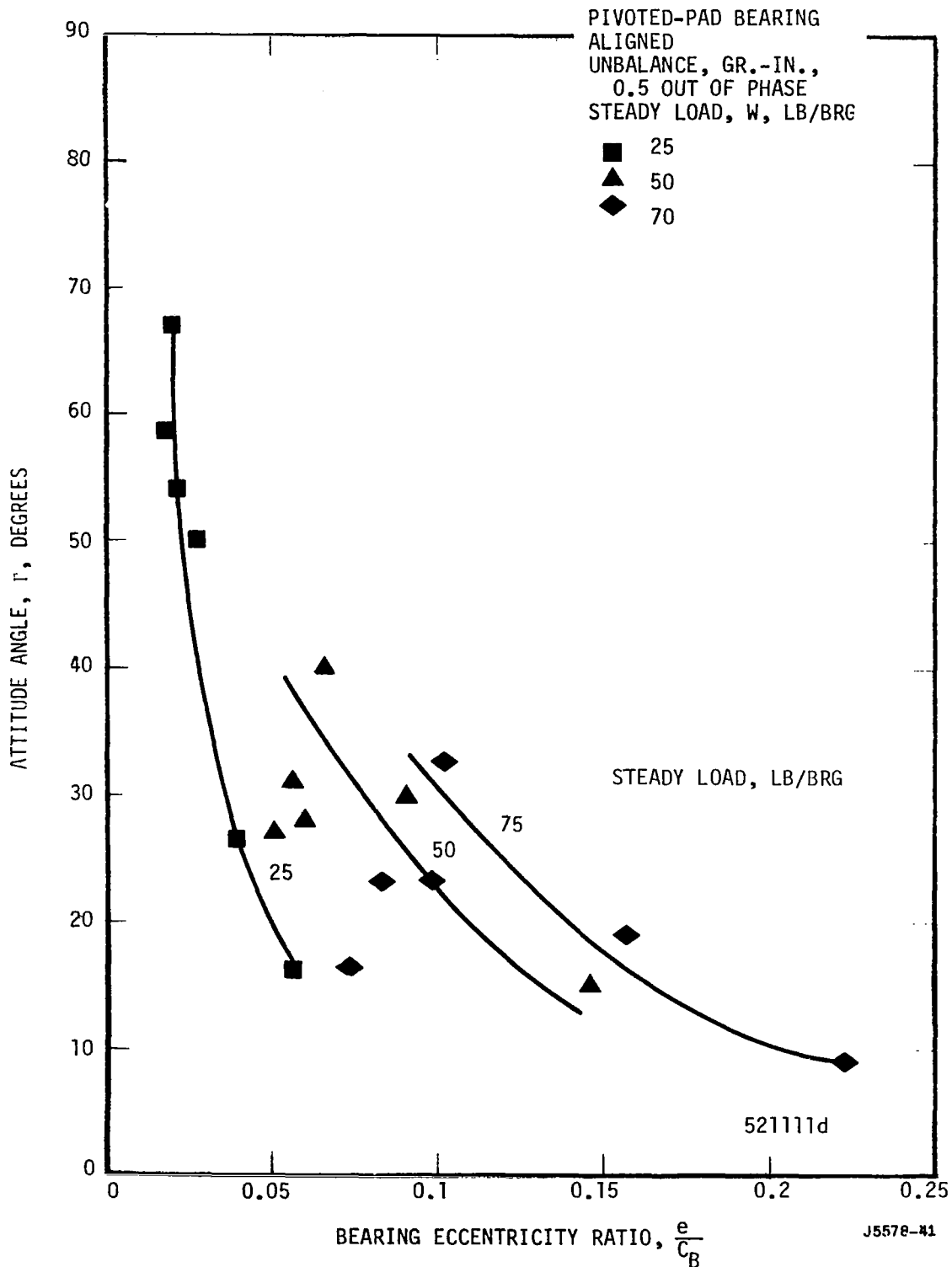
112

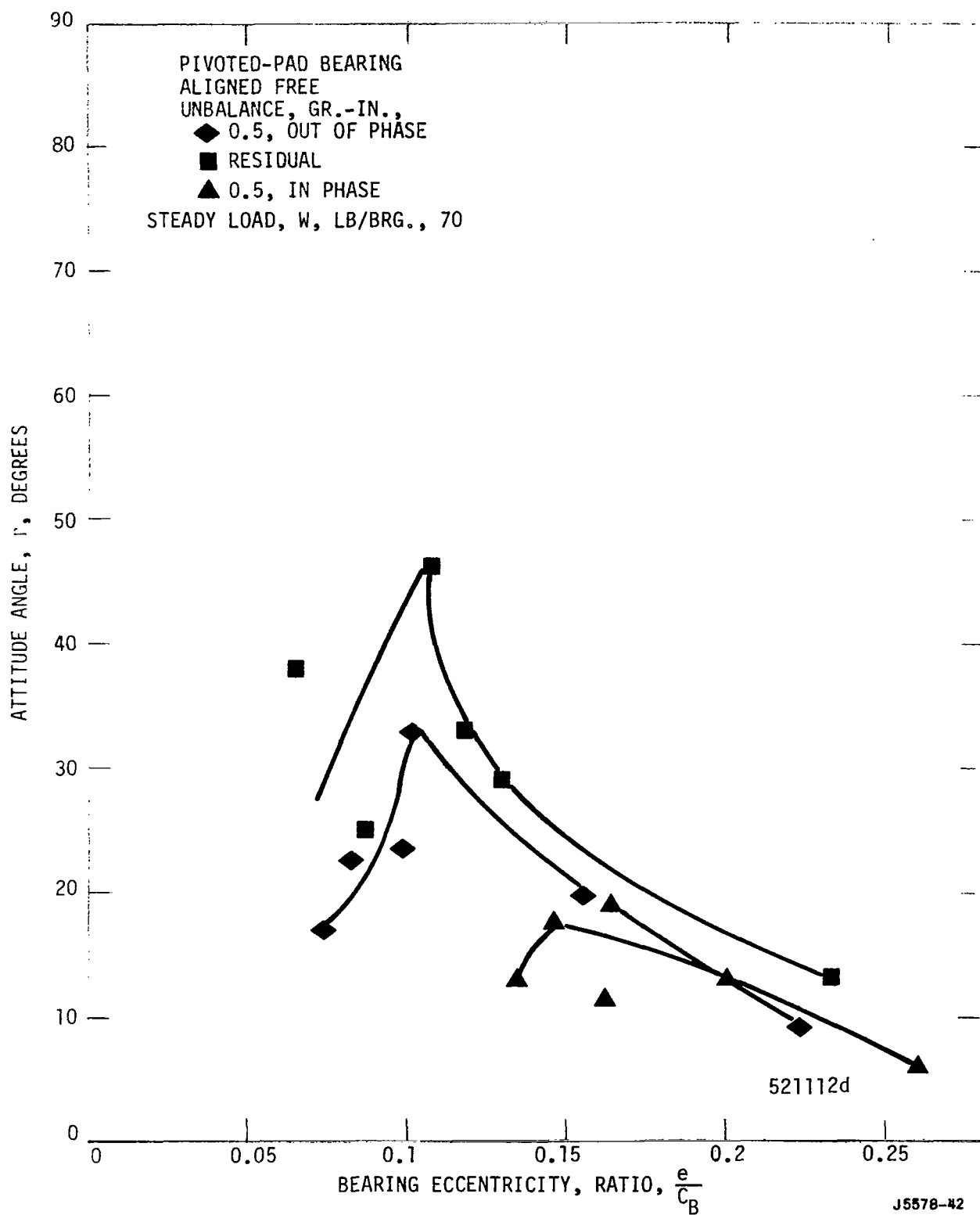Figure 43. Variation of Attitude Angle with Eccentricity Ratio and Steady Load.

113

Figure 44. Variation of Attitude Angle with Eccentricity Ratio and Unbalance.
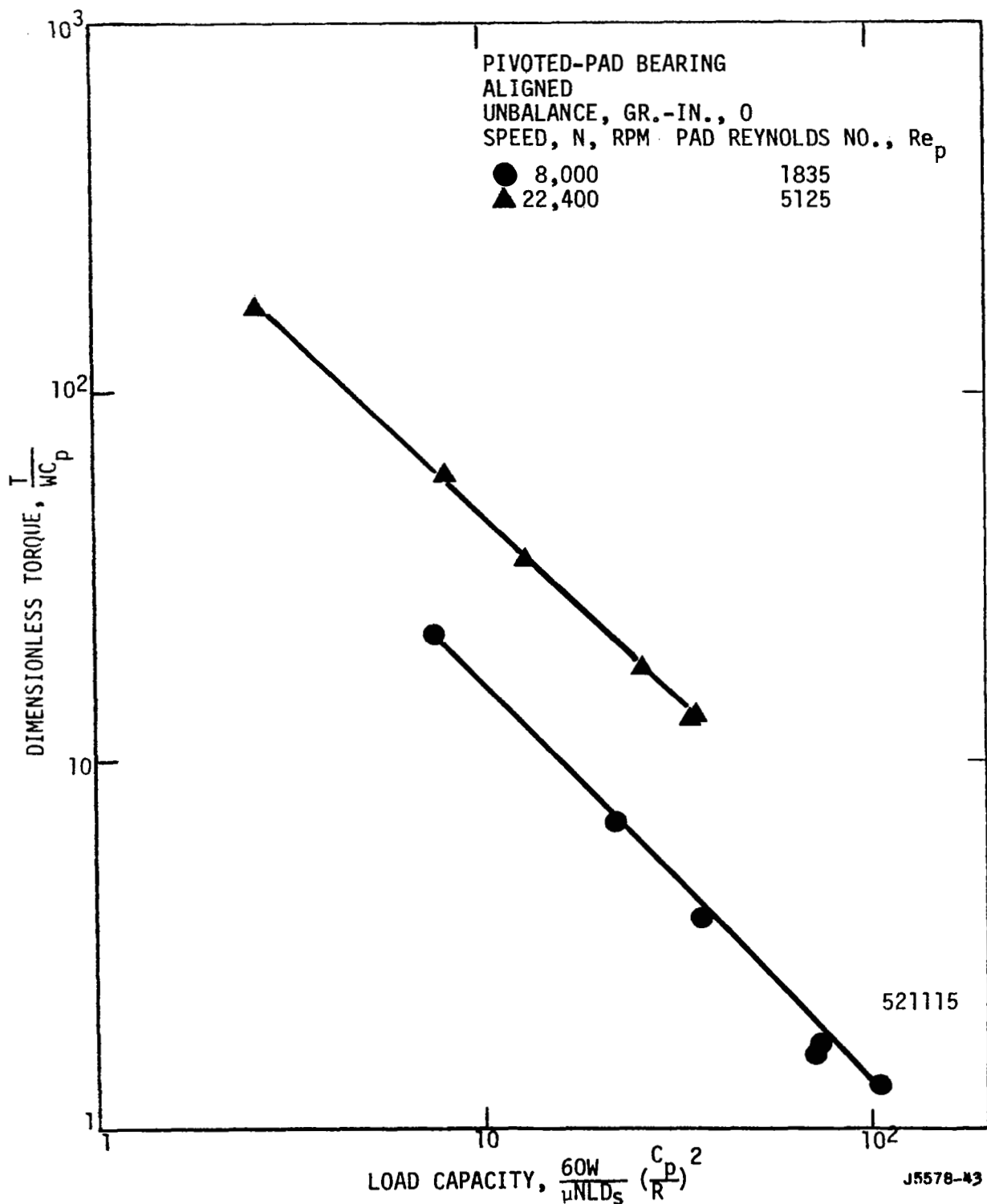
Figure 45. Variation of Dimensionless Torque with Load Capacity and Reynolds Number.

to Reynolds numbers of 1835 and 5125. The effect of Reynolds number on torque is clearly shown in this figure. A similar plot is shown in Figure 46 which is plotted for one rotative speed and two levels of unbalance. It is apparent that the level of unbalance has little or no effect on the torque. Shown in Figure 47 is the variation of the non-dimensional torque (Equation 9) with Sommerfeld number taken from Reference 7 for Reynolds numbers of 1860. Shown also on the figure are the experimental data for the same Reynolds number. The indications are that the measured torque is substantially higher than would be expected from theoretical considerations.

Shown in Figure 48 is the variation of the ratio of displace semi-major axis to the displacement of the center of gravity of the shaft with the pad Reynolds number. The curve is plotted for a steady load of 50 lbs/bearing and with no steady load. Through the lower and middle speed ranges of the plot the displacement semi-major axis caused the data for the two steady loads to fall on the same curve. However, in the region around 5000 pad Reynolds number, the data seems somewhat more erratic and this may be due to the fact that the shaft is approaching the critical speed. Shown in Figure 49 is a plot similar to the one shown on the previous figure, however, in this instance two levels of rotor unbalance are shown. It is seen that normalizing by the displacement of the center of gravity of the shaft causes the experimental data to fall on one curve. Shown in Figure 50 is the variation of the ratio of the displacement semi-major axis to the displacement of the center of gravity plotted against the pad Reynolds number for a steady load of zero and a rotor unbalance of 0.5 gr-in. Shown also is the rotor response calculation for the test conditions. The indications are that the theoretical predictions are approximately 25 percent conservative
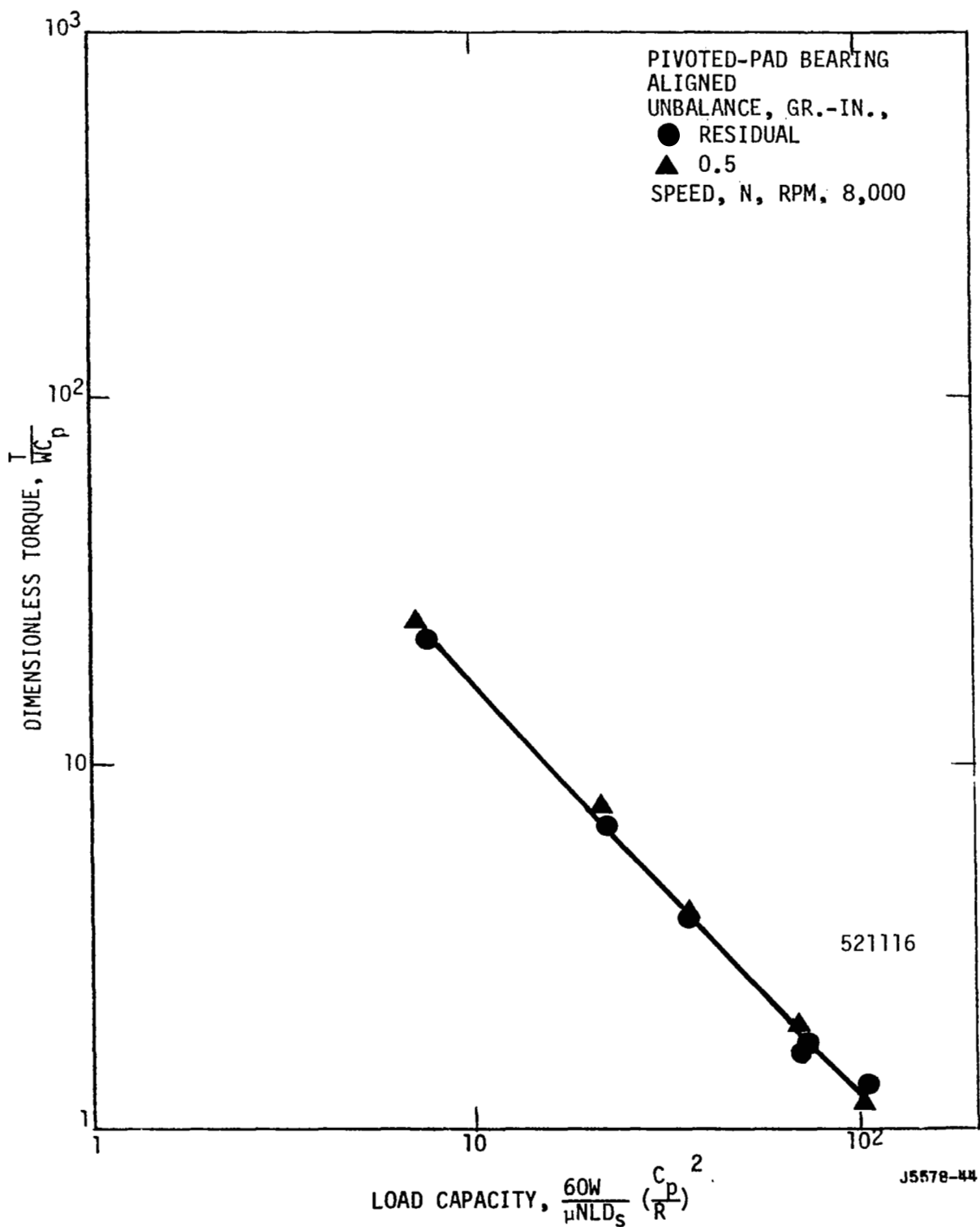
Figure 46. Variation of Dimensionless Torque with Load Capacity and Unbalance.

117
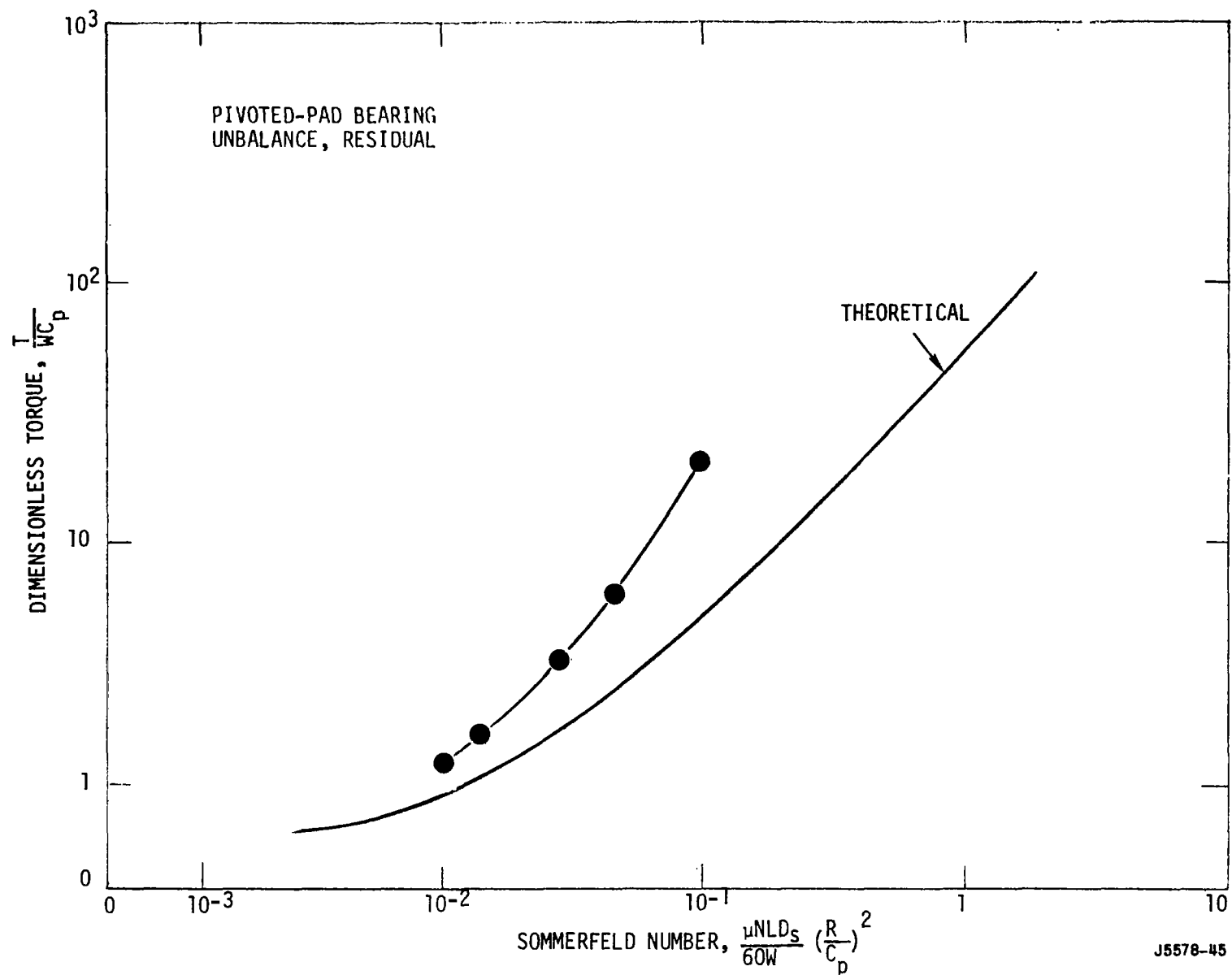
Figure 47. Comparison of Experimental and Theoretical Dimensionless Torque – Sommerfeld Data. Reynolds Number, 1860; Preload Coefficient, 0.52.

Figure 48. Variation of Displacement Semi-Major Axis with Reynolds Number
and Steady Load.

119

J5578-46

Figure 49. Variation of Displacement Semi-Major Axis with Reynolds Number and Unbalance.

PIVOTED-PAD BEARING
LOWER BEARING
ALIGNED
UNBALANCE, GR.-IN., 0.5
STEADY LOAD, W, LB/BRG., 0

THEORETICAL

521203

DISPLACEMENT SEMI-MAJOR AXIS/DISPLACEMENT C.G., J

PAD REYNOLDS NUMBER, $\frac{2\pi RN}{60} C_P \frac{\rho}{\mu}$

J5578-48

Figure 50. Comparison of Experimental and Theoretical Rotor Response.

121

for this case.

Shown in Figure 51 is the variation of the ratio of the force semi-major axis to the rotor unbalance plotted against the pad Reynolds number for two levels of load, zero and 50 lbs/bearing. The rotor unbalance for this plot is 0.5 gr.-in./bearing. It can be seen that the force measurements appear to be somewhat more erratic than the displacement measurements shown on previous curves. The curves for the two different steady loads seem not only to have a different level of the measured force measured, but also a different slope. Shown on Figure 52 is a similar plot in which the two levels of rotor unbalance are shown. These two curves seem to have similar trends but on a slightly different level. Shown in Figure 53 is a comparison of the theoretical and experimental data. In the middle speed range the theoretical predictions appear to be in the right order of magnitude but the trends are not the same.

Shown in Figure 54 is the variation of the maximum attainable speed for the pivoted-pad bearing as a function of steady load. In all instances the speed limitation when testing the pivoted-pad bearing was the excessive size of the synchronous whirl orbit. The data shown are the speeds attained within about the 200 rpm of the point at which it was felt dangerous to run the shaft for the five or ten minutes it required to take a data point and take a photograph. Reference to the figure indicates a gradual increase of maximum attainable speed as the steady load upon the bearing is increased. This plot is for a residual unbalance. Shown in Figure 55 is a similar plot in which three levels of unbalance are compared. It appears from the plot that the speed for the case of antisymmetric unbalance is less than the case

122

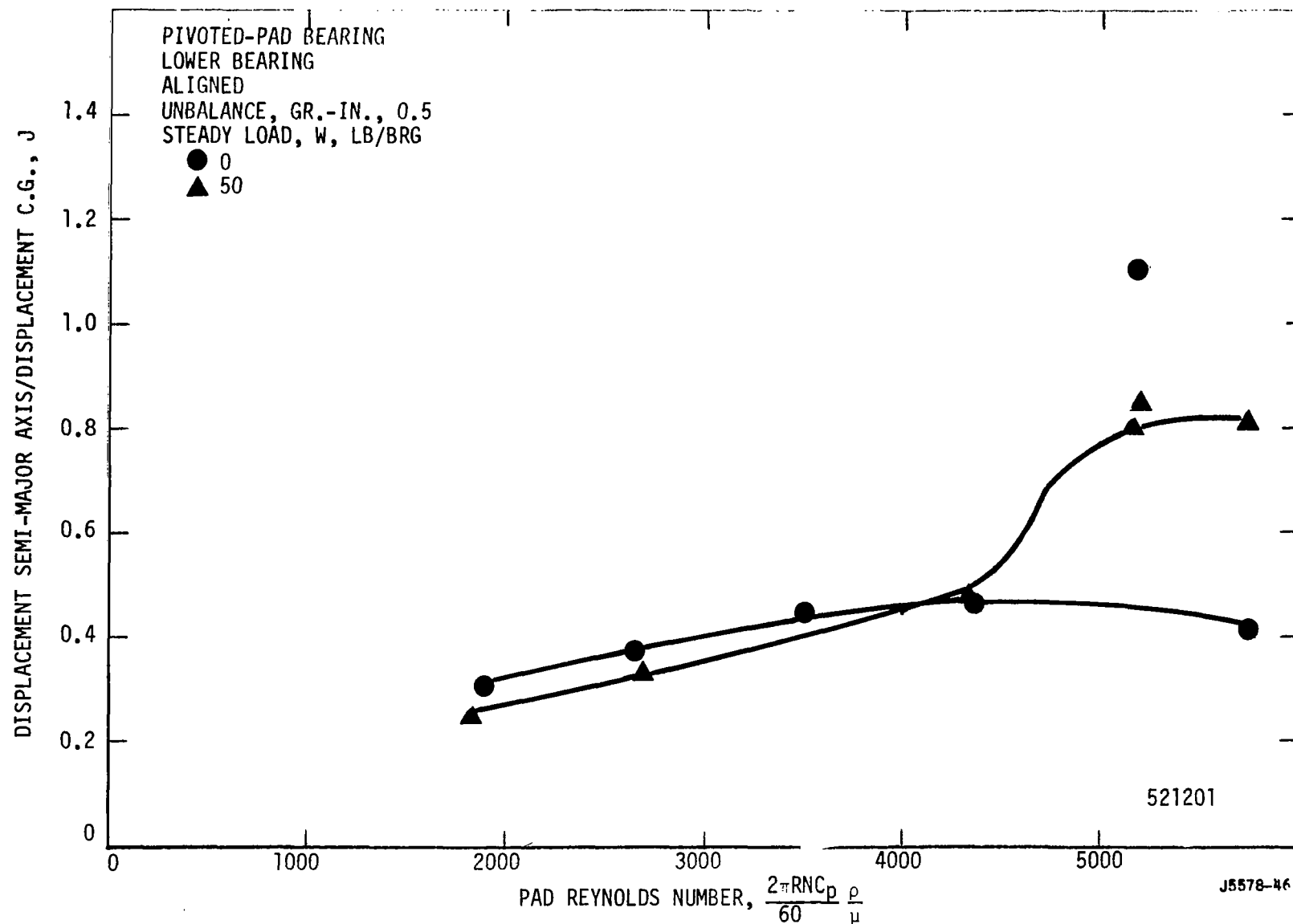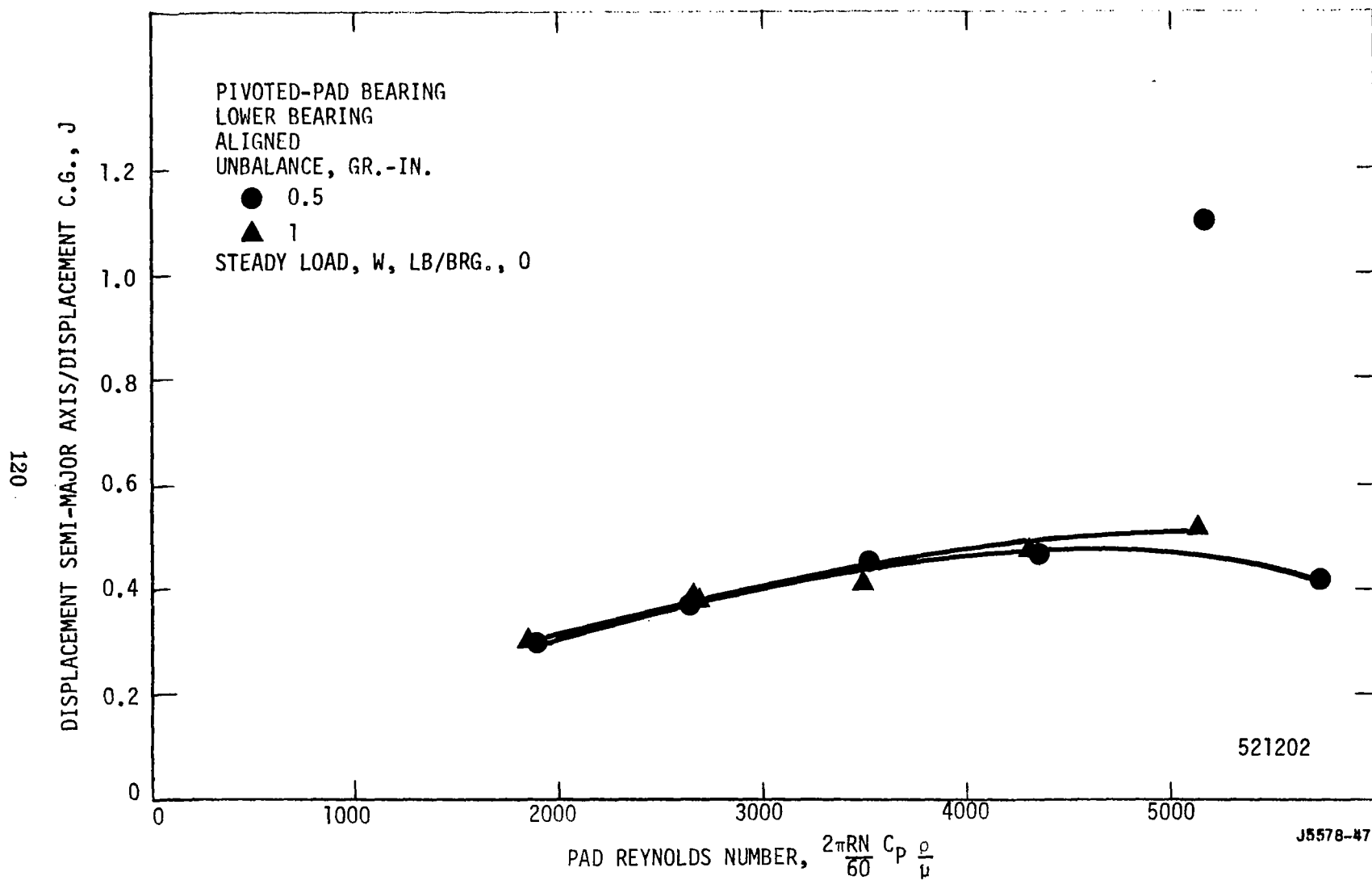Figure 51. Variation of Force Semi-Major Axis with Reynolds Number and Steady Load.

J5578-49

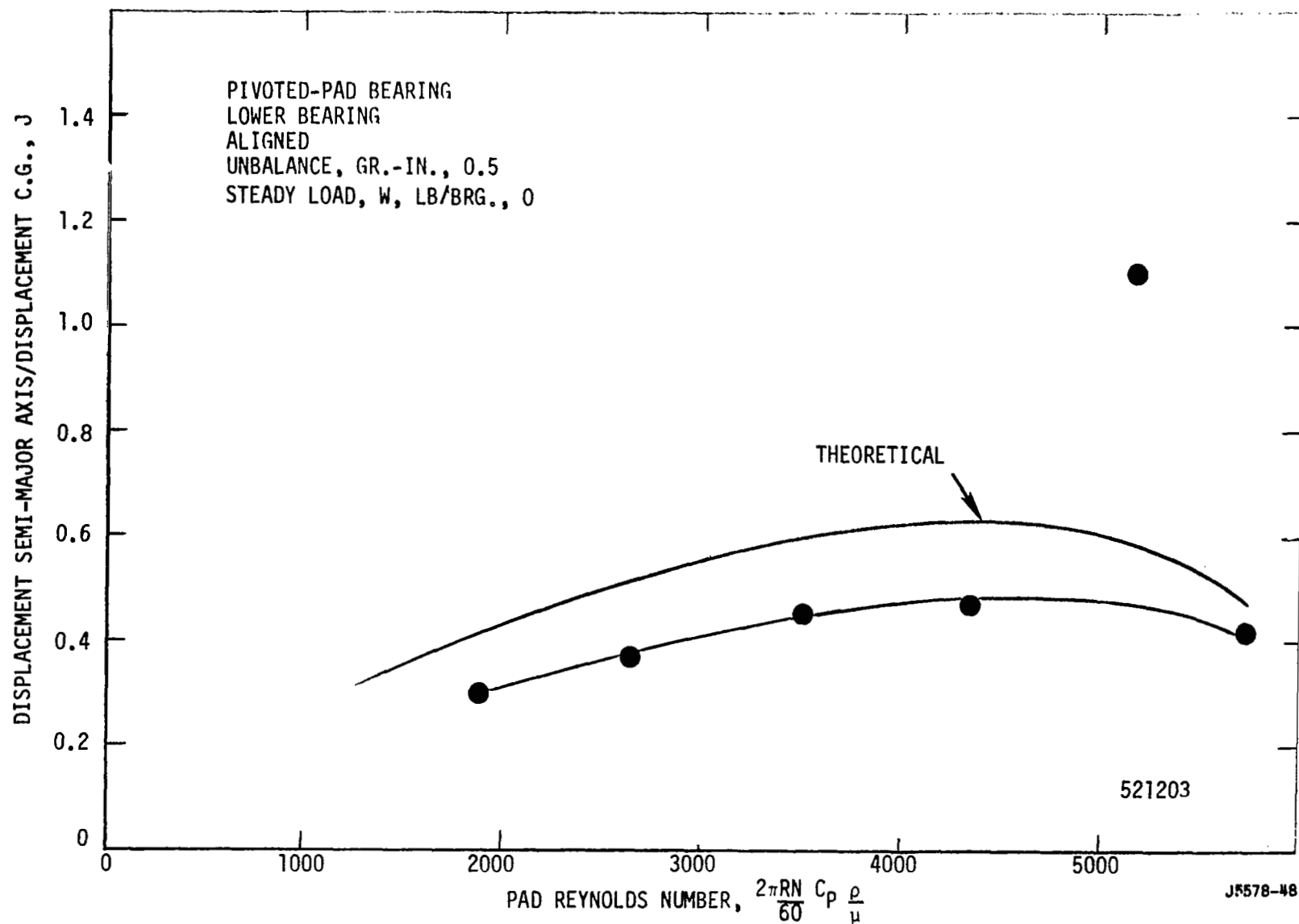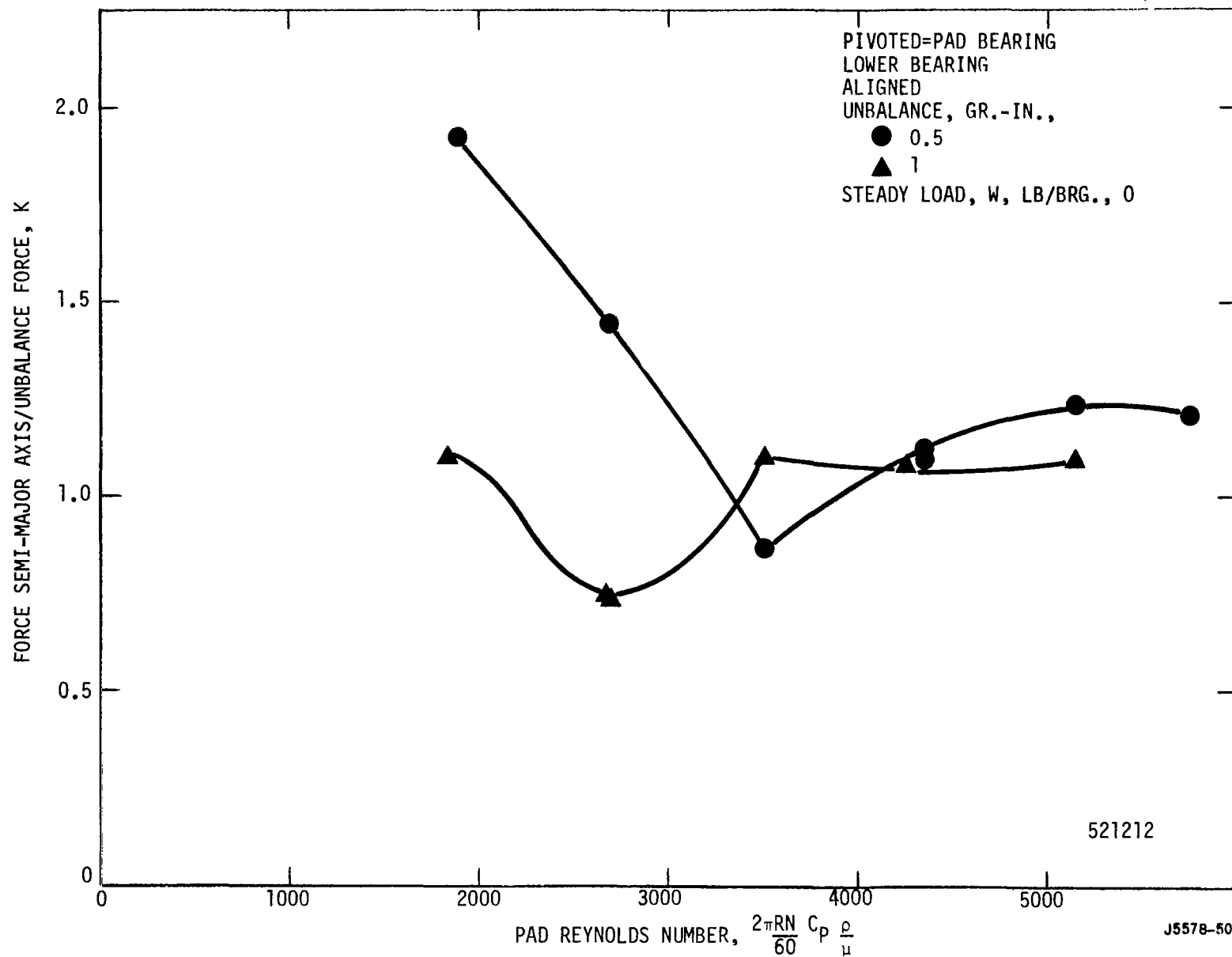Figure 52. Variation of Force Semi-Major Axis with Reynolds Number and
Unbalance.
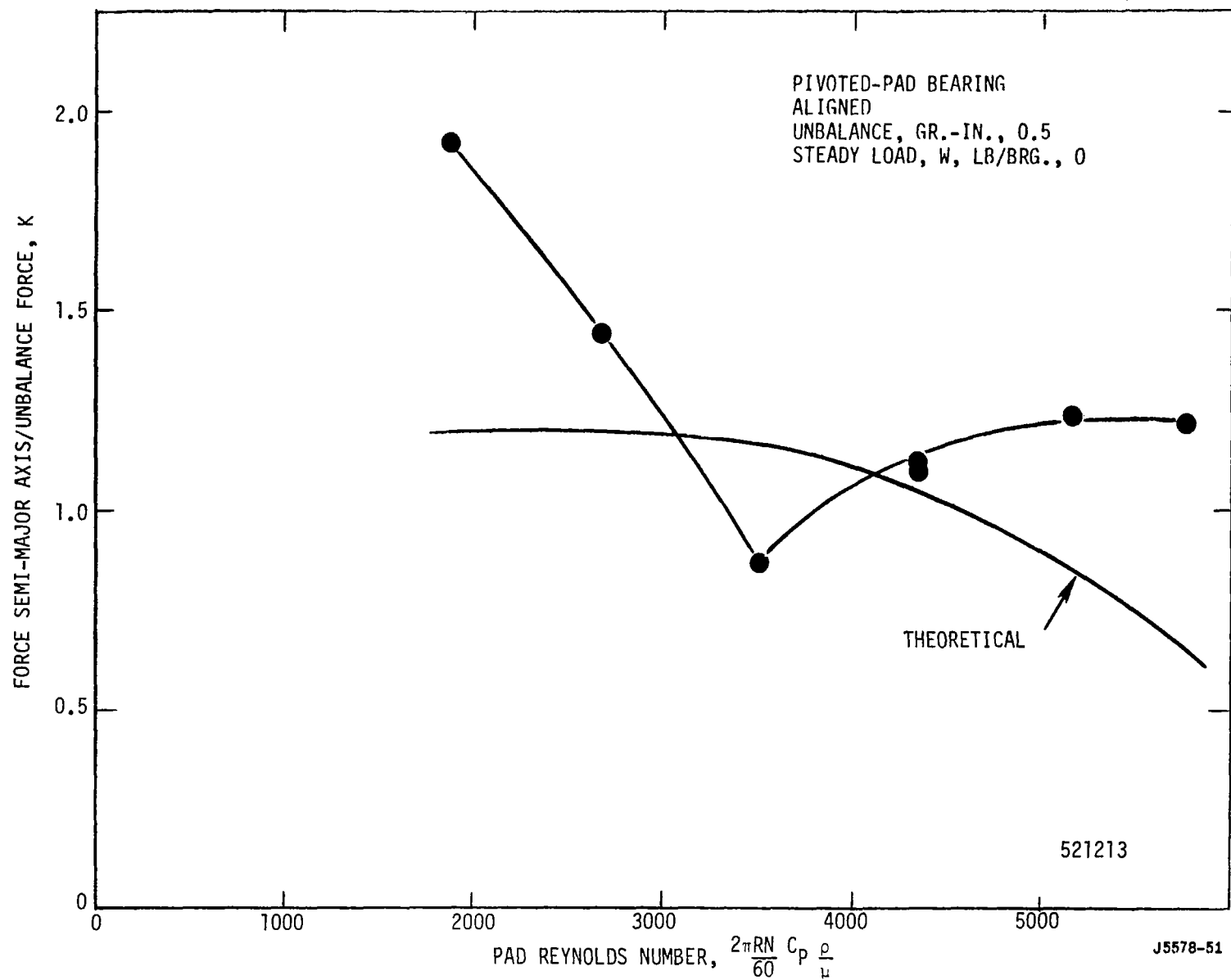
Figure 53. Comparison of Experimental and Theoretical Bearing Forces.
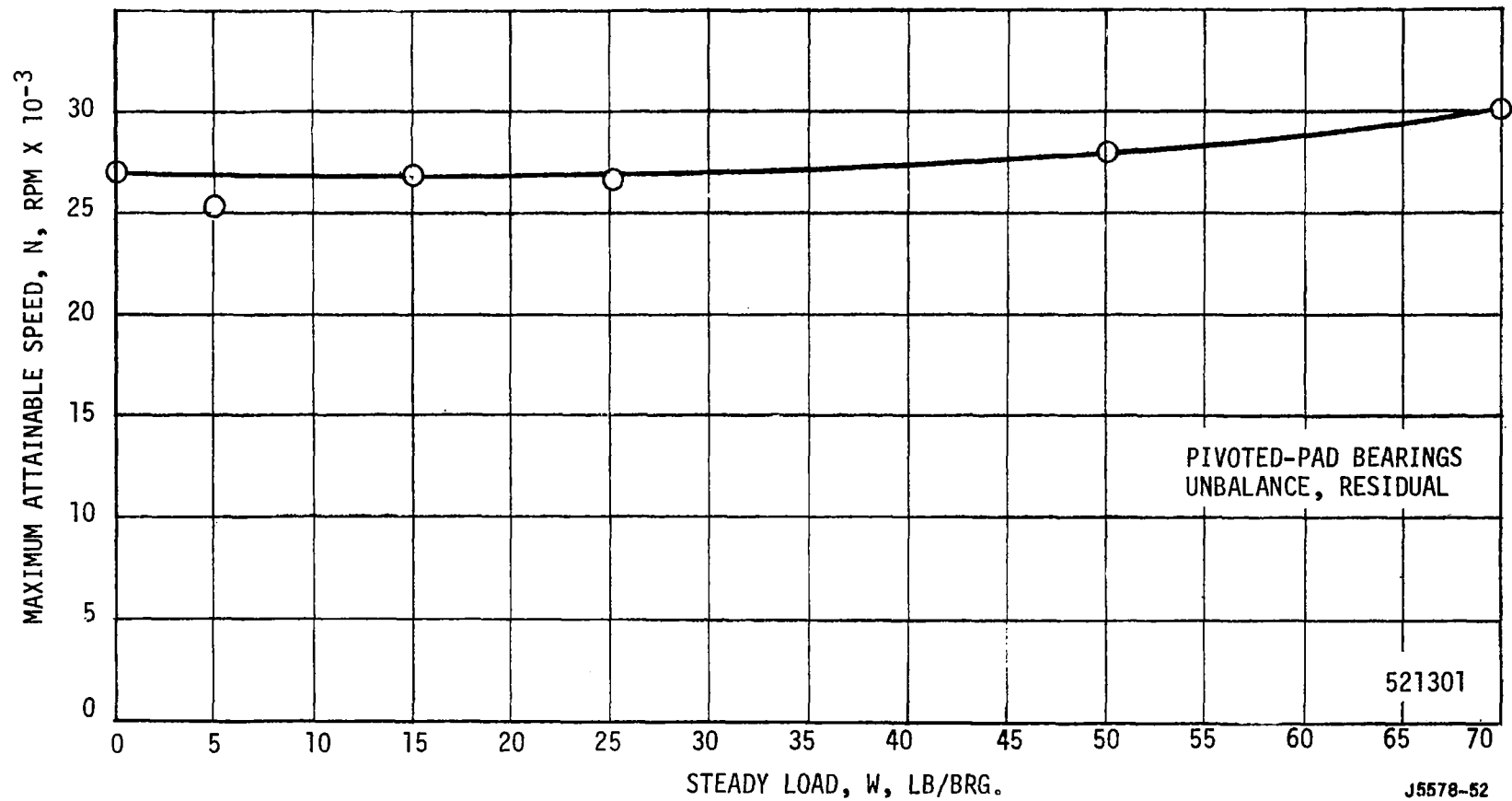
Figure 54. Variation of Maximum Attainable Speed with Steady Load.
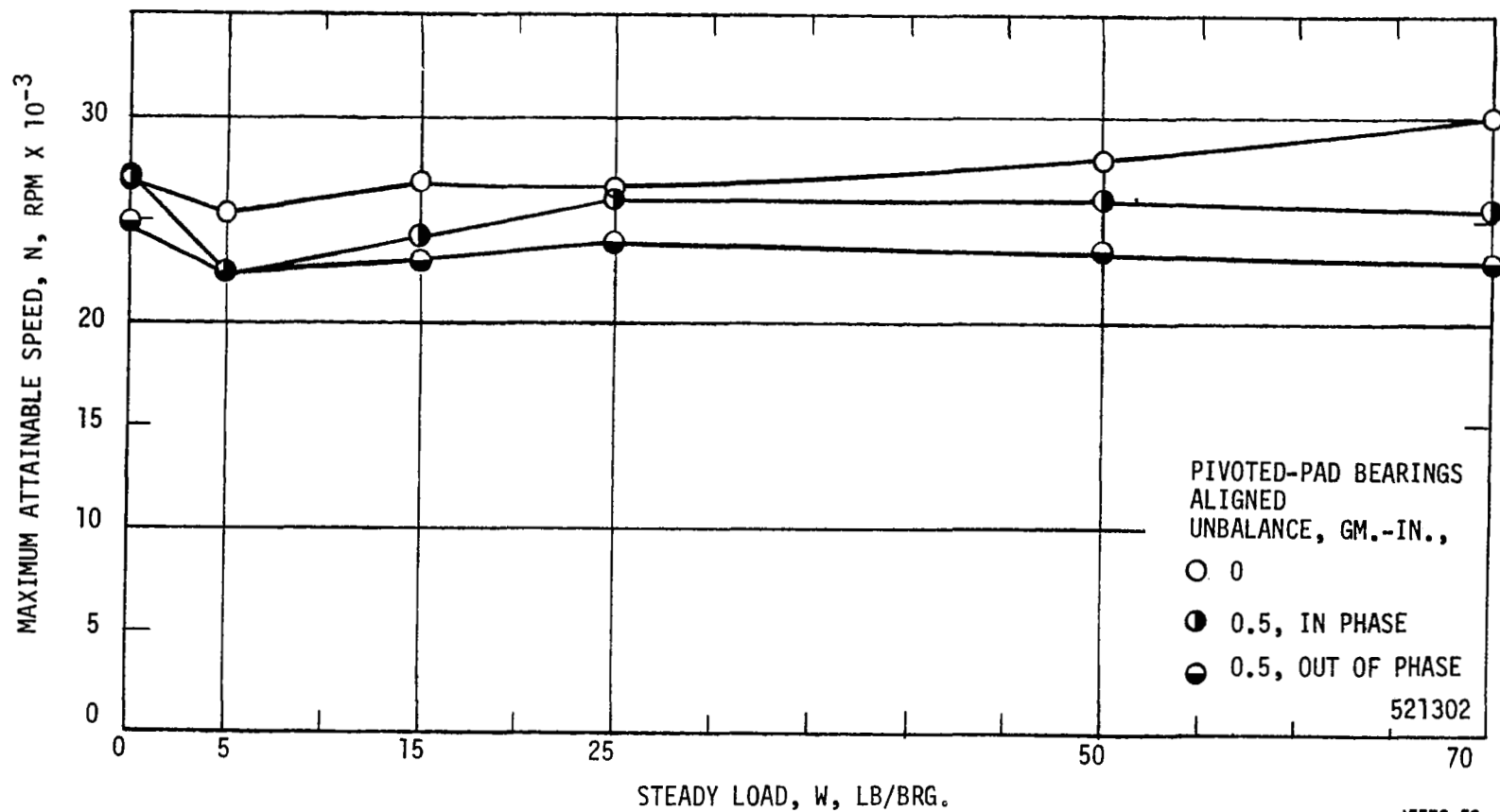
J5578-52

Figure 55. Variation of Maximum Attainable Speed with Steady Load and
Unbalance.

of symmetric unbalance. The difference in the maximum attainable speeds was 2000 or 3000 rpm for these two unbalances. At the highest steady load the rotor with residual unbalance reached the highest attainable speed of the three, namely 30,000 rpm.

3. Effect of Misalignment

Shown in Figure 56 is a sketch which depicts the way in which the bearings were misaligned for the test to be described in what follows. The aligned data was obtained by carefully aligning the center lines of the two test bearings with each other. In the second set of tests the lower bearing was deliberately adjusted so that its center line was 400 seconds out of alignment with the center line established by the upper bearing. In the final set of tests the bottom bearing was mis-aligned with the center line established by the top bearing by 400 seconds. In addition, the bearing was moved laterally 4 mils to increase the misalignment. Reference to the figure indicates the total misalignment of the upper and lower bearings for each of the three test conditions.

In order to explore the effect of misalignment on the pivoted-pad bearings, the lower bearing was misaligned 400 seconds and 4 mils from the upper bearings for a total misalignment of 467 seconds. Shown in Figure 57 is the variation of bearing eccentricity ratio with Sommer-feld number for a steady load of 70 lbs per bearing and for rotor un-balance of 0.5 gr-in/bearing. Results are compared for aligned and misaligned bearings. In the low range of bearing eccentricity ratio there is a somewhat lesser load capacity for the misaligned bearing,

128

ALIGNED 400 SEC 400 SEC, 4 MILS

TOTAL
MISALIGNMENT,
SEC   0   0   67

UPPER
BEARING

67 SEC

LOWER
BEARING

400 SEC

4 MILS

67 SEC   400 SEC

TOTAL
MISALIGNMENT,
SEC   0   400   467
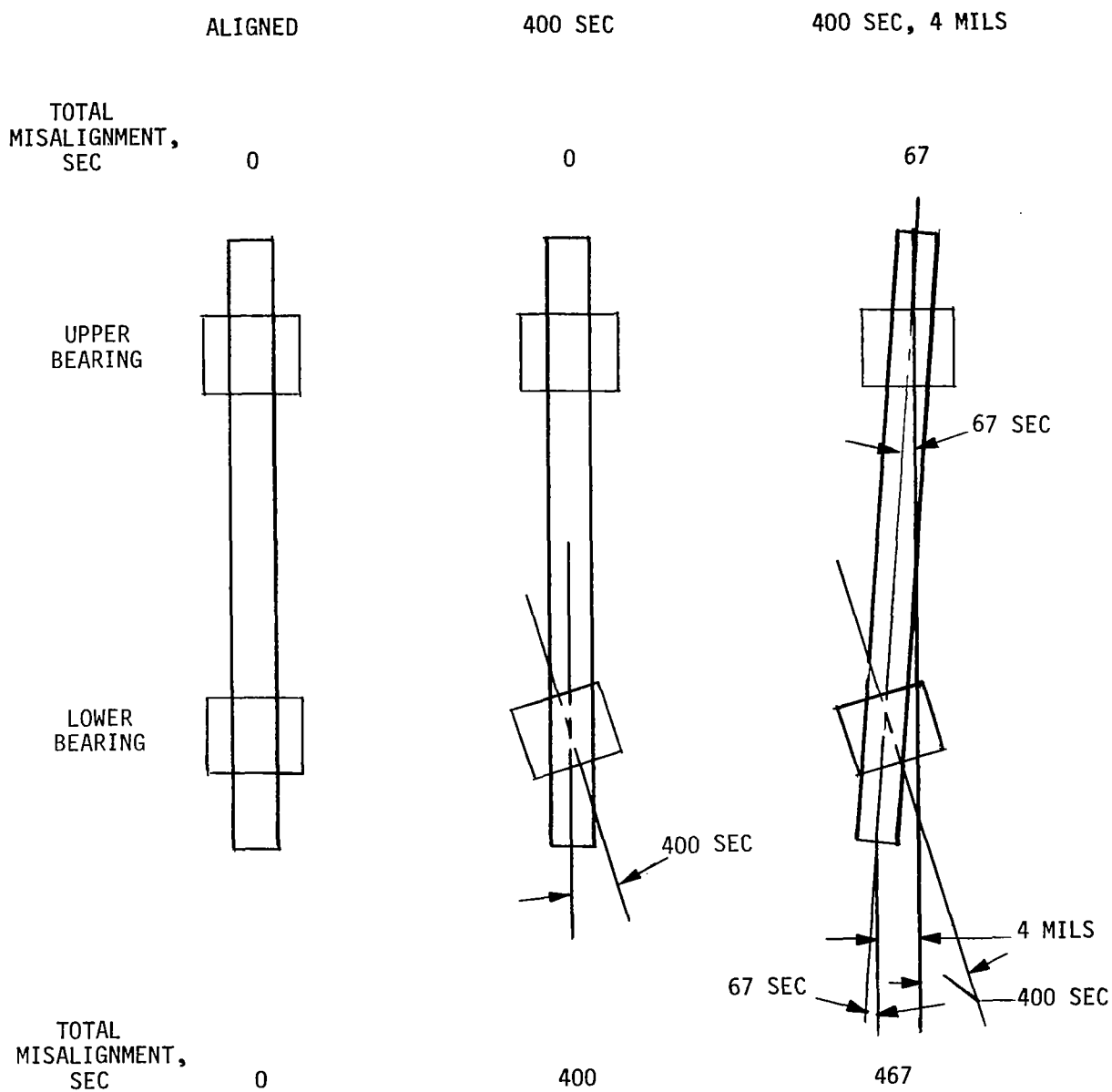
J5578-85

Figure 56. Schematic Diagram of Bearing Misalignment.

129
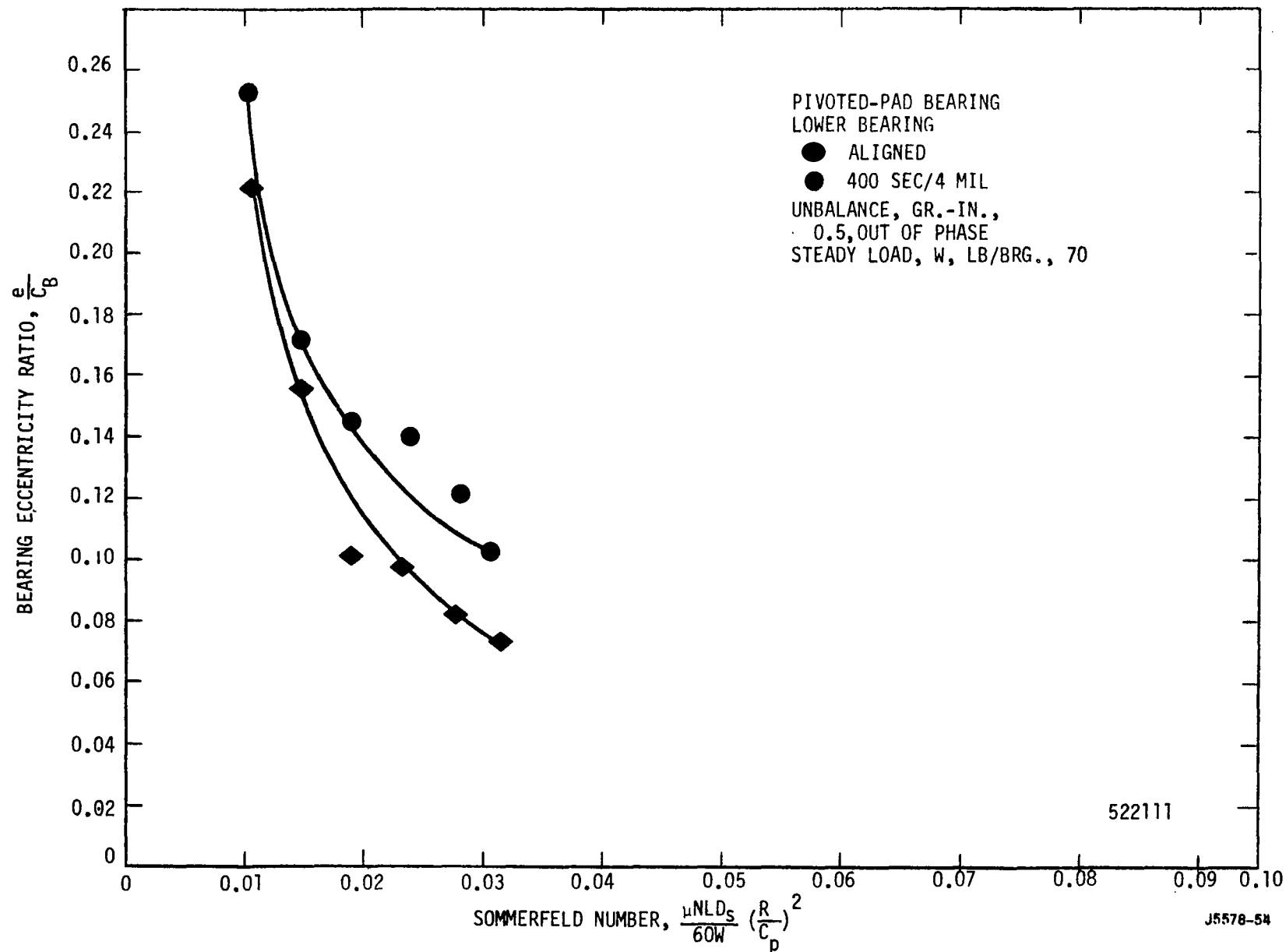
Figure 57. Effect of Misalignment on the Eccentricity Ratio – Sommerfeld
Number Variation.

J5578-54

however, at the high end of eccentricity range (nearer a typical opera-
tional point for a bearing) the difference in load capacity is negligible.
Shown in Figure 58 is the variation of attitude angle with bearing
eccentricity ratio for a sideload of 70 lbs/bearing and an unbalance of
0.5 gr-in bearing. The misaligned bearing appears to have a tendency
toward slightly higher attitude angles at the same value of bearing
eccentricity ratio. Shown in Figure 59 is the variation of non-dimen-
sional torque with pad Reynolds number. The small differences in torque
shown between the aligned and misaligned bearings is probably within
the data scatter.

Shown in Figure 60 is the variation of the ratio displacement
semi-major axis to the displacement of the center of gravity with pad
Reynolds number. At a pad Reynolds number less than 5,000 there is
very little effect of the misalignment on the displacement semi-major
axis. However, beyond a Reynolds number of 5,000 the data seems to
indicate a somewhat larger orbit size for the aligned case. The mis-
alignment causes a slightly diminished clearance and therefore causes
the bearing to be stiffer and results in a smaller amplitude as the
critical speed is approached. Shown in Figure 61 is the variation of
the ratio of force semi-major axis to the rotor unbalance as a function
of pad Reynolds number. Except at the higher speeds the data for aligned
and misaligned bearings lie fairly close together. At the higher speeds
the aligned data seems to show higher bearing reaction forces than the
misaligned data. Since each set of data appears to be consistent within
itself, there is no explanation for the variation in behavior at the
higher pad Reynolds numbers.

131

Figure 58. Effect of Misalignment on the Attitude Angle – Eccentricity Ratio Variation.
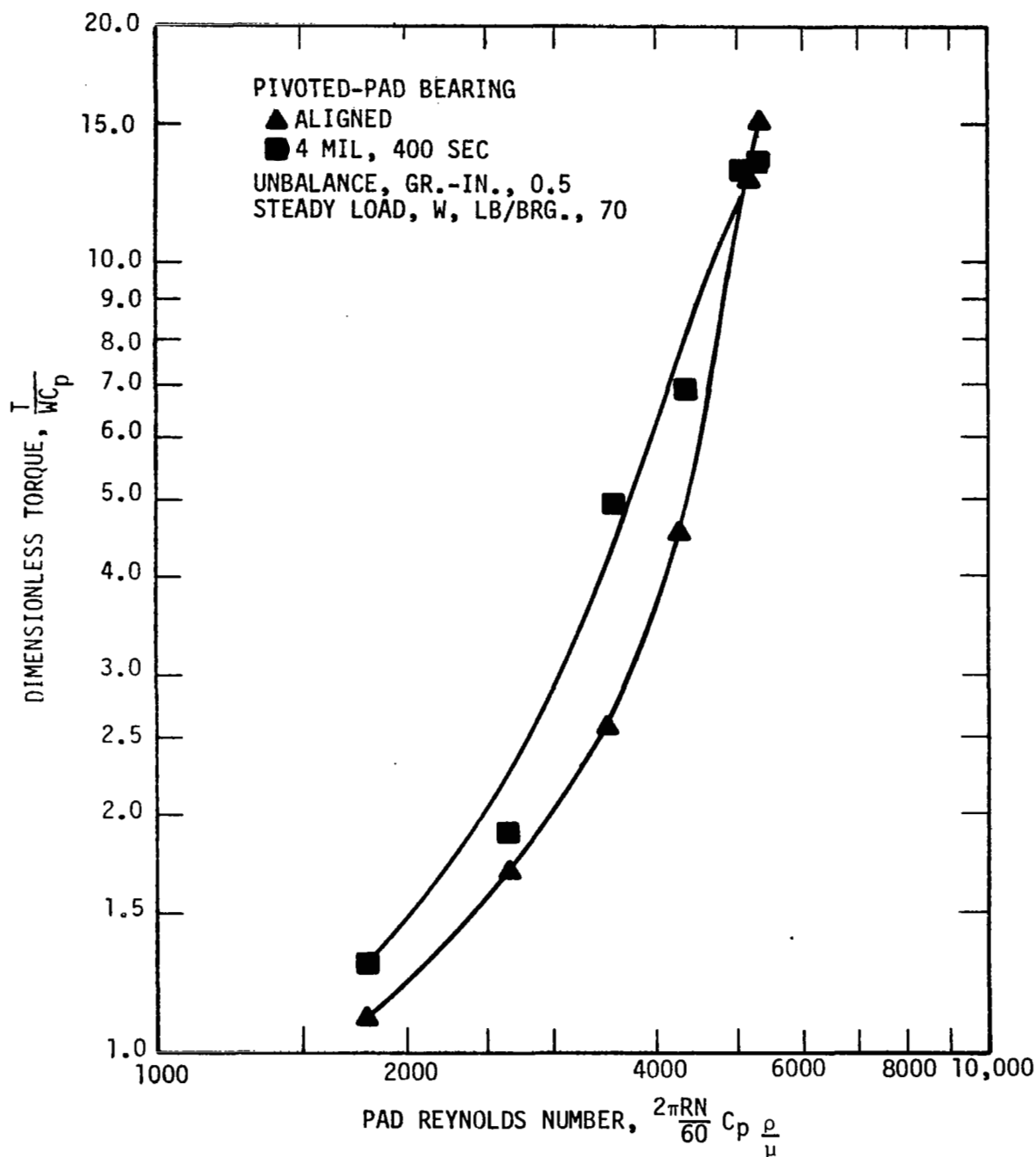
Figure 59. Effect of Misalignment on the Dimensionless Torque – Pad Reynolds Number Variation.

133
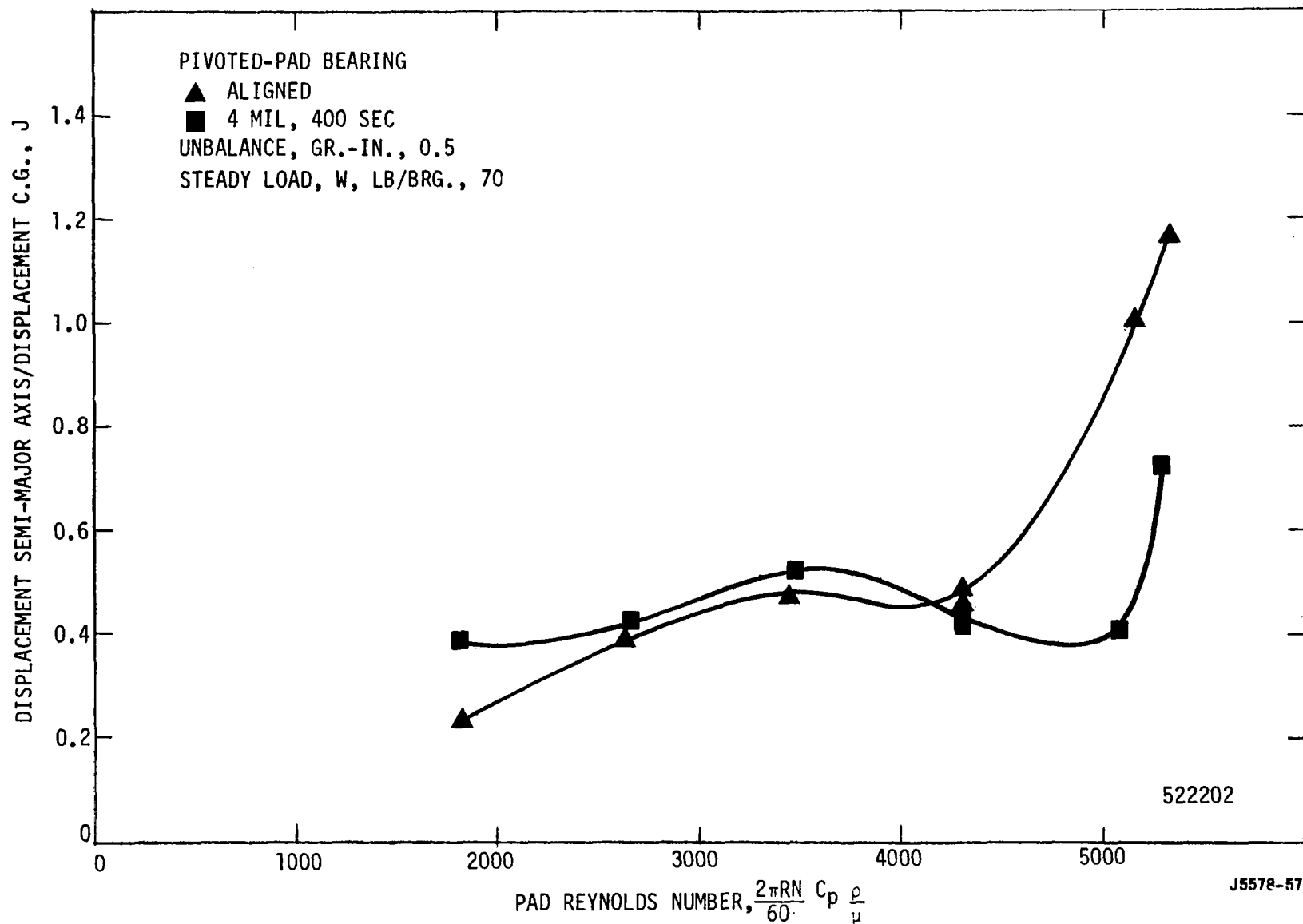
Figure 60. Effect of Misalignment on the Displacement Semi-Major Axis-
Pad Reynolds Number Variation.
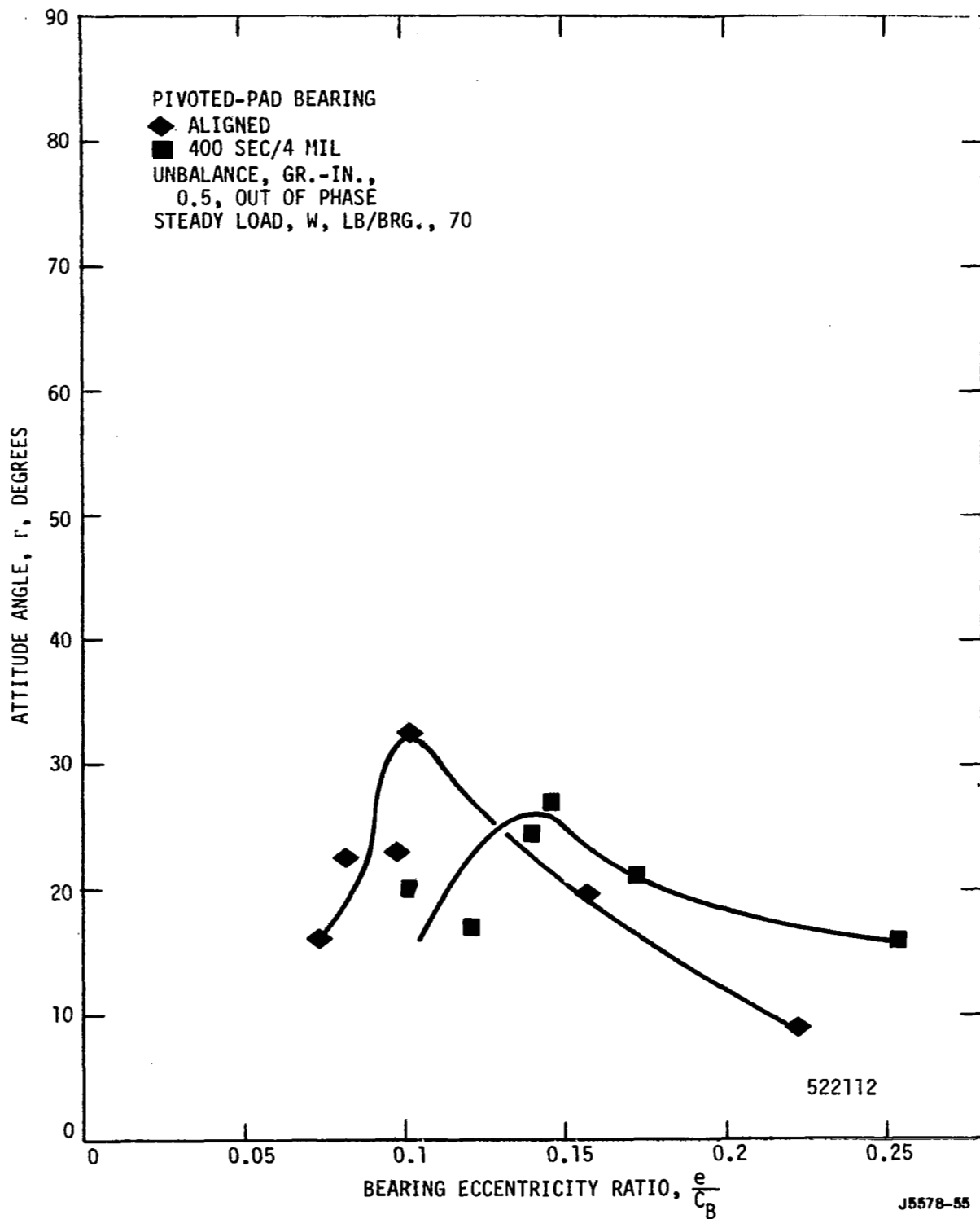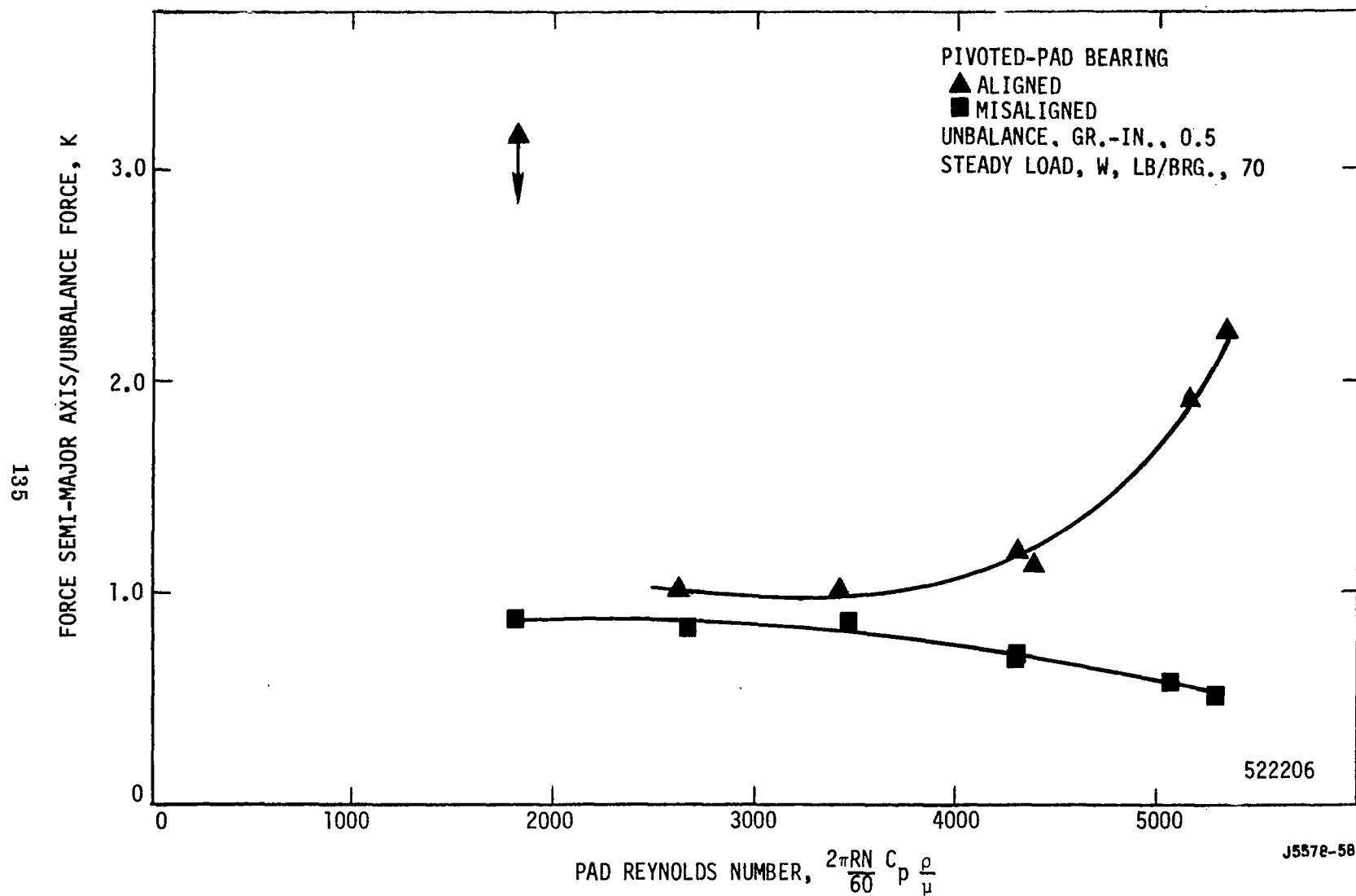
Figure 61. Effect of Misalignment on the Force Semi-Major Axis-Pad Reynolds Number Variation.

Shown in Figure 62 is the variation of the maximum attainable speed of the pivoted-pad bearings as a function of steady load. It is apparent from the plot that misalignment has a negligible effect upon this parameter.

4. Effect of Selectively Locking One Pad

To simulate the seizure of a pad due to pivot fretting, tests were first run with one pad locked symmetrically with respect to a plane passing through two diametrically opposed pivots and the center line of the bearing. The locked pad was the one which would be in the lower right-hand corner of Figure 31. Shown in Figure 63 is the variation of the bearing eccentricity ratio with the Sommerfeld number. Data is plotted for an antisymmetric unbalance of 0.5 gr-in/bearing and a steady load of 70 lbs/bearing. There is practically no difference between the data for free and locked pads. Shown in Figure 64 is the variation of attitude angle with bearing eccentricity ratio for free and locked pads. The locked pad data appears to have a tendency towards higher attitude angles than the free-pad data. Since the tangent of the attitude angle represents the ratio of the tangential to radial fluid forces on the shaft, high attitude angles have a tendency of producing fractional-frequency whirl. This condition did not occur in the test ranges covered, however, at higher steady loads it might. Shown in Figure 65 is the variation of the non-dimensional torque with the load capacity (reciprocal Sommerfeld number) for a Reynolds number of 2640. It is apparent that the free-pad and the locked-pad configurations have substantially the same torque. Shown in Figure 66 is a plot of non-dimensional torque against pad Reynolds

136
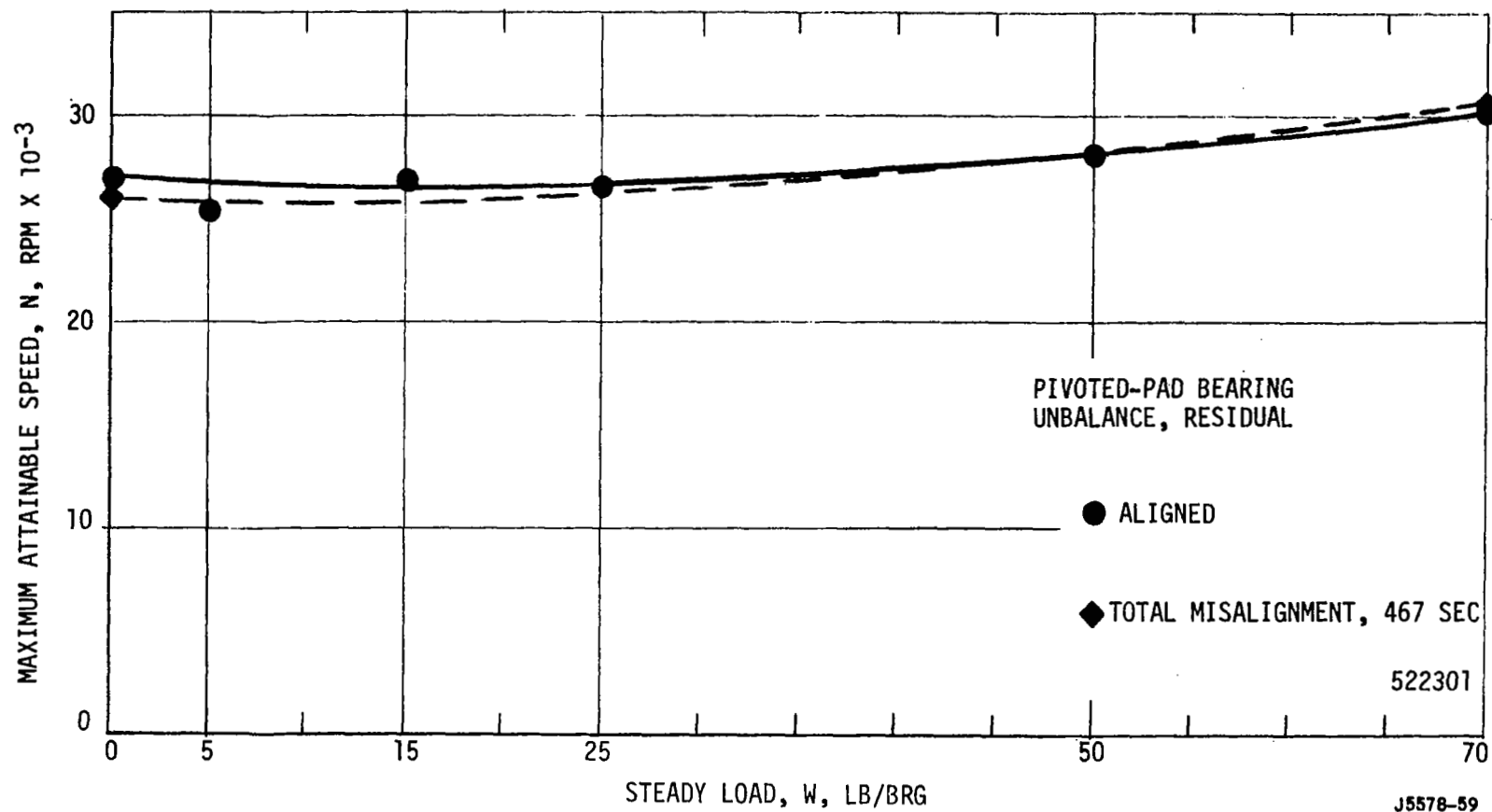
Figure 62. The Effect of Misalignment on the Maximum Attainable Speed–
Steady Load Variation.
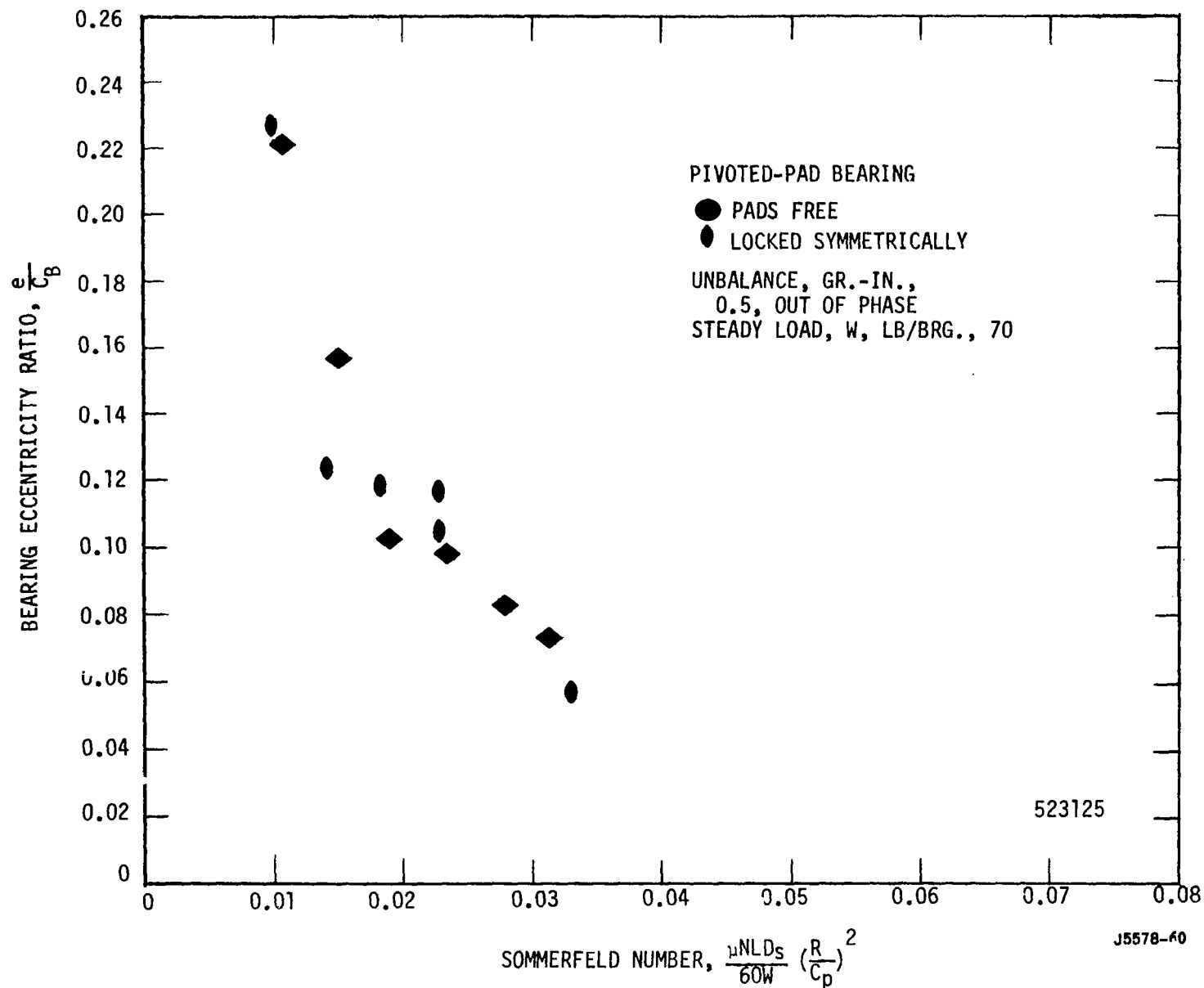
Figure 63. Effect of One Pad Locked Symmetrically on the Eccentricity
Ratio – Sommerfeld Number Variation.

J5578-60
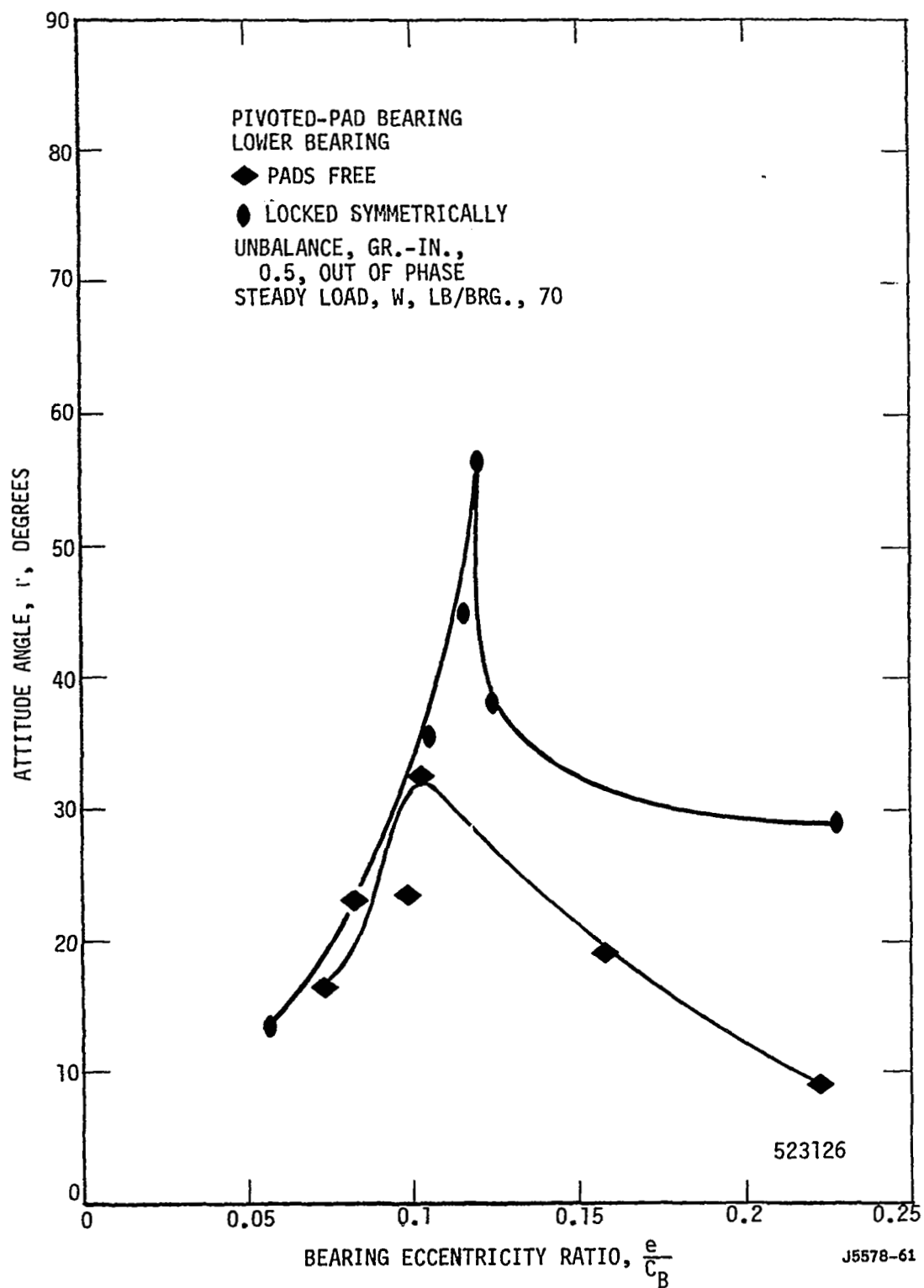
Figure 64.   Effect of One Pad Locked Symmetrically on the Attitude Angle –
Eccentricity Ratio Variation.

139
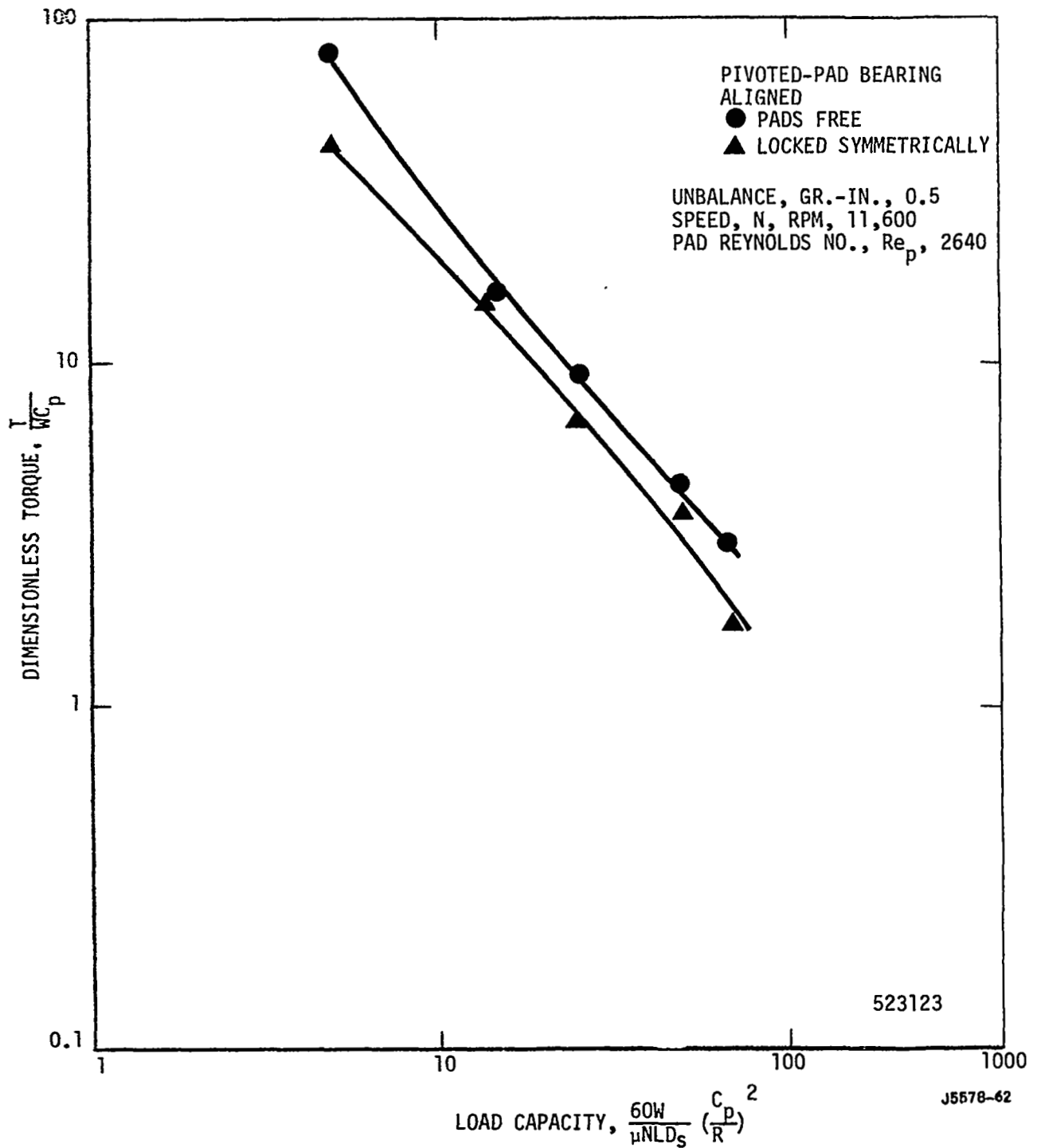
Figure 65. Effect of One Pad Locked Symmetrically on the Dimensionless
Torque – Load Capacity Variation at Constant Reynolds Number.

140
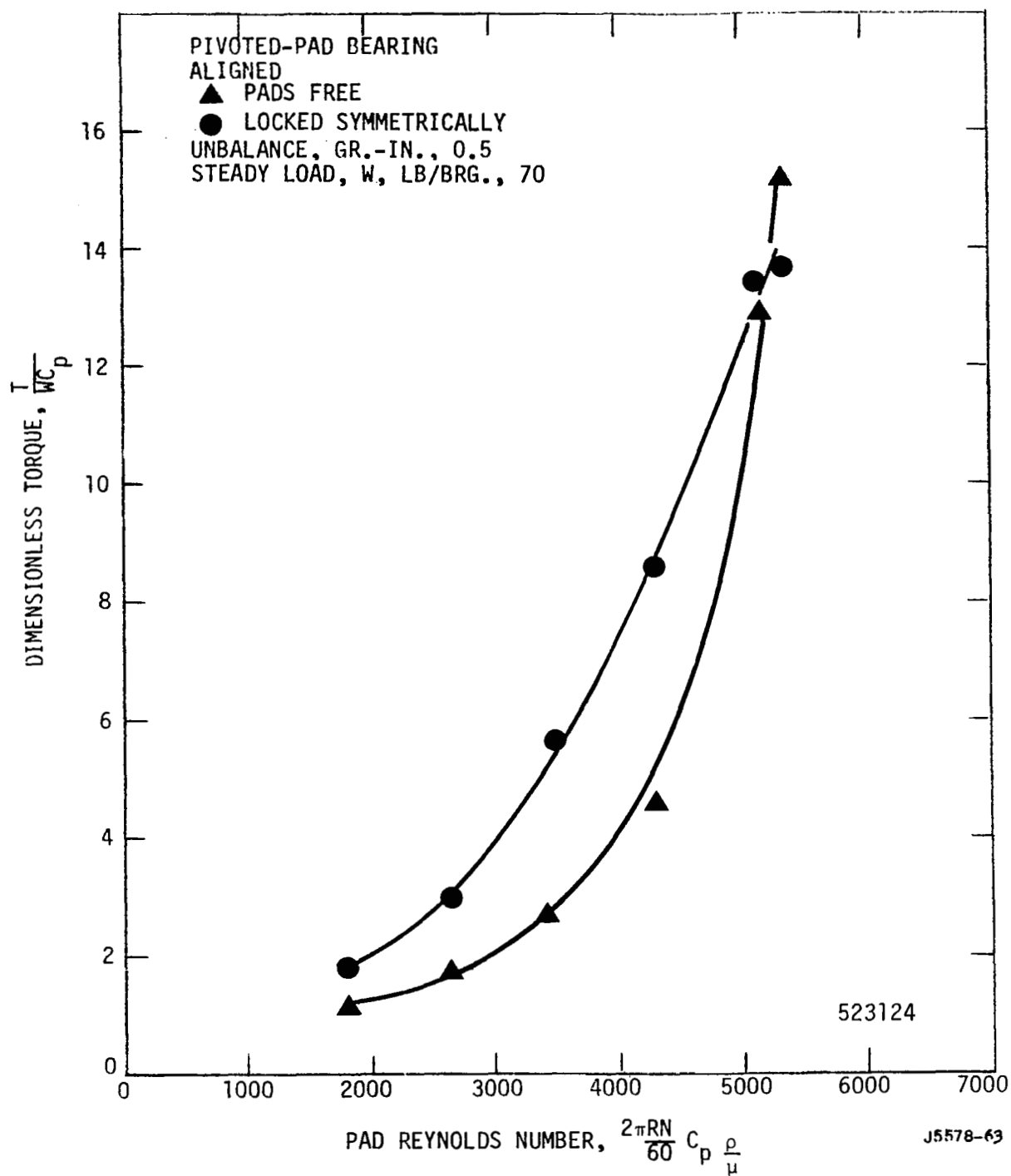
Figure 66. The Effect of One Pad Locked Symmetrically on the Dimensionless Torque – Reynolds Number Variation at Constant Steady Load.

141

number for a constant steady load and variable speed. The locked-pad data appears to have a somewhat higher torque than is obtained when all the pads are free.

Shown in Figure 67 is the variation of the ratio of displacement semi-major axis to displacement of the center of gravity of the shaft against pad Reynolds number for a steady load of 70 lbs/bearing. The orbit radius depicted on this plot is fairly independent of whether the pads are free or locked, except for the highest speed condition. There the apparent difference in the data may be a scatter rather than a trend. Shown in Figure 68 is the variation of the ratio force for semi-major axis to the unbalance force for the same conditions as the previous figure. Here again within the scatter of the data, the force-orbit appears to be approx. the same for both free and symmetrically-locked pad data.

In order to simulate an even more stringent operational condition growing out of pivot fretting, tests were run with one pad locked askew. In these tests the same pad as was locked before was locked with the pad tilted in the roll mode and pitched downward so that the leading edge is somewhat closer to the shaft than the trailing edge as shown in Figure 69. This makes one leading edge corner closer to the shaft than any other corner of the pad.

Shown in Figure 70 is the variation of bearing eccentricity ratio with Sommerfeld number for an antisymmetric unbalance of 0.5 gr-in and a steady load of 70 lb/bearing. It is seen that the data for the cases of free- and locked-pad lie fairly close together especially at typical design values of eccentricity, above 0.2. Shown in Figure 71 is the variation of the attitude angle with the bearing eccentricity ratio

142

Figure 67. Effect of One Pad Locked Symmetrically on the Displacement
Semi-Major Axis – Reynolds Number Variation.

143
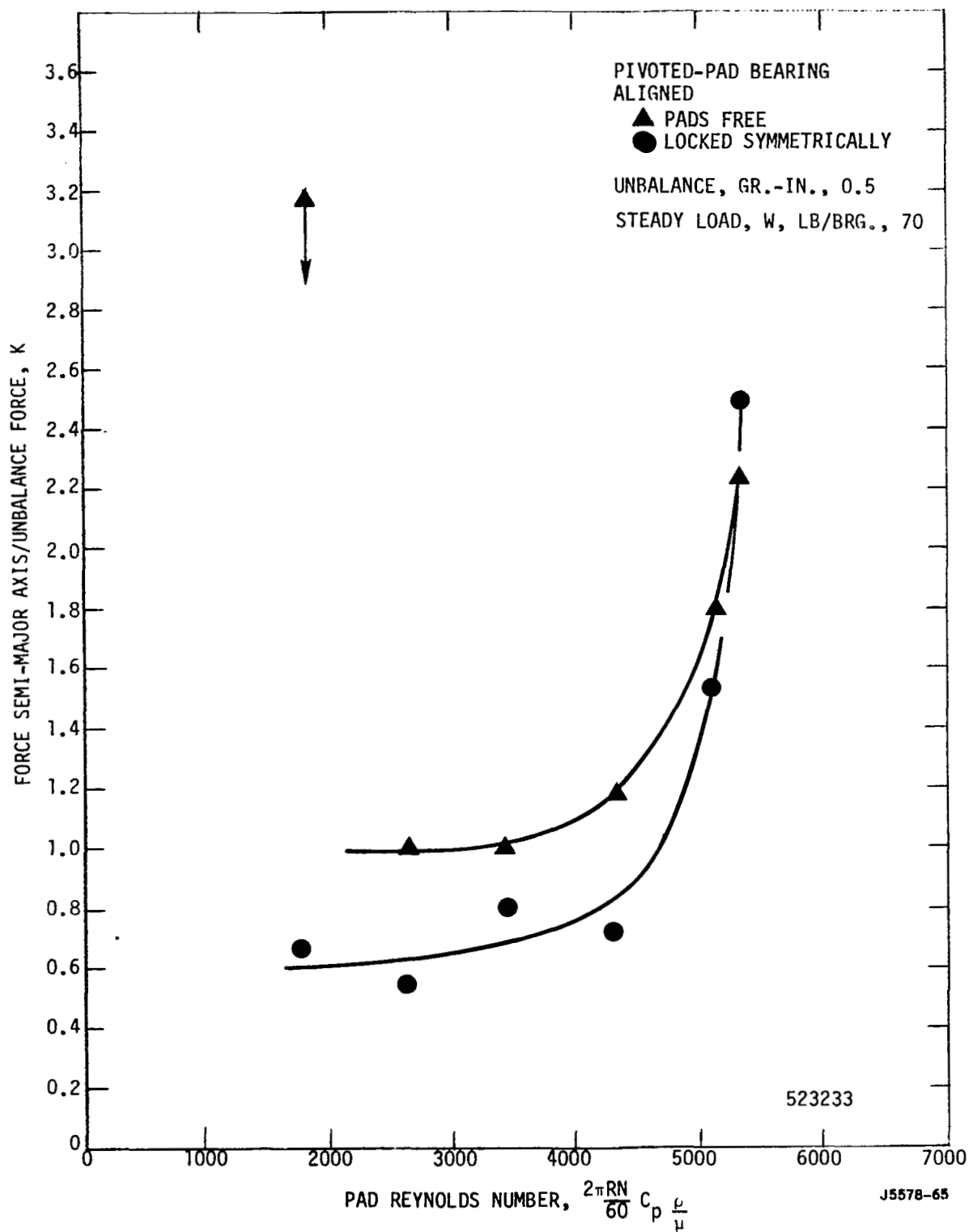
Figure 68. The Effect of One Pad Locked Symmetrically on the Force Semi-Major Axis - Reynolds Number Variation.

144

Figure 69. View Looking Downward on Pad Locked
Askew. Dimensions in Mils.

145
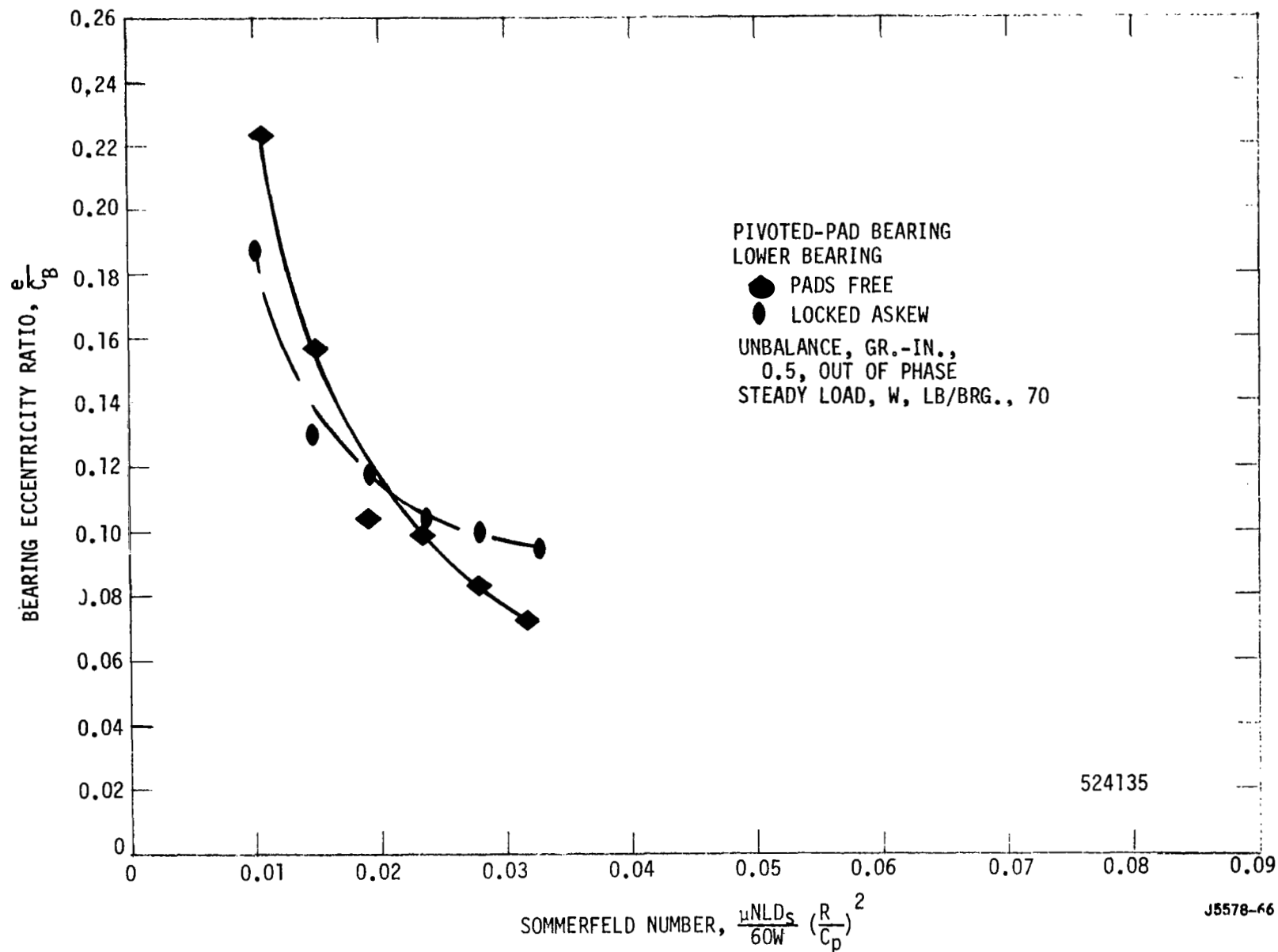
Figure 70. The Effect of One Pad Locked Askew on the Eccentricity Ratio - Sommerfeld Number Variation.
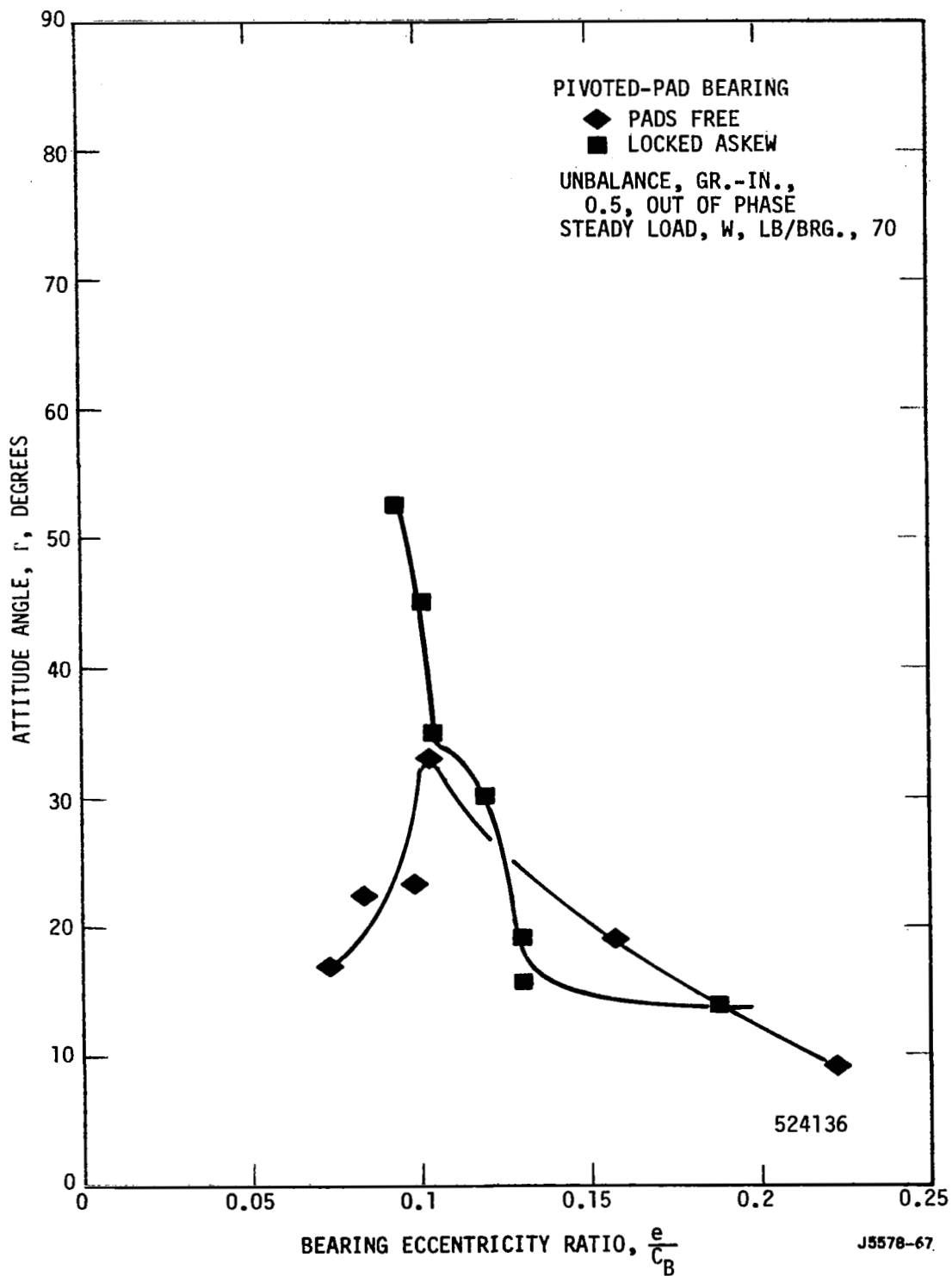
Figure 71.   The Effect of One Pad Locked Askew on the Attitude Angle –
Eccentricity Ratio Variation.

147

for the same conditions as the previous figure. Here the askewed locked-pad appears to have a somewhat higher tendency toward instability as indicated by higher attitude angles than the free-pad configuration. However, it should be remembered that no instability was noted in the range of conditions of the pivoted-pad bearing test. Shown in Figure 72 is the comparison at constant speed of the non-dimensional torque versus load capacity for the case of free- and askewed-locked pads. Here again the fixture of the pad has little, if any, effect on the torque. Another torque plot is shown on Figure 73 in which constant steady load instead of a constant rotative speed was used. Again there is little evidence of any effect of the locking of the pad upon the measured torque.

Shown in Figure 74 is the variation of the ratio of the displacement semi-major axis to the displacement of the center of gravity against the pad Reynolds number. The free-pad data appear to have a slightly higher orbit size than do the data for the locked-pad. For even the largest eccentricity ratios measured on this program (less than 0.24 for the pivoted-pad bearing), the film thickness is very small (0.00114 inches). Hence the design must consider not only the eccentricity of the shaft center line but also the shaft orbit. The shaft orbit further reduces the minimum film thickness as can be seen in Figure 31.

Shown in Figure 75 is the variation of the ratio of the force semi-major axis to the unbalance force against pad Reynolds number. In general, the data for the free pads appear to have the higher values of measured force.

148
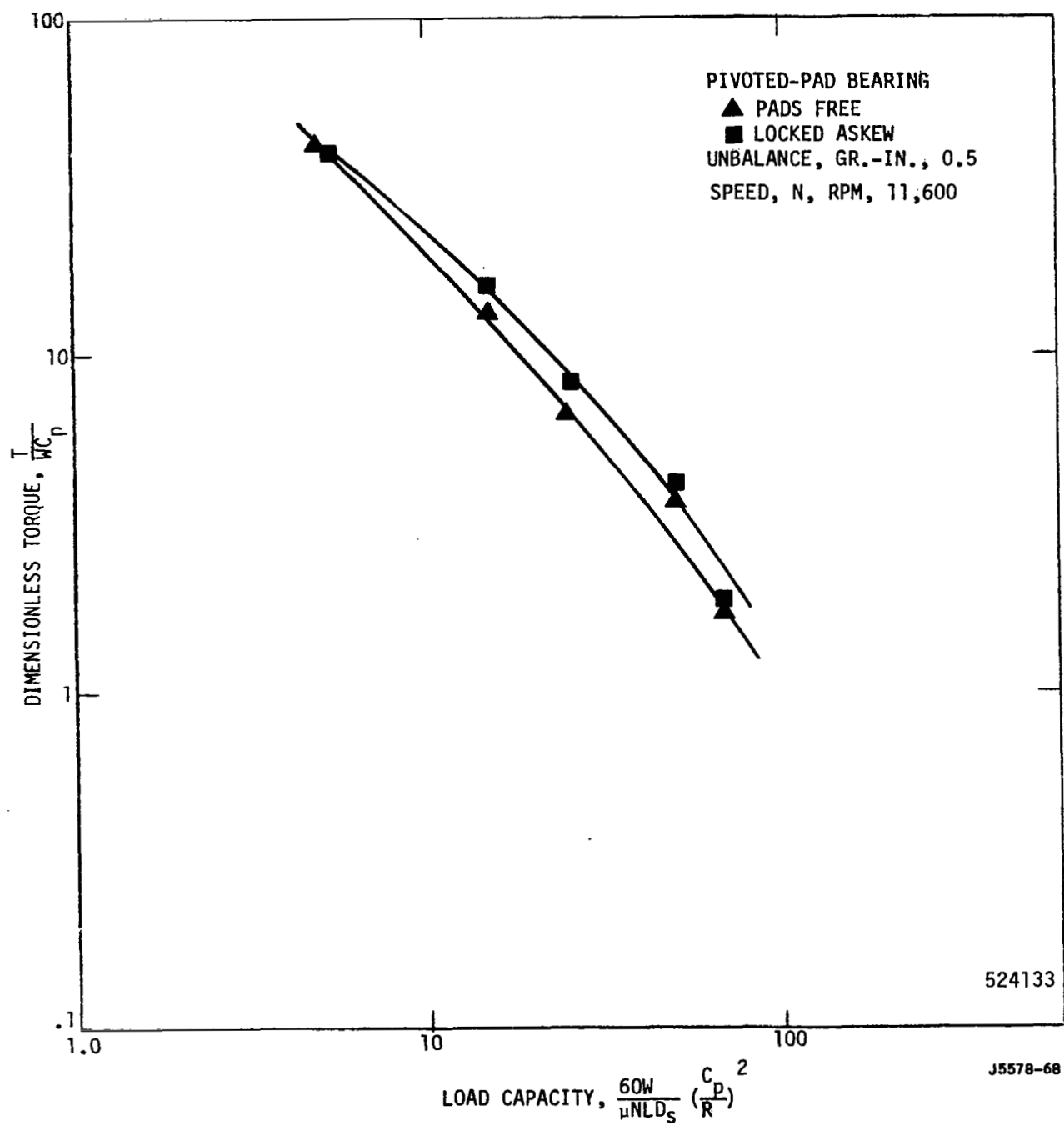
Figure 72. The Effect of One Pad Locked Askew on the Dimensionless Torque – Load Capacity Variation.
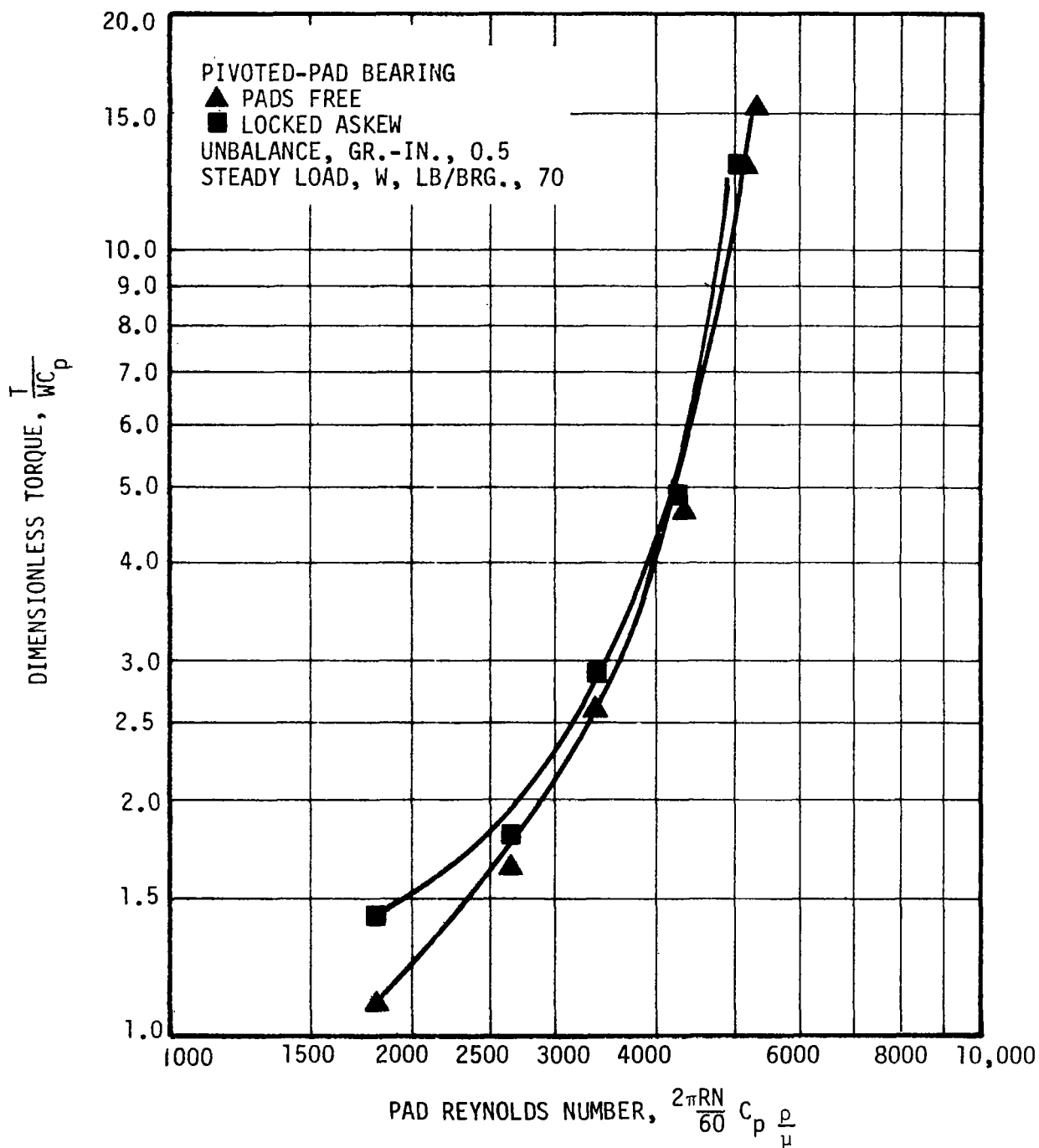
Figure 73. The Effect of One Pad Locked Askew on the Dimensionless Torque - Reynolds Number Variation.
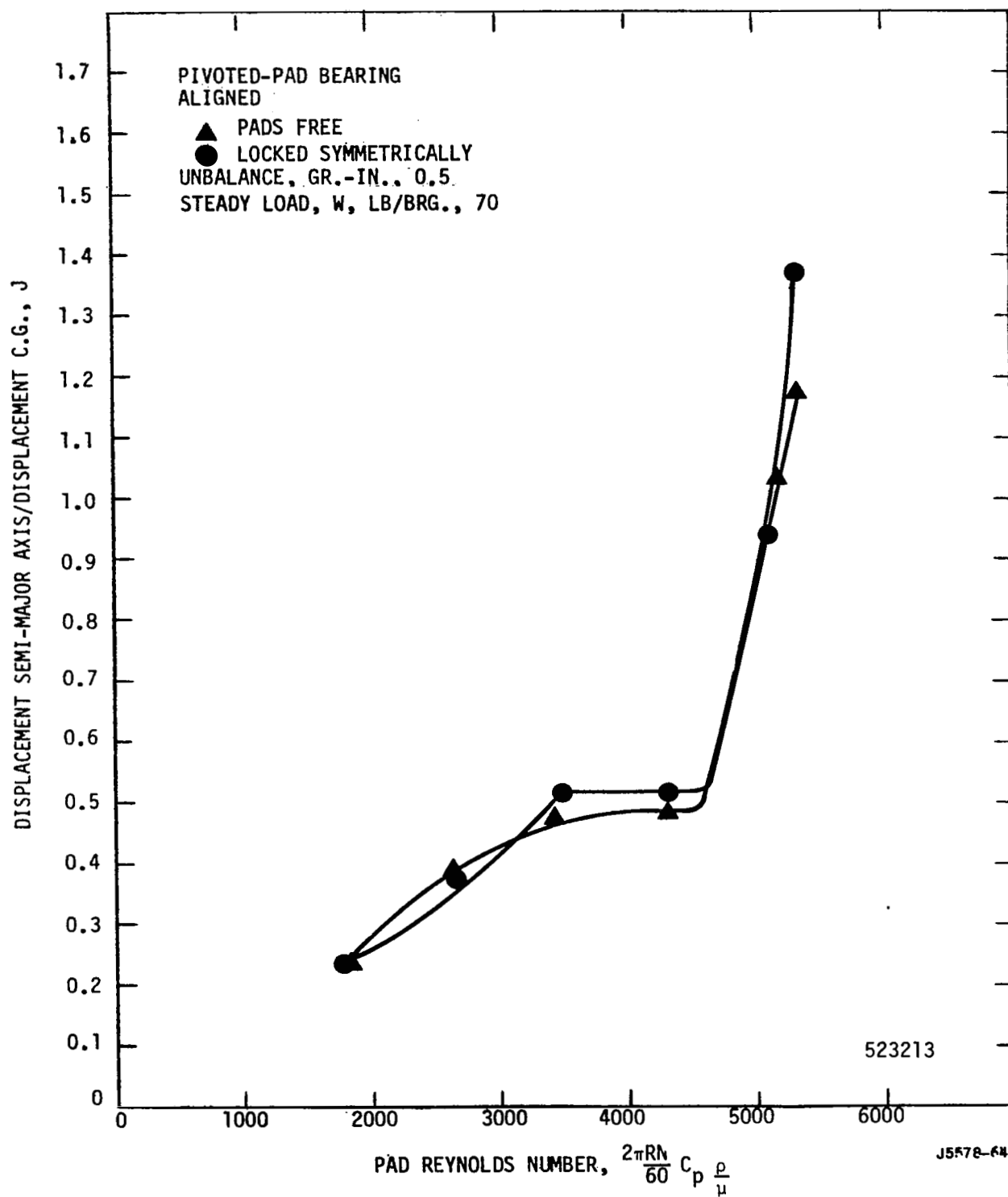
150
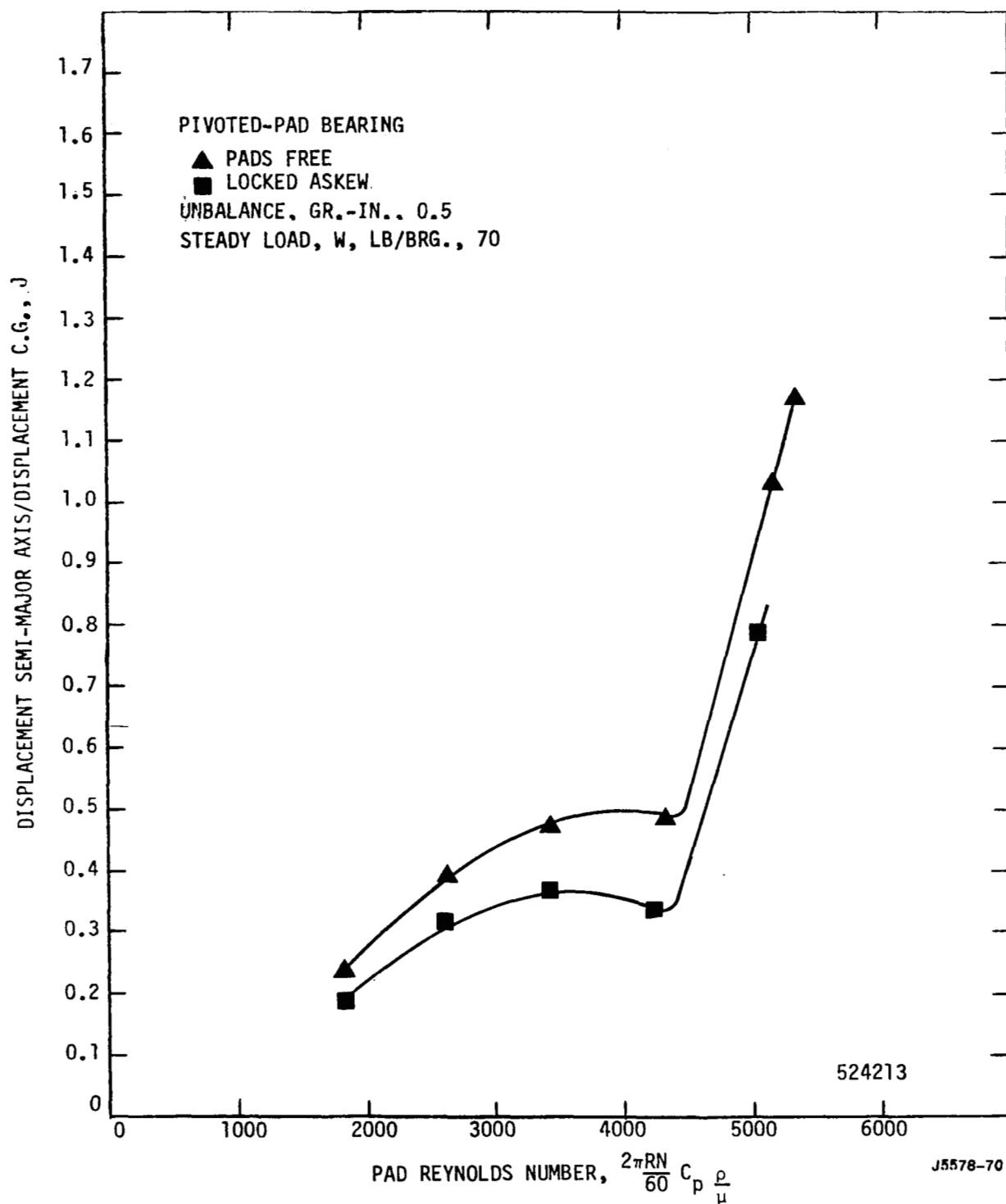
Figure 74. The Effect of One Pad Locked Askew on the Displacement Semi-Major Axis - Reynolds Number Variation.

151

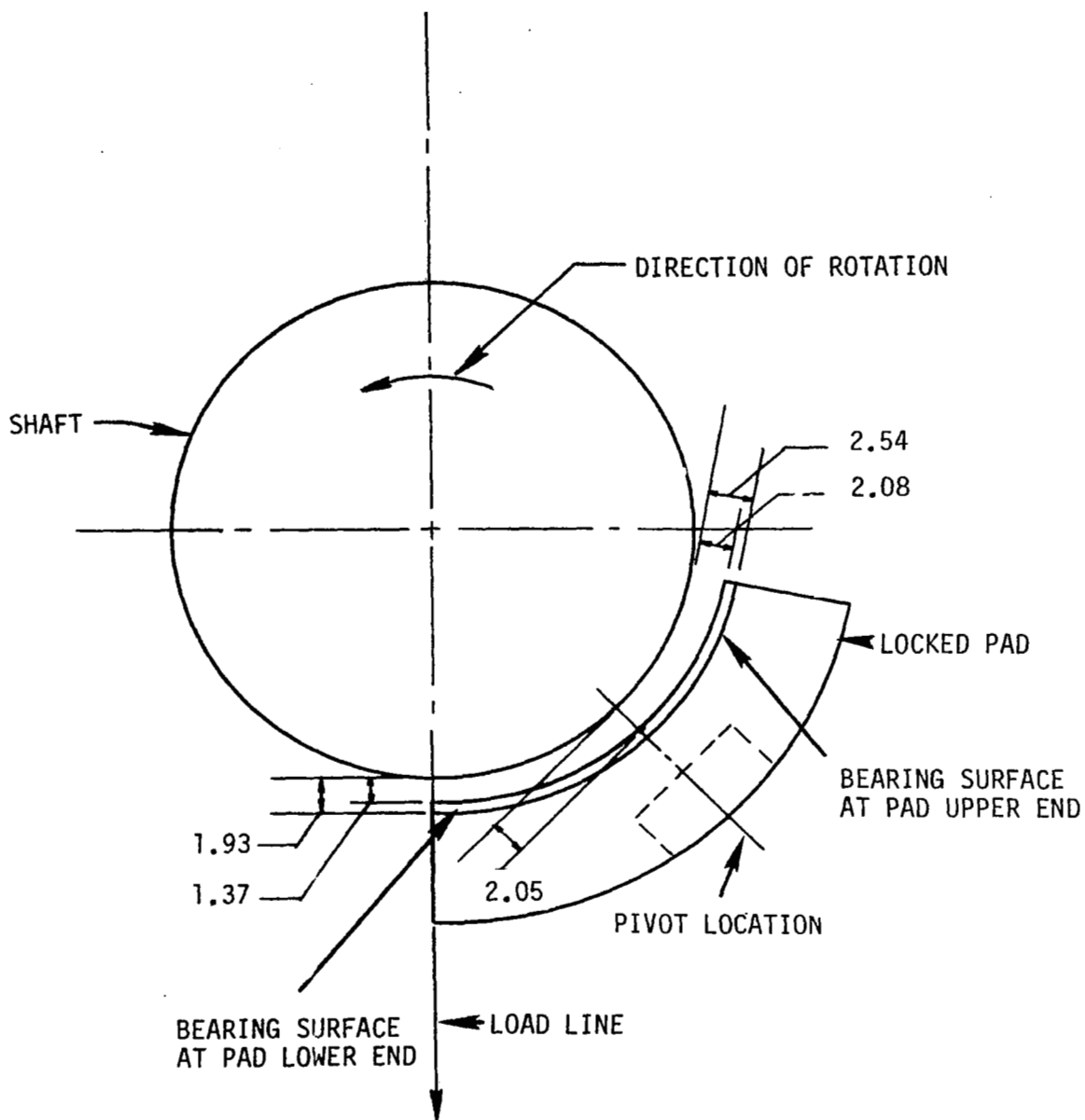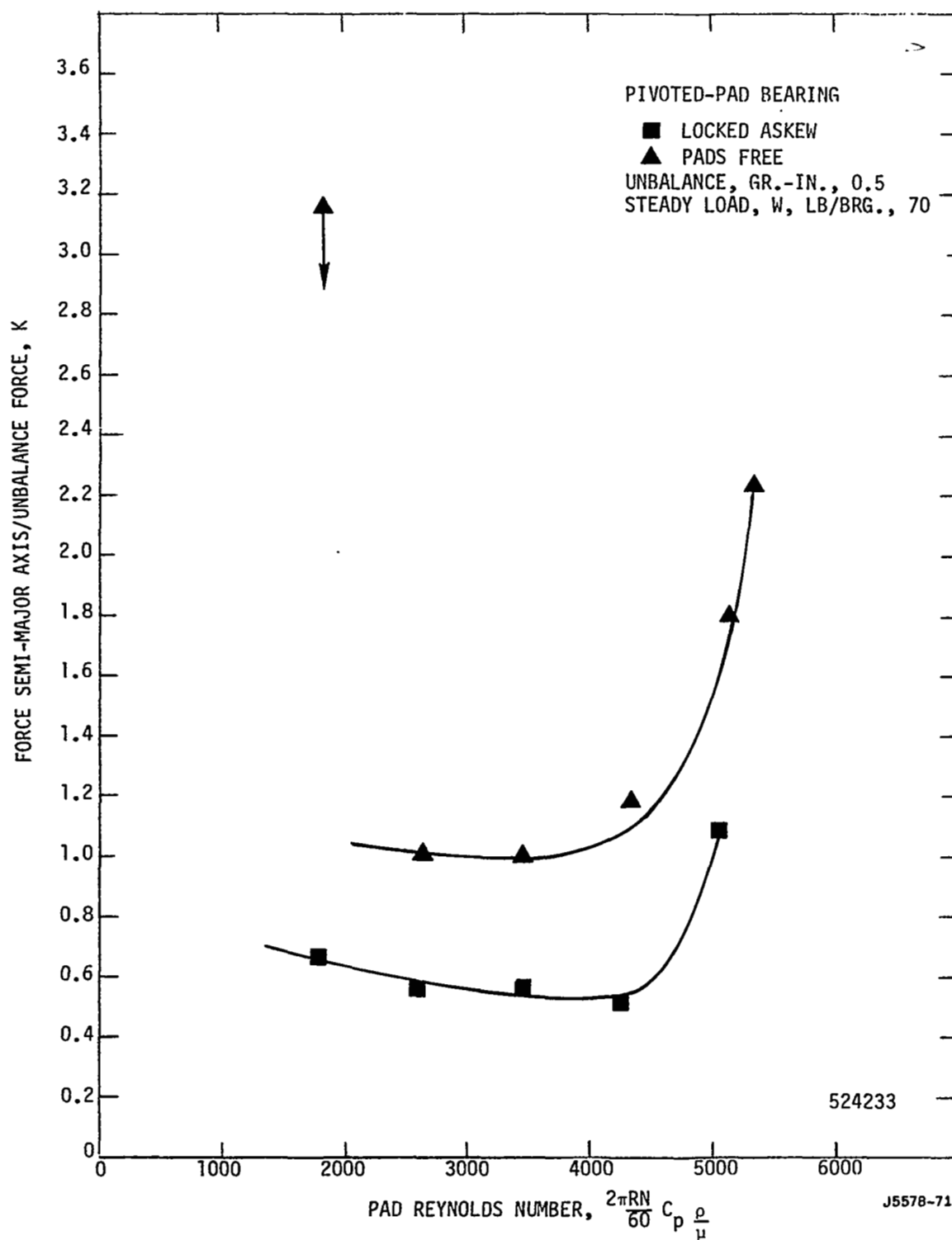Figure 75. The Effect of One Pad Locked Askew on the Force Semi-Major Axis – Reynolds Number Variation.

152

In Figure 76 the maximum attainable speeds are plotted as a function of steady load for the case of residual unbalance. Data is shown for all pads free, pads locked symmetrically, and pads locked askew. There is very little difference in the maximum attainable speed (approximately 1000 rpm) between the free pad and the pad-locked-askew data. However, for the pad-locked-symmetrically data it can be seen that a substantial decrease in maximum attainable speed was recorded. Shown in Figure 77 is a comparison of the free- and locked-pad test data for the case of an unbalance of 0.5 gr-in/bearing. Except for one or two data points it is apparent that with the symmetric unbalance there is little difference in the attainable speeds for the pivoted-pad bearings under the conditions of free or locked pads.

5. Discussion of Pivoted-pad Bearing Test Results

It should be stressed that no fractional-frequency whirl was observed in all the testing carried on the pivoted-pad bearings. These bearings attained various speed levels depending upon the steady load, the unbalance, the misalignment and the selective fixture of pads. A rotative speed of 31,000 rpm, which was limited by facility capability, was attained with the pivoted-pad bearing.

As indicated on several charts the measured load capacity of the pivoted-pad bearing exceeded significantly the theoretical values obtained from Reference 1. Similarly, the measured torque was sig-

153
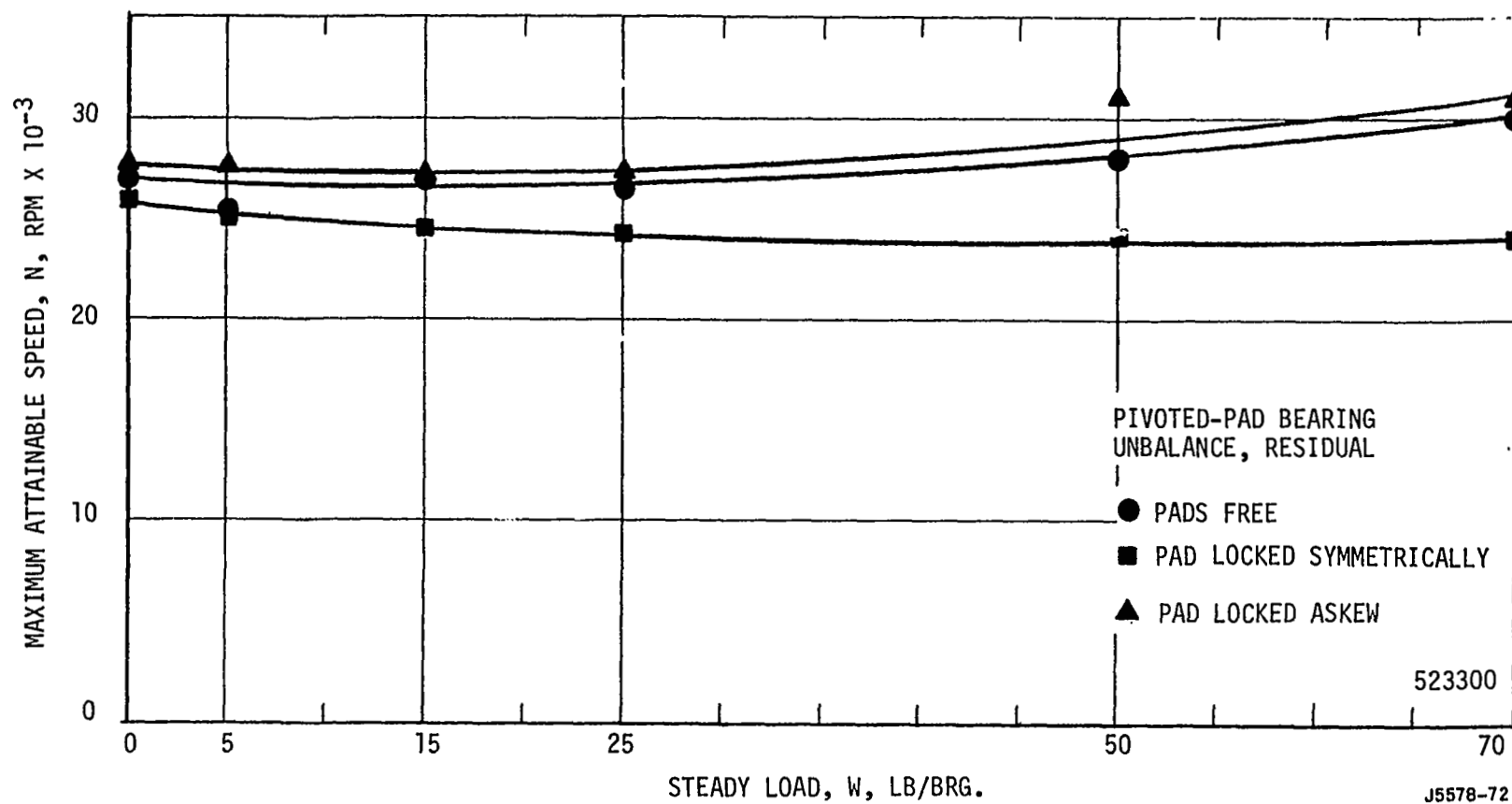
Figure 76. The Effect of One Locked Pad and Steady Load on Maximum Attainable Speed.
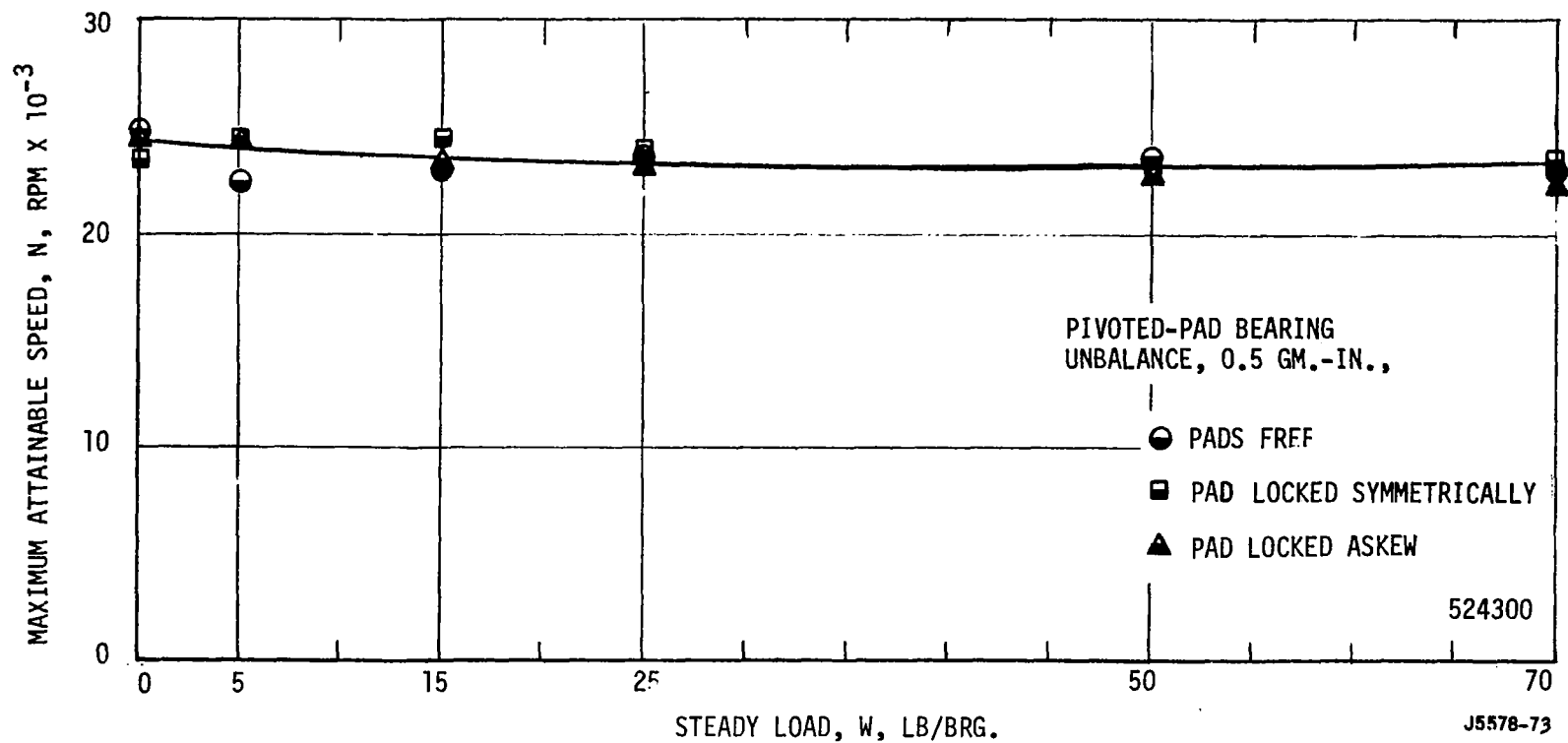
Figure 77. The Effect of One Locked Pad and Steady Load on the Maximum Attainable Speed.

nificantly higher than the theoretical torque. As would be expected, over the range of loads tested, misalignment had little or no effect on bearing load capacity, torque, and orbit size. In addition, these same parameters were unaffected by the locking of one pad, particularly for the case of the pad locked askew, which certainly would be the type of fixture that one would expect more often in actual operation than the case where the pad was locked symmetrically. Misalignment had a minor effect on maximum attainable speed and the case of one pad locked askew did not lower the maximum attainable speed significantly. For the case of one pad locked symmetrically, the maximum attainable speed was lowered from 2,000 to 6,000 rpm depending on the steady load at residual unbalance. Finally, the theoretical rotor response appeared to be conservative by approximately 25 percent.

B. THREE-LOBE BEARING

Shown in Figure 78 is a sketch of the bearing clearance locus and the shaft orbit for the three-lobe bearing. Shown on this sketch are the bearing clearance, the eccentricity of the bearing, the attitude angle, the semi-major axis of the displacement ellipse, and the maximum displacement of the shaft in the bearing. It is apparent from the sketch that the three-lobe bearing was loaded between two pads. The rotation is shown in the diagram to be counterclockwise.
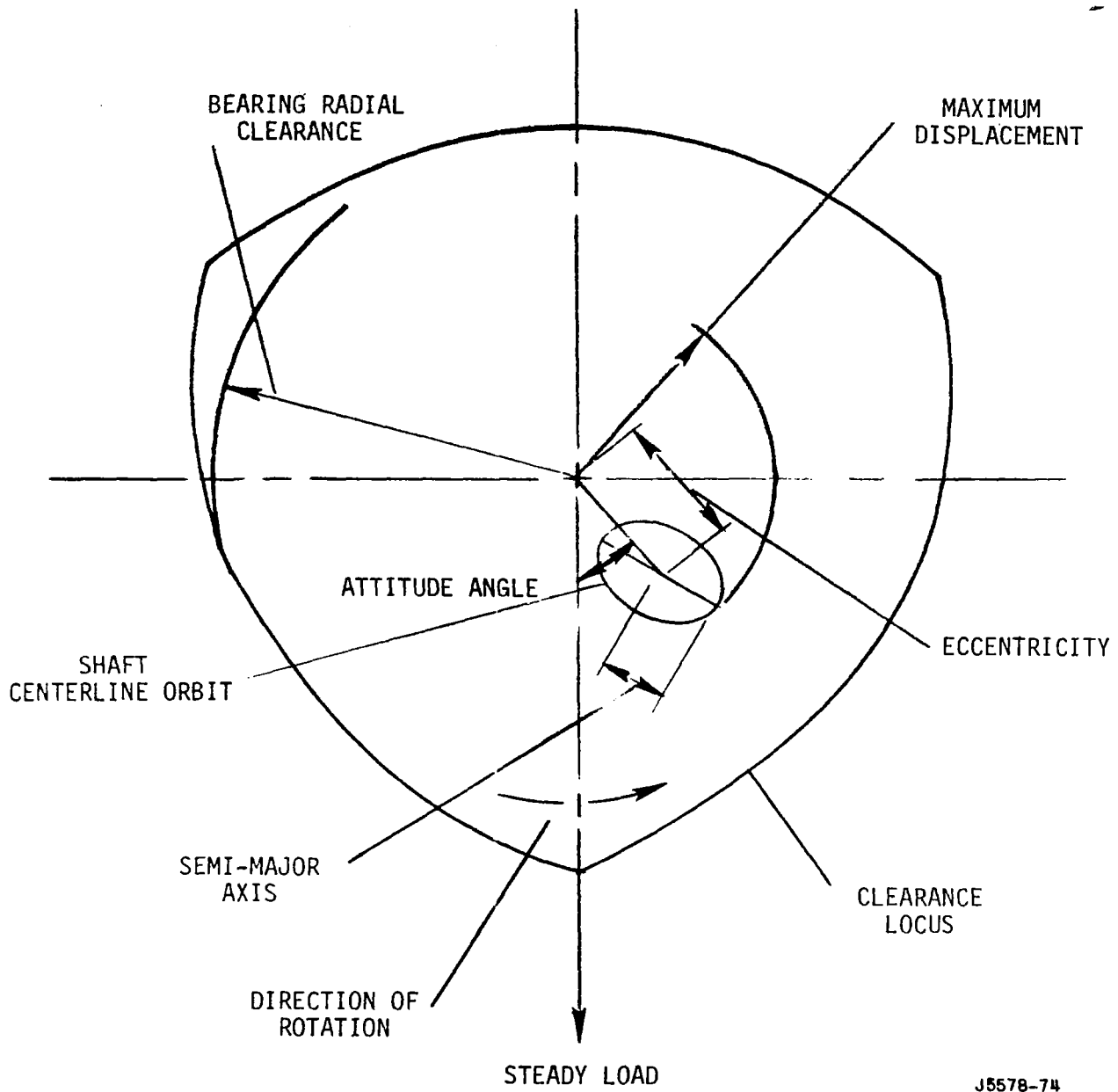
Figure 78. Typical Orbit for a Loaded Three-Lobe Bearing.

BEARING RADIAL
CLEARANCE

MAXIMUM
DISPLACEMENT

ATTITUDE ANGLE

ECCENTRICITY

SHAFT
CENTERLINE ORBIT

SEMI-MAJOR
AXIS

CLEARANCE
LOCUS

DIRECTION OF
ROTATION

STEADY LOAD

J5578-74

157

1. Aligned Test Data

Shown in Figure 79 is the variation of bearing eccentricity ratio with Sommerfeld number for three levels of steady load, 25, 50 and 70 lbs/bearing. The data was obtained for the case of residual unbalance. These data appear to lie on one curve and have the expected trend, namely, a decreasing eccentricity ratio as a Sommerfeld number increases. Shown in Figure 80 is the variation of attitude angle with bearing eccentricity ratio for the same set of conditions. In this plot it is possible to show approximate lines of constant load. The general level of attitude angle is higher for the three-lobe bearing than it was for the pivoted-pad bearing. Shown in Figure 81 is the variation of the non-dimensional torque with the reciprocal Sommerfeld number. The data is shown for the Reynolds numbers of 2906 and 5300. It is seen that the Reynolds number has little effect on the torque over the range tested. Shown in Figure 82 is the variation of torque against reciprocal Sommerfeld number and the comparison is made between three levels of unbalance, including residual unbalance. The data was obtained at approximately 8,000 rpm. The data indicates little effect of the unbalance on the non-dimensional torque.

Shown in Figure 83 is the variation of the ratio of the displacement semi-major axis to the displacement of the center of gravity of the shaft against the pad Reynolds number. The data indicate a slightly larger orbit size for the zero load case. Apparently at the steady load of 25 lb/bearing the bearing stiffness is increased, resulting in a somewhat smaller orbit size. Shown in Figure 84 is a similar plot is which the two levels of un-

158
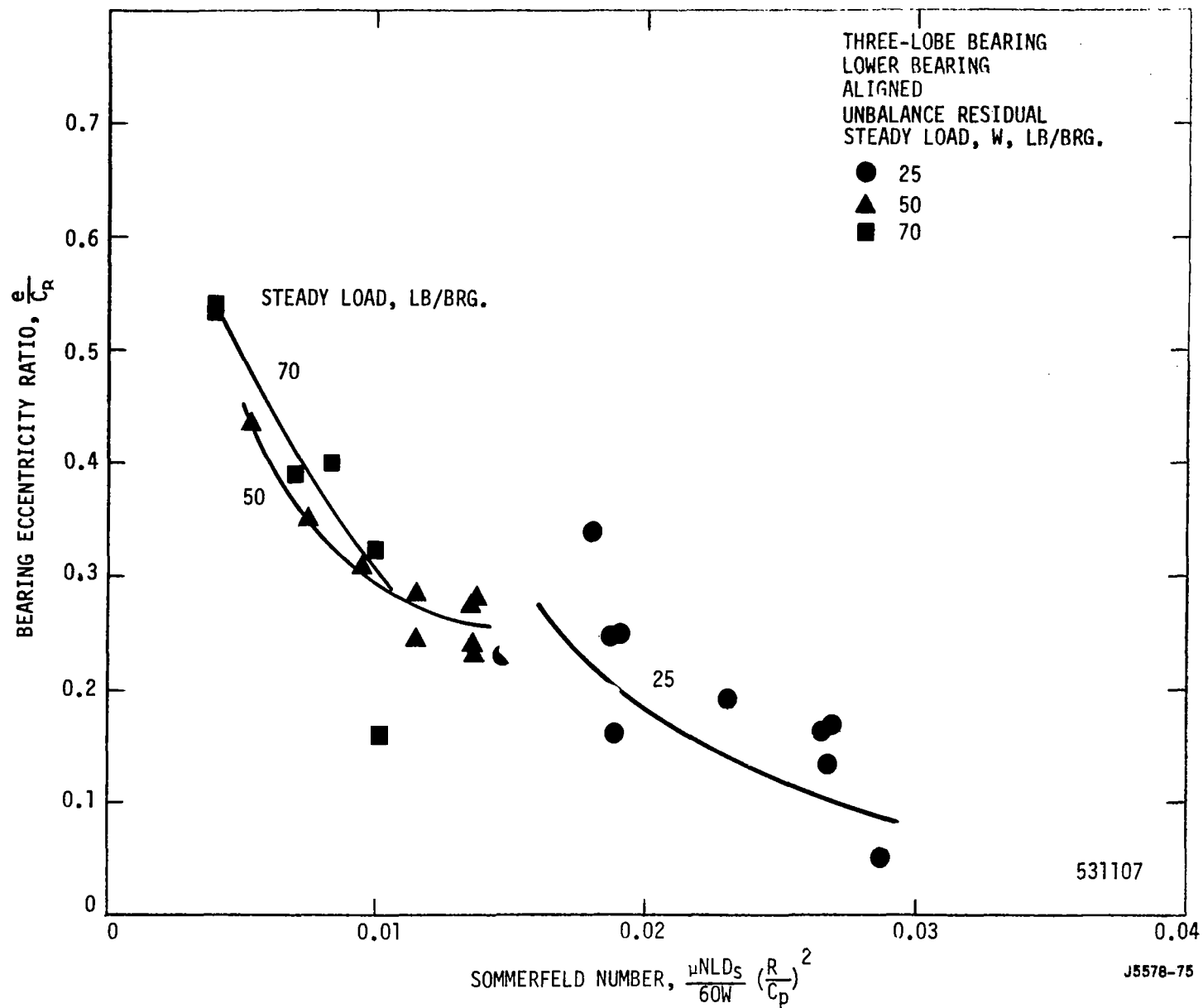
Figure 79. Variation of Eccentricity Ratio with Sommerfeld Number and
Steady Load.
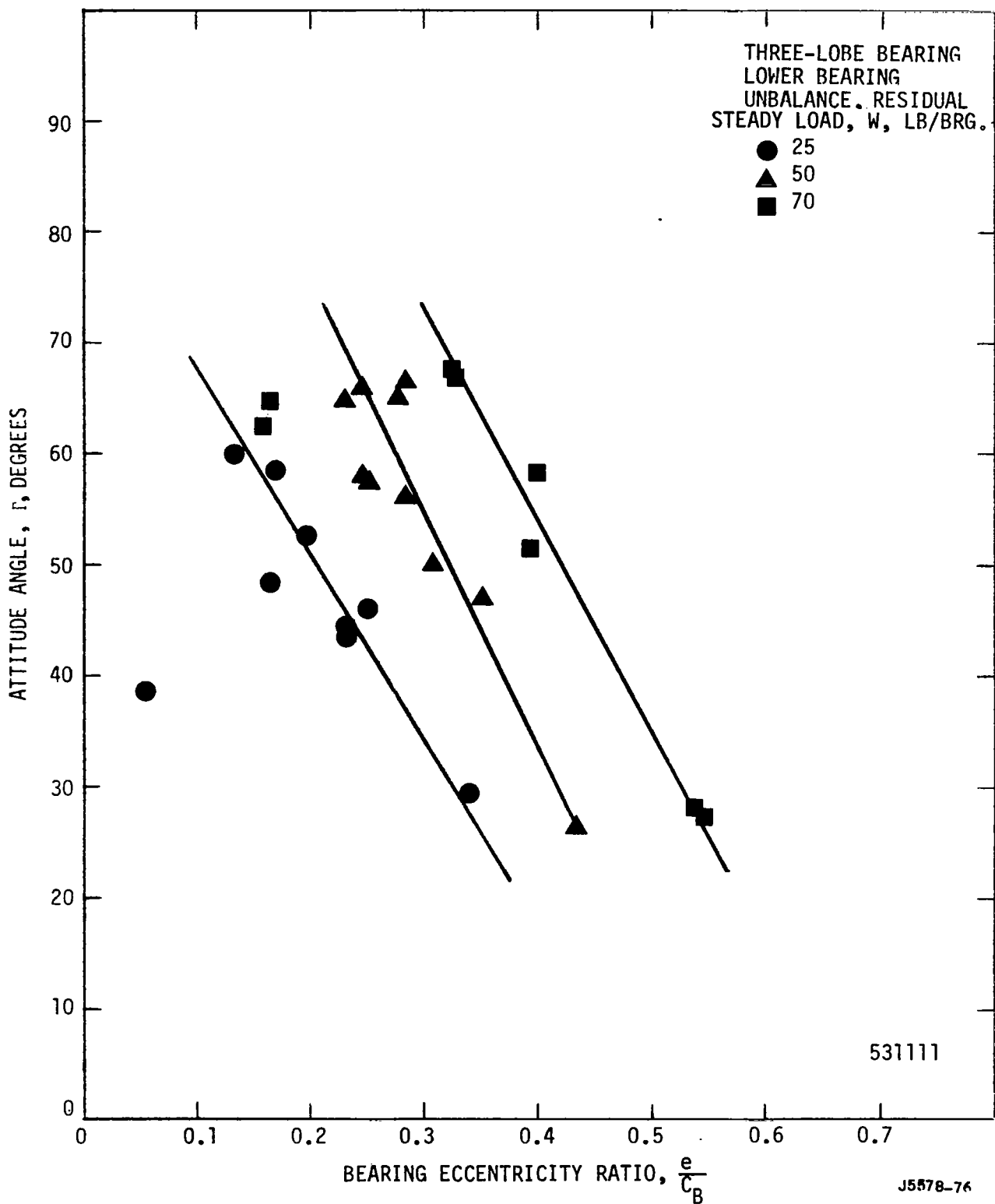
Figure 80.   Variation of Attitude Angle with Eccentricity Ratio and Steady
Load.
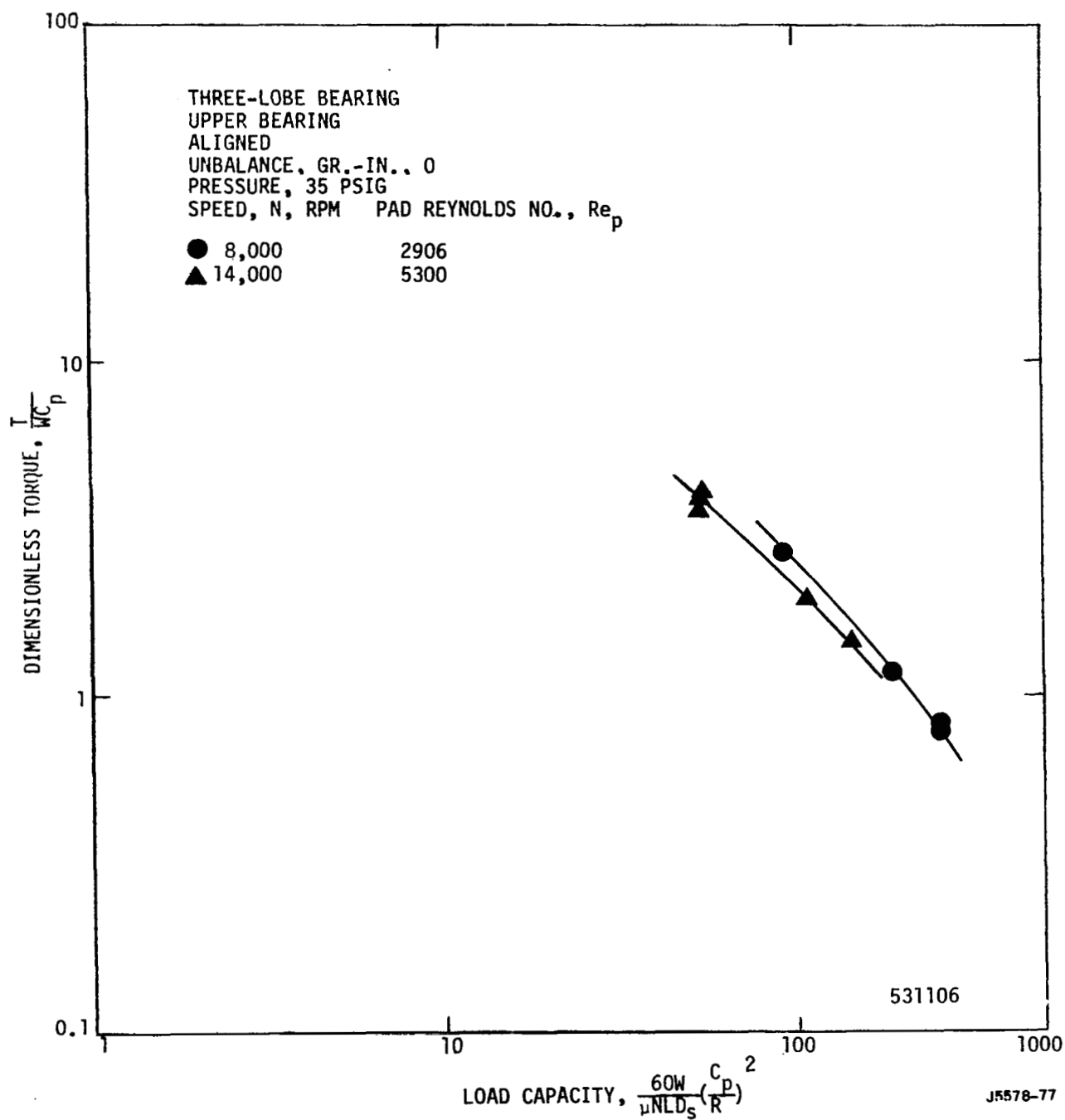
Figure 81. Variation of Dimensionless Torque with Load Capacity and Reynolds Number.
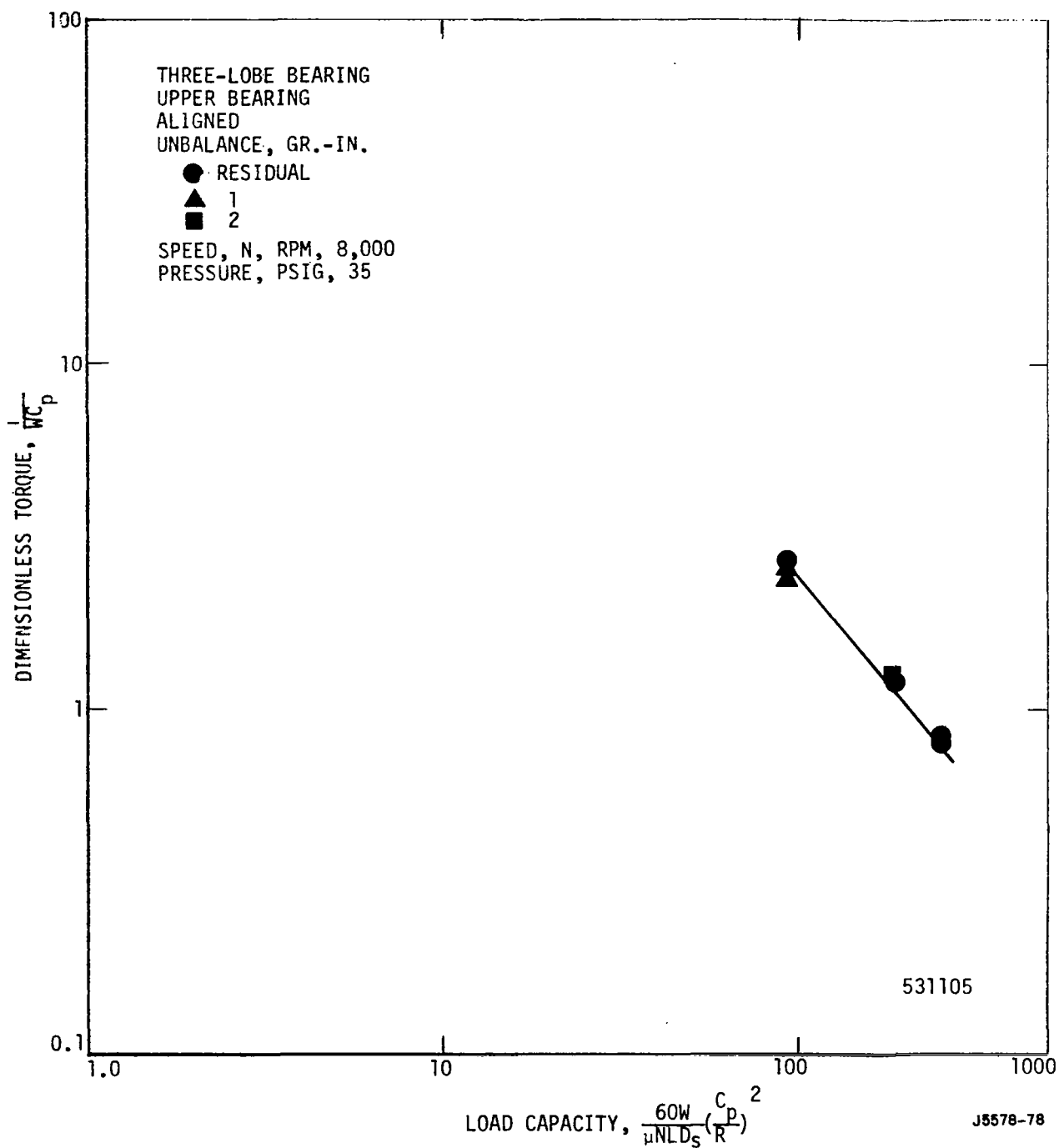
Figure 82. Variation of Dimensionless Torque with Load Capacity and Unbalance.
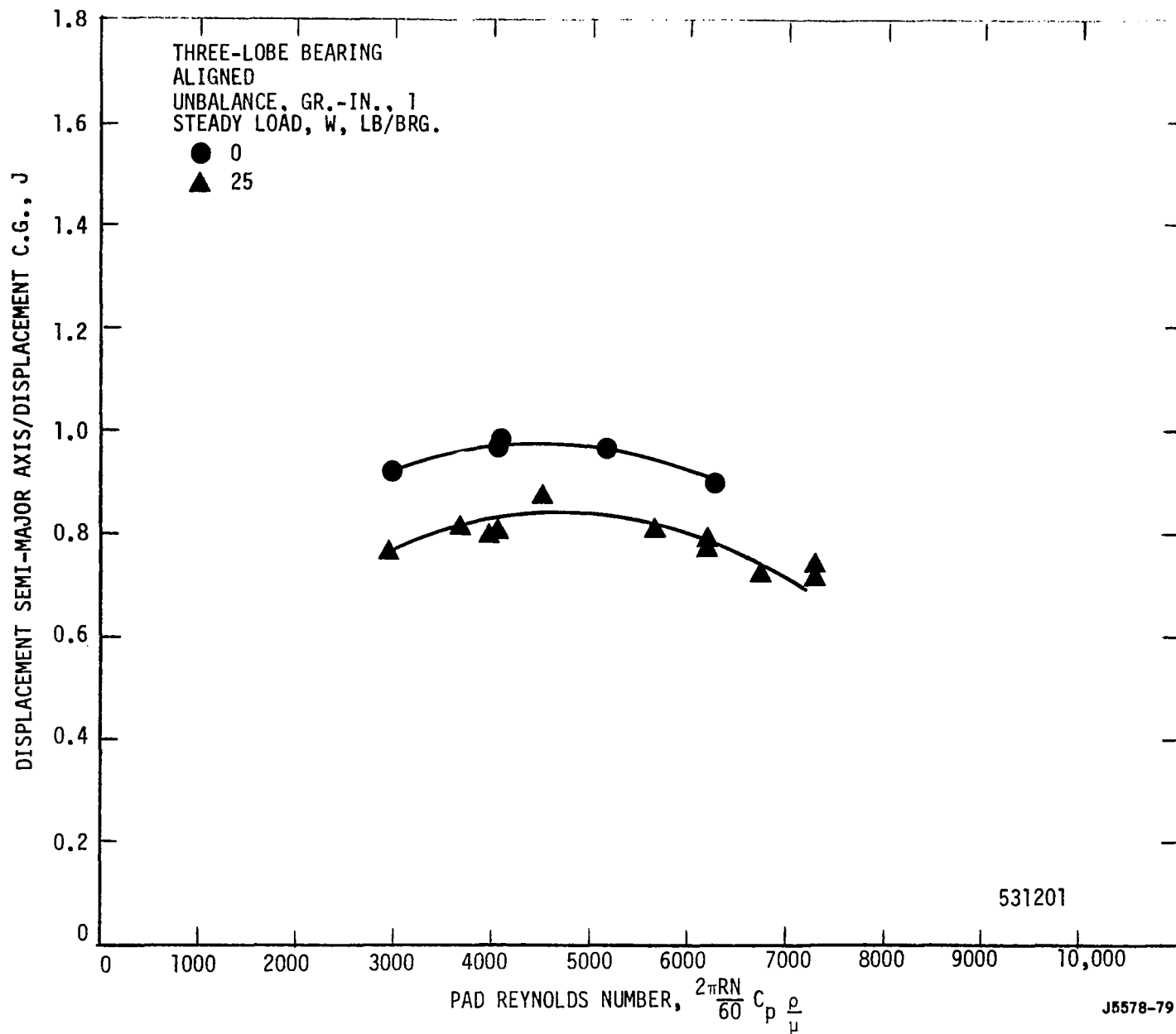
Figure 83. Variation of Displacement Semi-Major Axis with Reynolds Number and Steady Load.

163

J5578-79

531201
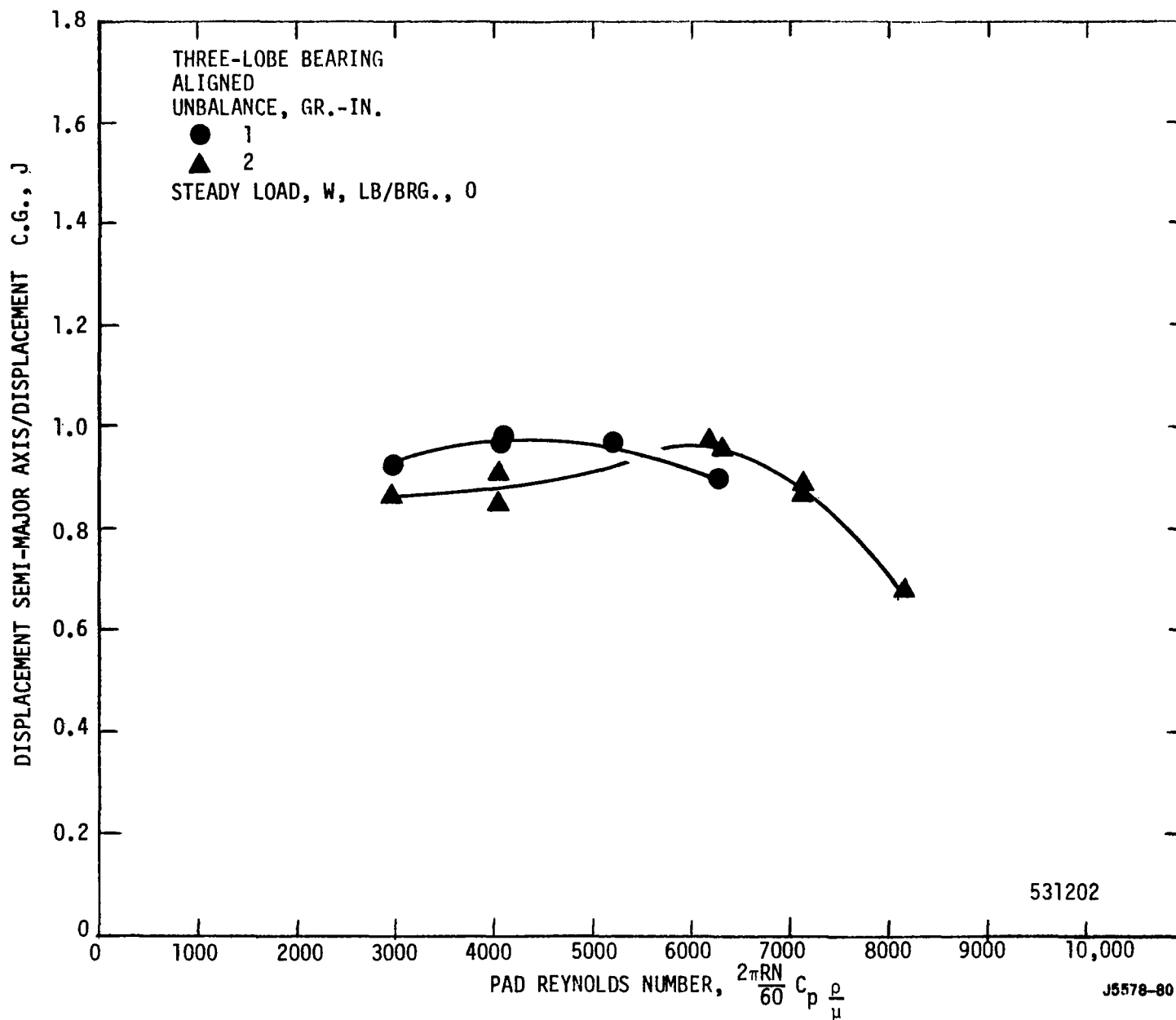
Figure 84.   Variation of Displacement Semi-Major Axis with Reynolds Number
and Unbalance.

balance are compared. The steady load in this case is zero. It is seen that

by normalizing with the displacement of the center of gravity the data nearly

lie on one curve. Shown in Figure 85 is the variation of the ratio of the

force semi-major axis to unbalance force as a function of pad Reynolds number.

Again the loads of zero and 25 lbs./bearing are shown. Little difference in

the measured force is exhibited by this figure. Shown in Figure 86 is another

plot of force versus pad Reynolds number. In this instance two levels of

unbalance are compared. Here it is seen that for the higher level of un-

balance the measured forces are slightly greater than for the case where the

unbalance is less. Shown in Figure 87 is the variation of the incipient

instability speed as a function of steady load for residual unbalance. The

incipient instability speed may be defined as that speed at which the bearing

first experiences fractional-frequency whirl. As the steady load increases,

the incipient instability speed appears to increase slightly from the 20,000

rpm attained at a steady load of zero. Shown in Figure 88 is the variation

of the incipient instability speed with lubricant pressure. This plot is for

a steady load of zero and the results for several levels of unbalance are

compared. It can be seen from the plot that some significant gains in

incipient instability speed are attained by increasing the lubricant pressure.

Under this mode of operation the bearing is operating similar to a hybrid

bearing. It was also found that in the testing of the three-lobe bearing

that it was easier to stabilize the bearing with lubricant pressure than it

was with steady load.
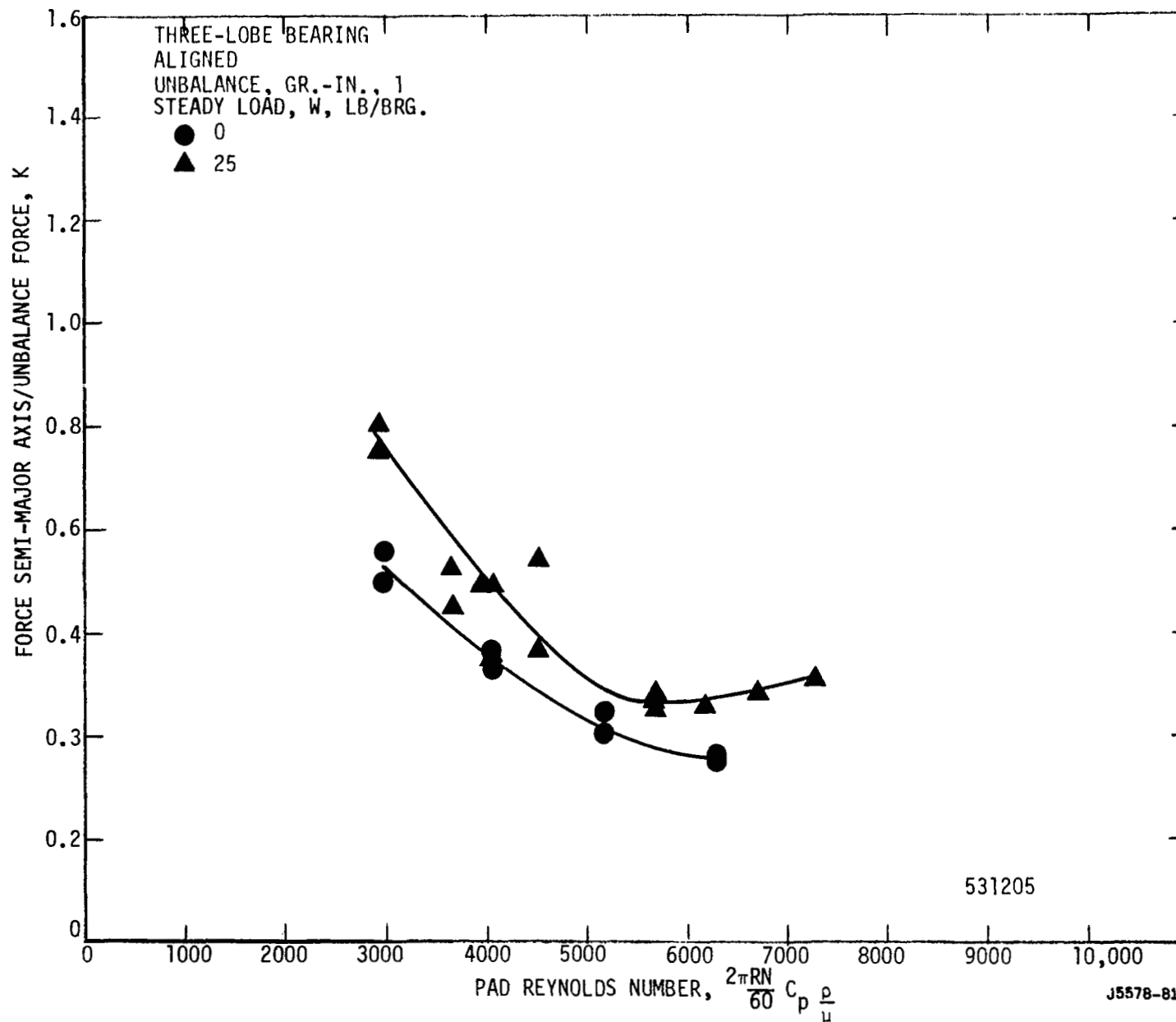
Figure 85. Variation of Force Semi-Major Axis with Reynolds Number and
Steady Load.
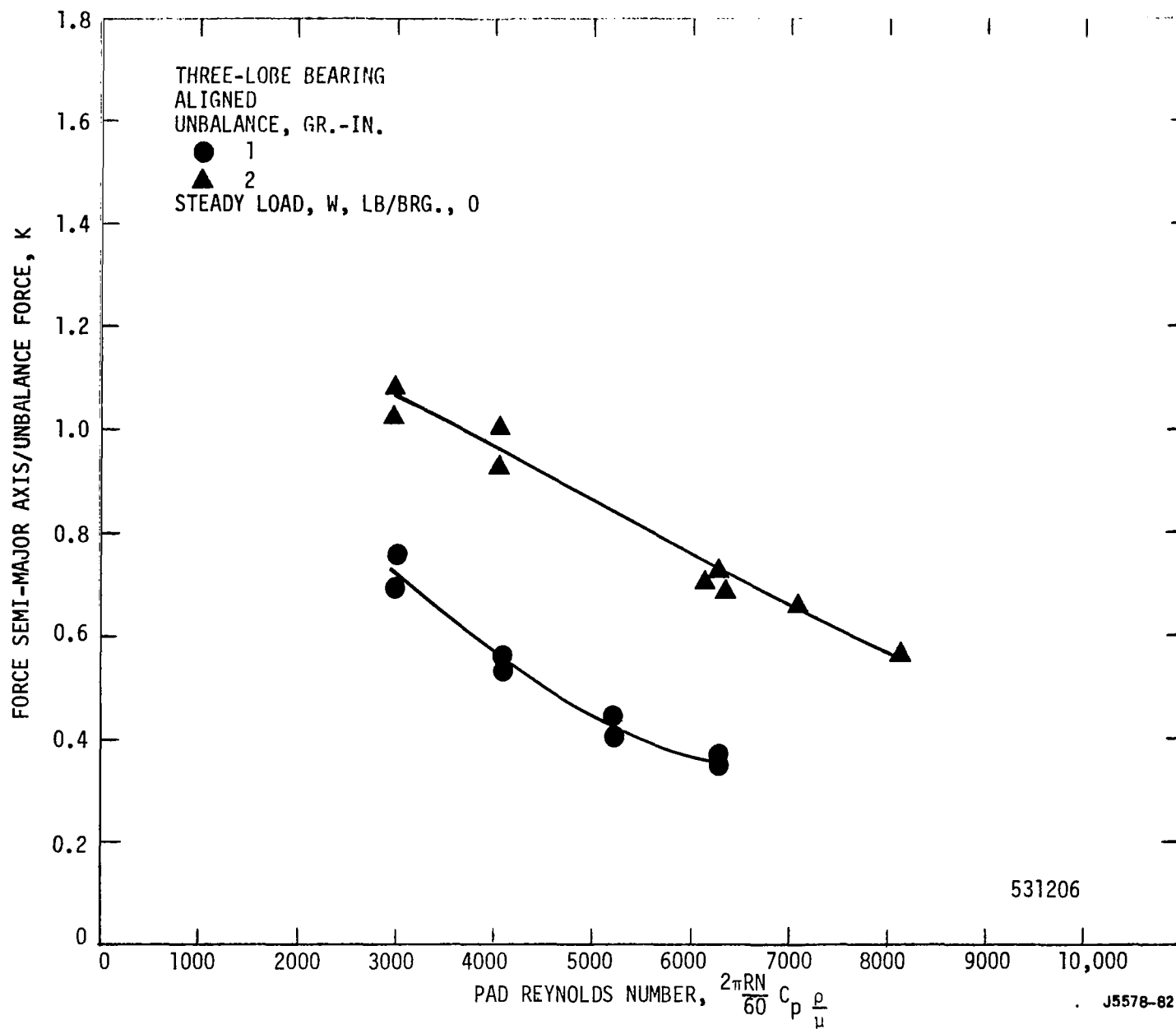
Figure 86. Variation of Force Semi-Major Axis with Reynolds Number and Unbalance.
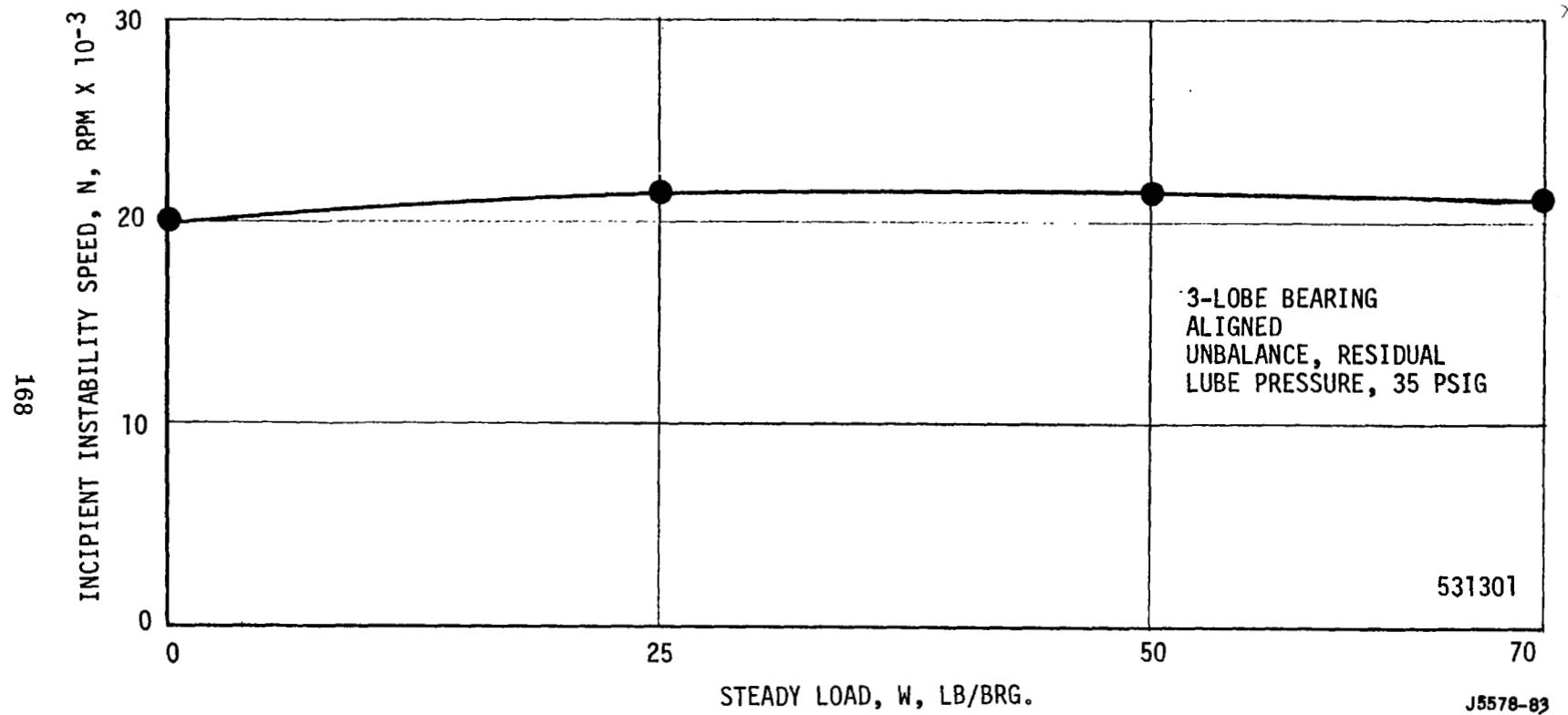
Figure 87. Variation of Incipient Instability Speed with Steady Load.
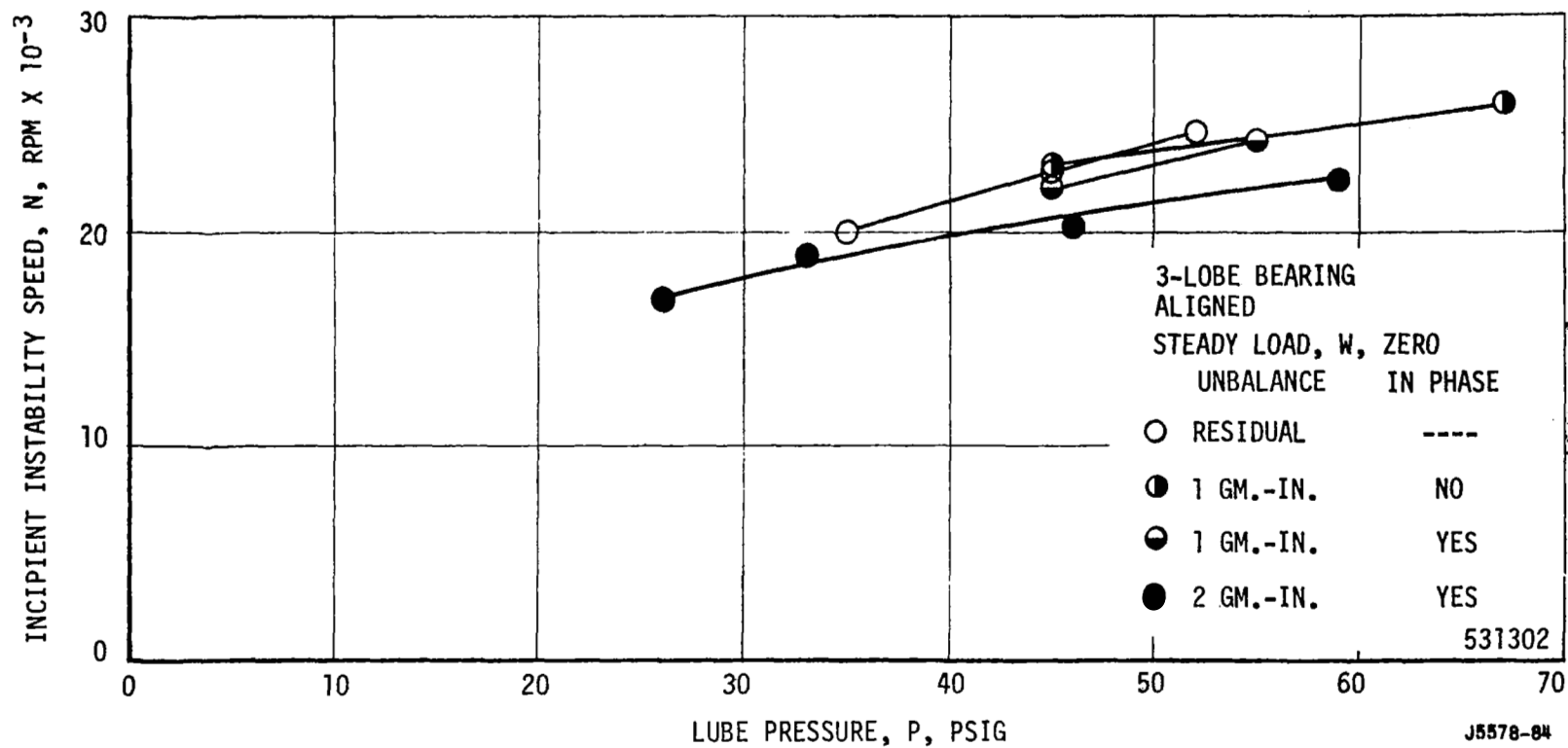
Figure 88. Variation of Incipient Instability Speed with Lubricant Pressure and Unbalance。

2. Effect of Misalignment

Figure 56 which was presented previously for the pivoted-pad bearing also applies to the misalignment of the three-lobe bearing.

Shown in Figure 89 is the variation of bearing eccentricity ratio with Sommerfeld number. These data are for residual unbalance and a steady load of 70 lbs/bearing. It can be seen that the misalignment has only a slight effect on the load capacity of the three-lobe bearing. Shown in Figure 90 is the variation of attitude angle with bearing eccentricity ratio for the same conditions as the previous plot. It can be seen that the misaligned configurations tend to have higher attitude angles for a given bearing eccentricity ratio than the aligned data. This indicates that under misaligned conditions, the bearing is slightly more subject to fractional-frequency whirl. Shown in Figure 91 is the variation of non-dimensional torque with the load capacity for a speed of 14,000 rpm and residual unbalance. It can be seen that misalignment had little or no effect on the bearing torque. A similar plot at a side load of 50 lbs/bearing is shown in Figure 92. Here again, the alignment of the bearing had only a small effect on the measured torque.

Shown in Figure 93 is the variation of the ratio of the displacement semi-major axis to the displacement of the center of gravity of the shaft against pad Reynolds number. This data is for a residual unbalance and a steady load of 50 lbs/bearing. The data indicates a definite increase in orbit size with the misaligned configurations. Shown in Figure 94 is the variation in the ratio of the displacement

170
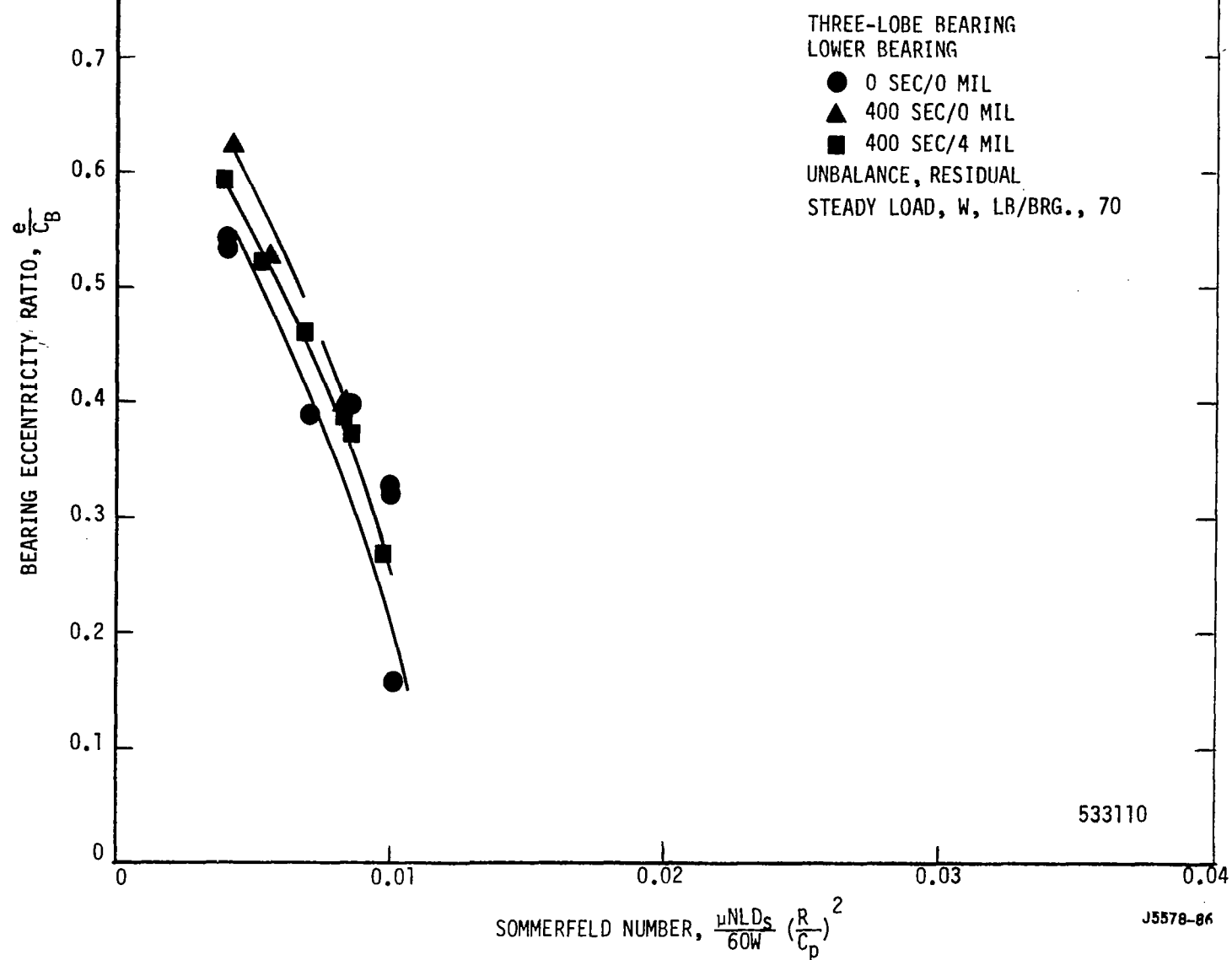
Figure 89. Effect of Misalignment on the Eccentricity Ratio - Sommerfeld Number Variation.
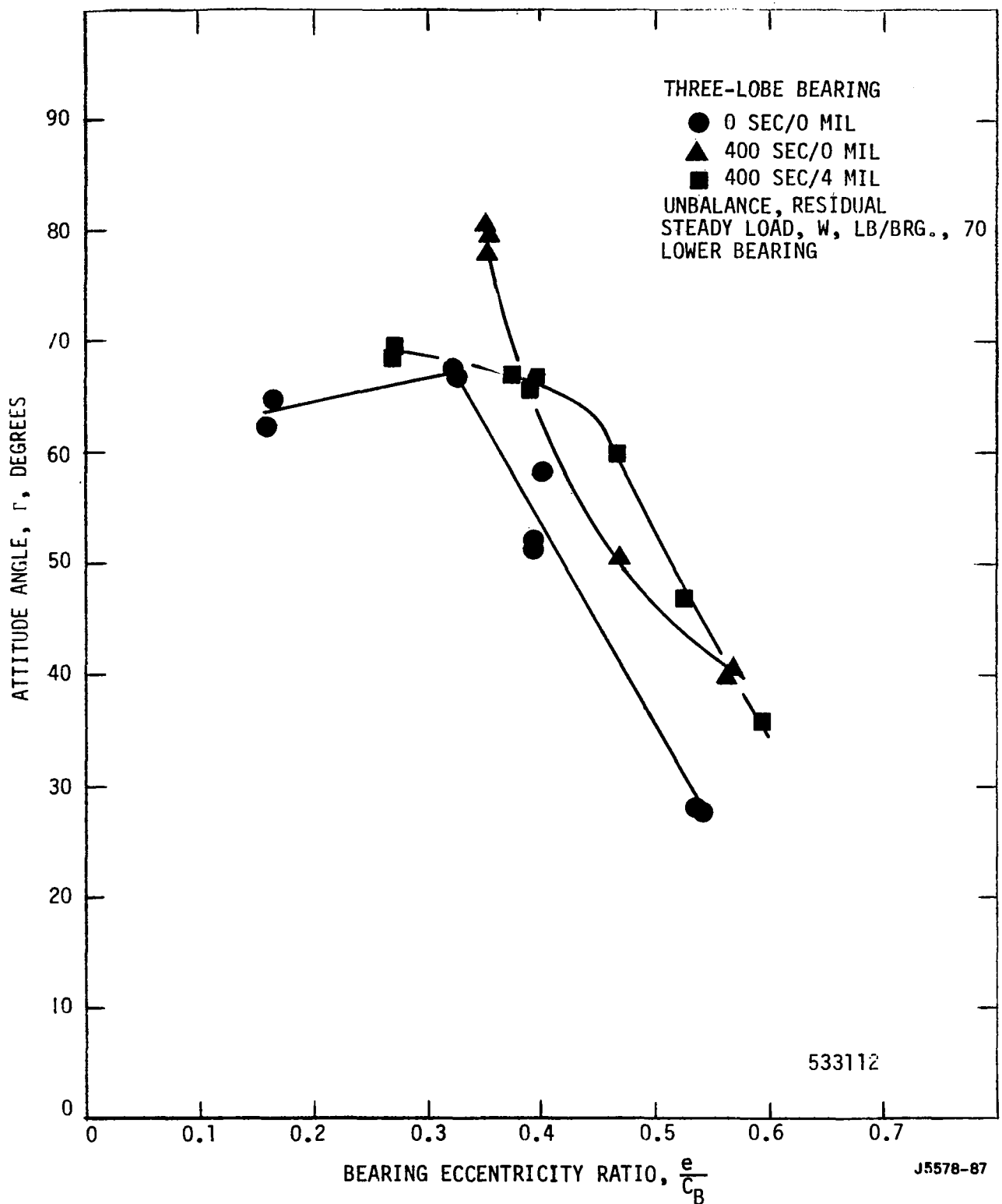
Figure 90. Effect of Misalignment on this Attitude Angle - Eccentricity
Ratio Variation.

172
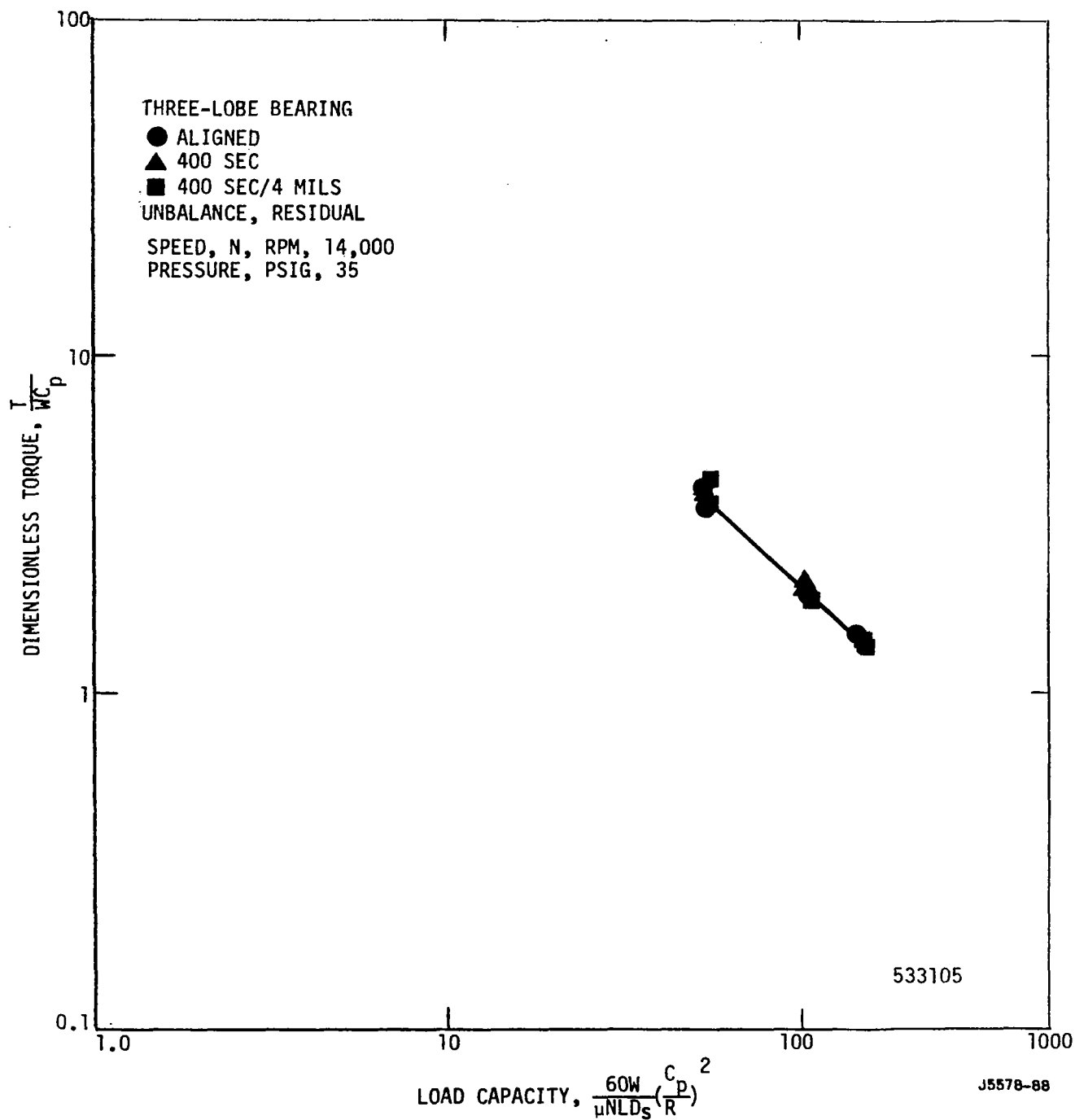
Figure 91. Effect of Misalignment on the Dimensionless Torque – Load Capacity Variation.
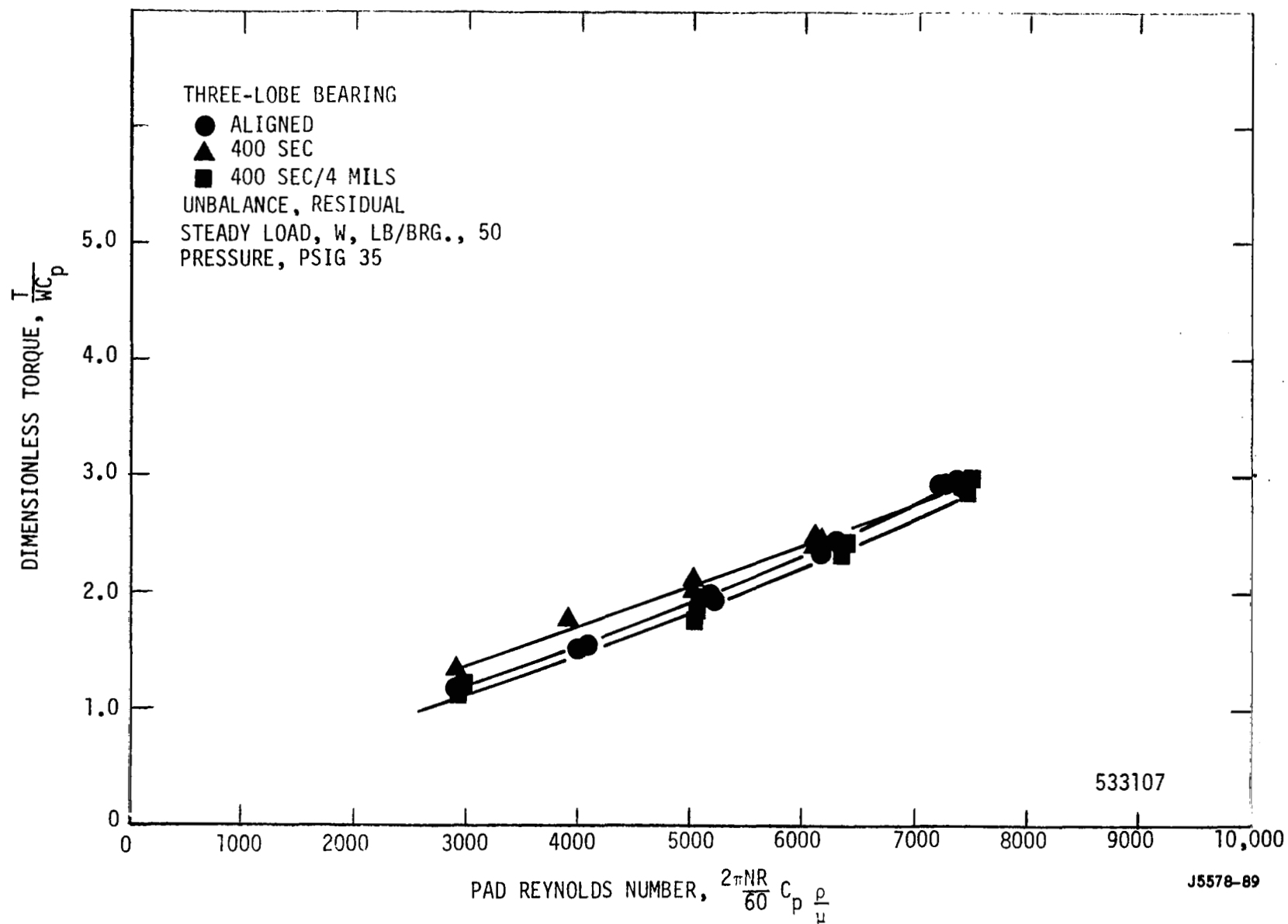
Figure 92. Effect of Misalignment on the Dimensionless Torque – Reynolds Number Variation.

Figure 93. The Effect of Misalignment on the Displacement Semi-Major Axis –
Reynolds Number Variation.
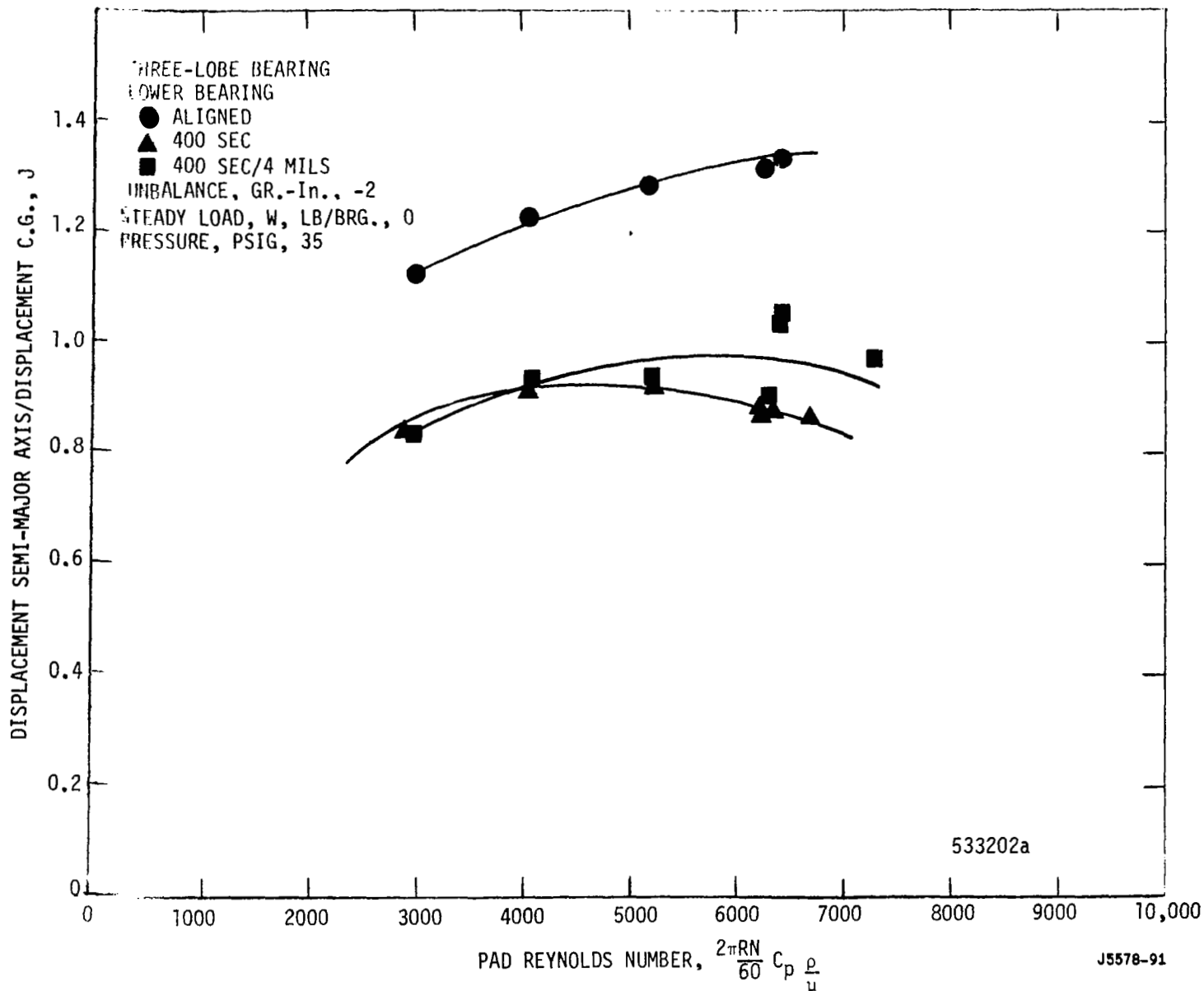
Figure 94. Effect of Misalignment on the Displacement Semi-Major Axis – Reynolds Number Variation.

semi-major axis to the displacement of the center of gravity against pad Reynolds number for the case of an unbalance of 2 gr-in. In this instance the aligned bearing has a significantly larger displacement orbit than both of the misaligned cases. Shown in Figure 95 is the variation of the ratio of the force semi-major axis to the unbalance force against pad Reynolds number for the case of residual unbalance and a steady load of 50 lbs/bearing. It is seen that the measured forces for the aligned case are larger than those for the misaligned cases. Shown in Figure 96 is the variation of ratio of the semi-major axis to the unbalance force against pad Reynolds number for the case of an unbalance of 2 gr-in and a steady load of zero. In this instance the measured forces are the same for the aligned and misaligned cases within the scatter of the data.

Shown in Figure 97 is the variation of the incipient instability speed with steady load for the case of residual unbalance and for several levels of misalignment. It is seen that within at the most 3,000 rpm, the speeds of the bearings for the three configurations are the the same. Shown in Figure 98 is the variation in incipient instability speed with lube pressure. This is for the case of anti-symmetric unbalance of 1 gr-in. Here again, the marked effect of lubricant pressure on the increasing incipient instability speed is seen but the level of misalignment appears to have little or no effect.

177
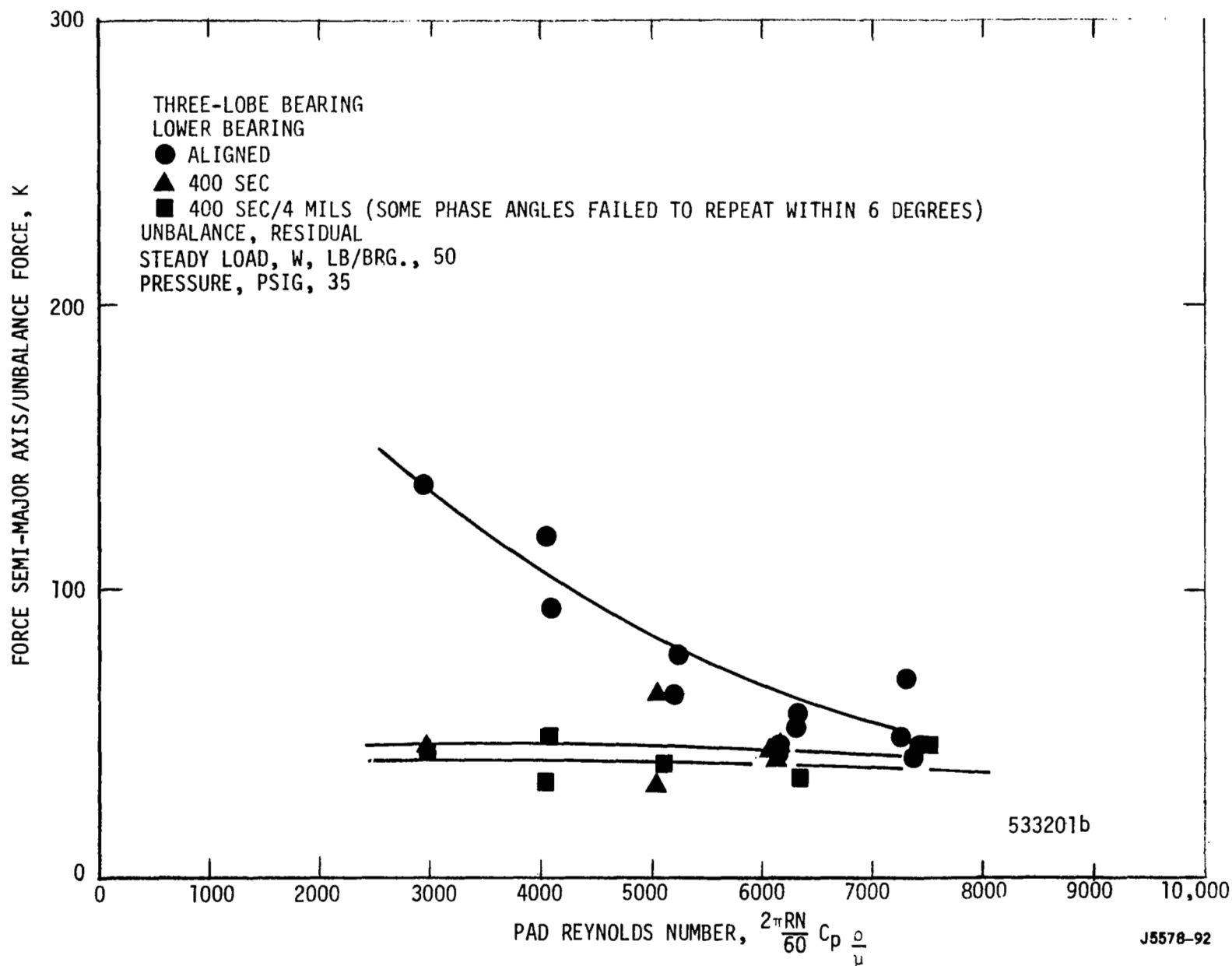
Figure 95. Effect of Misalignment on the Force Semi-Major Axis - Reynolds Number Variation.
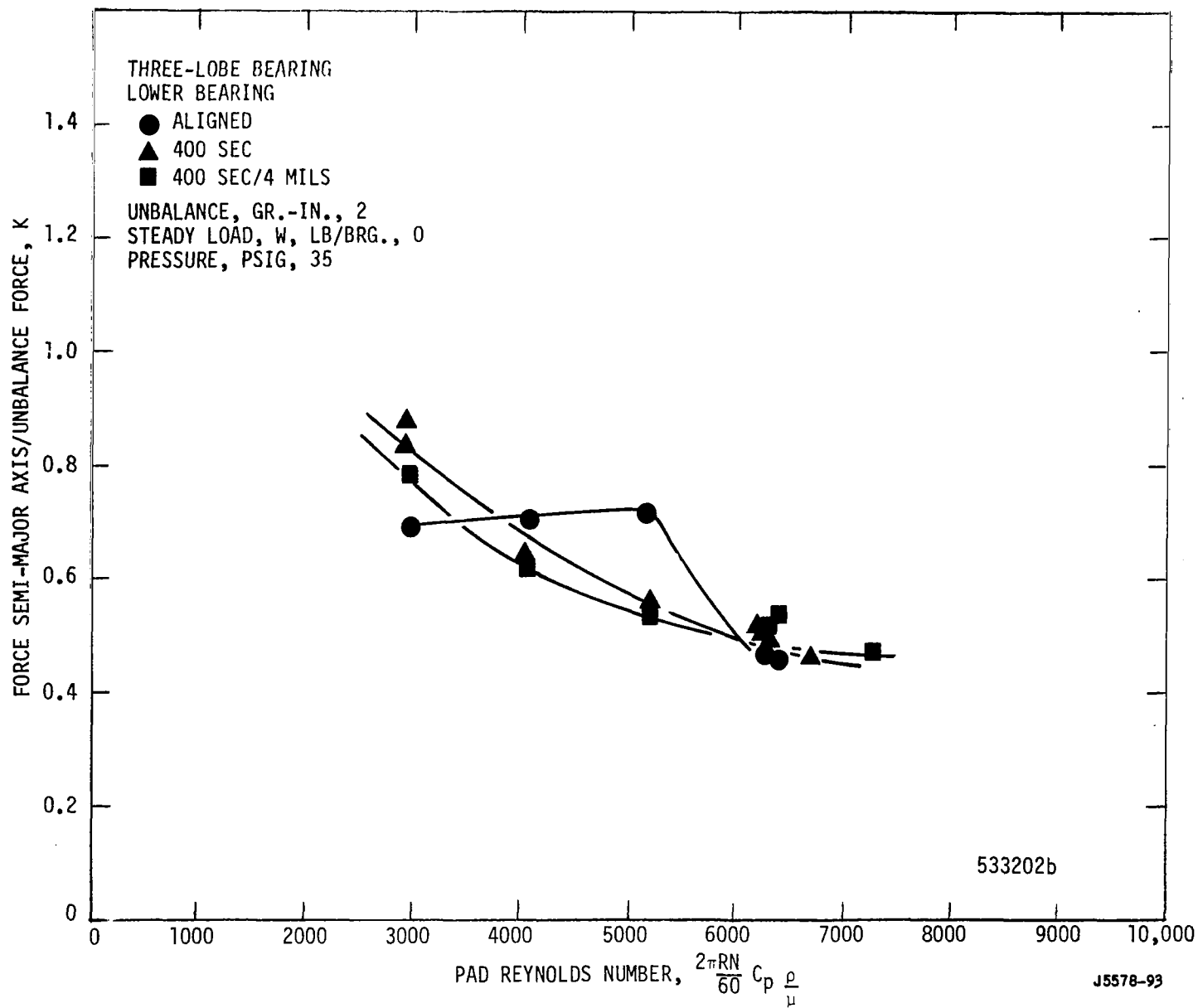
Figure 96. Effect of the Misalignment on the Force Semi-Major Axis - Reynolds Number Variation.

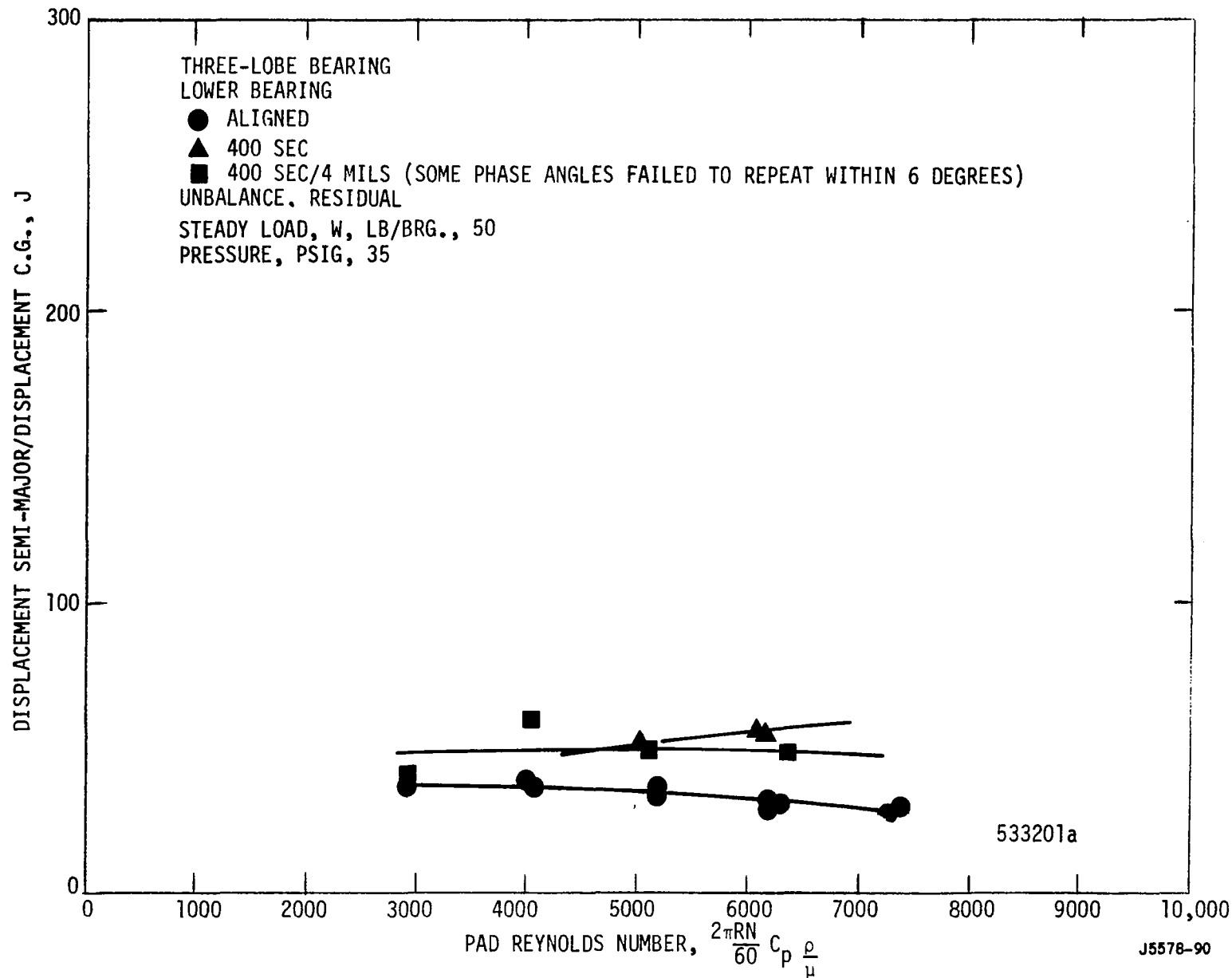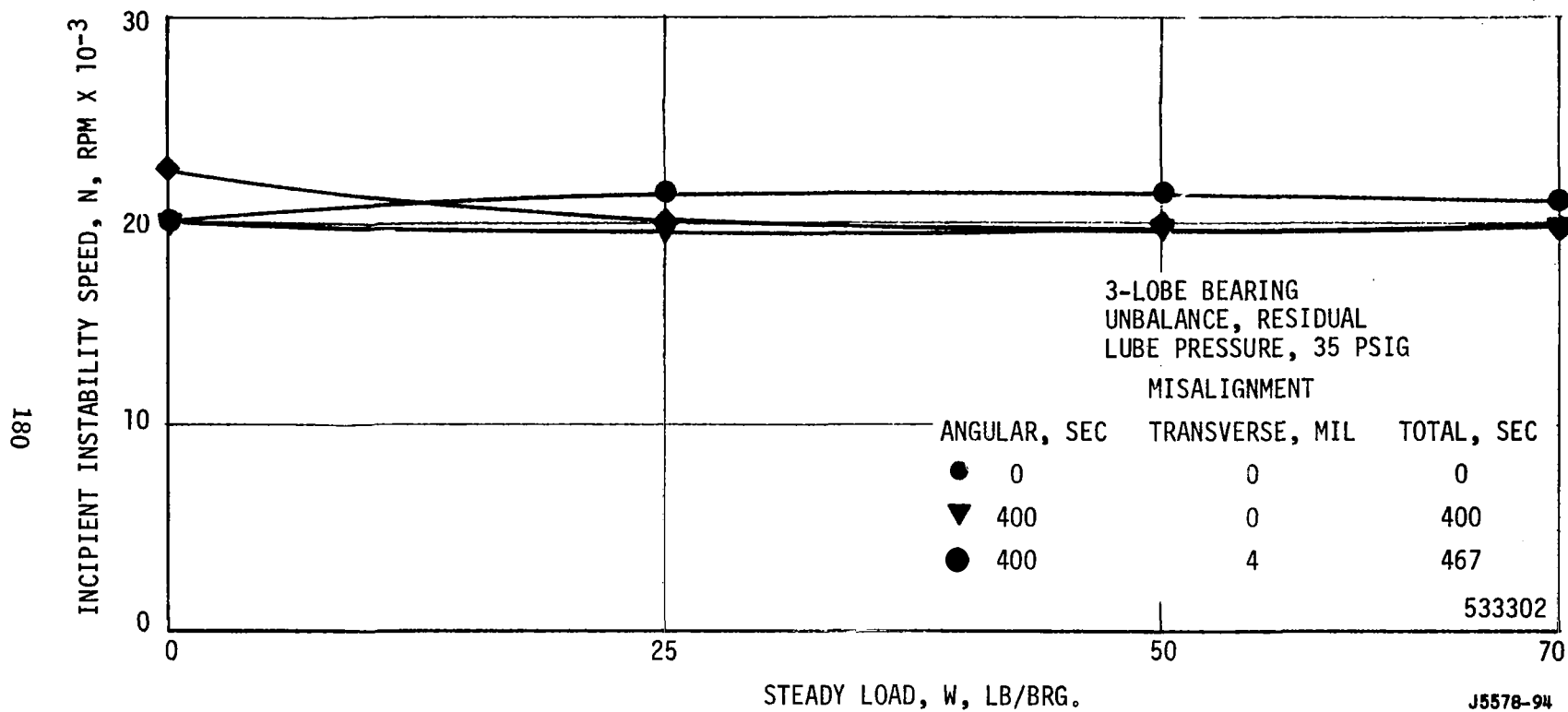Figure 97. Effect of Misalignment on the Incipient Instability Speed-Safety Load Variation.
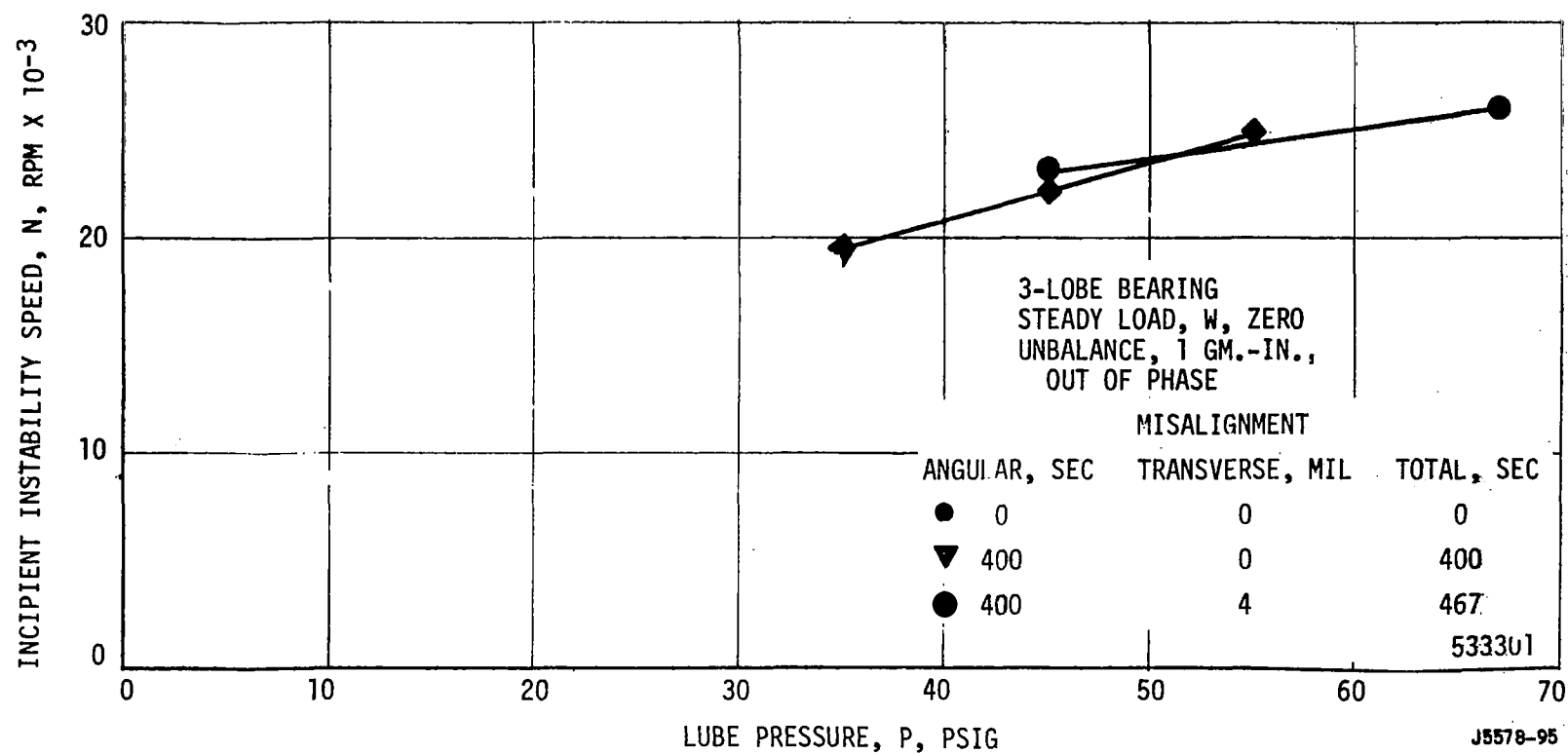
Figure 98. Effect of Misalignment on the Incipient Instability Speed-
Lubricant Pressure Variation.

3. Discussion of the Three-Lobe Bearing Results

The three-lobe bearing in general was free of fractional-frequency whirl in the range from 20,000 to 27,000 rpm, depending on the lube pressure utilized. It was significant that the increase of the lube pressure from 35 to 67 psig was significantly more effective in extending the stability range of the three-lobe bearing than increasing the steady load from zero to 70 lbs/bearing (the maximum attainable with the test facility). The misalignment of the three-lobe bearing caused approximately a 20 percent decrease in load capacity. It also decreased the orbit size by about 27 percent, the measured force by 30 percent, and the stable speed by approximately 3,000 rpm.

C. COMPARISON OF THE PIVOTED-PAD AND THREE-LOBE BEARING TEST DATA

The results shown in Figure 99 are for both the pivoted-pad and three-lobe bearings at a Reynolds number of between 2653 and 2933. Plotted is the load parameter (the ratio of pad Reynolds number to Sommerfeld number) against the bearing eccentricity ratio. As indicated on the ordinate scale the clearance ratio for the bearing appears to the third power in the lower parameter. In this clearance ratio the machined clearance is used as the characteristic dimension for both the pivoted-pad and the three-lobe bearing. Results of the data indicate that at a nearly fixed value of Reynolds number the three-lobe bearing is an extension of the data of the pivoted-pad bearing. This means that for the same diameter, length, speed, den-

182

The y-axis label reads: LOAD PARAMETER, $\frac{\pi \rho D_s}{\mu^2 L} \left(\frac{C_p}{R}\right)^3 W$

The x-axis label reads: BEARING ECCENTRICITY RATIO, $\frac{e}{C_B}$

Legend:
▲ PIVOTED-PAD BEARING
11,600, N, RPM
UNBALANCE, GR.-IN.,
0.5, OUT OF PHASE
PAD REYNOLDS NO., Re_p, 2653

■ THREE-LOBE BEARING
8,000, N, RPM
UNBALANCE, RESIDUAL
PAD REYNOLDS NO., Re_p, 2933

541004

J5578-96
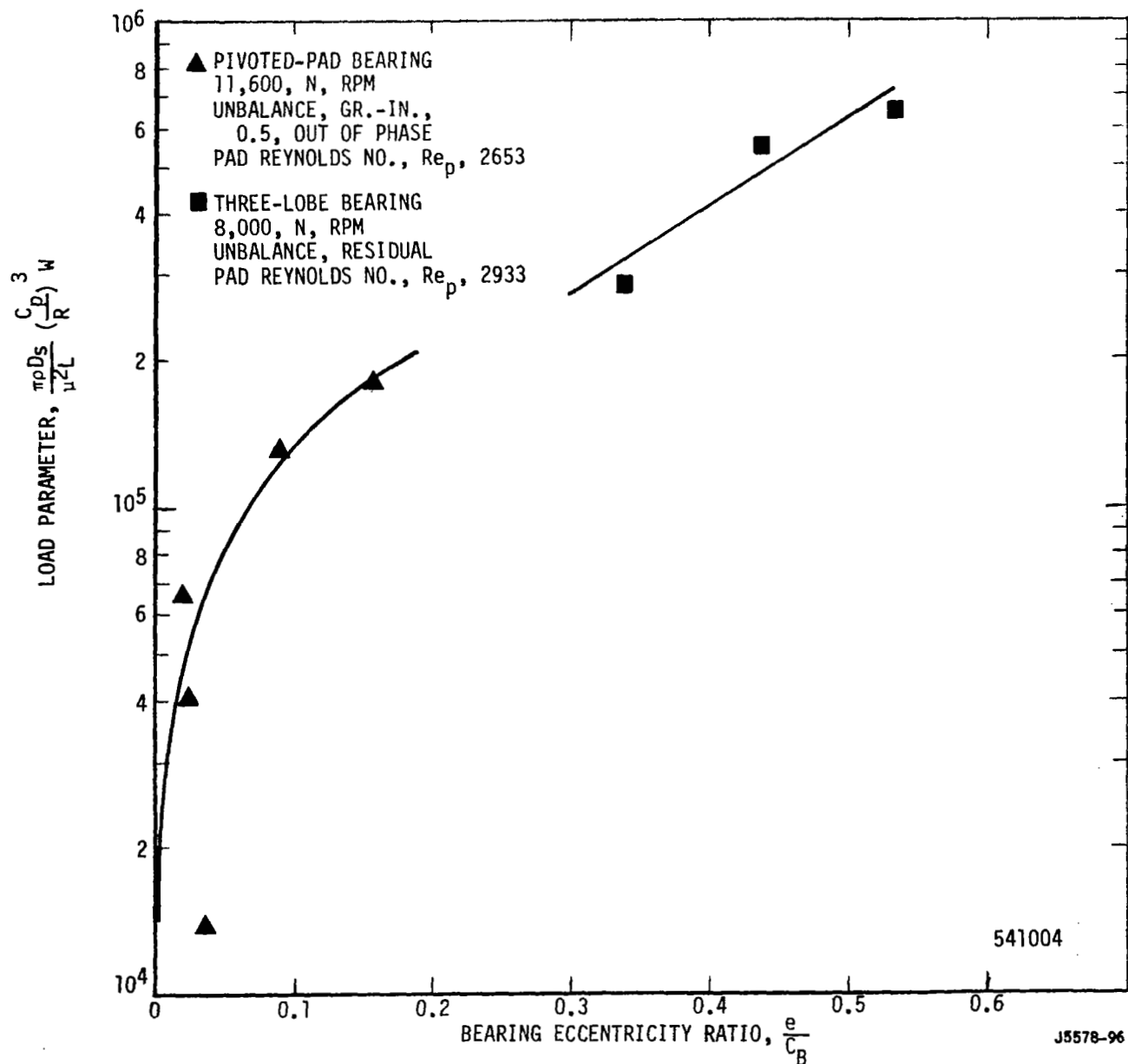
Figure 99. Comparison of Load Parameter Variations for Pivoted-Pad and
Three-Lobe Bearings at Low Reynolds Number.

sity, viscosity, and clearance, the two bearings will have the same eccentricity ratio for a given steady load. Figure 100 is a similar plot at a higher Reynolds number, namely 5125 for the pivoted-pad bearing and 5135 for the three-lobe bearing. Here again it is seen that the three-lobe bearing data is merely a continuation of the pivoted-pad data and a very smooth curve.

Shown in Figure 101 is the variation of non-dimensional torque with reciprocal Sommerfeld number. Reciprocal Sommerfeld number has the clearance ratio in it to the second power and therefore a valid comparison can be made between the two bearings at approximately the same Reynolds number, 5125. It is seen that the pivoted-pad bearing has a torque that is about 2.3 times the torque of the three-lobe bearing for the same conditions.

Shown in Figure 102 is the ratio of the displacement semi-major axis to the bearing clearance (assembled clearance) with pad Reynolds number. It is seen that by the normalizing of the displacement semi-major axes for the two bearings by the bearing clearance the displacement orbit of the three-lobe bearing is approximately 25 to 35 percent larger than for the pivoted-pad bearing. Shown in Figure 103 is the variation of the ratio of the force semi-major axis to the bearing unbalance against the pad Reynolds number. Whereas the pivoted-pad bearing has a force ratio just over unity, the force ratio for the three-lobe bearing is considerably lower than unity and decreases as the pad Reynolds number increases.

184
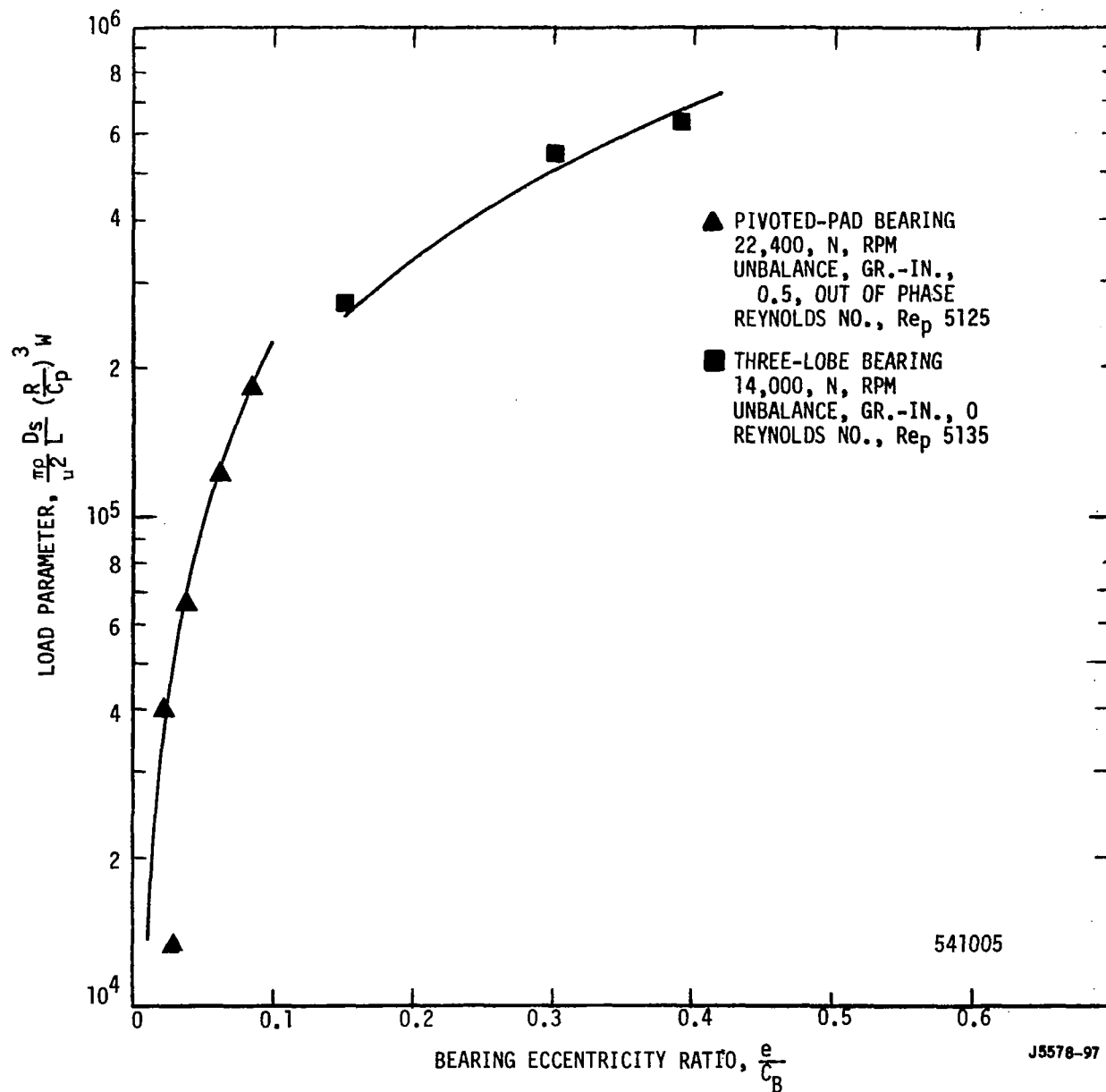
Figure 100. Comparison of Load Parameter Variations for Pivoted-Pad and Three-Lobe Bearings at High Reynolds Number.
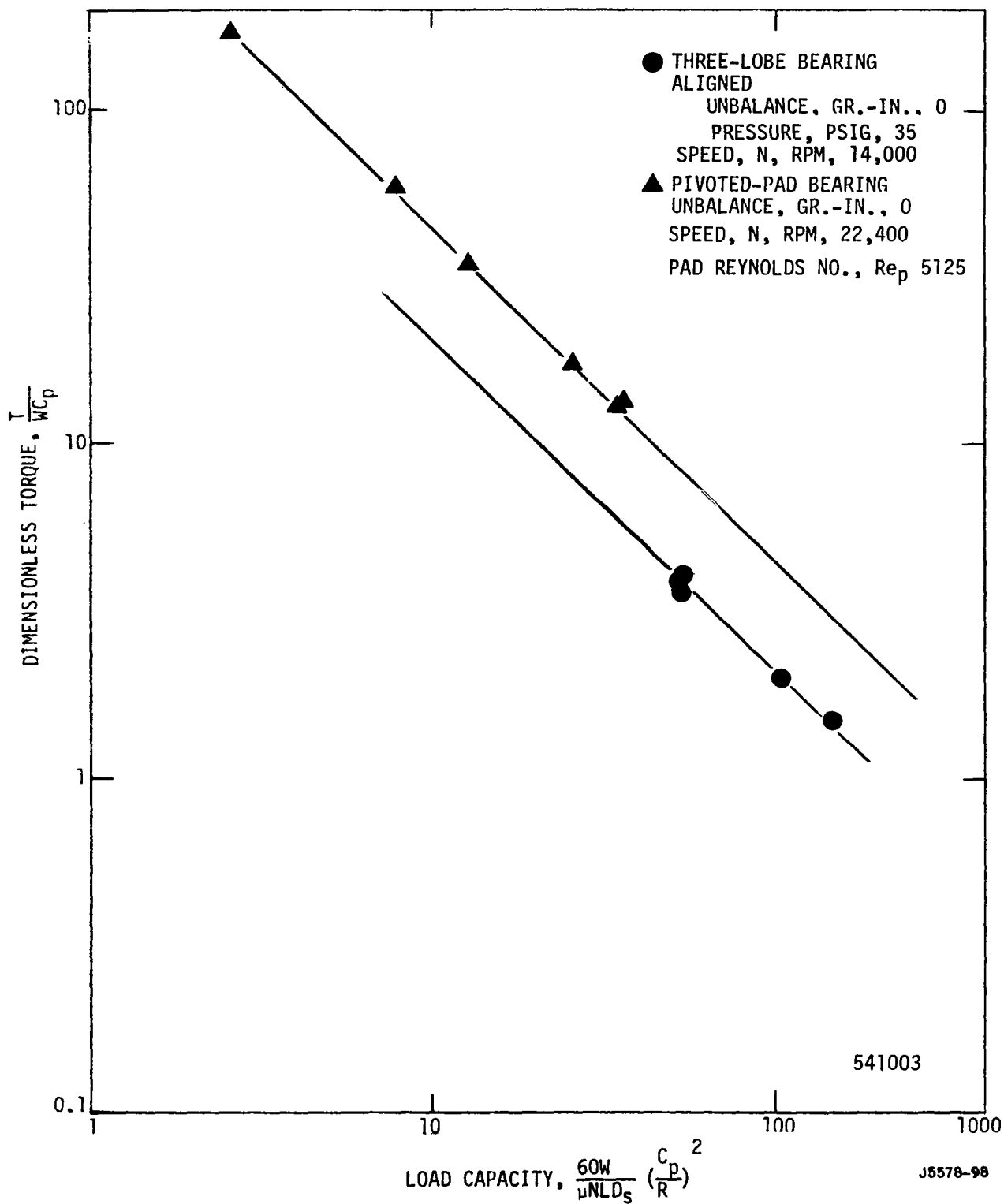
Figure 101. Comparison of Torque Variation for Pivoted-Pad and Three-Lobe Bearings.

186
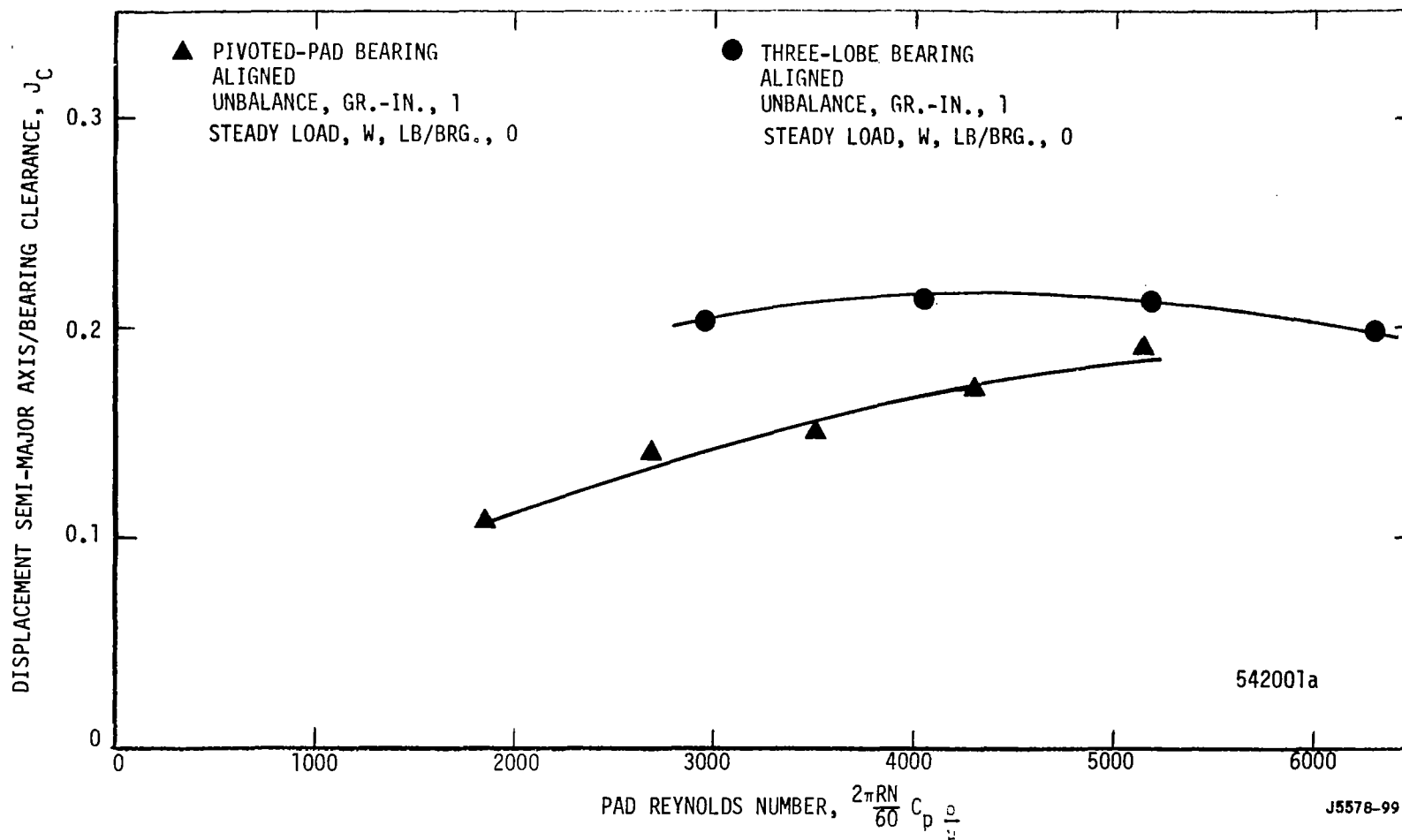
Figure 102. Comparison of Displacement Semi-Major Axis Variation for Pivoted-Pad
and Three-Lobe Bearings.

187
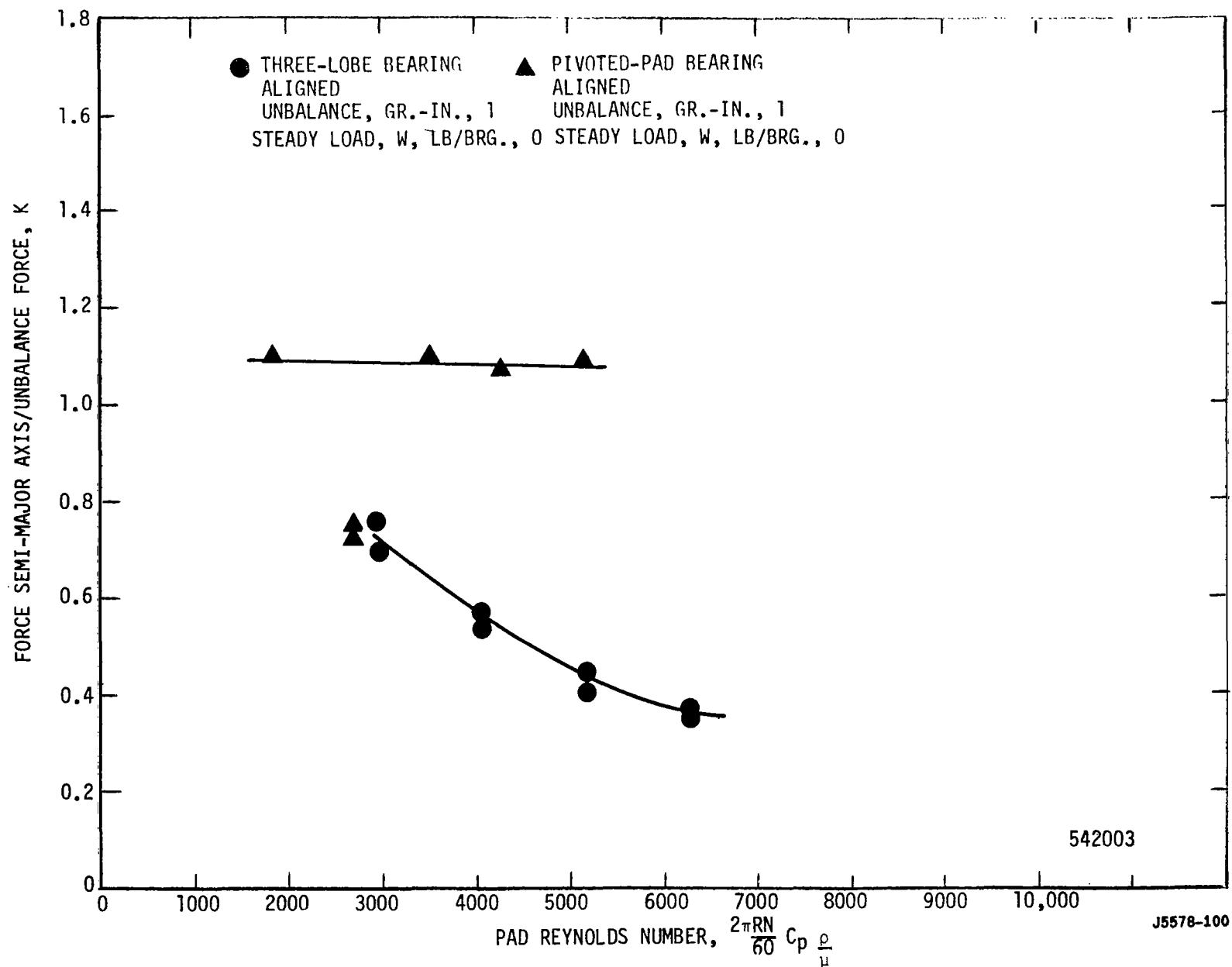
Figure 103. Comparison of Force Semi-Major Axis Variation for Pivoted-Pad and Three-Lobe Bearings

Shown in Figure 104 is a comparison of the maximum attainable speed for the three-lobe and pivoted-pad bearings aligned and at residual unbalance. The data is plotted against steady load. It is seen that the pivoted-pad bearing maximum attainable speed runs from about 27 to 30,000 rpm as the steady load increases from 0 to 70 lbs./bearing. Over the same range of steady load the maximum attainable speed of the three-lobe bearing differs by only about 2,000 rpm from 20,000 rpm. Shown in Figure 105 is a similar comparison with residual unbalance except in this instance both bearings have a total misalignment of 467 seconds. Here again it is apparent that the pivoted-pad bearing has a higher attainable speed than the three-lobe bearing. This difference amounts to as much as 10,000 rpm at a side load of 70 lbs./bearing and approximately 3,000 rpm at a steady load of zero.

D. **EXPERIMENTAL BEARING DYNAMIC COEFFICIENTS**

Theoretically in order to obtain bearing dynamic coefficients experimentally, the absolute x and y displacement and relative force amplitudes along with their phase angles must be obtained for two different dynamic test conditions at the same steady state conditions. For example the displacements, forces and phase angles could be obtained for the cases of symmetric and anti-symmetric unbalance. These data provide sufficient information to solve the eight simultaneous equations required for the determination of the eight dynamic bearing coefficients. The analysis leading to these dynamic coefficients from experimental data are presented in Reference 7.
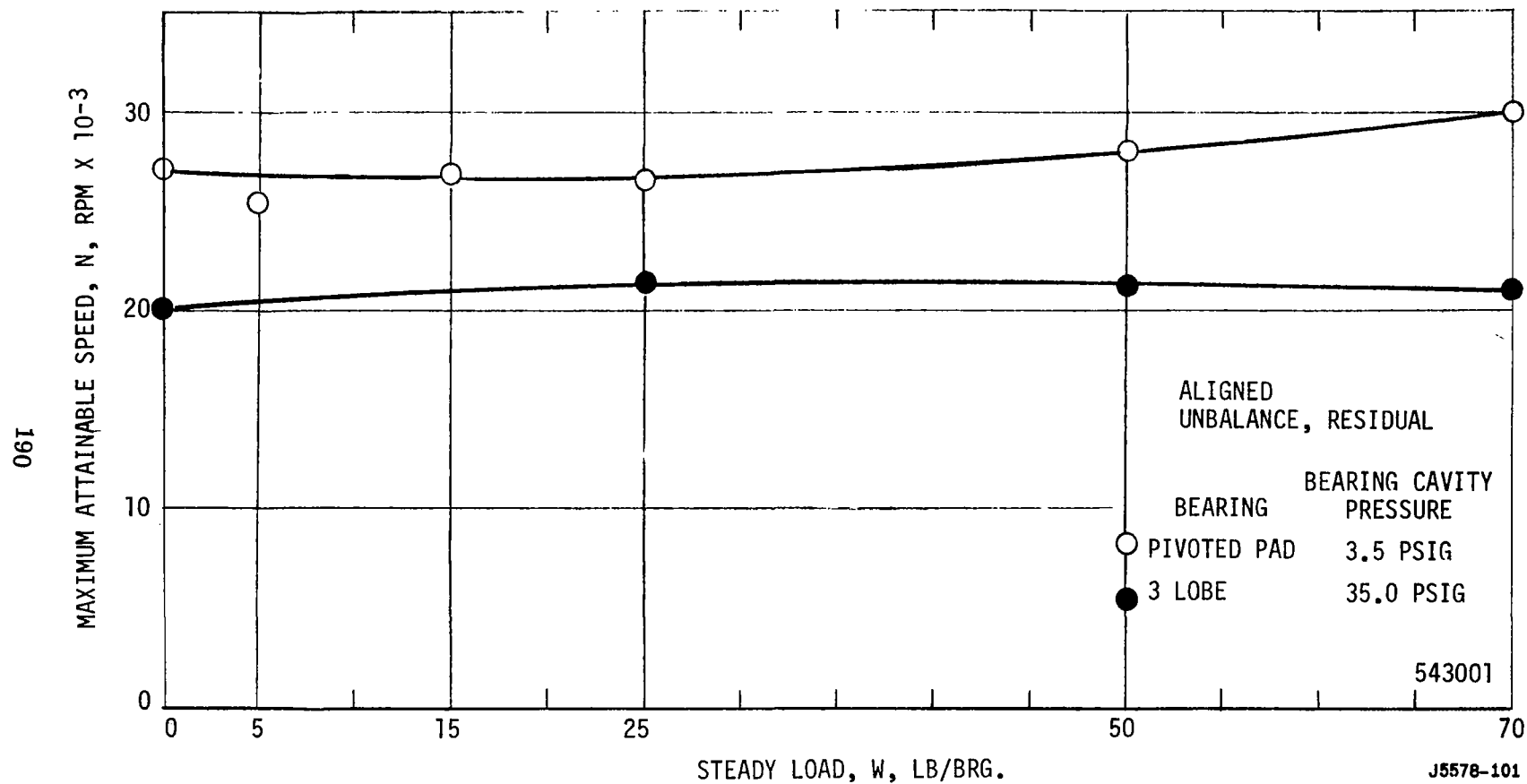
Figure 104. Comparison of the Maximum Attainable Speed Variation for Aligned
Pivoted-Pad and Three-Lobe Bearings.
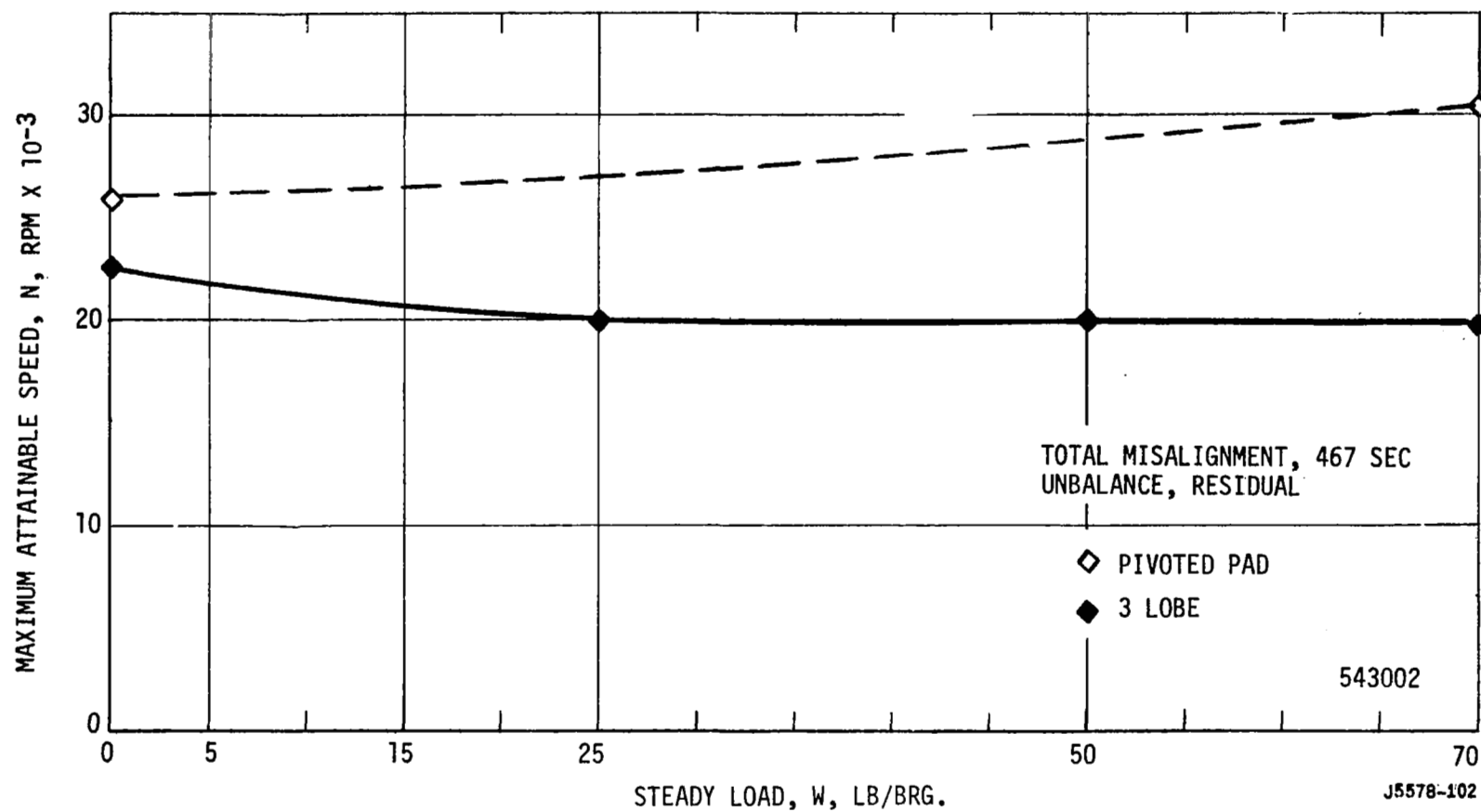
Figure 105. Comparison of Maximum Attainable Speed Variation for Misaligned Pivoted-Pad and Three-Lobe Bearings.

At least three approaches to the determination of the coefficients are available. The measured displacement and force amplitudes and phase angles can be used directly. This was tried and some bearing coefficients were obtained. However, these were not consistent and some values were negative without reason. The force measurements were suspected because of the larger scatter in force compared to displacement measurements and the large percentage change in the load-cell sensitivities before and after a test series.

A second approach is to calculate the forces that go with the measured displacements through the knowledge of the vibration characteristics of the shaft, determined analytically or experimentally. This method has been established but not checked out. The third approach is to provide and measure the response to known shaking forces applied through the frequency spectrum when the test unit is operating at a test condition of interest. This approach has been sucessfully applied to similar problems but has not been tried on the bearing test unit.

VIII. CONCLUSIONS AND RECOMMENDATIONS

In view of the experimental data presented in this report regarding the three-lobe bearing with a 5 mil diametral clearance and the pivoted-pad bearing with a 3.125 mil diametral clearance, the following conclusions were reached:

1. The pivoted-pad bearing is clearly superior to the three-lobe bearing in maximum attainable speed.

2. The pivoted-pad bearing is insensitive to misalignment and to the selective fixture of one pad at light steady loads.

3. The load capacity of the pivoted-pad bearing is the same as that of the three-lobe bearing.

4. The pivoted-pad bearing torque is 2.3 times the torque of the three-lobe bearing at the same load, speed, and diameter clearance.

The following recommendations are made for continuation of bearing technology.

1. Consider future effort to experimentally determine bearing dynamic coefficients. This would be an extension of the work initiated under this contract.

APPENDIX

DETERMINATION OF DISPLACEMENTS, FORCES AND PHASE ANGLES
FOR EXPERIMENTAL DATA

The relationship between displacement and force measurement axes is shown in Figure 106. The force measurement axes are designated by x and y and are positive in the directions shown. These axes are conventional in that the positive x axis is lined up with the positive direction of the steady load and the positive y axis is angularly displaced 90 degrees from the x axis in the direction of rotation. The displacement measurement axes are designated x' and y' and the positive directions of each are 45 degrees away from the positive x and y axes in a direction opposite rotation.

As indicated on Figure 1 there are two instrumentation planes equidistant (1.87 inches) from the central plane of each test bearing each containing displacement sensors and load cells. From these measurements average or equilibrium displacements, displacement and force amplitudes and phase angles must be determined at the central planes of each test bearing. In addition, the displacement measurements must be interpreted in the x-y plane rather than the x'-y' plane where the measurements were made. This appendix describes how these transformations were made. The symbols used are defined in the Nomenclature List at the end of the appendix.

Experimental data obtained from the bearing tests can be most easily interpreted in terms of the following harmonic equations:
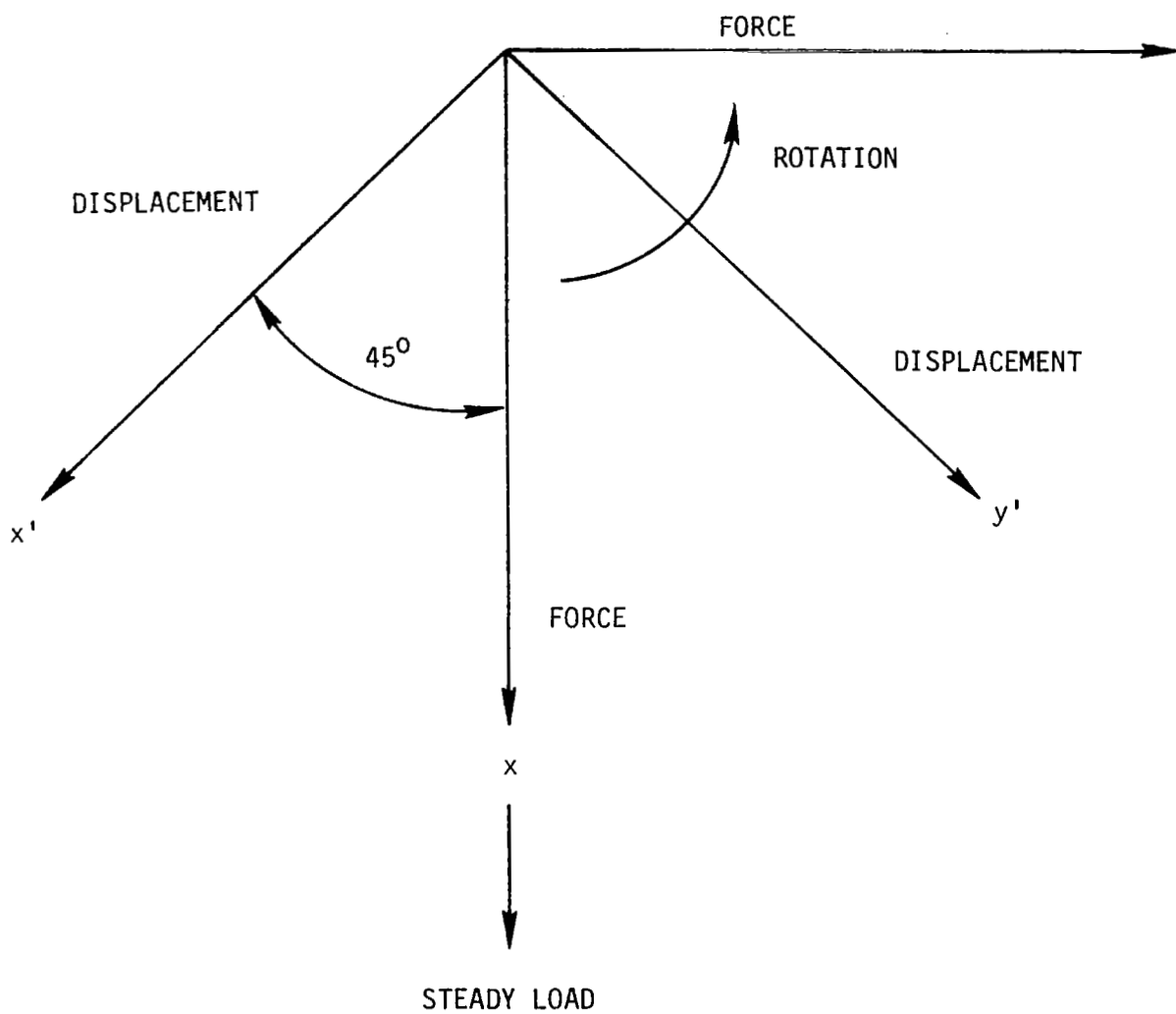
Figure 106. Relationship Between Displacement and Force
Measurement Axis.

$$x' = C'\cos(\omega t - \phi'_x)$$

$$y' = D'\sin(\omega t - \phi'_y)$$

$$F_x = G \cos(\omega t - \nu_x)$$

$$F_y = H \sin(\omega t - \nu_y) \tag{1}$$

where x' and y' are displacements with respect to an orthogonal set of measurement axes and F_x and F_y are forces with respect to measurement axes that do not necessarily coinside with the axes used for measuring displacements. The constants C', D', G and H are displacement and force amplitudes measured in the respective directions during testing and ϕ'_x, ϕ'_y, γ_x and γ_y are phase angles measured with respect to a common (ωt) reference angle. In the tests conducted, phase angles defined as Φ'_x and Φ'_y are measured which define a zero x' and y' amplitude, respectively, having a positive rate of change (slope) with respect to a zero amplitude point on a reference signal that also has a positive slope. Similar angles defined as Φ_{fx} and Φ_{fy} which determine zero force amplitudes in the x and y directions, respectively, are measured with respect to the same reference signal

Inspection of equation (1) shows that y' = 0 when (ωt) = ϕ'_y and that y' = 0+ when (ωt) = ϕ'_y+. This indicates that ϕ'_y is an angle where y' = 0 with a positively increasing value. This occurs when (ωt) = Φ'_y as measured in the bearing tests and therefore:

$$\phi'_y = \Phi'_y \tag{2}$$

By similar reasoning it can be shown that

$$\gamma_y = \Phi_{fy} \tag{3}$$

Equation (1) also shows that $x' = +C'$ when $(\omega t) = \phi_x'$. This occurs when $(\omega t) = \Phi_x' + 90°$ indicating that

$$\phi_x' = \Phi_x' + \frac{\pi}{2} \tag{4}$$

Similarly, it can be shown that

$$\gamma_x = \Phi_{fx} + \frac{\pi}{2} \tag{5}$$

Transformation of the Displacement Amplitudes and Phase Angles into the Force (x-y) Plane

The parametric equations of an ellipse whose major and minor axes are skew with respect to a reference x-y coordinate system are:

$$x = C \cos (\omega t - \beta - \xi_x) \tag{6}$$

$$y = D \sin (\omega t - \beta - \xi_y) \tag{7}$$

where

    C =   maximum $|x|$ in the reference coordinate system

    D =   maximum $|y|$ in the reference coordinate system

    ξ_x, =   phase angles such that the position vector lies on
    ξ_y one of the principal axes of the ellipse at $t = 0$

    β =   constant phase angle to shift the position vector to
          any arbitrary position at $t = 0$

197

It is important to note that for each different orientation of the reference coordinate system with respect to the principal axes of the ellipse, unique values for C, D, ξ_x and ξ_y exist.

Shown in Figure 107 is an ellipse with major and minor semi-axes A and B, respectively. This ellipse represents the motion path of the rotor during operation. Let the x'-y' coordinate system, located at a rotation angle of α_1 from the major axis of the ellipse, represent the coordinate system in which displacements are measured during testing. The maximum amplitude of displacement in this coordinate system would be C' and D' inches, respectively, in the x' and y' directions. Coordinate system x-y represents the direction in which forces are measured during testing and it is located at an angle of θ° with respect to the x'-y' coordinate system and at a rotation angle of α_2° with respect to the major axis of the ellipse. Amplitudes C and D represent the maximum displacements of the rotor in the x and y coordinate directions.

In order to compute the values of C, D, ξ_x and ξ_y in the x-y coordinate system in terms of the same measured parameters in the x'-y' coordinate system, it is necessary to develop some fundamental relationships for ellipses.

Shown in Figure 108 is an ellipse with an X-Y coordinate system aligned with the major and minor semi-axes A and B. Rotated at an angle α from the X-Y coordinate system is a second coordinate system with coordinate directions x-y. The parametric equation of the ellipse in the X-Y coordinate system are
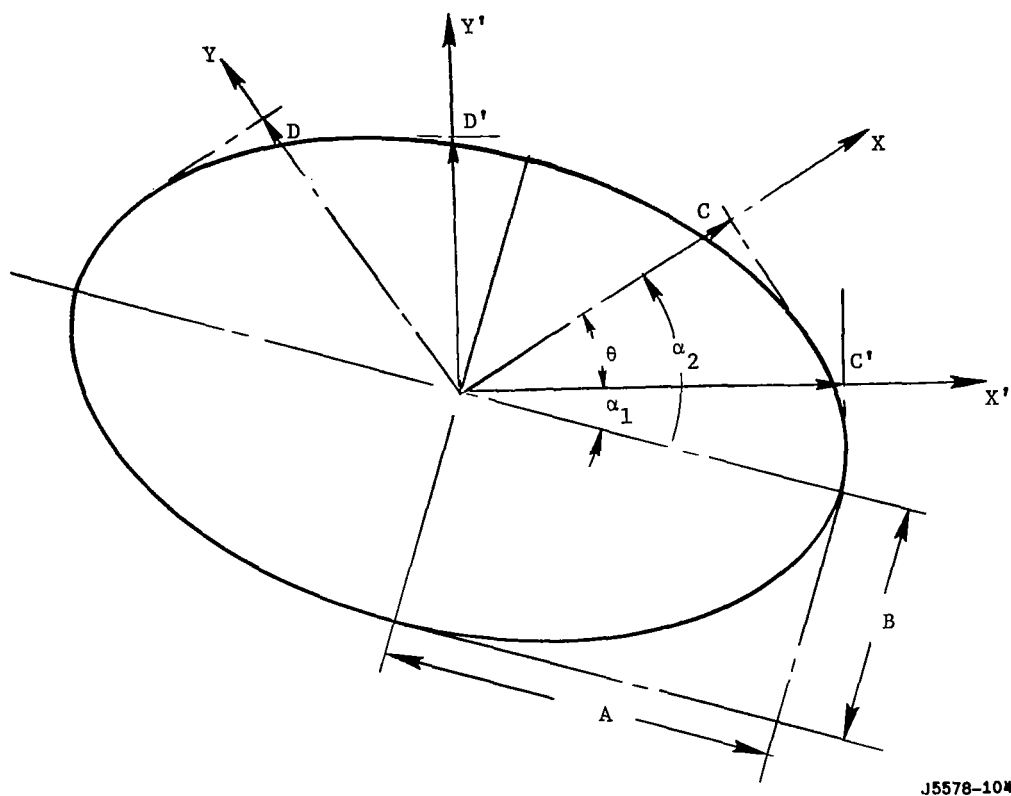
Figure 107. Elliptical Orbit Showing Displacement And Force Measuring Axis.
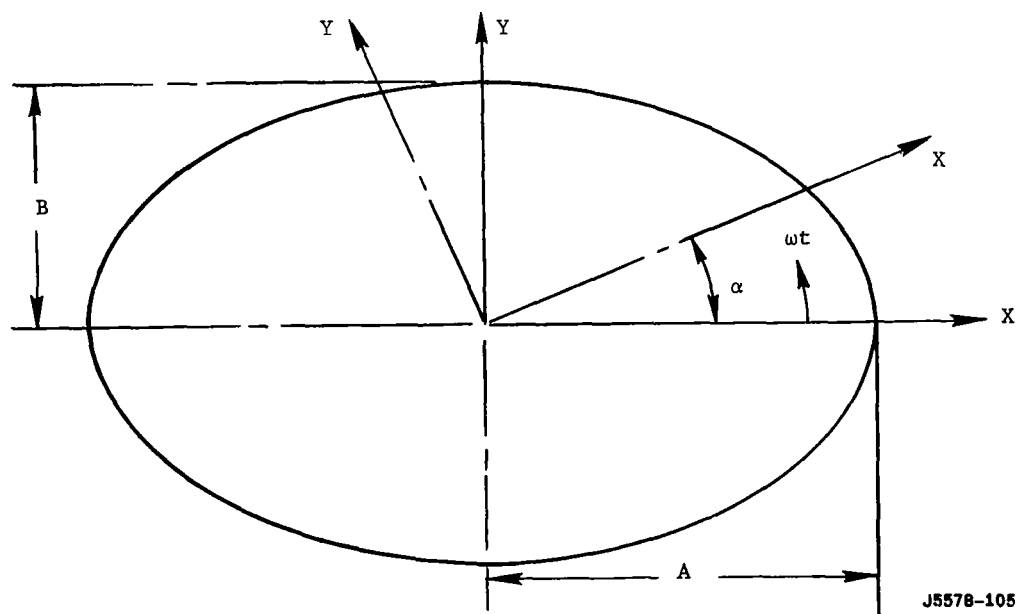
Figure 108. Geometrical Properties of Elliptical Orbit.

$$X = A \cos (\omega t) \tag{8}$$

$$Y = B \sin (\omega t) \tag{9}$$

where (ωt) is measured from the positive X axis.

The coordinate transformation from the X-Y to the x-y system is given by:

$$x = X \cos \alpha + Y \sin \alpha \tag{10}$$

$$y = - X \sin \alpha + Y \cos \alpha \tag{11}$$

Substituting equations (8) and (9) into equations (10) and (11) gives

$$x = A \cos (\omega t) \cos \alpha + B \sin (\omega t) \sin \alpha \tag{12}$$

$$y = - A \cos (\omega t) \sin \alpha + B \sin (\omega t) \cos \alpha \tag{13}$$

It is desired to express equations (12) and (13) in the following form:

$$x = C \cos (\omega t - \xi_x) \tag{14}$$

$$y = D \sin (\omega t - \xi_y) \tag{15}$$

Equating equations (12) and (14) gives the following

$$A \cos (\omega t) \cos \alpha + B \sin (\omega t) \sin \alpha = C \cos (\omega t - \xi_x) \tag{16}$$

When $\omega t = 0$, equation (16) becomes:

$$A \cos \alpha = C \cos (-\xi_x) = C \cos \xi_x \tag{17}$$

200

When $\omega t = \frac{\pi}{2}$, equation (16) becomes:

$$B \sin \alpha = C \cos \left(\frac{\pi}{2} - \xi_x\right) = C \sin \xi_x \tag{18}$$

Dividing equation (17) by equation (18) gives:

$$\frac{B \sin\alpha}{A \sin\alpha} = \frac{\sin \xi_x}{\cos \xi_x} = \tan \xi_x$$

or

$$\xi_x = \tan^{-1} \left[\frac{B}{A} \tan \alpha\right] \tag{19}$$

Also from equations (17) and (18) it is seen that

$$C = \frac{A \cos \alpha}{\cos \xi_x} = \frac{B \sin \alpha}{\sin \xi_x} \tag{20}$$

By equating equations (13) and (15) and using the same procedure, the following relationships are developed:

$$\xi_y = \tan^{-1} \left[\frac{A}{B} \tan \alpha\right] \tag{21}$$

$$D = \frac{A \sin \alpha}{\sin \xi_y} = \frac{B \cos \alpha}{\cos \xi_y} \tag{22}$$

The following useful identities can be obtained from equations (20) and

$$C \cos \xi_y = A \cos \alpha$$

$$D \cos \xi_y = B \cos \alpha$$

Squaring both sides and adding the above equations gives:

$$C^2\cos^2\xi_x + D^2\cos^2\xi_y = (A^2 + B^2)\cos^2 \alpha \tag{23}$$

The following relations are also obtained from equations (20) and (22):

$$C \sin \xi_x = B \sin \alpha$$

$$D \sin \xi_y = A \sin \alpha$$

Again, squaring both sides and adding the above equations, gives:

$$C^2 \sin^2 \xi_x + D^2 \sin^2 \xi_y = (A^2 + B^2) \sin^2 \alpha \tag{24}$$

Adding equations (23) and (24) gives.

$$C^2 (\sin^2 \xi_x + \cos^2 \xi_x) + D^2 (\sin^2 \xi_y + \cos^2 \xi_y) = (A^2 + B^2)(\sin^2 \alpha + \cos^2 \alpha)$$

which gives the identity

$$A^2 + B^2 = C^2 + D^2 \tag{25}$$

Since A and B are constant for a given ellipse, it is seen that the sum of the square of the x and v amplitudes for any arbitrary orientation of the coordinate axes is always a constant.

Using the trigonometric identity

$$\cos(\xi_x - \xi_y) = \cos \xi_x \cos \xi_y + \sin \xi_x \sin \xi_y$$

and the following relations from equations (20) and (22)

$$\sin \xi_x = \frac{B}{C} \sin \alpha$$

$$\cos \xi_x = \frac{A}{C} \cos \alpha$$

$$\sin \xi_y = \frac{A}{D} \sin \alpha$$

$$\cos \xi_y = \frac{B}{D} \cos \alpha \tag{26}$$

the following result can be obtained:

$$\cos(\xi_x - \xi_y) = \frac{AB}{CD} \sin^2 \alpha + \frac{AB}{CD} \cos^2 \alpha$$

or

$$\cos(\xi_x - \xi_y) = \frac{AB}{CD} \tag{27}$$

The final important identity is developed from the trigonometric equation

$$\sin(\xi_x - \xi_y) = \sin\xi_x \cos\xi_y - \cos\xi_x \sin\xi_y$$

Substituting equation (26) into the above expression gives

$$\sin(\xi_x - \xi_y) = \frac{B^2}{CD} \sin \alpha \cos \alpha - \frac{A^2}{CD} \sin \alpha \cos \alpha$$

or

$$\sin(\xi_x - \xi_y) = \frac{(B^2 - A^2)}{CD} \sin \alpha \cos \alpha = \frac{B^2 - A^2}{2CD} \sin 2\alpha$$

From this expression, the rotational angle is obtained as

$$\alpha = \frac{1}{2} \sin^{-1} \left[\frac{2CD}{A^2 - B^2} \sin(\xi_y - \xi_x) \right] \tag{28}$$

Returning now to Figure 107, it will be assumed that values for the displacement amplitudes C' and D' are known from test data. Also values for ϕ_x' and ϕ_y' have been determined from the test results. Referring to equations (1), (6) and (7) it is seen that the measured phase angles ϕ_x' and ϕ_y' are the same as the angles $(\theta + \xi_x)$ and $(\theta + \xi_y)$ and that

$$\phi_x' = \theta + \xi_x \tag{29}$$

$$\phi_y' = \theta + \xi_y \tag{30}$$

Subtracting the above equations gives

$$(\zeta_x' - \zeta_y') = \phi_x' - \phi_y' \tag{31}$$

The measured information mentioned above is now used to compute C, D, ϕ_y and ϕ_x for the x-y coordinate system. From equations (25), (27), and (31) the following expressions are obtained:

$$A^2 + B^2 = (C')^2 + (D')^2 \tag{32}$$

$$AB = C'D'\cos(\phi_x' - \phi_y') \tag{33}$$

Solving equations (32) and (33) for A and B gives

$$A = \sqrt{\frac{1}{2}\left[(C')^2 + (D')^2\right]\left\{1 + \sqrt{1 - 4\left(\frac{C'D'\cos(\phi_x' - \phi_y')}{(C')^2 + (D')^2}\right)^2}\right\}} \tag{34}$$

$$B = \sqrt{(C')^2 + (D')^2 - A^2} \tag{35}$$

The rotation angle α_1 is obtained from equation (28)

$$\alpha_1 = \frac{1}{2}\sin^{-1}\left[\frac{2C'D'}{A^2 - B^2}\sin(\phi_y' - \phi_x')\right] \tag{36}$$

Phase angles ζ_x' and ζ_y' are obtained from equations (19) and (21)

$$\zeta_x' = \tan^{-1}\left[\frac{B}{A}\tan\alpha_1\right] \tag{37}$$

$$\zeta_y' = \tan^{-1}\left[\frac{A}{B}\tan\alpha_1\right] \tag{38}$$

From Figure 107 the rotational angle α_2 for the x-y coordinate system is given as:

$$\alpha_2 = \theta + \alpha_1 \tag{39}$$

The phase angles ξ_x and ξ_y in the second coordinate system are computer using the α_2 rotational angle computed by equation (39)

$$\xi_x = \tan^{-1}\left[\frac{B}{A} \tan \alpha_2\right] \tag{40}$$

$$\xi_y = \tan^{-1}\left[\frac{A}{B} \tan \alpha_2\right] \tag{41}$$

Using the preceeding information, the required constants for the parametric equations of the elliptical path in the x-y coordinate systems are:

$$C = \frac{A \cos \alpha_2}{\cos \xi_x} \tag{42}$$

$$D = \frac{A \sin \alpha_2}{\sin \xi_y} \tag{43}$$

$$\phi_x = \phi_x' + \xi_x - \xi_x' \tag{44}$$

$$\phi_y = \phi_y' + \xi_y - \xi_y' \tag{45}$$

Transformation of the Displacement and Force Amplitudes and
Phase Angles to the Bearing Central Plane

The displacements of the rotor at the central plane of the bearing will be computed from the displacements measured at the inboard and outboard instrumentation planes. A simple linear variation of displacement will be assumed.

Denoting displacement measurement at the two ends of the bearing by the subscripts 1 and 2, the following equations describe the measured motions in the x-direction.

$$x_1 = C_1\cos(\omega t - \phi_{x1}) \tag{46}$$

$$x_2 = C_2\cos(\omega t - \phi_{x2}) \tag{47}$$

Assuming a linear variation in displacement between the ends of the bearing, the displacement at the bearing center is expressed as:

$$x_c = \frac{1}{2}(x_1 + x_2)$$

or

$$x_c = \frac{1}{2}\left[C_1\cos(\omega t - \phi_{x1}) + C_2\cos(\omega t - \phi_{x2})\right] \tag{48}$$

It is desired to express x_c in the form:

$$x_c = C_c\cos(\omega t - \phi_{xc}) \tag{49}$$

The constant C_c and ϕ_{xc} can be determined by equating equations (48) and (49) and solving to obtain:

$$C_c = \frac{1}{2}\sqrt{(C_1)^2 + (C_2)^2 + 2C_1C_2\cos(\phi_{x1} - \phi_{x2})} \tag{50}$$

and

$$\phi_{xc} = \tan^{-1}\left[\frac{C_1\sin\phi_{x1} + C_2\sin\phi_{x2}}{C_1\cos\phi_{x1} + C_2\cos\phi_{x2}}\right] \tag{51}$$

Starting with the following two equations for rotor displacement in the y-direction at the ends of the bearing

$$y_1 = D_1\sin(\omega t - \phi_{y1}) \tag{52}$$

$$y_2 = D_2\sin(\omega t - \phi_{y2}) \tag{53}$$

and assuming y-displacement at the bearing center to be described by the
equation

$$y_c = D_c \sin(\omega t - \phi_{yc}) \tag{54}$$

the D_c and ϕ_c coefficients can be obtained as follows:

$$D_c = \frac{1}{2} \sqrt{(D_1)^2 + (D_2)^2 + 2D_1 D_2 \cos(\phi_{y1} - \phi_{y2})} \tag{55}$$

and

$$\phi_{yc} = \tan^{-1}\left[\frac{D_1 \sin\phi_{y1} + D_2 \sin\phi_{y2}}{D_1 \cos\phi_{y1} + D_2 \cos\phi_{y2}}\right] \tag{56}$$

A single force value will be obtained by vectorially adding the force
components measured at the inboard and outboard instrumentation planes. In
a manner similar to that used for displacement amplitude and starting with
the following equations for measured force components at the instrumentation
planes

$$F_{x1} = G_1 \cos(\omega t - \nu_{x1})$$

$$F_{y1} = H_1 \sin(\omega t - \nu_{y1})$$

$$F_{x2} = G_2 \cos(\omega t - \nu_{x2})$$

$$F_{y2} = H_2 \sin(\omega t - \nu_{y2}) \tag{57}$$

the following expressions for the resultant total force at the center of
the bearing can be obtained:

$$F_{xc} = G_c \cos(\omega t - \nu_{xc}) \tag{58}$$

207

$$F_{yc} = H_c \sin(\omega t - \gamma_{yc}) \tag{59}$$

where

$$G_c = \sqrt{G_1^2 + G_2^2 + 2G_1 G_2 \cos(\gamma_{x1} - \gamma_{x2})} \tag{60}$$

$$\gamma_{xc} = \tan^{-1} \left[\frac{G_1 \sin\gamma_{x1} + G_2 \sin\gamma_{x2}}{G_1 \cos\gamma_{x1} + G_2 \cos\gamma_{x2}} \right] \tag{61}$$

$$H_c = \sqrt{H_1^2 + H_2^2 + 2H_1 H_2 \cos(\gamma_{y1} - \gamma_{y2})} \tag{62}$$

$$\gamma_{yc} = \tan^{-1} \left[\frac{H_1 \sin\gamma_{y1} + H_2 \sin\gamma_{y2}}{H_1 \cos\gamma_{y1} + H_2 \cos\gamma_{y2}} \right] \tag{63}$$

Force Ellipse Quantities

In a manner similar to that for displacements, except that no rotation of axes is required, the parameters defining the force ellipse at the bearing central plane are derived; they are

$$A_F = \sqrt{\frac{1}{2} \left[G_c^2 + H_c^2 \right] \left\{ 1 + \sqrt{1 - 4 \left(\frac{G_c H_c \cos(\gamma_{xc} - \gamma_{yc})}{G_c^2 + H_c^2} \right)^2} \right\}} \tag{64}$$

$$B_F = \sqrt{G_c^2 + H_c^2 - A_F^2} \tag{65}$$

$$\alpha_1 = \frac{1}{2} \sin^{-1} \left[\frac{2G_c H_c}{A_F^2 - B_F^2} \sin(\gamma_{yc} - \gamma_{xc}) \right] \tag{66}$$

Equilibrium Displacements

The conversion from the x'-y' plane to the x-y plane is made as follows:

$$\bar{x} = \bar{x}' \cos(45°) + \bar{y}' \sin(45°) \tag{67}$$

$$\bar{y} = \bar{y}' \cos(45°) - \bar{x}' \sin(45°) \tag{68}$$

The eccentricity and the attitude angle of the shaft at the central plane of the bearing are given by

$$e = \left[\left(\frac{\bar{x}_1 + \bar{x}_2}{2} \right)^2 + \frac{y_1 + y_2}{2}^2 \right]^{1/2} \tag{69}$$

$$\Gamma = \tan^{-1} \left[\frac{y_1 + y_2}{x_1 + x_2} \right] \tag{70}$$

A   displacement semi-major axis, in.

A_F force semi-major axis, lb.

B   displacement semi-minor axis, in.

BF   force semi-minor axis, lb.

C   x-displacement amplitude in x-y force plane, in.

C'   x-displacement amplitude in x'-y' plane, in.

C_B bearing radial assembled clearance, in.

C_C x-displacement amplitude in (x-y) plane at bearing central plane, in.

C_L loader bearing radial machined clearance, in.

C_P pad (or lobe) radial machined clearance, in.

D   y-displacement amplitude in x-y force plane, in.

D'   y-displacement amplitude in x'-y' (displacement) plane, in.

D_C y-displacement amplitude in (x-y) force plant at bearing central plane, in.

D_L diameter of the loader bearing journal, in.

D_S diameter of the test bearing shaft, in.

e   shaft eccentricity, in.

F_x x-component of fluid-film force, lb.

F_y y-component of fluid-film force, lb.

F_{xc} x-component of fluid-film force at bearing central plane, lb.

F_{yc} y-component of fluid-film force at bearing central plane, lb.

G   x-force amplitude, lb.

G_C x-force amplitude at bearing central plane, lb.

g   gravitational constant, 386 in/sec^2

H   y-force amplitude, lb.

H_C y-force amplitude at bearing central plane, lb.

J   ratio of displacement semi-major axis to displacement of center of gravity

J_C ratio of displacement semi-major axis to bearing clearance

K   ratio of force semi-major axis to unbalance force

L   test-bearing length, in.

L_L loader-bearing length, in.

M_C shaft moment coefficient

N   rotative speed, rpm

P   pad lubricant pressure, psig

R   shaft radius, in.

Re_p Reynolds number

R_L loader bearing journal radius, in.

S   Sommerfeld number

S_L loader-bearing Sommerfeld number

t   time, sec.

T   torque per test bearing, in-lb.

T_L torque per loader bearing, in-lb.

U   journal peripheral speed, in/sec.

U_L loader bearing journal peripheral speed, in/sec.

u   rotor unbalance per bearing, lb-in.

W   steady load per bearing, lb.

$\bar{W}$ load parameter

W_S shaft weight, lb.

x   displacement amplitude in force plane (x-y), in.

x' displacement amplitude in displacement plane (x'-y'), in.

X   coordinate of an ellipse, in.

x_c displacement amplitude at bearing central plane, in.

$\bar{x}$ average (equilibrium) displacement in x-y plane, in.

y   displacement amplitude in force plane (x-y), in.

y'   displacement amplitude in displacement plane (x'-y'), in.

Y   coordinate of an ellipse, in.

y_c displacement amplitude in force plane (x-y), in.

$\bar{y}$ average (equilibrium) displacement in (x-y) plane, in.

α angle between x and X axis, deg.

α_1 angle between semi-major axis and x' axis, deg.

α_2 angle between semi-major axis and X axis, deg.

β constant phase angle to shift position vector to any arbitrary position at t = 0, deg.

γ_x x-force phase angle, deg.

γ_{xc} x-force phase angle at bearing central plane, deg.

γ_y y-force phase angle, deg.

γ_{yc} y-force phase angle at bearing central plane, deg.

Γ attitude angle, deg.

ϵ_B bearing eccentricity ratio

θ angle between x- and x'-axis, deg.

μ lubricant viscosity, lb sec/in^2

ξ_x x-phase angle in x-y plane such that position vector lies on principal axis of ellipse at t = 0, deg.

$\xi_{x'}$ x-phase angle in x'-y' plane such that position vector lies on principal axis of ellipse at t = 0, deg.

212

ξ_y y-phase angle in x-y plane such that position vector lies on principal axes of ellipse at t = 0, deg.

$\xi_{y'}$ y-phase angle in x'-y' plane such that position vector lies on principal axes of ellipse at t = 0, deg.

ρ lubricant density, lb.sec.^{2}/in.^{4}

τ dimensionless torque parameter

ϕ_x x-displacement phase angle in x-y plane, deg.

$\phi_{x'}$ x-displacement phase angle in x'-y' plane, deg.

ϕ_{xc} x-displacement phase angle at bearing central plane, deg.

Φ_x' measured x-phase angle in x'-y' plane, deg.

Φ_{Fx} measured force x-phase angle in x-y plane, deg.

ϕ_y y-displacement phase angle in x-y plane, deg.

ϕ_y' y-displacement phase angle in x'-y' plane, deg.

ϕ_{yc} y-displacement phase angle at bearing central plane, deg.

Φ_y' measured y-phase angle in x'-y' plane, deg.

Φ_{Fy} measured force y-phase angle in x-y plane, deg.

ω angular velocity, rad./sec.

REFERENCES

1. J.D. McHugh: Low Viscosity Bearing Stability Investigation, Final Report, NASA-CR-54039, October 1961 - December 1963.

2. H.E. Nichols, R.J. Rossbach, W.H. Bennethum, J.C. Amos, and W.D.C. Richards: Hydrodynamic Journal Bearing Program, Quarterly Progress Report No. 4, NASA-CR-72068, January-April 1966.

3. H.E. Nichols, W.D.C. Richards, R.J. Rossbach, and W.H. Bennethum: Hydrodynamic Journal Bearing Program, Quarterly Progress Report No. 6, NASA-CR-72175, July-October 1966.

4. H.E. Nichols, W.D.C. Richards, R.J. Rossbach, and W.H. Bennethum: Hydrodynamic Journal Bearing Program, Quarterly Progress Report No. 5, NASA-CR-72160, April-July 1966.

5. J.D. McHugh, H.E. Nichols and W.D.C. Richards: Hydrodynamic Journal Bearing Program, Quarterly Progress Report No. 3, NASA-CR-72034, October-January 1966.

6. J.D. McHugh, H.E. Nichols, W.D.C. Richards, and H.C. Lee: Hydrodynamic Journal Bearing Program, Quarterly Progress Report No. 2, NASA-CR-72033, July-October 1965.

7. F.K. Orcutt: Steady-Stage and Dynamic Properties of Journal Bearings in Laminar and Superlaminar Flow Regimes, NASA-CR-732, April 1967.

REFERENCES (Continued)

8. G.I. Taylor: Stability of a Viscous Liquid Contained Between Two

    Rotating Cylinders. Phil. Trans. Ray. Soc. (London), Series A,

    Volume 223, 1923.

9. H. Schlichting (J. Kistin): Boundary Layer Theory. McGraw-Hill,

    New York, 1960.